Universidade de Aveiro
Departamento de Electrónica, Telecomunicações e Informática
2020

Sherif Adeshina Busari

Ondas milimétricas e MIMO massivo para otimização da capacidade e cobertura de redes heterogeneas de 5G

Millimeter-wave Massive MIMO for Capacity-Coverage Optimization in 5G Heterogeneous Networks

Programa de Doutoramento em Telecomunicações das Universidades do Minho, Aveiro e Porto

Universidade do Minho

universidade de aveiro

U.PORTO
FEUP FACULDADE DE ENGENHARIA
UNIVERSIDADE DO PORTO

Sherif Adeshina Busari

Ondas milimétricas e MIMO massivo para otimização da capacidade e cobertura de redes heterogeneas de 5G

Tese apresentada às Universidades do Minho, Aveiro e Porto para cumprimento dos requesitos necessários à obtenção do grau de Doutor em Telecomunicações no âmbito do programa doutoral MAP-Tele, realizada sob a orientação científica do Doutor Jonathan Rodríguez González, Investigador Principal do Instituto de Telecomunicações, Universidade de Aveiro.

Apoio financeiro da Fundação para a Ciência e a Tecnologia (FCT), Portugal através da bolsa com a referéncia PD/BD/113823/2015.

Sherif Adeshina Busari

Millimeter-wave Massive MIMO for Capacity-Coverage Optimization in 5G Heterogeneous Networks

A thesis submitted to the Universities of Minho, Aveiro and Porto in partial fulfilment of the requirements for Doctoral degree in Telecommunications under the MAP-Tele doctoral program. The thesis was conducted under the supervision of Doctor Jonathan Rodríguez González, Principal Researcher, Instituto de Telecomunicações, Universidade de Aveiro.

This work is supported by the Fundação para a Ciência e a Tecnologia (FCT), Portugal under the grant with reference number PD/BD/113823/2015.

o júri / the jury

presidente / president

Doutor Vitor Brás de Sequeira Amaral
Professor Catedrático
Universidade de Aveiro
(por delegação do Reitor da Universidade de Aveiro)

vogais / examiners committee

Doutora Noélia Susana Costa Correia
Professora Auxiliar
Departamento de Engenharia Electrónica e Informática
Universidade do Algarve

Doutor Ramiro Sámano Robles
Research Associate
CISTER Research Centre
Instituto Superior de Engenharia do Porto

Doutor Aníbal Manuel de Oliveira Duarte
Professor Catedrático
Departamento de Electrónica, Telecomunicações e Informática
Universidade de Aveiro

Doutor Alexandre Júlio Teixeira Santos
Professor Associado com Agregação
Departamento de Informática
Universidade do Minho

Doutor Jonathan Rodríguez González
Investigador Principal (Orientador)
Instituto de Telecomunicações
Universidade de Aveiro

agradecimentos / acknowledgments

This PhD journey has been both exciting and challenging, and many people and entities have contributed in varied capacities towards this phase of my life. First, my gratitude goes to my Supervisor Prof. Jonathan Rodríguez González for granting me the opportunity to undertake the PhD program under his worthy supervision. His mentorship and support have been of great benefit to me. He always provides timely, painstaking and valuable feedbacks on my work, and I have benefitted immensely from his pool of knowledge and expertise. Next, I would like to express my sincere appreciation to Dr. Shahid Mumtaz and Dr. Kazi Mohammed Saidul Huq for all the help, guidance, supervision and motivation throughout the period. Your technical and non-technical support were invaluable. It has been a great honor to work with both of you. Also, my appreciation goes to Ms. Cláudia Barbosa for her assistance and prompt actions in resolving all administrative issues and to António Morgado for his timely help in translating the title and abstract of this thesis to portuguese. The chair and members of the jury are highly appreciated for their valuable time in reviewing this thesis and providing insightful comments.

I acknowledge and deeply appreciate the financial support (PhD Scholarship - PD/BD/113823/2015) that I received from the Fundação para a Ciência e a Tecnologia (FCT), Portugal. Also, the work in this thesis has been supported by two European Commission H2020 projects (SPEED-5G and 5GENESIS), the THz-BEGUN project of FCT/MEC, and the European Regional Development Fund (FEDER), through COMPETE 2020, POR ALGARVE 2020, FCT under i-Five Project (POCI-01-0145-FEDER-030500). Next, I extend my gratitude to the management and staff of the Instituto de Telecomunicações (IT), Aveiro, Portugal for providing the enabling environment to undertake the research, and also to the MAP-Tele Doctoral program scientific committee. All the members of the Mobile Systems/4TELL Research Group of IT are appreciated. I also appreciate many friends and colleagues who have contributed in one way or the other during the period, particularly Dr. Isiaka Alimi, Dr. Oluyomi Aboderin, Engr. Akeem Mufutau and Engr. Stephen Ogodo as well as their respective families. I am very grateful to the Federal University of Technology Akure (FUTA), Nigeria for granting me study leave to pursue the PhD program. All staff of the Electrical and Electronics Engineering department of FUTA are deeply appreciated for their support. Also, I thank Prof. Buliaminu Kareem and Prof. Akinlabi Oyetunji of FUTA for their immense help.

I appreciate the tremendous love, prayers and support of my parents; Mr. Lateef Ayoola Busari and Mrs. Musiliat Kehinde Busari, my siblings and in-laws. I am highly and deeply indebted to my wife Hafsah Olajumoke Sulaimon. Thank you for your love, support, understanding, encouragement and prayers. I am also indebted to my lovely children; Hameedah, Muhammad and Mahfuz for tolerating my busy schedule during the program. Above all, my gratitude goes to God, the Almighty, for His countless blessings. He says: *"And He gave you of all that you asked for, and if you count the Blessings of Allāh, never will you be able to count them ...."* Qur'ān 14 vs 34.

Palavras-chave

Canal 3D, 5^a geração, agregados com formatação de feixe híbrida, MIMO massivo, ondas milimétricas, redes celulares ultra densas

Resumo

As redes LTE-A atuais não são capazes de suportar o crescimento exponencial de tráfego que está previsto para a próxima década. De acordo com a previsão da Ericsson, espera-se que em 2020, a nível global, 6 mil millhões de subscritores venham a gerar mensalmente 46 exabytes de tráfego de dados a partir de 24 mil milhões de dispositivos ligados à rede móvel, sendo os telefones inteligentes e dispositivos IoT de curto alcance os principais responsáveis por tal nível de tráfego. Em resposta a esta exigência, espera-se que as redes de 5^a geração (5G) tenham um desempenho substancialmente superior às redes de 4^a geração (4G) atuais. Desencadeado pelo UIT (União Internacional das Telecomunicações) no âmbito da iniciativa IMT-2020, o 5G irá suportar três grandes tipos de utilizações: banda larga móvel capaz de suportar aplicações com débitos na ordem de vários Gbps; comunicações de baixa latência e alta fiabilidade indispensáveis em cenários de emergência; comunicações massivas máquina-a-máquina para conectividade generalizada. Entre as várias tecnologias capacitadoras que estão a ser exploradas pelo 5G, as comunicações através de ondas milimétricas, os agregados MIMO massivo e as redes celulares ultra densas (RUD) apresentam-se como sendo as tecnologias fundamentais. Antecipa-se que o conjunto destas tecnologias venha a fornecer ás redes 5G um aumento de capacidade de $1000\times$ através da utilização de maiores larguras de banda, melhoria da eficiência espectral, e elevada reutilização de frequencias respectivamente. Embora estas tecnologias possam abrir caminho para as redes sem fios com débitos na ordem dos gigabits, existem ainda vários desafios que têm que ser resolvidos para que seja possível aproveitar totalmente a largura de banda disponível de maneira eficiente utilizando abordagens de formatação de feixe e de modelação de canal adequadas. Nesta tese investigamos a melhoria de desempenho do sistema conseguida através da utilização de ondas milimétricas e agregados MIMO massivo em cenários de redes celulares ultradensas de 5^a geração e em cenários 'infrastrutura celular-para-qualquer coisa' (do inglês: cellular infrastructure-to-everything) envolvendo utilizadores pedestres e veículares. Como um componente fundamental das simulações de sistema utilizadas nesta tese é o canal de propagação, implementámos modelos de canal tridimensional (3D) para caracterizar de forma precisa o canal de propagação nestes cenários e assim conseguir uma avaliação de desempenho mais condizente com a realidade. Para resolver os problemas associados ao custo do equipamento, complexidade e consumo de energia das arquiteturas MIMO massivo, propomos um modelo inovador de agregados com formatação de feixe híbrida. Este modelo genérico revela as oportunidades que podem ser aproveitadas através da sobreposição de sub-agregados no sentido de obter um compromisso equilibrado entre eficiência espectral (ES) e eficiência energética (EE) nas redes 5G. Os principais resultados desta investigação mostram que a utilização conjunta de ondas milimétricas e de agregados MIMO massivo possibilita a obtenção, em simultaneo, de taxas de transmissão na ordem de vários Gbps e a operação de rede de forma energeticamente eficiente.

Keywords 3D channel, 5G, hybrid beamforming, massive MIMO, mmWave, UDN

Abstract

Today's Long Term Evolution Advanced (LTE-A) networks cannot support the exponential growth in mobile traffic forecast for the next decade. By 2020, according to Ericsson, 6 billion mobile subscribers worldwide are projected to generate 46 exabytes of mobile data traffic monthly from 24 billion connected devices, smartphones and short-range Internet of Things (IoT) devices being the key prosumers. In response, 5G networks are foreseen to markedly outperform legacy 4G systems. Triggered by the International Telecommunication Union (ITU) under the IMT-2020 network initiative, 5G will support three broad categories of use cases: enhanced mobile broadband (eMBB) for multi-Gbps data rate applications; ultra-reliable and low latency communications (URLLC) for critical scenarios; and massive machine type communications (mMTC) for massive connectivity. Among the several technology enablers being explored for 5G, millimeter-wave (mmWave) communication, massive MIMO antenna arrays and ultra-dense small cell networks (UDNs) feature as the dominant technologies. These technologies in synergy are anticipated to provide the $1000\times$ capacity increase for 5G networks (relative to 4G) through the combined impact of large additional bandwidth, spectral efficiency (SE) enhancement and high frequency reuse, respectively. However, although these technologies can pave the way towards gigabit wireless, there are still several challenges to solve in terms of how we can fully harness the available bandwidth efficiently through appropriate beamforming and channel modeling approaches. In this thesis, we investigate the system performance enhancements realizable with mmWave massive MIMO in 5G UDN and cellular infrastructure-to-everything (C-I2X) application scenarios involving pedestrian and vehicular users. As a critical component of the system-level simulation approach adopted in this thesis, we implemented 3D channel models for the accurate characterization of the wireless channels in these scenarios and for realistic performance evaluation. To address the hardware cost, complexity and power consumption of the massive MIMO architectures, we propose a novel generalized framework for hybrid beamforming (HBF) array structures. The generalized model reveals the opportunities that can be harnessed with the overlapped subarray structures for a balanced trade-off between SE and energy efficiency (EE) of 5G networks. The key results in this investigation show that mmWave massive MIMO can deliver multi-Gbps rates for 5G whilst maintaining energy-efficient operation of the network.

Table of Contents

List of Acronyms

1G	First generation
2D	Two-dimensional
3D	Three-dimensional
3G	Third generation
3GPP	Third generation partnership project
4G	Fourth generation
5G	Fifth generation
6G	Sixth generation
ABF	Analog beamforming
AE	Antenna element
AI	Artificial intelligence
AoA	Angle of arrival
AoD	Angle of departure
AP	Access point
AS	Angular spread
AWGN	Additive white Gaussian noise
B5G	Beyond-5G
BBU	Baseband unit
BS	Base station
C-I2P	Cellular infrastructure-to-pedestrian
C-I2V	Cellular infrastructure-to-vehicle
C-I2X	Cellular infrastructure-to-everything
C-V2X	Cellular vehicle-to-everything
CL	Coupling loss
CN	Condition number
CSI	Channel state information
DBF	Digital beamforming
DL	Downlink
DoF	Degree of freedom
DS	Delay spread
DSRC	Dedicated short-range communication
ECDF	Empirical cumulative distribution function

EE	Energy efficiency
eMBB	Enhanced mobile broadband
GF	Geometry factor
HBF	Hybrid beamforming
HetNet	Heterogeneous network
HPBW	Half power beamwidth
i.i.d	Independent and identically distributed
I2I	Indoor-to-indoor
ICI	Inter-cell interference
IMT	International mobile telecommunications
IoT	Internet of things
ISD	Inter-site distance
ITS	Intelligent transport system
ITU	International telecommunication union
KF	K-Factor
KPI	Key performance indicator
LIS	Large intelligent surface
LLS	Link level simulator
LOS	Line of sight
LSP	Large-scale parameter
LTE-A	Long term evolution-advanced
MAC	Medium access control
MC	Macrocell
MIMO	Multiple-input multiple-output
ML	Machine learning
mMTC	Massive machine type communications
mmWave	Millimeter-wave
MPC	Multipath component
MU-MIMO	Multi-user MIMO
MUI	Multi-user interference
NF	Noise figure
NGMN	Next-generation mobile network
NLOS	Non-LOS
NLS	Network level simulator
NR	New radio
O2I	Outdoor-to-indoor
O2O	Outdoor-to-outdoor
OFDM	Orthogonal frequency division multiplexing
PDP	Power delay profile
PHY	Physical layer

PL	Path loss
PLE	Path loss exponent
PS	Phase shifter
QML	Quantum machine learning
RAN	Radio access network
RB	Resource block
RF	Radio frequency
RIS	Reconfigurable intelligent surface
RMS	Root-mean-square
RSRP	Reference signal received power
RX	Receiver
SC	Small cell
SCM	Spatial channel model
SE	Spectral efficiency
SF	Shadow fading
SINR	Signal to interference plus noise ratio
SIR	Signal to interference ratio
SISO	Single-input single-output
SLS	System level simulator
SNR	Signal to noise ratio
SP	Subpath
SSCM	Statistical spatial channel model
SSF	Small-scale fading
SSP	Small-scale parameter
SVD	Singular value decomposition
THz	Terahertz
TTI	Transmission time interval
TX	Transmitter
UDN	Ultra-dense network
UE	User equipment
ULA	Uniform linear array
UMa	Urban macrocell
UMi	Urban microcell
UPA	Uniform planar array
URLLC	Ultra-reliable and low latency communications
V2I	Vehicle-to-infrastructure
V2V	Vehicle-to-vehicle
WiFi	Wireless fidelity
WRC	World radiocommunications conference
ZF	Zero forcing

List of Symbols

B	Bandwidth
B_c	Coherence bandwidth
G_o	Maximum boresight gain
G_{AE}	Antenna element gain
G_{RX}	RX antenna gain
G_{TX}	TX antenna gain
J	Number of BSs
K	Number of UEs
L	Number of rays or MPCs
N_{RX}	Number of RX antenna elements
N_{RX}^{RF}	Number of RX RF chains
N_{TX}	Number of TX antenna elements
N_{TX}^{RF}	Number of TX RF chains
N_{UE}	Number of UEs
N_{cl}	Number of clusters
N_o	Thermal noise power density
N_{sp}	Number of subpaths/MPCs
N_{sub}^{RX}	Number of RX elements in a subarray
N_{sub}^{TX}	Number of TX elements in a subarray
N_s	Number of streams
$PL_{\mathbf{eff}}$	Effective PL
PL_{max}	Maximum PL
P_{BH}	Power consumption of the backhaul
P_{LOS}	LOS probability
P_{RAN}	Power consumption of the RAN
P_{RX}	Receive power
P_T	Transmit power
P_{total}	Total power consumptionn of the network
T_c	Channel correlation time
T_t	Data transmission time
T_u	Channel update time
Ω_{TX}	Density of TXs
$\bar{n}$	Path loss exponent
$\mathbf{H}$	Channel matrix
$\mathbf{n}$	Noise vector
$\mathbf{x}$	Transmit signal vector

$\triangle N$	Subarray spacing
η_{EE}	Energy efficiency
η_{SE}	Spectral efficiency
λ	Wavelength
$(\cdot)^H$	Conjugate transpose operator
ϕ_{3dB}	Azimuth 3dB HPBW
ρ	Normalized transmit power
σ	Noise
σ_n^2	Noise power
τ	Propagation time delay
θ_{3dB}	Elevation 3dB HPBW
Θ	Distance-dependent phase change
φ	Phase
ϑ	Velocity-induced Doppler shift
ξ	Average antenna efficiency
d	Distance
d_{2D-in}	2D indoor distance
d_{2D-out}	2D outdoor distance
d_{3D}	3D distance
d_r	Road distance
f_D	Doppler frequency
f_c	Carrier frequency
h_{RX}	RX height
h_{TX}	TX height
h_{dir}	Directional CIR
v_{RX}	Velocity of users

List of Figures

List of Tables

List of Algorithms

Chapter 1

Introduction

This chapter introduces the main concepts investigated in this thesis. It provides an overview on massive MIMO, millimeter-wave communication and ultra-dense small cell network as three key technologies for enhancing the performance of next-generation mobile networks, building on the initial release of 5G. This provides the context for the motivation and objectives of this thesis, the scientific methodology applied for the investigation and the thesis contributions. The chapter ends with the organization of the thesis which presents an executive summary of the concepts covered and elaborated in later chapters.

1.1 Introduction

Since the early 80's, operators and regulators of mobile wireless communication systems roll out a new generation of cellular networks almost every decade. The year 2020 is expected to herald a new dawn with the introduction and possible commercial deployment of the fifth generation (5G) cellular networks that will significantly outperform prior generations (i.e., from the first generation (1G) to the fourth generation (4G)). Widespread adoption of 5G networks is anticipated by 2025. The 5G era is foreseen to usher in next-generation mobile networks (NGMNs) that will deliver super high speed connectivity coupled with higher reliability and spectral efficiency (SE), and lower energy consumption than today's legacy networks. The aim is to evolve a cellular network that remarkably pushes forward the limits of legacy mobile networks across all key performance indicators (KPIs). This is motivated by a mix of economic demands (mobile traffic growth, cost, energy, etc.) and socio-technical concerns (health, environment, technological advances, etc.) which render current standards and systems unsustainable [1, 2].

The 5G networks, also known as the international mobile telecommunications (IMT)-2020, are anticipated to support three broad categories of use cases, namely: enhanced mobile broadband (eMBB), ultra-reliable and low latency communications (URLLC) and massive machine type communications (mMTC) [3]. The eMBB use case targets mobile broadband services requiring high data rates and cell capacities (e.g., cellular mobile and vehicular networks); URLLC is for scenarios with stringent reliability and latency requirements (e.g., medical and public safety applications); and mMTC targets massive connectivity based on the internet of things (IoT) paradigm [4]. The minimum technical requirements for 5G have been approved in [5] and a summary of the KPIs for the uses cases is given in [3].

For the downlink (DL) eMBB use case in dense urban 5G scenarios, which is the main

focal point of this thesis, the minimum target values according to the international telecommunication union (ITU) radiocommuication standard [5] include: 20 Gbps (peak data rate), 100 Mbps (user experienced data rate), 30 bps/Hz (peak SE), 0.225 bps/Hz (5% user SE) and 7.8 bps/Hz/TRxP (average SE), among others [3]. The ambitious goals set for 5G networks, as compared to the 4G long term evolution-advanced (LTE-A) systems include: 1000× higher mobile data traffic per geographical area, 100× higher typical user data, 100× more connected devices, 10× lower network energy consumption and 5× reduced end-to-end (E2E) latency [6, 7].

Between 1G and 4G, mobile networks have moved from analog to digital, voice-only to multimedia (voice and data), circuit-switched to packet-switched networks, and from 2.4 kbps throughput to a peak data rate of 100 Mbps (for highly-mobile users) and up to 1 Gbps (for stationary/pedestrian users) [6, 8]. With the introduction of several architectural and technology changes, 5G aims to markedly surpass the performance of legacy networks and its evolution has been highly dynamic migrating from research and field trials to standardization and real deployments, around 2020 and beyond. Moreover, sixth generation (6G) networks research is starting to ramp up. The 6G networks are expected to address the shortcomings of 5G networks and surpass their performance across all KPIs. The evolution from 1G to 6G is illustrated in Figure 1.1. A quantitative comparison of the key performance metrics of 4G networks with the corresponding targets for 5G and 6G networks are shown in Table 1.1.

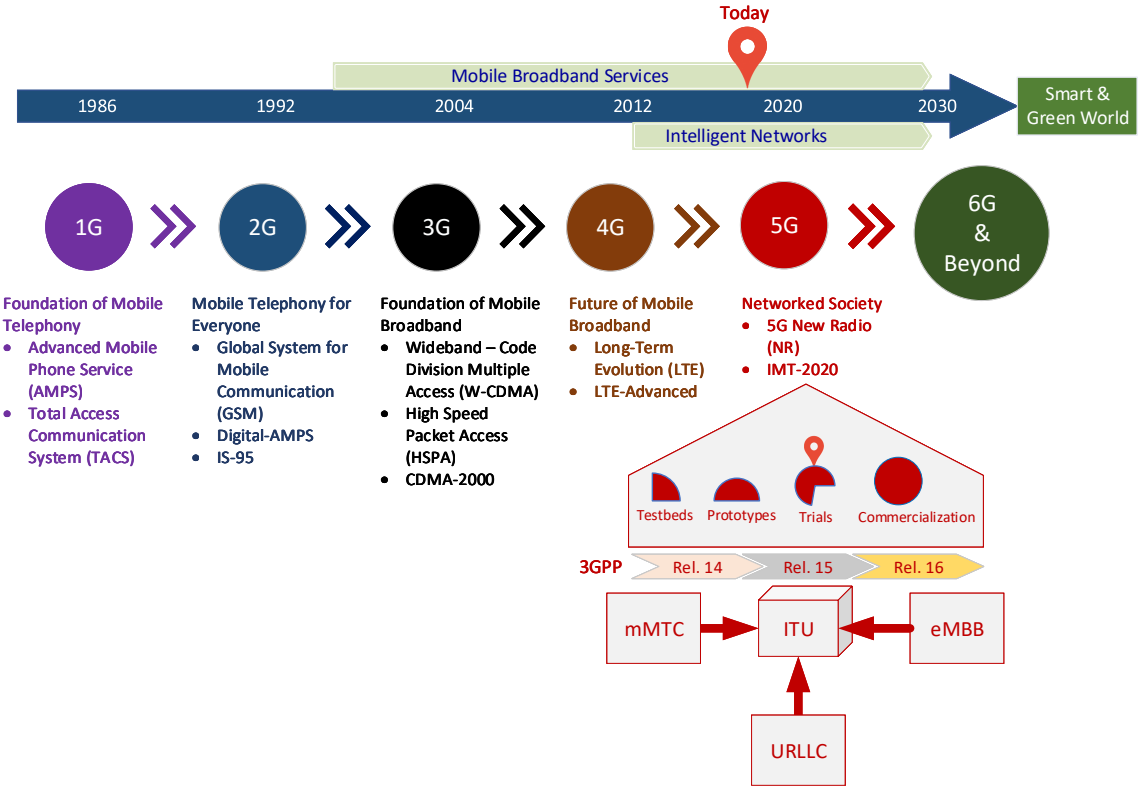

Figure 1.1: Evolution of mobile wireless communication from 1G to 6G (adapted from [9]).

Table 1.1: Performance comparison of 4G, 5G and 6G networks (adapted from [1, 2, 10–13]).

Performance metrics	**4G**	**5G**	**6G**
Peak data rate (Gbps)	1	20	1000
User experienced data rate (Gbps)	0.01	1	100
Connection density (devices/km^2)	10^5	10^6	10^{16}
Mobility support (kmph)	350	500	1000
Area traffic capacity (Mbit/s/m^2)	0.1	10	50
Latency (ms)	10	5	0.1
Reliability (%)	99	99.999	99.99999
Positioning accuracy (m)	1	0.1	0.01
Spectral efficiency (bps/Hz)	3	10	100
Network energy efficiency (J/bit)*	1	0.01	0.001
**Normalized with 4G value.*			

To realize the promising set targets, several enabling technologies are being explored for 5G. The ten key enablers are shown in Figure 1.2. The dominant technology that consistently features in the list of enablers is the millimeter-wave (mmWave) massive multiple-input multiple-output (MIMO) system. It is a promising technology that combines the prospects of huge available bandwidth in the mmWave spectrum (30-300 GHz) with the expected gains from massive MIMO arrays (with several tens or hundreds of antenna elements (AEs)) enabling the opportunity to deliver the anticipated and stringent peak data rates envisaged for 5G [2].

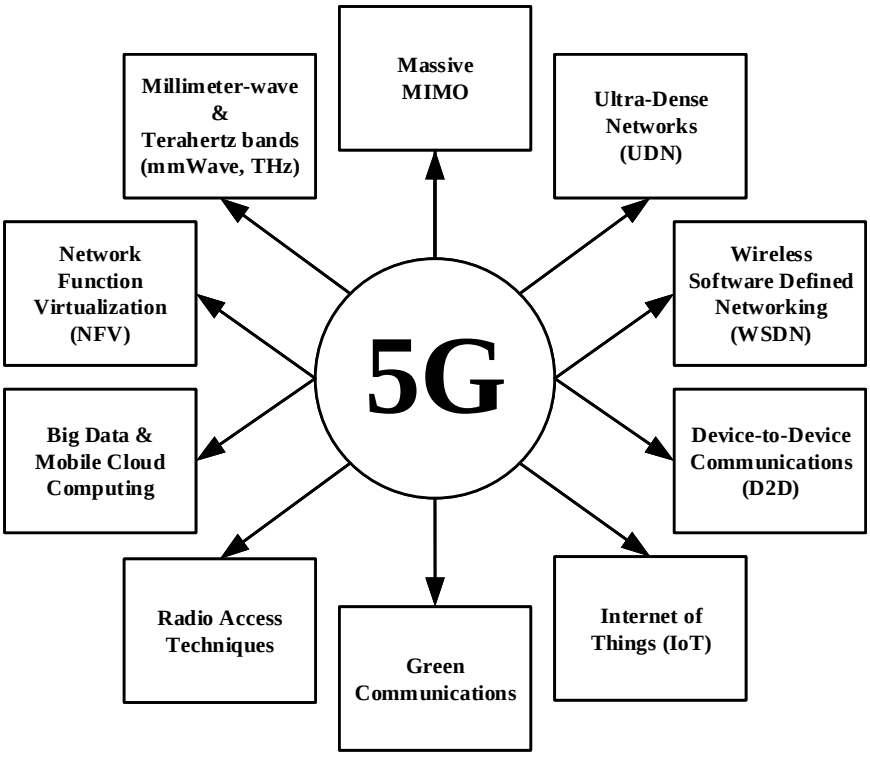

Figure 1.2: The ten key enabling technologies for 5G (adapted from [14]).

When the mmWave massive MIMO technology is used in the heterogeneous network (HetNet) topology (involving a dense deployment of small cells (SCs) within the coverage area of the umbrella macrocell (MC), otherwise referred to as the ultra-dense network (UDN)), 5G networks can be projected to reap the benefits of the three enablers on a very large scale, and thereby support a plethora of high-speed services and bandwidth-hungry applications not hitherto possible [15]. These three enablers (mmWave, massive MIMO and UDN) constitute the subject of investigation in this thesis.

1.2 Overview of the Big Three Enablers

Future cellular systems (5G and beyond) will employ the so-called "big three" technologies: (i) mmWave communications (employing large quantities of new bandwidth); (ii) massive MIMO (using many more antennas to facilitate throughput gains in the spatial dimension); and (iii) UDN (featuring extreme densification of infrastructure). The expected capacity gains from these technologies are due to the combined impact of large additional spectrum, SE enhancement and high frequency reuse, respectively [16]. These three enablers will lead to several orders of magnitude in throughput gain with the goal to support the explosive demand for mobile broadband services foreseen for the next decade. In the following, we provide a brief overview of the three technologies.

1.2.1 Millimeter-Wave Communications

The mmWave frequency band (i.e., the extremely high frequency (EHF) range of the electromagnetic (EM) spectrum representing 30-300 GHz and corresponding to wavelength 1-10 mm) has an abundant bandwidth of up to 252 GHz. With a reasonable assumption of 40% availability over time [17], these mmWave bands will possibly open up $\sim$100 GHz new spectrum for mobile broadband applications. In this spectrum block, about 23 GHz bandwidth is being identified for mmWave cellular in the 30-100 GHz bands, excluding the 57-64 GHz oxygen absorption band which is best suited for indoor fixed wireless communications (i.e., the unlicensed 60 GHz band). As a key enabler for the multi-gigabit-per-second (Gbps) wireless access in NGMNs, mmWave wireless connectivity offers extremely high data rates to support many applications such as short-range communications, vehicular networks, and wireless in-band fronthauling/backhauling, among others [18].

1.2.2 Massive MIMO

Massive MIMO is a technology which scales up the number of AEs by several orders of magnitude in constrast to conventional MIMO systems (i.e., from up to 8 to ≥ 64) [19], thus capitalizing on the benefits of MIMO on a much larger scale [20]. It has the potential to increase the capacity of mobile networks in manifolds through aggressive spatial multiplexing while simultaneously improving the radiated energy efficiency (EE). Using the excess degree of freedom (DoF) resulting from the large number of antennas, massive MIMO can harness the available space resources to improve SE. Moreover, with the aid of beamforming, it can also suppress interference by directing energy to desired terminals only. This avoids fading dips and thereby reduces the latency on the air interface [21, 22]. When deployed in the mmWave regime, the corresponding downscaling of the massive MIMO antennas drastically reduces cost and power, not only by using low-cost low-power components, but also by eliminating

expensive and bulky components (such as large coaxial cables) and high-power radio frequency (RF) amplifiers at the front-end [8, 20].

1.2.3 Ultra-Dense Networks

UDN refers to the hyper-dense deployment of SC base stations (BSs) within the coverage areas of the MC BSs. It has been identified as the single most effective way to increase network capacity based on its potentials to significantly raise throughput, increase SE and EE as well as enhance seamless coverage for cellular networks [15]. In decreasing order of capabilities, SCs are classified as metro-, micro-, pico- or femtocells based on power range, coverage distance and the number of concurrent users to be served. The rationale behind them is to bring users physically close to their serving BSs to enable higher data rates. The overlay of SCs on traditional MCs leads to a multi-tier HetNet where the host MC BSs handle more efficiently control plane signaling (e.g., resource allocation, synchronization, mobility management, etc.) while the SC BSs provide high-capacity and spectrally-efficient data plane services to the users [6]. This HetNet topology has the potential to deliver many benefits. It increases network capacity based on increased cell density and high spatial and frequency reuse. Moreover, it enhances SE based on improved average signal to interference plus noise ratio (SINR) with tighter interference control. It also improves EE based on reduced transmission power and lower path loss (PL) resulting from the shorter distance between each user equipment (UE) and its serving BS [6, 15, 23–26]. The three enablers exhibit a symbiotic relationship as illustrated in Figure 1.3.

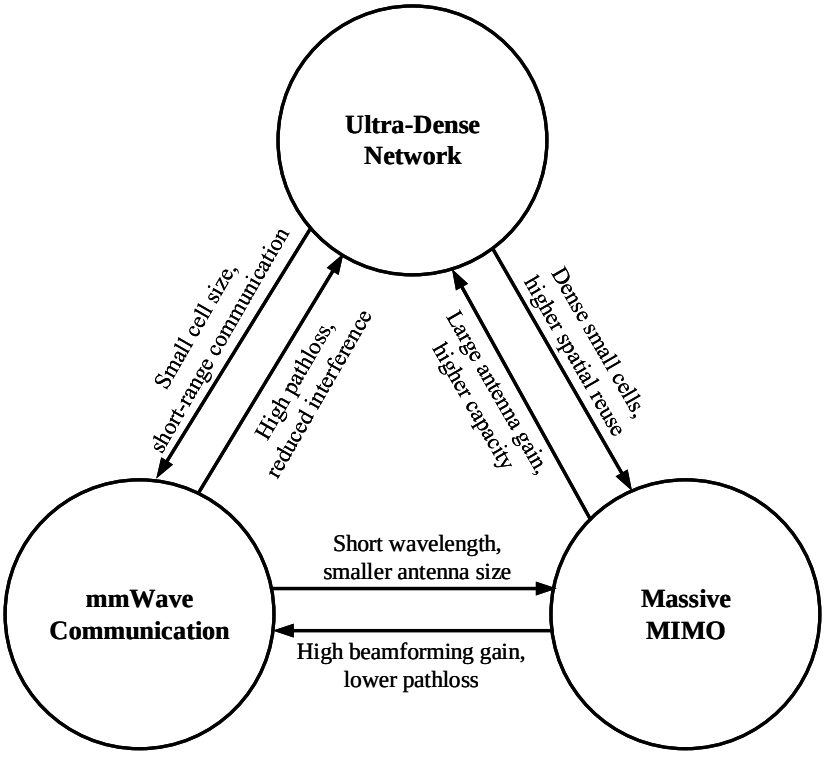

Figure 1.3: The symbiotic cycle of the three prominent 5G enablers.

Overall, these three technology enablers are complementary in many respects. Large swathes of bandwidth required for 5G needs the mobile network to migrate to higher frequencies, especially the promising mmWave (and terahertz (THz)) bands. These high frequencies require many antennas to overcome the PL in such an environment. Furthermore, higher frequencies need smaller cells to mitigate blockage and PL effects, and the effects in turn cause the interference due to densification to decay quickly [23]. The amalgam of the three features produces the HetNet architecture and the mmWave massive MIMO paradigm that have emerged as key subjects of research for 5G and beyond. This promising architecture is poised to open up new frontiers of services and applications for NGMNs. It shows potentials to significantly raise user throughput, enhance the systems' SE and EE as well as increase the capacity of mobile networks using the joint capabilities of the three enablers.

1.3 Thesis Motivation

Several emerging use cases are being identified to address the explosive traffic demand in NGMNs, where the worldwide monthly traffic is projected to grow from 5 exabytes (EB) in 2015 to 136 EB by 2024 as shown in Figure 1.4. A large chunk of the traffic will be generated indoors, and through video applications [27].

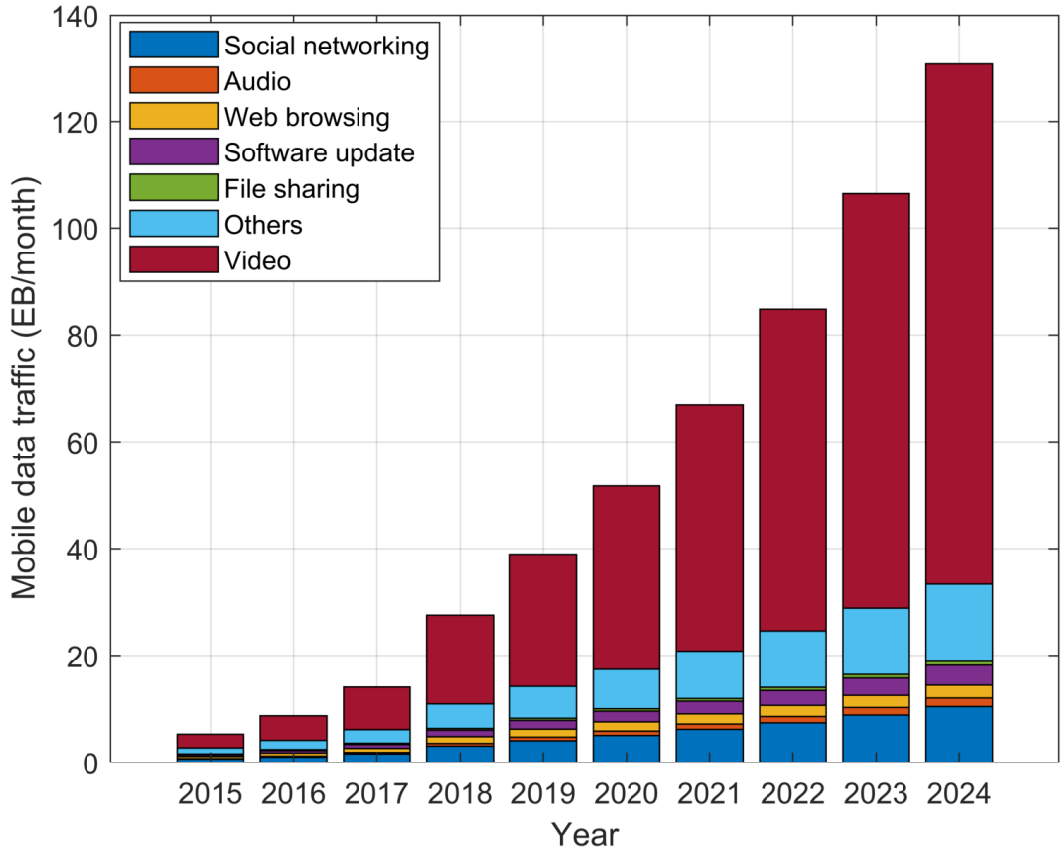

Figure 1.4: Mobile traffic forecast for 2015-2024 (adapted from [28]).

In urban metropolitan cities with dense high-rise buildings, UEs are distributed on different floors. Thus, the propagation environment becomes three-dimensional (3D) where users need to be separated not only in the azimuth (horizontal) domain, but also in the elevation (vertical) domain [29]. In addition, SCs will be densely deployed to serve as the high rate hotspot tier while the MC serves as the coverage tier. This UDN architecture that is illustrated in Figure 1.5 (on next page) is one of the two scenarios investigated in this thesis.

While the system model in Figure 1.5 requires 3D channel models, the legacy networks and the traditional massive MIMO systems employ two-dimensional (2D) channel models with antenna array elements arranged linearly in the azimuth direction only [30]. However, 2D channel models underestimate system performance [31–34] as they do not account for array features such as elevation beamforming. The extra spatial DoF provided by the elevation domain enables interference mitigation, leading to considerable increase in SE [30]. Thus, 3D channel models are critical for the accurate and realistic performance characterization of 5G networks. The challenge, therefore, is to extend the modeling approach to the elevation domain and evaluate the system performance of the 3D 5G UDNs.

Another important scenario for 5G is the cellular vehicle-to-everything (C-V2X) paradigm, where "X" could be a vehicle, infrastructure, grid, network, pedestrian user, etc. This thesis, however, focuses on the cellular infrastructure-to-everything (C-I2X) paradigm that is shown in Figure 1.6n (on next page). In this second scenario, lampost-based access points (APs) are used to provide ultra-broadband connectivity to pedestrian users, high mobility vehicles and/or a combination of both. Applying mmWave spectrum at street-level sites is currently being explored for capacity improvement in 5G networks and for offloading traffic from the regular BSs [35].

While the 5G UDN and C-I2X architectures can provide higher system capacities, they intuitively imply higher overall power consumption due to dense deployment of infrastructure. However, 5G networks are required to be green, soft and super-fast (i.e., energy-efficient, self-organizing and high-rate, respectively) [36]. Thus, energy-efficient design schemes that will minimize the power consumption in order to lower the networks' energy utilization and carbon dioxide (CO_2) gas emission footprints are critical [37]. Therefore, antenna array architectures and algorithms that can deliver ultra-high data rates whilst maintaining a balanced trade-off in EE, as well as hardware cost and complexity of the network are critical design goals and thus key research challenges.

Motivated by these challenges, the subject of investigation of this thesis is the interplay of mmWave communication and massive MIMO that targets towards capacity and coverage optimization of 5G networks. We focus specifically on the implementation of 3D μWave and mmWave channels, design and analyses of beamforming schemes with massive MIMO arrays, and system-level performance evaluation of the networks in UDN and C-I2X application scenarios, with a view to enhancing cell throughputs and delivering cost-effective, energy-efficient and super high speed connectivity in realizing the 5G goals.

1.4 Thesis Objectives

The goal of this research is to optimize the capacity and coverage of 5G cellular networks for cost-effective and ultra-high speed wireless connectivity. Motivated by this goal, the research objectives are to:

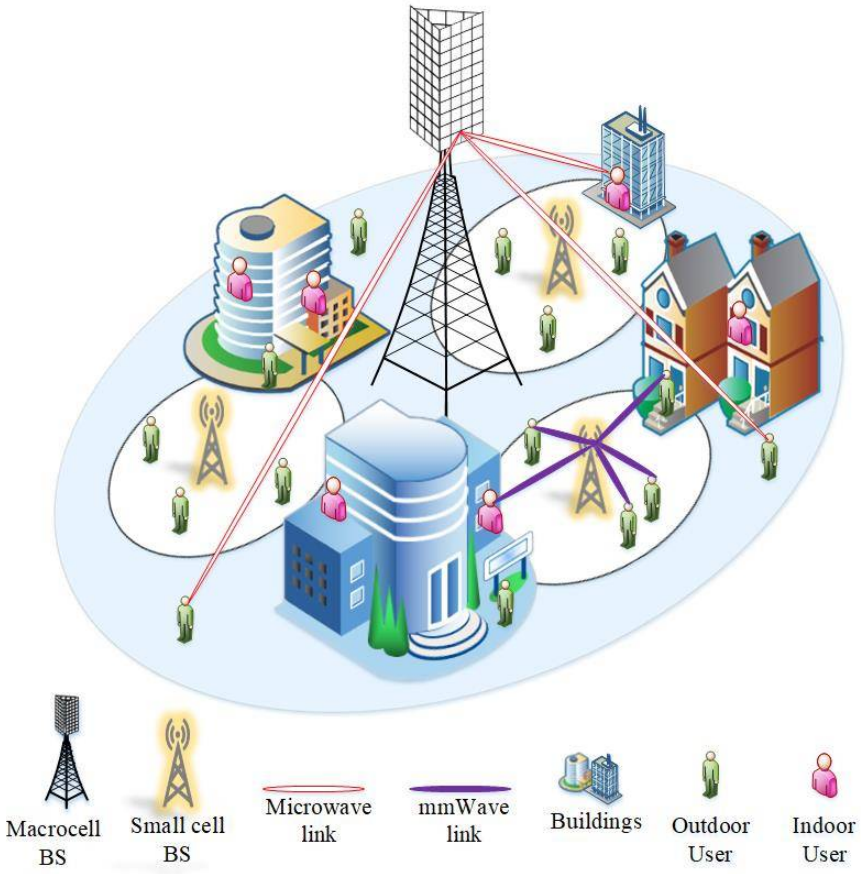

Figure 1.5: Network layout for 5G UDN (Scenario 1).

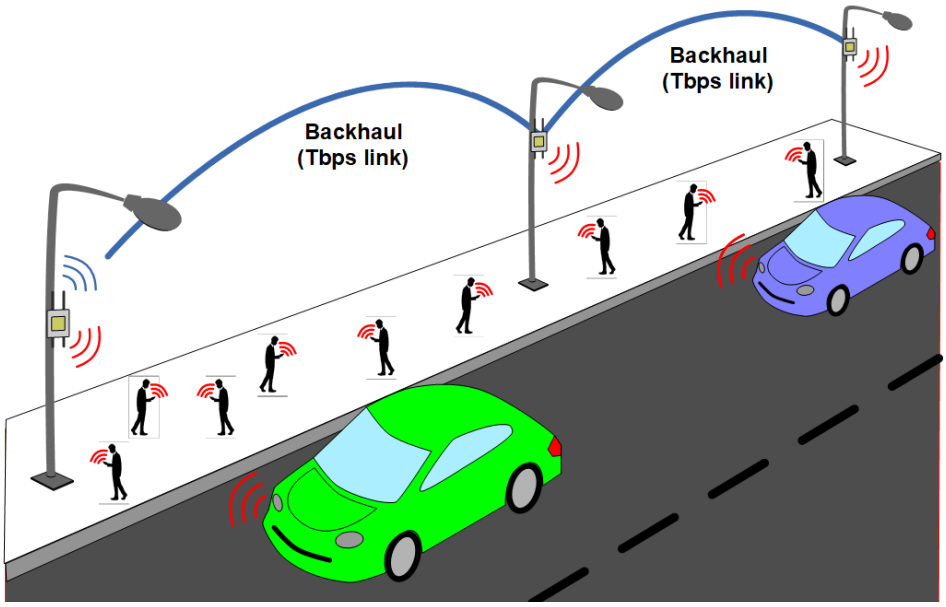

Figure 1.6: Network layout for C-I2X (Scenario 2).

- **Investigate the joint application of mmWave and massive MIMO for enhancing 5G cell throughputs:** The legacy UDNs employing μWave MIMO cannot support the next-generation applications due to limited bandwidth, low SE and high cross-tier interference from dense cells. To address this challenge, this thesis investigates the joint application of mmWave and massive MIMO in delivering ultra-high system capacities by using large mmWave bandwidth, enhancing SE with massive MIMO and eliminating cross-tier interference using a two-tier (μWave-mmWave) architecture whilst enhancing coverage with densely-deployed SCs. In the resulting 5G HetNets, the mmWave SCs that are anticipated to provide multi-Gbps throughput suffer from SINR bottleneck due to the degrading impact of noise (due to larger bandwidth), opportunistic nature of mmWave propagation (resulting from the susceptibility to blockage), high PL and potentially high interference due to the density of the SCs. This is addressed in this thesis through appropriate 3D beamforming for 5G UDN and C-I2X channels.
- **Investigate the SE and EE trade-off of mmWave massive MIMO architectures:** Digital beamforming (DBF) (used in conventional MIMO systems) is costly and power-hungry for massive MIMO, especially at mmWave bands. On the other hand, analog beamforming (ABF) suffers SE limitations despite its low cost and complexity. Consequently, hybrid beamforming (HBF) is being extensively explored as the candidate architecture for mmWave massive MIMO for balanced SE-EE trade-off. In HBF, the mapping from the low-dimensional RF chains to the high-dimensional antennas impacts on the SE-EE performance. Until now, only the sub-connected and fully-connected mapped structures are popular with limited investigation on the overlapped subarray structure. Consequently, a novel generalized framework for HBF array structure is proposed in this thesis for a systematic analysis of performance of the different array structures.

This thesis, therefore, explores the intersection of massive MIMO, mmWave communications and UDN in delivering a disruptive and adaptive HetNet platform for capacity and coverage optimization of 5G networks whilst ensuring energy-efficient, cost-effective and low-complexity operation of the networks.

1.5 Scientific Methodology Applied

The main objective of this research is to provide a system-level performance evaluation on the three key 5G technology enablers investigated in this thesis. Numerical simulations, mathematical analyses and field trials are the three main approaches employed in evaluating the performance of any new communication system. Though analytically tractable, mathematical methods are often constrained with simplifying assumptions that potentially limit their use in modeling large-scale, highly-complex and dynamic networks. Realistic performance can be measured in live operating environments. However, the economic and operational requirement of such field or live tests are costly as well as practically infeasible for the early design and development stages. Hence, simulations have become an increasingly important approach for the assessment of networks' performance due to obvious cost and implementation advantages. Simulations can provide the verification and validation of the key characteristics and behaviors of the overall system [38–40].

Depending on the performance metrics under investigation, simulators can be categorized into three: link level simulator (LLS), system level simulator (SLS) and network level simulator (NLS) [41]. While the LLS examines detailed, bit-level physical layer (PHY) functionalities of a single link, the SLS evaluates performance of links involving many BSs and UEs at the medium access control (MAC) layer, with the PHY abstracted usually through look-up tables. SLS focuses on the radio access networks (RANs) or air interface and facilitates analyses on resource allocation, capacity, coverage, SE and EE, among others. The performance of protocols across all layers of the network, including control signaling and backhaul/fronthaul issues are evaluated with a NLS using metrics such as latency, packet loss, etc. Besides metric-based classification, simulators can also be grouped based on radio access technologies supported (cellular, vehicular, wireless fidelity (WiFi), etc.), coding language (MATLAB, python, C++, etc.), licensing option (open source, proprietary, free of charge for academic use) or network scenario capabilities (LTE, 5G, beyond-5G (B5G), dedicated short-range communication (DSRC), etc) [39].

For this thesis, the SLS approach has been used as the main performance assessment methodology supported by theoretical analysis to understand the performance of the system on a wide scale deployment. In terms of implementation, we adopted a baseline LTE-A SLS [38] and added advanced 5G features and functionalities. The evolved 5G-compliant SLS (illustrated in Figure 1.7 on next page) is employed for the 5G UDN performance evaluations in this thesis. Similarly, we implemented and added advanced features on a baseline channel-only simulator [42] and transformed it into a 5G-compliant SLS for the investigation of performance pertaining to the C-I2X scenarios. The evolved C-I2X SLS is illustrated in Figure 1.8 (shown on next page).

1.6 Thesis Contributions

This PhD study mainly contributes towards providing system-level and analytical understanding of 5G UDN and C-I2X scenarios with respect to enhancing system capacity and coverage, as well as the SE and EE performance of networks using mmWave massive MIMO. The main contributions and novelty of this PhD study lies in the following. This thesis:

(i) contributes to the development of two 5G-compliant SLSs as tools for investigating the performance of advanced 5G scenarios, features, algorithms and models. With the implementation of the 5G new radio (NR) frame structure, 3D channel models, multi-tier/multi-band HetNet, spatial consistency, blockage and mobility models, and precoding/beamforming algorithms, the tools enable the characterization, analyses and performance evaluation of 3D μWave and mmWave channels, both individually and jointly for the sake of coexistence or interoperability for future emerging 5G UDN and C-I2X application scenarios involving cellular and vehicular users.

(ii) analyzes the performance enhancements realizable with mmWave massive MIMO relative to legacy systems such as LTE-A and DSRC in C-I2X scenarios. Also, the performance trade-offs realizable with the overlapped subarray HBF structures when compared to the fully-connected and sub-connected structures are investigated in this thesis. In addition, we evaluate the performance of zero forcing (ZF)-based HBF in multi-user MIMO setups in contrast to analog beamsteering and singular value decomposition (SVD) precoding algorithms.

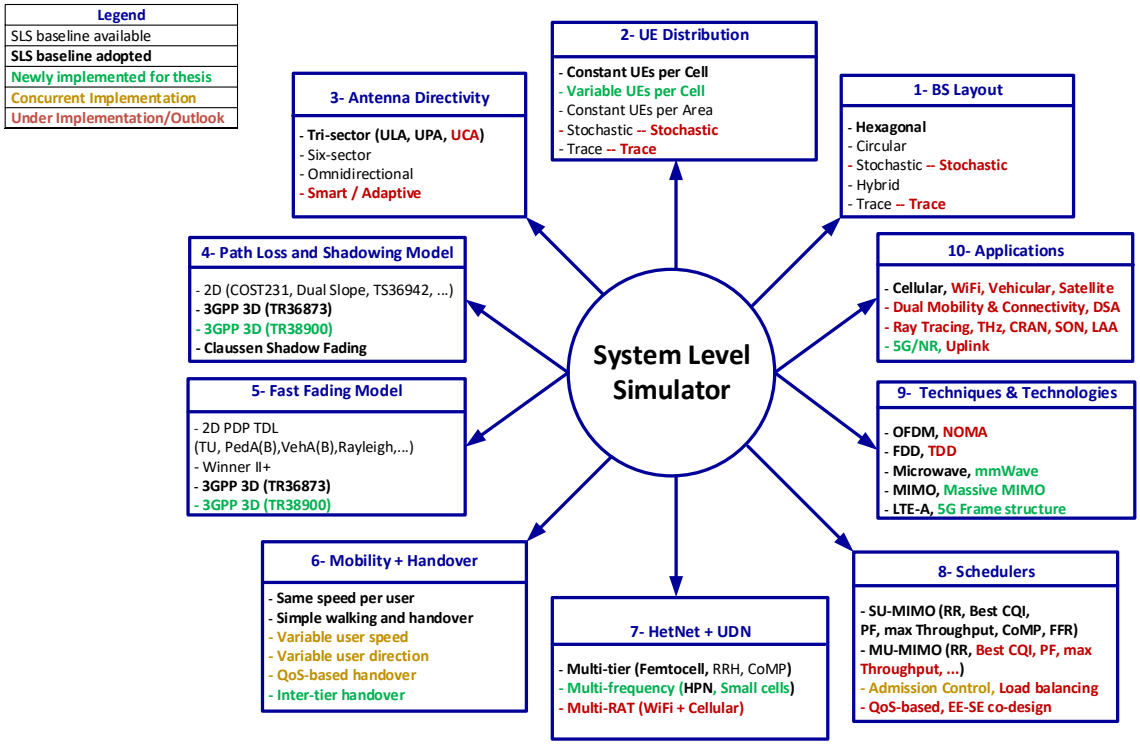

Figure 1.7: Evolved 5G system level simulator

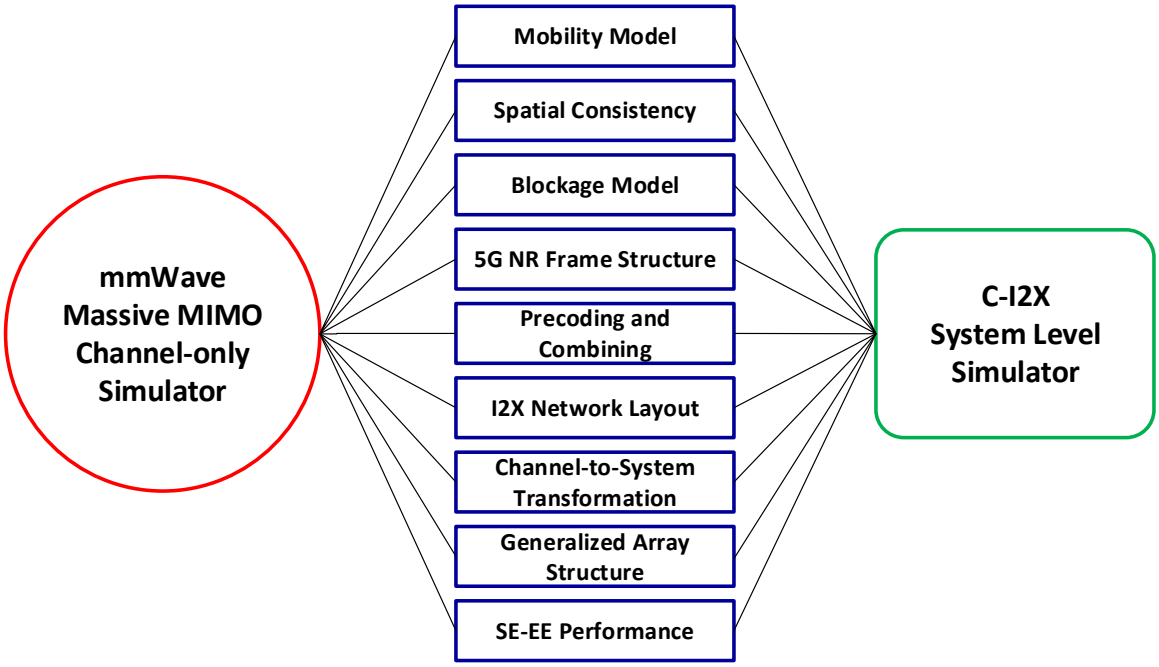

Figure 1.8: C-I2X system level simulator

(iii) proposes a novel generalized framework for the design and analysis of HBF antenna array structures for any massive MIMO hybrid configuration. The generalized model enables the investigation of the SE and EE as well as the power and hardware costs of the system, together with the performance trade-offs. The proposed model provides insights for the cost-effective, high-rate and energy-efficient operation of next-generation networks and beyond.

The results of this PhD study have been disseminated in the underlisted scientific publications: six international peer-reviewed journal articles and seven conference papers, a book chapter and five posters.

- **Journal Articles**

J1. **S. A. Busari**, K. M. S. Huq, S. Mumtaz, L. Dai and J. Rodriguez, "Millimeter-Wave Massive MIMO Communication for Future Wireless Systems: A Survey", *IEEE Communications Surveys and Tutorials*, vol. 20, no. 2, pp. 836-869, May 2018.

J2. **S. A. Busari**, S. Mumtaz, S. Al-Rubaye and J. Rodriguez, "5G Millimeter-Wave Mobile Broadband: Performance and Challenges", *IEEE Communications Magazine*, vol. 56, no. 6, pp. 137-143, June 2018.

J3. **S. A. Busari**, M. A. Khan, K. M. S. Huq, S. Mumtaz and J. Rodriguez, "Millimetre-wave massive MIMO for cellular vehicle-to-infrastructure communication", *IET Intelligent Transport Systems*, vol. 13, no. 6, pp. 983-990, June 2019.

J4. **S. A. Busari**, K. M. S. Huq, S. Mumtaz, J. Rodriguez, Y. Fang, D. C. Sicker, S. Al-Rubaye and A. Tsourdos, "Generalized Hybrid Beamforming for Vehicular Connectivity using THz Massive MIMO", *IEEE Transactions on Vehicular Technology*, vol. 68, no. 9, pp. 8372-8383, Sept. 2019.

J5. K. M. S. Huq, **S. A. Busari**, J. Rodriguez, V. Frascolla, W. Buzzi and D. C. Sicker, "Terahertz-enabled Wireless System for Beyond-5G Ultra-Fast Network: A Brief Survey", *IEEE Network*, vol. 33, no. 4, pp. 89-95, July/August, 2019.

J6. M. A. Khan, **S. A. Busari**, K. M. S. Huq, S. Mumtaz, S. Al-Rubaye, J. Rodriguez, and A. Al-Dulaimi, "A novel mapping technique for ray tracer to system-level simulation", *Computer Communications*, vol. 150, pp. 378-383, Jan. 2020.

- **Conference Papers**

C1. **S. A. Busari**, S. Mumtaz and J. Rodriguez, "Hybrid Precoding Techniques for THz Massive MIMO in Hotspot Network Deployment", *IEEE Vehicular Technology Conference (VTC-Spring) Workshop 2020*, Antwerp, Belgium, pp. 1-6, May, 2020.

C2. **S. A. Busari**, K. M. S. Huq, S. Mumtaz and J. Rodriguez, "Terahertz Massive MIMO for Beyond-5G Wireless Communication", *IEEE International Conference on Communications (ICC) 2019*, Shanghai, P.R. China, pp. 1-6, May, 2019.

C3. **S. A. Busari**, K. M. S. Huq, G. Felfel and J. Rodriguez, "Adaptive Resource Allocation for Energy-Efficient Millimeter-Wave Massive MIMO Networks", *IEEE Global Communications Conference (GLOBECOM) 2018*, Dubai, United Arab Emirates, pp. 1-6, Dec., 2018.

C4. **S. A. Busari**, K. M. S. Huq, S. Mumtaz and J. Rodriguez, "Impact of 3D Channel Modeling for ultra-high speed Beyond-5G Networks", *IEEE Global Communications Conference (GLOBECOM) Workshop 2018*, Dubai, United Arab Emirates, pp. 1-6, Dec., 2018.

C5. **S. A. Busari**, S. Mumtaz, K. M. S. Huq, J. Rodriguez, and H. Gacanin, "System-Level Performance Evaluation for 5G mmWave Cellular Network", *IEEE Global Communications Conference (GLOBECOM) 2017*, Singapore, pp. 1-7, Dec., 2017.

C6. M. Neija, S. Mumtaz, K. M. S. Huq, **S. A. Busari**, J. Rodriguez, Z. Zhou, "An IoT Based E-Health Monitoring System Using ECG Signal", *IEEE Global Communications Conference (GLOBECOM) 2017*, Singapore, pp. 1-6, Dec., 2017.

C7. **S. A. Busari**, S. Mumtaz, K. M. S. Huq and J. Rodriguez, "X2-Based Handover Performance in LTE Ultra-Dense Networks using NS-3", *IARIA The Seventh International Conference on Advances in Cognitive Radio, COCORA 2017*, Venice, Italy, Vol. 7, pp. 31 - 36, April, 2017.

- **Book Chapter**

B1. **S. A. Busari**, S. Mumtaz, K. M. S. Huq and J. Rodriguez, "Millimeter Wave Channel Measure", Chapter in, *Encyclopedia of Wireless Networks*, Shen X., Lin X., Zhang K. (Eds), Springer International Publishing, Berlin, May, 2018.

- **Posters**

P1. **S. A. Busari**, K. M. S. Huq, S. Mumtaz and J. Rodriguez, "A Novel Generalized Hybrid Beamforming for THz Massive MIMO Networks", *2019 MAP-Tele Workshop*, Porto, Portugal, Sept. 2019.

P2. **S. A. Busari**, K. M. S. Huq, S. Mumtaz and J. Rodriguez, "Millimeter-wave Massive MIMO for Capacity and Coverage Optimization", *Science and Technology Summit in Portugal (Ciência 2019)*, Lisbon, Portugal, July 2019.

P3. **S. A. Busari**, K. M. S. Huq, S. Mumtaz and J. Rodriguez, "THz Massive MIMO for C-I2X in B5G networks", *Research Summit - Universidade de Aveiro*, Aveiro, Portugal, July 2019.

P4. **S. A. Busari**, K. M. S. Huq, S. Mumtaz and J. Rodriguez, "Millimeter-wave Massive MIMO for Capacity and Coverage Optimization", *Instituto de Telecomunicações Research Day*, Aveiro, Portugal, Sept. 2018.

P5. **S. A. Busari**, K. M. S. Huq, S. Mumtaz and J. Rodriguez, "Millimeter-wave Mobile Broadband for 5G Heterogeneous Cellular Networks", *2017 MAP-Tele Workshop*, Aveiro, Portugal, Sept. 2017.

1.7 Organization of the Thesis

The remainder of this PhD thesis is organized as follows.

Chapter 2: Millimeter-wave Massive MIMO UDN for 5G Networks.
The first two sections of this chapter provide a background on the evolution and trend towards the mmWave massive MIMO system for 5G UDNs. The background connects how the networks have transformed: from employing single antennas to deploying massive MIMO antenna arrays; from operating in the sub-6 GHz μWave bands to moving to the mmWave and THz bands; and from using the legacy umbrella MCs to transitioning to the ultra-dense SC network topology. The overview of these so-called "big three" 5G technologies and their interplay for NGMNs are given. The third section then provides the state of the art on mmWave massive MIMO channel models as the basis for the implementation of the 3D channel models that are used for the investigation in later chapters. The fourth section of this chapter is dedicated to beamforming techniques and array structures for mmWave massive MIMO which are the focus of Chapter 4 where a generalized HBF framework is proposed. The last section of the chapter presents the concluding remarks.

Chapter 3: 3D Channel Modeling for 5G UDN and C-I2X.
This chapter focuses on the performance of 5G UDNs and C-I2X networks using 3D channel models. The chapter principally covers three aspects. The first part evaluates the individual performance of 3D μWave and mmWave channels in order to provide insights for coexistence in NGMNs. The second part considers the joint performance of the 3D μWave and mmWave channels in the light of 5G UDNs. The third principal part is dedicated to the performance of cellular infrastructure-to-vehicle (C-I2V) channels involving street-level lampost-mount APs and vehicles. This part compares the mmWave massive MIMO channel in this propagation environment with the DSRC and LTE-A channels. The challenges in these 5G scenarios are then highlighted and analysed.

Chapter 4: Novel Generalized Framework for Hybrid Beamforming.
This chapter focuses on beamforming techniques and the SE and EE analyses of 5G UDNs and C-I2X networks. The chapter principally covers three aspects. The first part proposes a novel generalized framework for HBF in mmWave massive MIMO networks. The proposed framework facilitates the comparative analysis and performance evaluation of the different HBF configurations: the fully-connected, sub-connected and the overlapped subarray architectures. The performance of the different array structures is evaluated using a C-I2X application scenario involving lampost-mount APs and a combination of pedestrian and vehicular users. The second part considers the cellular infrastructure-to-pedestrian (C-I2P) use case between street-level APs and pedestrian users, and evaluates the performance of the system using three beamforming approaches: analog beamsteering (AN-BST), hybrid precoding with zero forcing (HYB-ZF) and the SVD as upper bound (SVD-UB) precoding. The impacts of various system parameters such as transmit power, bandwidth, carrier frequency, antenna gain, number of RF chains and data streams are analyzed. Also, the SE and EE performance and trade-off are presented with a view to providing useful insights for enabling high rate, spectrally-efficient and green operation of next-generation mobile networks.

Chapter 5: Conclusions and Future Works.
This chapter provides the summary, principal findings and recommendations on the concepts investigated in this thesis: channel modeling, beamforming and system-level performance of mmWave massive MIMO for 5G UDN and C-I2X scenarios. The future research directions are then presented as related open issues for NGMNs, in the areas of THz channel modeling, ultra-

massive MIMO, quantum machine learning (QML) and EE optimization for the forthcoming 6G era.

The schematic diagram for the overall organization of the thesis is shown in Figure 1.9.

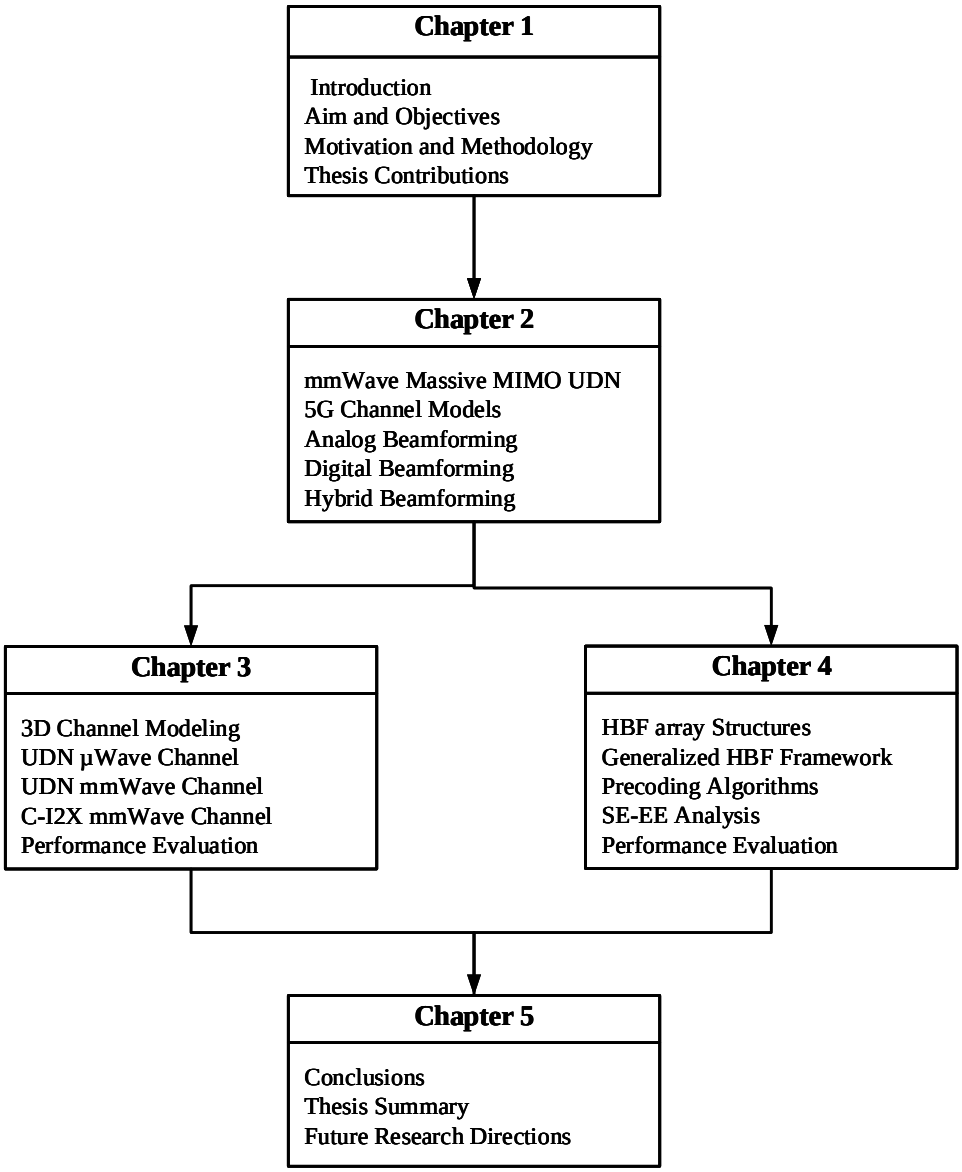

Figure 1.9: Thesis organization.

Chapter 2

Millimeter-wave Massive MIMO UDN for 5G Networks

The first two sections of this chapter provide a background on the evolution and trend towards the mmWave massive MIMO system for 5G UDNs. The background elaborates on how the networks have transformed: from employing single antennas to deploying massive MIMO antenna arrays; from operating in the sub-6 GHz μWave bands to moving to the mmWave and THz bands; and from using the legacy umbrella macrocells to transitioning to the ultra-dense SC network topology. The overview of these so-called "big three" 5G technologies and their interplay for next-generation mobile networks are given. The third section then provides the state of the art on mmWave massive MIMO channel models as the basis for the implementation of the 3D channel models that play a pivotal role in later chapters. The fourth section of this chapter is dedicated to beamforming techniques and array structures for mmWave massive MIMO which are the focus of Chapter 4 where a generalized HBF framework is proposed. The last section of the chapter presents the concluding remarks.

2.1 Evolution towards mmWave Massive MIMO UDNs

Over time, mobile network technologies have continued to evolve, pushing legacy systems towards their theoretical limits and motivating research for next-generation networks with better performance capabilities in terms of reliability, latency, throughput, SE, EE and cost, among others [23]. Thus, cellular networks have undergone remarkable transitions: from SISO at μWave frequencies to the latest legacy system with massive MIMO at μWave frequencies (hereafter referred to as conventional massive MIMO). However, the projections of explosive growth in mobile traffic, unprecedented increase in connected wireless devices and proliferation of increasingly smart applications and broadband services have motivated research for the development of 5G mobile networks. These networks are expected to deliver super high speed connectivity and high data rates, provide seamless coverage, support diverse use cases and satisfy a wide range of performance requirements where legacy cellular networks have reached their theoretical limits. This has prompted the academic and industrial communities to consider mmWave massive MIMO with a view to exploiting the joint capabilities of mmWave communications and massive MIMO antenna arrays [2].

Notably from 4G, the performance of cellular networks has significantly improved since the adoption of the HetNet architecture such that the UDN layout has been identified as the single

most effective way to increase system capacity in next-generation networks [15]. The overlay of SCs on traditional MC BSs provides multi-dimensional benefits for mobile networks. It leads to enhanced coverage and capacity due to increased cell density leading to higher spatial and frequency reuse. It also improves SE due to higher SINR with tighter interference control and increases EE due to lower transmission powers and reduced inter-site distance (ISD) of the SCs (when compared with the MCs) [43, 44]. In addition, cross-tier interference is eliminated when the MC and SC tiers operate on different frequency bands, thereby further increasing the potentials of the topology. Intra-tier interference can be controlled by maintaining the optimal cell density threshold and through advanced interference mitigation techniques. For 5G networks, therefore, UDNs employing mmWave massive MIMO are expected to provide the 1000-fold network capacity increase (when compared to LTE-A) for meeting the foreseen explosive traffic demands of mobile networks [23]. In the following sub-sections, we present an overview of the road towards mmWave massive MIMO UDNs.

Notations: Throughout this thesis, we use the following notations. $\mathbf{X}$ is a matrix, $\mathbf{x}$ is a vector and x is a scalar. $|\cdot|$ is the magnitude of a vector or determinant of a matrix, $\|\cdot\|$ is the norm of a vector, $\|\cdot\|_F$ denotes the Frobenius norm while $[\mathbf{X}]_{i,j}$ represents the elements of $\mathbf{X}$ in the i^{th} row and j^{th} column. The identity matrix is $\boldsymbol{I}$ while the inverse, transpose and conjugate transpose operators are denoted with $(\cdot)^{-1}$, $(\cdot)^{T}$ and $(\cdot)^{H}$, respectively. $\mathbf{X} \gg \mathbf{Y}$ means $\mathbf{X}$ is far greater than $\mathbf{Y}$, and $tr(\cdot)$ is the trace operator.

2.1.1 SISO to massive MIMO

Single-input single-output (SISO) systems employ single antennas, one positioned at the transmitter (TX) or BS, and another at the receiver (RX) or UE. MIMO systems use multiple antennas at both sides. MIMO offers higher capacity and reliability than SISO systems as its channels have considerable advantages over SISO channels in terms of multiplexing, diversity and array gains [45, 46]. The diversity gains of MIMO scale with the number of independent channels between the TX and the RX, while the maximum multiplexing gain is given by the lesser number of antennas on either the TX or RX units (i.e., $\min(N_{RX}, N_{TX})$). However, maximum multiplexing and diversity gains cannot be simultaneously harnessed from MIMO systems as a fundamental trade-off exists between both. The best of the two gains cannot be achieved concurrently [46]. Massive MIMO, on the other hand, uses a much larger number of antennas (e.g., $N_{TX} = 64, \ldots, 1024$) than those used in conventional MIMO systems with $N_{TX} = \{2, \ldots, 8\}$. To analyze the different configurations, consider a generic system model shown in Figure 2.1 (on next page).

The multi-cellular DL system consists of J BSs each equipped with N_{TX} antennas and K UEs with N_{RX} antennas per UE. For $\forall j \in \{1, 2, \ldots, J\}$ and $\forall k \in \{1, 2, \ldots, K\}$, the received signal vector, $\mathbf{y}$ can be modeled as (2.1) and (2.2).

$$\mathbf{y} = \mathbf{H}\mathbf{x} + \mathbf{n}, \tag{2.1}$$

$$\begin{bmatrix} y_1^{k,j} \\ \vdots \\ y_{N_{RX}}^{k,j} \end{bmatrix} = \begin{bmatrix} h_{1,1}^{k,j} & \cdots & h_{1,N_{TX}}^{k,j} \\ \vdots & \ddots & \vdots \\ h_{N_{RX},1}^{k,j} & \cdots & h_{N_{RX},N_{TX}}^{k,j} \end{bmatrix} \begin{bmatrix} x_1^{j} \\ \vdots \\ x_{N_{RX}}^{j} \end{bmatrix} + \begin{bmatrix} n_1^{k} \\ \vdots \\ n_{N_{RX}}^{k} \end{bmatrix}, \tag{2.2}$$

where **H**, **x** and **n** represent the channel matrix, transmit signal vector and the noise vector, respectively and **n** is assumed to be the additive white Gaussian noise (AWGN) following a complex normal distribution $\mathcal{CN}(0,\sigma)$ with zero mean and σ standard deviation. For analytical tractability, we focus on a single cell (i.e., $J = 1$) under the following four scenarios: SISO, point-to-point or single-user MIMO (SU-MIMO), (conventional) multi-user MIMO (MU-MIMO) and massive MIMO.

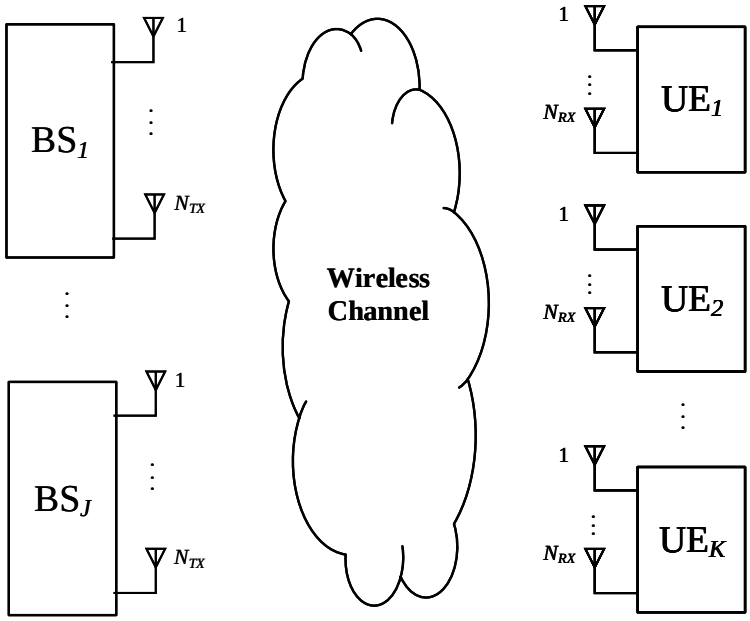

Figure 2.1: Generic system model

(a) SISO $[N_{TX} = 1, N_{RX} = 1, K = 1]$

For the SISO scenario, **H**, **x** and **n** in (2.1) become scalars. The received signal y thus reduces to (2.3). The SE (bits/s/Hz) of the single link can thus be expressed as (2.4).

$$y_1 = h_{1,1}x_1 + n_1, \tag{2.3}$$

$$\eta_{SE}^{SISO} = \log_2(1 + SNR) = \log_2\left(1 + h^2\frac{P_T}{\sigma_n^2}\right), \tag{2.4}$$

where P_T is the transmit power, SNR is the signal to noise ratio, σ_n^2 is the noise power and h is the channel coefficient.

(b) SU-MIMO $[N_{TX} > 1, N_{RX} > 1, K = 1]$

Here, both the TX and RX are equipped with multiple antennas. For the SU-MIMO system, the received signal vector, $\mathbf{y} \in \mathbb{C}^{N_{RX}\times 1}$, can be expressed as (2.5).

$$\mathbf{y} = \sqrt{\rho}\mathbf{H}\mathbf{x} + \mathbf{n}, \tag{2.5}$$

where $\mathbf{x} \in \mathbb{C}^{N_{TX} \times 1}$, $\mathbf{n} \in \mathbb{C}^{N_{RX} \times 1}$, $\mathbf{H} \in \mathbb{C}^{N_{RX} \times N_{TX}}$ and ρ is a scalar representing the normalized transmit power. Assuming perfect channel state information (CSI) at the receiver, the SE (bits/s/Hz) for the SU-MIMO is given by (2.6).

$$\eta_{SE}^{SU-MIMO} = \log_2 \left| \left(\mathbf{I}_{N_{RX}} + \frac{\rho}{N_{TX}} \mathbf{H}\mathbf{H}^H \right) \right|. \tag{2.6}$$

The expression in (2.6) is bounded by (2.7) where the actual achievable SE depends on the distribution of the singular values of $\mathbf{H}\mathbf{H}^H$ [45].

$$\log_2 \left(1 + \rho N_{RX}\right) \leq \eta_{SE}^{SU-MIMO} \leq \min\left(N_{RX}, N_{TX}\right) \log_2 \left(1 + \frac{\rho \max\left(N_{RX}, N_{TX}\right)}{N_{TX}} \right). \tag{2.7}$$

The SU-MIMO configuration leads to increased data rates and average SE without any increase in the SNR or the bandwidth of such systems, as required by the Shannon capacity theorem on the theoretical limit for SISO systems. This additional increase in capacity comes from spatial multiplexing through multi-stream transmissions from the multiple antennas. It is also possible to use the additional antennas for beamforming (and thus increase the SNR) or for diversity (so as to increase the reliability of the system) [15, 47]. While the channel capacity of SISO systems increases logarithmically with an increase in system's SNR, MIMO systems' capacities increase linearly with increasing number of antennas (i.e., scales with the smaller of the number of TX or RX antenna when the channel is full rank). The gains can be limited (i.e., not exactly linear increase) when the channel is not full rank [48]. This increase is, however, at the expense of the additional cost of deployment of multiple antennas, space constraints (particularly for mobile terminals) and increased signal processing complexities [49].

(c) MU-MIMO $[N_{TX} > 1, N_{RX} \geq 1, K > 1]$

MIMO systems have two basic configurations: SU-MIMO and MU-MIMO [45, 50]. MU-MIMO offers greater advantages [20] over SU-MIMO and these include:

- MU-MIMO exploits multi-user diversity in the spatial domain by allocating a time-frequency resource to multiple users while SU-MIMO transmissions dedicate all time-frequency resources to a single terminal. This results in significant gains over SU-MIMO, particularly when the channels are spatially correlated [50].

- MU-MIMO BS antennas simultaneously serve many users, where relatively cheap single-antenna devices can be employed at user terminals while expensive equipment is only needed at the BS thereby bringing down cost.

- MU-MIMO system is less sensitive to the propagation environment when compared to the SU-MIMO system. Therefore, rich scattering is generally not required in the MU-MIMO case.

For the MU-MIMO scenarios, the BS transmits simultaneously to multiple users. In the simple case where each UE has a single antenna, the receive, transmit and noise vectors in (2.5) become: $\mathbf{y} \in \mathbb{C}^{K\times 1}$, $\mathbf{x} \in \mathbb{C}^{N_{TX}\times 1}$ and $\mathbf{n} \in \mathbb{C}^{K\times 1}$, respectively. The channel matrix becomes $\mathbf{H} \in \mathbb{C}^{K\times N_{TX}}$ and the achievable SE can be expressed as (2.8).

$$\eta_{SE}^{MU-MIMO} = \max \log_2 \left| \left(\mathbf{I}_{N_{RX}} + \rho \mathbf{H} \mathbf{P} \mathbf{H}^H \right) \right|, \tag{2.8}$$

where $\mathbf{P}$ is a positive diagonal matrix with power allocations $\mathbf{P} = \{p_1, p_2, \cdots, p_K\}$ which maximizes the sum transmission rate [45].

Overall, MIMO is a smart technology aimed at improving the performance of wireless communication links [47]. Compared to the SISO systems, MIMO systems have been shown from studies and commercial deployment scenarios in different wireless standards, such as the IEEE 802.11 (WiFi), IEEE 802.16 (Worldwide Interoperability for Microwave Access (WiMAX)), the third generation (3G) Universal Mobile Telecommunications System (UMTS) and the High Speed Packet Access (HSPA) family series as well as the LTE, to offer significant improvements in the performance of cellular systems, with respect to both capacity and reliability [45, 51]. In addition, MIMO system implementations have shifted to MU-MIMO in recent years due to its superior benefits, which have made it the candidate for several wireless standards [20, 45]. However, despite its great significant advantages over SISO and SU-MIMO antenna systems, MU-MIMO has been identified as a non-scalable technology, and as a sequel, massive MIMO is evolving to scale up the benefits of MIMO significantly. Unlike MU-MIMO which has roughly the same number of terminals and service antennas, massive MIMO has an excess of service antennas over active terminals which can be used for enhancements such as beamforming, in order to bring about improved throughput and EE [20].

(d) Massive MIMO $[N_{RX} \gg N_{TX}, N_{RX} \to \infty$ **or** $N_{TX} \gg N_{RX}, N_{TX} \to \infty, K > 1]$

Massive MIMO is also known as large-scale antenna system, full dimension MIMO, very large MIMO and hyper MIMO. It employs an antenna array system with a few hundred BS antennas simultaneously serving many tens of user terminals on the same time-frequency resource [20, 50]. It has the potential to enormously improve SE by using its large number of BS transmit antennas to exploit spatial domain DoF for high-resolution beamforming and for providing diversity and compensating PL, thereby improving the EE, data rates, and link reliability [19, 52]. With the practical acquisition of CSI, massive MIMO achieves an order-of-magnitude higher SE in real life than the small-scale conventional MIMO system. The third generation partnership project (3GPP) has been steadily increasing the maximum number of antennas in progressive LTE releases and massive MIMO will be a key ingredient in 5G [53].

When the number of antennas grows large such that $N_{TX} \gg N_{RX}$, $N_{TX} \to \infty$, the achievable SE for the massive MIMO system in (2.6) tends to (2.9), and when $N_{RX} \gg N_{TX}$, $N_{RX} \to \infty$, it approximates to (2.10). Equations (2.9) and (2.10) assume that the row or column vectors of the channel $\mathbf{H}$ are asymptotically orthogonal $\dfrac{\mathbf{H}\mathbf{H}^H}{N_{TX}} \approx \mathbf{I}_{N_{RX}}$ and demonstrate

the advantages of massive MIMO, where the capacity grows linearly with the number of the employed antenna at the BS or the UE, as the case may be [45]. Even at mmWave frequencies, it is still possible to employ massive MIMO arrays for spatial multiplexing, alongside beamforming, in order to increase system capacity [54, 55]. However, the multiplexing gain reduces in line of sight (LOS) propagation environments [45].

$$\eta_{SE}^{Massive-MIMO} \approx N_{RX} \log_2 (1 + \rho), \tag{2.9}$$

$$\eta_{SE}^{Massive-MIMO} \approx N_{TX} \log_2 \left(1 + \rho \frac{N_{RX}}{N_{TX}}\right). \tag{2.10}$$

Massive MIMO requires CSI for both uplink (UL) and DL and depends on phase coherent signals from all the antennas at the BS. It is an enabling technology for enhancing the EE, SE, reliability, security and robustness of future broadband networks, both fixed and mobile. However, despite these obvious benefits, massive MIMO implementation is faced with some challenges which have been subjects of research studies. These challenges, among others, include the following [8, 19, 20, 50]:

- need for simple, linear and real-time techniques and hardware for optimized processing of the vast amounts of generated baseband data, at associated internal power consumption.
- need for new and realistic characterization and modeling of radio channels taking into account the number, geometry and distribution of the antennas.
- need for accurate CSI acquisition, and feedback mechanisms and techniques to combat pilot contamination and effects of hardware impairments due to the use of low-cost, low-power components.
- need for the development of commercial and scalable prototypes and deployment scenarios to engineer the heterogeneous network solutions for future mobile systems.

These challenges are being addressed by various works with a view to enabling the practical use of massive MIMO for 5G and beyond. As of 2020, practical massive MIMO systems are already being tested, trialed and deployed [56–58]. The summary of the benefits and challenges of SISO, SU-MIMO, MU-MIMO and massive MIMO are shown in Table 2.1 (where ✓ means benefit, × means challenge and the number/amount of the symbols signifies the normalized quantity relative to SISO) [59].

Table 2.1: Summary of benefits and challenges for antenna technologies.

Features	**SISO**	**SU-MIMO**	**MU-MIMO**	**Massive MIMO**
Diversity gain	×	✓	✓✓	✓✓✓✓
Multiplexing gain	×	✓✓	✓✓✓	✓✓✓✓
Array gain	×	✓✓	✓✓	✓✓✓✓
Computational complexity	×	××	× × ×	× × ××
Channel estimation	×	××	× × ×	× × ××
Pilot contamination	×	××	× × ×	× × ××

2.1.2 Microwave to mmWave Communication

In legacy networks, the operation of cellular networks has been mainly limited to the congested sub-6 GHz μWave frequency bands. Though these bands have favorable propagation characteristics, however the total available bandwidth of 1-2 GHz is grossly insufficient to support the foreseen traffic demand of next-generation mobile services and applications. This challenge pushes for the exploration of under-utilized higher frequency bands where there is an abundant amount of bandwidth. In the 30-100 GHz mmWave band, there is more than 10$\times$ bandwidth than that available at μWave bands as shown in Table 2.2. In the 0.1-10 THz bands, there is even much more (contiguous) bandwidth available as shown in Table 2.3.

Table 2.2: Available bandwidth for mmWave frequency bands (adapted from [8,19,23,24,60]).

Frequency (GHz)	22.5-23.5	27.5-31.2	38.6-40.0	40.5-42.5	45.5-46.9
Bandwidth (GHz)	1.0	1.3	1.4	2.0	1.4
Frequency (GHz)	47.2-48.2	48.2-50.2	71.0-76.0	81.0-86.0	92.0-95.0
Bandwidth (GHz)	1.0	2.0	5.0	5.0	2.9

Table 2.3: Available bandwidth for THz frequency bands (adapted from [61, 62]).

Frequency (THz)	0.1-0.2	0.2-0.27	0.27-0.32	0.33-0.37	0.38-0.44	0.44-0.49
Bandwidth (GHz)	100	70	50	35	65	56
Frequency (THz)	0.49-0.52	0.52-0.66	0.66-0.72	0.84-0.94	0.66-0.84	0.94-1.03
Bandwidth (GHz)	40	123	60	142	47	58
Frequency (THz)	1.03-1.3	1.3-1.35	1.35-1.49	1.49-1.56	1.56-1.83	1.83-1.98
Bandwidth (GHz)	38	51	92	29	25	56

When compared to the congested sub-3 GHz μWave bands used by the second generation (2G)-4G cellular networks, and the additional television white space (TVWS) and other sub-6 GHz μWave frequencies approved at the ITU's world radiocommunications conference (WRC) 2015, the mmWave (and THz) bands offer several advantages in terms of larger bandwidth which translate directly to higher capacity and data rates, and smaller wavelengths enabling massive MIMO and adaptive beamforming techniques. The relatively closer spectral allocations in the mmWave bands lead to a more homogeneous propagation, unlike the disjointed spectrum in legacy networks. On the other hand, mmWave signals are prone to higher PL, higher penetration loss, severe atmospheric absorption and more attenuation due to rain, when compared with μWave signals. In addition, they are vulnerable to blockages by objects. Thus, directional communication is being employed in mmWave systems to limit the severe propagation losses and mitigate interference thereby ensuring higher throughput and better EE [8, 60, 63, 64].

However, recent research studies and channel measurement campaigns carried out at different mmWave frequencies (e.g., 28, 38, 60 and 73 GHz) have revealed that mmWave signals can mitigate the aforementioned challenges by employing adaptive beamforming techniques to suppress interference and use relay stations to circumvent obstacles thereby avoiding blockages [19, 65–67], as shown in Figure 2.2. More so, for the 50-200 m cell size envisaged for mmWave SCs, the expected 1.4 dB attenuation (i.e., 7 dB/km) due to heavy rainfalls has a minimal effect [60]. The high PL limits inter-cell interference (ICI) and allows more frequency reuse, which improves the overall system capacity [68]. In addition, the huge spectrum of-

fered by the mmWave band will enable radio access (BS-UE), fronthaul (BS-baseband unit (BBU)) and backhaul (BBU-core network) links to support much higher capacity than legacy 4G networks [60]. In fact, the supposed drawback of short-distance or short-range mmWave communication perfectly fits into the UDN trend and opens up new avenues for short-range applications such as the potential use in data centers and C-I2X use cases.

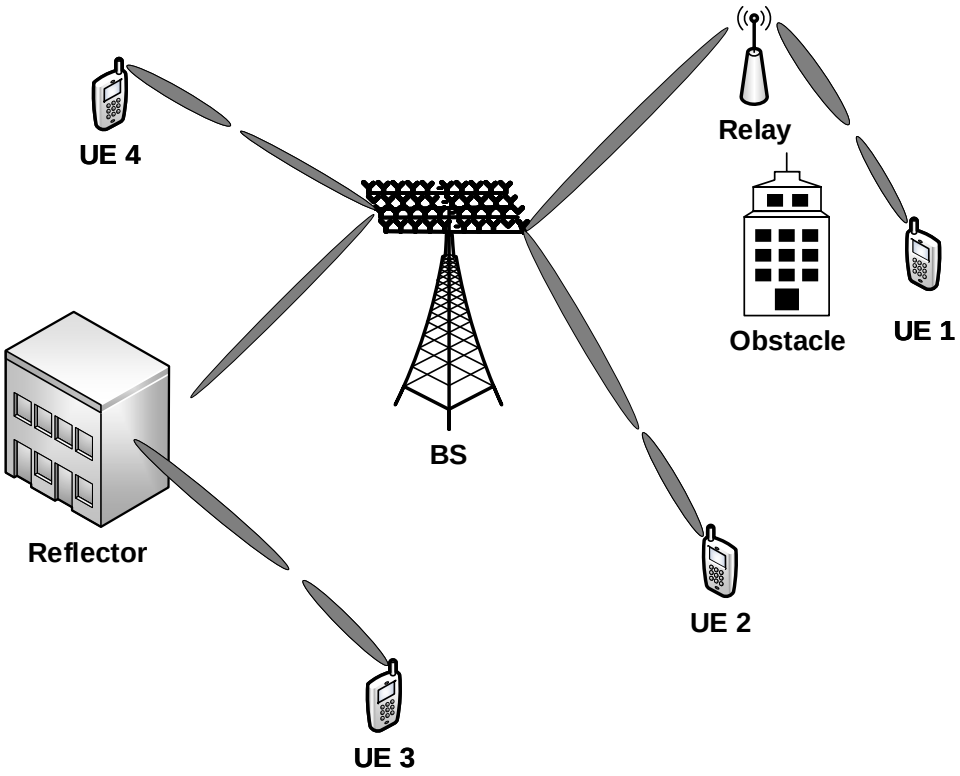

Figure 2.2: Directional communication with mmWave massive MIMO (adapted from [65]).

2.1.3 Legacy Macrocell to Ultra-Dense Small Cell Deployment

The early generations of cellular networks had cell sizes on the order of hundreds of square kilometers. However, the cell sizes have been increasingly shrinking, as this has been amply demonstrated the most-effective way to increase system capacity [3,16,69,70]. For 5G, extreme densification of SCs within the coverage area of the MC is targeted as one of the core methods to improve the area SE ((bits/s/Hz)/m^2) towards realizing the 1000× increase in network capacity, relative to legacy 4G system [16]. This UDN topology enables traffic offloading to the SCs (with coverage in the range of tens of meters), particularly for indoor hotspot and dense urban SCs. The smaller cell sizes of these SCs allow the reuse of spectrum across a geographical area and reduces the number of users competing for resources at each BS [3,16]. In addition, the shorter ISD between the SCs and their UEs leads to higher SINR and increased user throughputs [43,44].

In the first deployment phase of 5G, the orthogonal deployment of cells is envisaged where the MCs and SCs operate at different sub-6 GHz frequencies. For the second phase of 5G, the deployment of UDNs at μWave, mmWave and even THz frequencies is expected to provide

much larger peak data rates in the range of multi-Gbps or even Tbps [15,69,70]. By employing the enabling technologies such as mmWave and massive MIMO, for example, 5G UDNs will support the foreseen explosive traffic demands of future mobile networks, whilst satisfying performance requirements such as better reliability, reduced latency and higher SE and EE, among others [23]. Despite the anticipated BS densification gains, increasing cell density may also result in increased other-cell interference (OCI), thus necessitating interference mitigation techniques such as cooperative scheduling, coordinated multipoint, etc [3]. Also due to OCI, an unlimited increase in the number of SCs is counter-productive. Therefore, the optimal density threshold must be maintained in order to reap the full benefits of UDN. More so, extreme densification will also lead to other challenges in the areas of mobility support, user association, load balancing, costs of installation, maintenance, backhauling, etc [16].

2.2 Dawn of mmWave Massive MIMO

MmWave massive MIMO is a promising candidate technology for exploring new frontiers for NGMNs, starting with 5G networks. It benefits from the combination of large available bandwidth (mmWave frequency bands) and high antenna gains (achievable with massive MIMO antenna arrays), enhanced SE and EE, increased reliability, compactness, flexibility, and improved overall system capacity. This is expected to break away from today's technological shackles, taking a step towards addressing the challenges of the explosively-growing mobile data demand and open up new scenarios for future applications [2]. For mmWave massive MIMO systems, maximum benefits can be achieved when different TX-RX antenna pairs experience independently-fading channel coefficients. This is realizable when the AEs' spacing is at least 0.5λ, where λ reduces with increasing carrier frequency (f_c), a higher number of elements in antenna arrays of same physical dimension can be realized at mmWave than at μWave frequencies [59].

At mmWave frequencies, the dimensions of the AEs (as well as the inter-antenna spacing) become incredibly small (due to their dependence on λ). It thus becomes possible to pack a large number of AEs in a physically-limited space, thereby enabling compact massive MIMO antenna array, not only at the BSs, but also at the UEs [71, 72]. As of 2019, the maximum numbers of antennas under consideration by 3GPP (for example at 70 GHz) are 1024 for the BSs and 64 for the UEs. As for the RF chains, the maximum numbers are 32 and 8 for the BSs and UEs, respectively [3, 4].

Several works have shown that $\lambda/2$ element spacing leads to low spatial correlation. However, inter-element spacing less than $\lambda/2$ can facilitate a reduction in the total area of the array. The potentially resulting higher spatial correlation can, however, be suppressed by proper tuning of the antennas mutual coupling. using inter-element spacing of 0.37λ (in contrast to the conventional 0.5λ), the authors in [73] showed that mutual coupling can be controlled by placing a slot between each pair of antenna elements. This leads to improvement in SNR as well as reduction in the size of antenna array. With low radiation power (due to small antenna size) and high propagation attenuation, it becomes necessary to use highly-directional, steerable, configurable or smart antenna arrays for mmWave massive MIMO in order to ensure high received signal power for successful detection [74]. An overview of the architecture and the propagation characteristics of mmWave massive MIMO is given in the following subsections.

2.2.1 Architecture

A representative architecture for the 5G network is shown in Figure 2.3. The architecture is a multi-tier HetNet composed of the MC and SC BSs, with massive MIMO and μWave/mmWave communication capabilities. It features several scenarios that are subject to ongoing research in realizing the 5G goals. Some of these scenarios are highlighted as follows [59]:

- Split control and data plane framework where the control signals are handled by the long-range μWave massive MIMO MC BS (for efficient mobility and other control signaling) while data signals are handled by the mmWave massive MIMO SCs for high capacity.
- Dual-mode or dual-band SCs where close-by users are served by mmWave access links while further-away users are served at μWave frequency band, thereby serving as a dynamic cell and emulating the "cell breathing" concept from legacy networks.
- In-band backhauling where both the access and backhaul links are on the same (mmWave) frequency band to reduce cost and optimize spectrum utilization.
- Vehicular communication where the μWave MC BSs serve the long-range and highly mobile users while the SCs serve the pedestrian/low-mobility users.
- Virtual cells where a user, particularly cell-edge user, chooses its serving BS without being constrained to be served only by the closest BS as in the legacy user association and handover approach based on coverage zone. This also extends to the multi-connectivity approach where a user is attached to more than one BS at the same time [75].

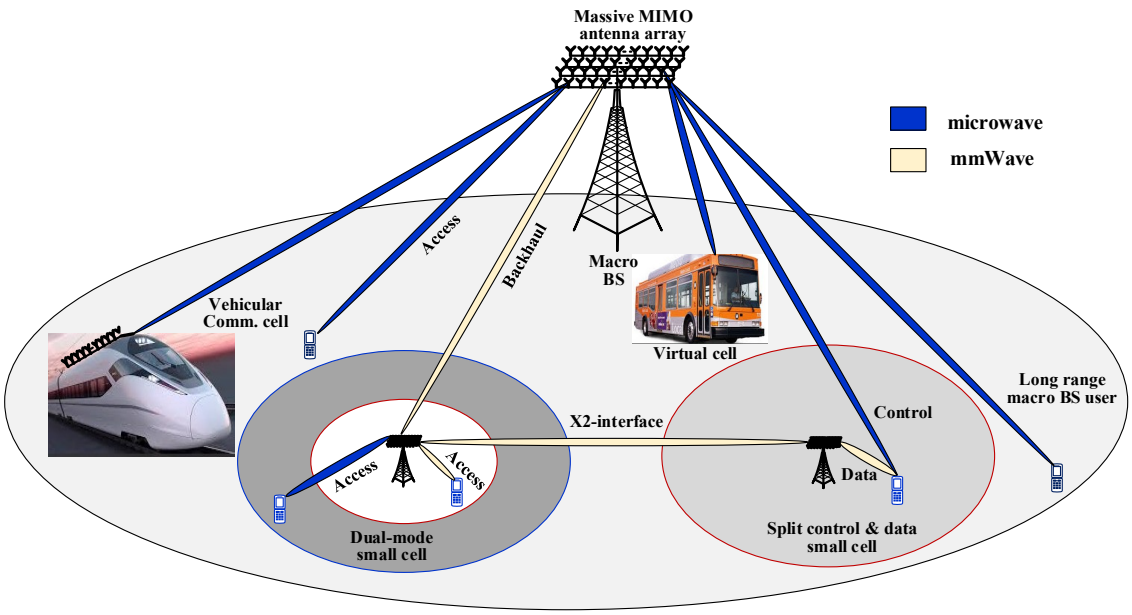

Figure 2.3: Candidate 5G architecture based on μWave/mmWave massive MIMO UDN.

The architecture in Figure 2.3 brings to the forefront many opportunities in terms of possible scenarios, use cases, and applications. Some of the scenarios have been considered lately for legacy systems and will be advanced in 5G while new ones will also emerge. The realization of the architecture in Figure 2.3 is being pursued for 5G through multi-disciplinary and cross-layer approaches.

2.2.2 Propagation Characteristics

Marked differences exist in the propagation characteristics of mmWave massive MIMO networks and those of legacy/conventional cellular systems. At mmWave frequencies, and as the number of BS antennas goes to infinity, the channel characteristics generally become deterministic. Different users experience asymptotic channel orthogonality and fewer user terminals can be supported due to reduced coverage area [2]. Also, signals propagated at mmWave frequencies experience higher PL (which increases with increase in f_c) [17] and also have reduced penetrating power through solids and buildings. Thus, they are significantly more prone to the effects of shadowing, diffraction and blockage, as λ is typically less than the physical dimensions of the obstacles [76–78]. In addition, mmWave signals suffer more attenuation due to rain [79], have increased susceptibility to atmospheric absorption [80] and experience higher attenuation due to foliage than μWave signals [81]. The attenuations due to atmospheric/molecular absorption and rain as a function of f_c are presented in Figures 2.4 and 2.5 (shown on next page), respectively.

As shown in Figure 2.4, the specific attenuation due to atmospheric and molecular absorption have peaks around 60 and 180 GHz. The authors in [82], using air composition and atmospheric data, have shown that the peaks are due to the high absorption coefficient of oxygen (O_2) and water vapor (H_2O) at 60 GHz and 180 GHz, respectively. These two frequency bands are thus best suited for short distance indoor applications, and the unlicensed 60 GHz mmWave WiFi has already taken the lead in this direction through its standardization. Further, the experienced attenuation and molecular noise at mmWave frequencies (excluding the 60 GHz band) vary with the time of the day, and the season of the year, being more pronounced during the night than the day, and more during winter than in summer, due to the combined effect of the fall in temperature and the corresponding rise in humidity [82]. Though the impact of these attenuation effects limits communication coverage and link quality, the impact is however minimal for the average SC sizes of 50-200 m envisaged for 5G SC networks. More so, beamforming is being employed to increase the array gains and improve the SNR, in order to counter the effects of the comparatively higher PL at mmWave frequencies (when compared to the μWave propagation) [4, 60].

Overall, the losses in mmWave systems are higher than those of μWave systems. However, the smaller wavelength (which enables massive antenna arrays) and the huge available bandwidth in the bands can compensate for the losses to maintain and even drastically boost performance gains with respect to SE and EE, provided evolving computational complexity, signal processing, and other implementation issues are addressed [53, 83]. The marked differences in propagation characteristics at μWave and mmWave frequencies necessitate changes in the architecture and applications of cellular networks, as evident in the candidate architecture earlier shown in Figure 2.3.

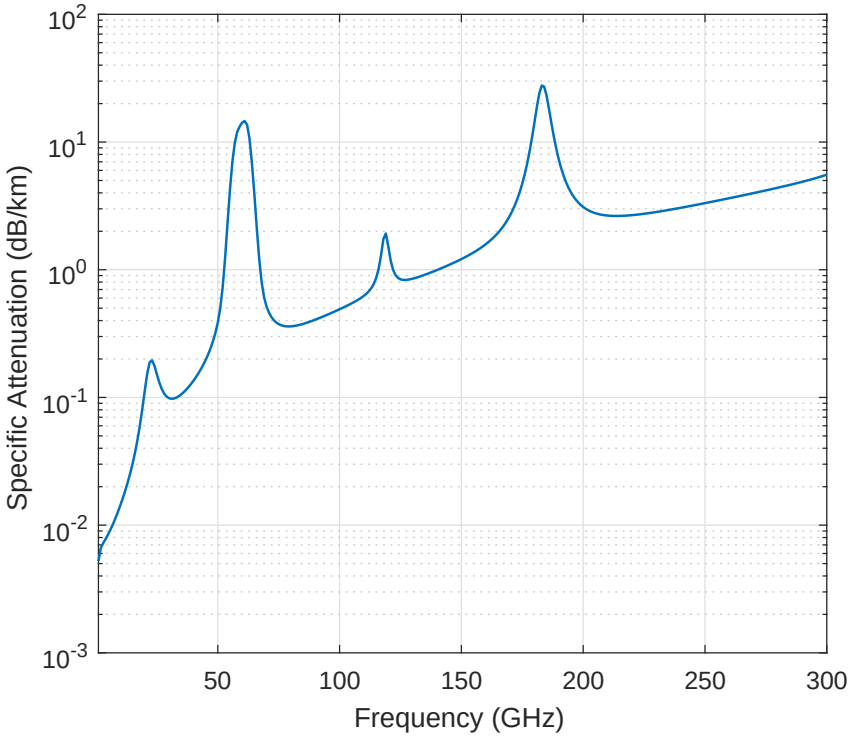

Figure 2.4: Atmospheric and molecular absorption at mmWave frequencies [4].

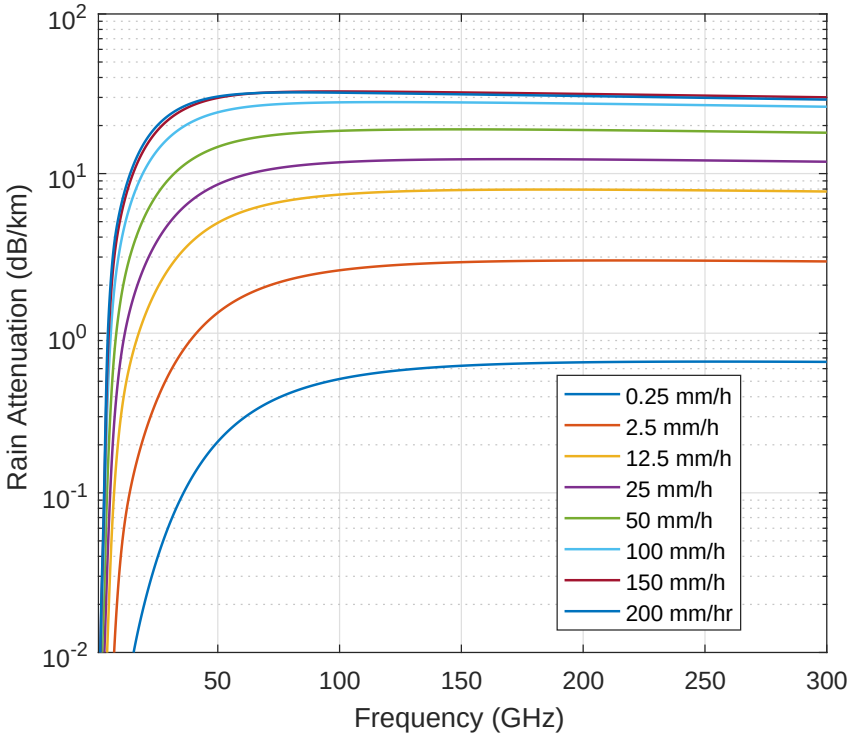

Figure 2.5: Rain attenuation at mmWave frequencies [4].

In Table 2.4, we present a summary of the fundamental differences between conventional (μWave or sub-6 GHz) massive MIMO and mmWave massive MIMO. The comparison in Table 2.4 shows the challenges which have to be addressed or exploited in order to realize the anticipated benefits of mmWave massive MIMO networks. Table 2.5 compares the potential use cases based on the propagation characteristics in LOS, non-LOS (NLOS), outdoor-to-outdoor (O2O), indoor-to-indoor (I2I) and outdoor-to-indoor (O2I) environments [53]. Neglecting the small-scale fading (SSF), the received power (as a function of the separation distance (d)) can be modeled as (2.11) and (2.12) for the μWave and mmWave massive MIMO systems, respectively. Unlike in μWave (2.11), it can be seen that that the shadow fading (SF) and the path loss exponent (PLE) in the mmWave case (2.12) are functions of blockage (ϱ) [2].

Table 2.4: Comparison of μWave and mmWave massive MIMO propagation properties.

Properties	**μWave massive MIMO**	**mmWave massive MIMO**
Path loss	Lower PL compared to mmWave at same d. At $f_c = 2$ GHz and $d = 500$ m typical of MCs, PL_{max} = 93.4, 136.8 and 169.3 dB can be expected in LOS, NLOS and O2I scenarios, respectively [84].	Higher pathloss compared to μWave at same d. At $f_c = 28$ GHz and for d=100 m typical of SCs, maximum PL_{max} of 103.3, 123.8 and 154.2 dB can be expected in LOS, NLOS and O2I scenarios, respectively [85].
Shadow Fading	Independent random variable, small and independent of blockage, NLOS propagation. Typical values are 4, 6 and 7 for LOS, NLOS, and O2I, respectively [84].	Large, dependent on other random variables and mainly caused by blockage, LOS/near-LOS propagation. Typical values are 3.1, 7.8 and 9 for LOS, NLOS, and O2I, respectively [85].
Interference	Distance-dependent. Dominated by a few nearby ones, leads to background interference floor for large number of interferers.	Not really distance-dependent, assumes an ON-OFF type of behavior. Strongly attenuated by randomly-aligned antenna gain patterns and blockage.
SINR	Changes slowly from cell center to cell edge.	Undergoes extremely-random rapid fluctuations; assumes an ON-OFF depending on the beam steering efficiency, blockage, and random beam alignment.
Antenna Array	Singly-massive, only the BSs have massive antenna array.	Double-massive, both the BSs and the UEs have massive antenna array capability.
Signal Processing	Moderately-complex, particularly CSI acquisition and feedback.	Highly-complex due very large amount of CSI.
Handover	Usually done at cell edges based on signal strength for load balancing considerations.	Occurs more frequently because of blockage, beam alignment, and high network density.

$$P_{RX}^{\mu Wave}(d) \approx P_T G_{TRxP} X_{SF}(d) \left(\frac{\lambda}{4\pi}\right)^2 d^{-\alpha}, \tag{2.11}$$

$$P_{RX}^{mmWave}(d, \varrho) \approx P_T G_{TRxP} X_{SF}(d, \varrho) \left(\frac{\lambda}{4\pi}\right)^2 d^{-\alpha(d,\varrho)}, \tag{2.12}$$

where P_T is the TX power, P_{RX} is the receive power, G_{TRxP} is the combined gains of the TX and RX, X_{SF} is the SF function and α is the PLE. Other differences between μWave massive MIMO and mmWave massive MIMO are further highlighted in Table 2.5.

Table 2.5: Comparison of μWave and mmWave massive MIMO use cases (adapted from [53]).

Use case	**μWave massive MIMO**	**mmWave massive MIMO**
Broadband access	High data rates in most propagation scenarios (e.g., ∼100 Mbps/user using 40 MHz of bandwidth), with uniformly good quality of service (QoS).	Huge data rates (e.g., 10 Gbps/user using several GHz of bandwidth) in some propagation scenarios.
IoT, mMTC	Beamforming gain gives power-saving and better coverage than legacy networks.	Not fit for low data rate applications, which will incur significant power overhead.
URLLC	Channel hardening improves reliability over legacy networks.	Difficult due to unreliable propagation.
Mobility support	Same great support as in legacy networks.	Theoretically possible but very challenging.
High throughput fixed link	Narrow beamforming is possible with 100 antennas, 20 dB beamforming gain is achievable; only array size limits the gain.	Possibly even higher beamforming gain than at sub-6 GHz, since more antennas fit into a given area.
High user density	Spatial multiplexing of tens of UEs is feasible and has been demonstrated in field-trials.	Same capability as at sub-6 GHz in theory, but practically limited if hybrid implementation is used.
O2O, I2I communication	High data rates and reliability in both LOS and NLOS scenarios.	Huge data rates in LOS hotspots, but unreliable due to blockage phenomena.
O2I communication	High data rates and reliability	Highly difficult/infeasible due to propagation losses.
Backhaul, fronthaul	Can multiplex many links, but relatively modest data rates per link.	Great for LOS links, particularly for fixed antenna deployments, but less suitable for NLOS links.
Operational regime	Mainly interference-limited in cellular networks, due to high SNR from beamforming gains and substantial inter-user interference.	Mainly noise-limited in indoor scenaros, due to the huge bandwidth and limited ICI, but can be interference-limited in outdoor scenarios.

In terms of benefits, the larger bandwidth available in the mmWave bands when compared to the μWave bands enables new applications such as wireless fronthauling, the higher PL favors high-rate, short-range communications while the shorter wavelength allows the antennas at both the BSs and UEs to scale up (i.e., go massive) due to the dramatic reduction in antenna sizes. However, new challenges evolve. The combination of the huge bandwidth and massive antenna arrays translate to heavy computational load and signal processing due to the large amount of CSI that have to be processed for channel estimation, channel feedback, precoding, etc. Also, mmWave signaling will lead to a higher frequency of handovers in UDN if not properly managed.

Notwithstanding the promising potentials of mmWave massive MIMO technology, a broad range of challenges spanning the length and breadth of communications theory and engineering has to be addressed. The challenges arise due to the differences in the architecture and propagation characteristics of mmWave massive MIMO networks when compared to prior systems. Among others, the key challenges include: channel modeling, antenna and RF transceiver architecture design, waveforms and multiple access schemes, information theoretic issues, channel estimation techniques, modulation and EE issues, MAC layer design, interference management, mobility management, health and safety issues, system-level modeling, experimental demonstrations, tests and characterization, standardization and business models [2].

2.2.3 Health and Safety Issues

With the mmWave bands being promising candidates for future broadband mobile communication networks, it is essential to understand the impacts of mmWave radiation on the human body and the potential health effects related to its exposure. In addition, the current safety rules regarding RF exposure do not specify limits above 100 GHz whereas spectrum use will inevitably move to these bands over time, hence the need for further investigations to codify safety metrics at these frequencies [2]. The mmWave band constitutes RF spectrum with f_c between 30-300 GHz. The photon energy in these bands ranges from 0.1 to 1.2 milli-electron volts (meV). Unlike the ultraviolet (UV), X-ray and gamma rays, mmWave radiation is non-ionizing and so cannot cause cancer. Therefore, the main safety concern is heating of the eyes and skin caused by the absorption of mmWave energy in the human body and constitutes the major biological effect that can be caused by the absorption of EM mmWave energy by tissues, cells and biological fluid [2, 86].

Based on findings from mmWave radiation studies, the authors in [86] concluded that both the eyes and the skin (whose tissues would receive the most radiation) do not appear prone to damage from exposure experienced from mmWave communication technologies in the far-field, while more studies are required regarding exposure to communication devices (such as mobile devices with high-gain, adaptive and smart antennas) in the near-field. Similarly, according to the authors of [87], more than 90% of the transmitted EM power is absorbed within the epidermis and dermis layers and little power penetrates further into deeper tissues. However, heating of human tissue may extend deeper than the epidermis and dermis layers. Also, the steady state temperature elevations at different body locations may vary even when the intensities of EM radiations are the same. The authors concluded that power density (PD) is not likely to be as useful as specific absorption rate (SAR) for assessing safety, especially in the near-field, and the proposed temperature-based technique is an acceptable dosimetric quantity for demonstrating safety and setting exposure limits for mmWave radiations [86, 87].

2.2.4 Standardization Activities

The attractive capabilities and high commercial potentials of mmWave communications have spurred several international activities aimed at standardizing it for wireless personal area networks (WPANs) and wireless local area networks (WLANs). These efforts include the IEEE 802.15.3c, WirelessHD and WiGiG (IEEE 802.11ad and IEEE 802.11ay) [60, 63, 64]. Early efforts focused on the 60 GHz band for WiFi and WiGiG standards due to the earlier notion that mmWave bands are unsuitable for mobile communications [16]. However, several

new findings from research, trials and deployment (such as MiWEBA [88, 89] and MiWaveS [90, 91]) have established the suitability of incorporating mmWave communications into cellular networks [65, 92]. Massive MIMO, on the other hand, has been under consideration for standardization by 3GPP since LTE-A Release 12 [16]. The release work programme, which was largely completed in March 2015, considered four areas of significant enhancements and enablers: SCs and HetNets, multi-antennas (e.g., massive MIMO and elevation beamforming), proximity services and procedures for supporting diverse traffic types [93]. 3GPP's Release 14 (completed June 2017) featured major 5G enablers, including MIMO enhancements. Further works on massive MIMO standardization featured in 3GPP's 5G New Radio (NR) (also referred to as Release 15 or 5G Phase 1) completed in 2018 and enhancements will continue through Release 16 (5G Phase 2) expected to be finalized by December 2019. Standardization of both mmWave communications and massive MIMO will open up new opportunities for next-generation cellular networks [3, 4].

The three major players for 5G standardization are the ITU, 3GPP and the Institute of Electrical and Electronics Engineers (IEEE). Candidate technologies are being evaluated by ITU-Radiocommunication through its 5D working party (WP). The allocation of mmWave spectrum for cellular applications is expected to be finalized at WRC 2019. Also, ITU-T has been conducting system review and proof-of-concept studies on IMT-2020 by its Study Group 13 [3, 4, 16]. As the third major player, IEEE has recently undertaken a 5G track to enhance existing standards and to evolve new technologies for the mmWave unlicensed bands. These efforts include: IEEE 802.11 ad/aj/ay, IEEE 802.15.3c, ECMA-387, P1918.1, P1914.3, and IEEE 802.22, among others. The completion timelines for these activities vary among the different specification groups. These activities will lead to the first certified 5G standards. The standardization is expected to be completed by late 2019, ahead of the much-anticipated 2020 timeline for commercial deployment [3, 4, 16].

2.3 5G Channel Measurement and Modeling

Several new technologies are being explored for 5G systems in order to provide anywhere and anytime connectivity for anyone and anything. Each of these technologies introduces new propagation properties and sets specific requirements on 5G channel modeling. For example, the mmWave massive MIMO channel is intrinsically an ultra-broadband channel with huge bandwidth and spatial multiplexing capability to significantly enhance wireless access and improve cell and user throughputs [68, 94]. Inspecting from a propagation perspective, mmWave signals exhibit LOS or near-LOS propagation with absolute increase in PL with increasing f_c [95], specular reflection attenuation [96], diffuse scattering [97, 98], very high diffraction attenuation [99] and frequency dispersion effect, which with the prospect of huge bandwidth, allows the propagation to be considered as frequency-dependent [21, 99]. In general, 5G channel models should support: wide frequency range (e.g., 350 MHz-100 GHz), broad bandwidths (10 MHz-4 GHz), wide range of scenarios (indoor, urban, suburban, rural, etc.), double-directional 3D antenna and propagation modeling, frequency dependency, smooth time evolution, spatial and frequency consistency, large antenna arrays and high mobility, among others [100].

Typically, channel measurement campaigns are undertaken at different times, cities, environments and under different scenarios. Following the channel measurement activities, channel parameters (such as PL, PLE, SF, penetration loss, power delay profile (PDP), delay

spreads (DSs), angular spreads (ASs), coherence bandwidth, etc.) are estimated from the obtained data or field results to develop channel models. Considering all necessary factors (such as frequency, propagation environment, scenario, etc.), the developed channel models provide statistical, mathematical and analytical frameworks for simulation studies and performance evaluation of wireless communication networks. Such frameworks are also used to compare and/or validate empirical data from field deployment and operation tests. Thus, efficient and accurate channel models are central to system design and performance evaluation. Using channel sounding techniques, several measurement campaigns have been undertaken by different groups, in different cities, at different frequencies (10-100 GHz) and for diverse scenarios and setups, to characterize the mmWave channel. References [4, 100] provide excellent summaries of the results (with respect to the PL, PLE, SF, PDP, DS, AS, Rician K-Factor (KF), coherence bandwidth, etc.) of the cross-continent channel measurement efforts between 2012 and 2018. A summary of the capabilities of the 5G channel models adapted for this thesis are given in Table 2.6.

Table 2.6: Comparison of adapted 5G channel models (adapted from [100]).

Features	**3GPP TR 36.873** [84]	**3GPP TR 38.900** [85]	**NYUSIM** [42, 101, 102]
Modeling approach	GBSM, map-based hybrid model	GBSM, map-based hybrid model	Statistical
Frequency range (GHz)	< 6	6-100	0.5-100
Bandwidth [<6, > 6] GHz	10% of f_c	10% of f_c	[100 MHz, 2 GHz]
Support large array	yes	yes	yes
Support spherical waves	no	no	no
Support dual mobility	no	no	no
Support 3D propagation	yes	yes	yes
Support mmWave	no	yes	yes
Dynamic modeling	yes	yes	yes
Spatial consistency	yes	yes	yes
High mobility	limited	limited	limited
Blockage modeling	yes	yes	yes
Gaseous absorption	yes	yes	yes

Based on the modeling approach adopted, the channel models are classified as shown in Figure 2.6 (shown on next page). The respective models take their name (as used in Tables 2.6) using a bottom-up naming approach. For example, RS-GBSM represents a Regular-Shaped Geometry-Based Stochastic Model, while TDL-NGSM is a Tapped Delay Line Non-Geometry based Stochastic Model. Deterministic channel models characterize the physical propagation parameters in a deterministic manner by solving the Maxwell's equations or approximated propagation equations. These models are site-specific and they rely on the detailed or precise information of the propagation environment, including the location of the BSs, UEs and scatterers. Thus, they have high accuracy, but introduce high computational complexity. An example of deterministic channel models is ray tracing (RT), where the positions of the TX and RX are specified and then all possible rays are predicted. The map-based deterministic models use RT and 3D maps. The stochastic models, on the other hand, describe channel parameters using certain statistical or probability distributions. The stochastic models are more analytically tractable and can be adapted to various scenarios and settings. However,

they have lower accuracy when compared to the deterministic models [100]. Hybrid models use a combination of the deterministic and stochastic approaches [75]. Other representative 5G channel models that have resulted from the respective measurement campaigns are compared in Table 2.7 (shown on next page) [100].

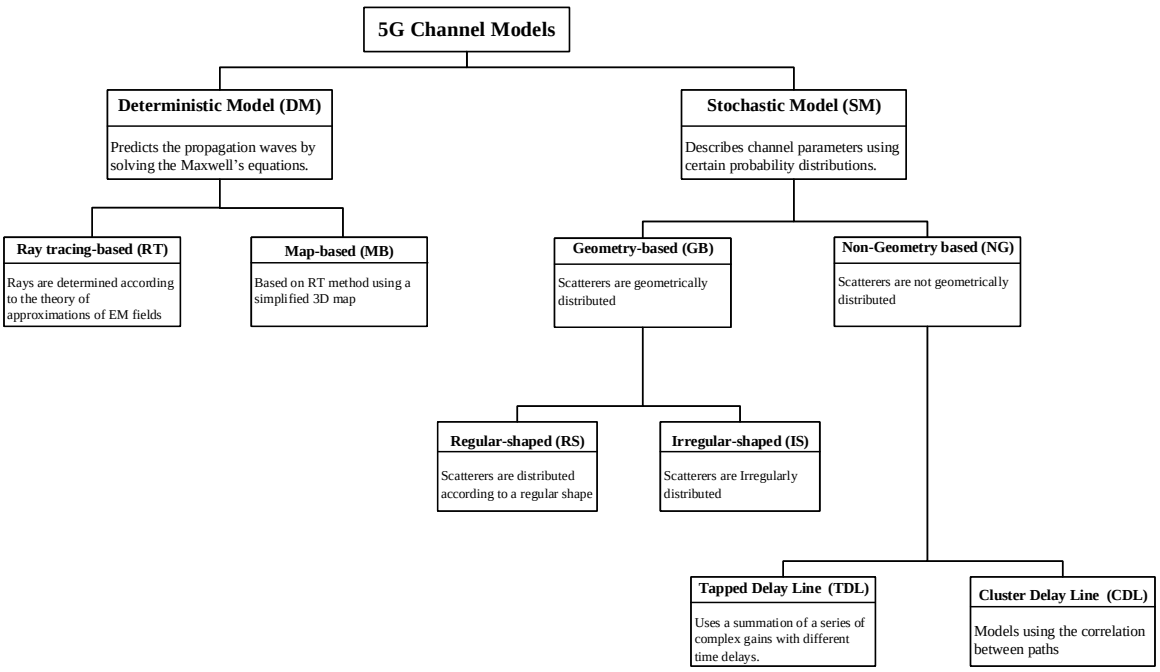

Figure 2.6: Classification of 5G channel models based on modeling approach (adapted from [100]).

In this section, we provide a background to 5G channel modeling involving the interplay of massive MIMO and mmWave communication in cellular and C-I2X scenarios.

2.3.1 mmWave Massive MIMO Channels

At mmWave frequencies, the assumption of asymptotic pair-wise orthogonality between channel vectors under independent and identically distributed (i.i.d) Rayleigh fading channel, which is valid for conventional massive MIMO, no longer holds. The number of independent multipath components (MPCs) becomes limited and so channel vectors exhibit correlated fading [68,112]. For a mutuallly orthogonal channel, every pair of column vectors of the channel $\mathbf{H}$ satisfies the condition in (2.13). With the assumption of i.i.d. Rayleigh fading channel, the condition in (2.13) is asymptotically achieved with very large N_{TX}, which by the law of large numbers gives (2.14).

$$h_m^H h_n = 0, \forall m \neq n, \tag{2.13}$$

$$\frac{1}{N_{TX}} h_m^H h_n \longrightarrow 0, N_{TX} \longrightarrow \infty, \forall m \neq n. \tag{2.14}$$

Table 2.7: Comparison of other representative 5G channel models (adapted from [100]).

Features	**3GPP TR 38.901** [103]	**QuaDRiGa** [104, 105]	**mmMAGIC** [106]	**5GCMSIG** [107]	**MG5GCM** [108]
Modeling approach	GBSM, map-based hybrid	GBSM	GBSM, GGBSM	GBSM, GGBSM	GBSM
Frequency range (GHz)	0.5-100	0.45-100	6-100	0.5-100	-
Bandwidth [< 6, > 6] GHz	10% of f_c	1 GHz	2 GHz	[100 MHz, 2 GHz]	-
Support large array	yes	yes	yes	limited	yes
Support spherical waves	no	yes	yes	no	yes
Support dual mobility	no	no	no	no	yes
Support 3D propagation	yes	yes	yes	yes	yes
Support mmWave	yes	yes	yes	yes	yes
Dynamic modeling	yes	yes	yes	yes	yes
Spatial consistency	yes	yes	yes	yes	no
High mobility	limited	yes	yes	yes	yes
Blockage modeling	yes	yes	no	yes	no
Gaseous absorption	yes	yes	no	no	no

Features	**METIS** [109]		**COST 2100** [110]	**MiWEBA** [88]	**IMT-2020** [111]
Modeling approach	Stochastic	Map-based	GBSM	Q-D based	GBSM, map-based
Frequency range (GHz)	up to 70	up to 100	< 6	57-66	0.5-100
Bandwidth [< 6, > 6] GHz	[100 MHz, 1 GHz]	10% of f_c	-	2.16 GHz	[100 MHz, 10% of f_c]
Support large array	no	yes	-	yes	yes
Support spherical waves	no	yes	no	yes	no
Support dual mobility	limited	yes	no	yes	no
Support 3D propagation	yes	yes	yes	yes	yes
Support mmWave	partly	yes	no	yes	yes
Dynamic modeling	no	yes	yes	limited	yes
Spatial consistency	SF only	yes	yes	yes	yes
High mobility	limited	no	yes	no	limited
Blockage modeling	no	yes	no	yes	yes
Gaseous absorption	no	yes	no	yes	yes

However, mmWave massive MIMO channels are neither i.i.d. nor is the N_{TX} infinite. Therefore, the condition for mutual orthogonality in (2.13) cannot be satisfied in reality [112]. MmWave massive MIMO channel models, therefore, have to consider this non-orthogonality for propagation in realistic environments. Similarly, the assumption of planar waves in conventional massive MIMO would have to be replaced with spherical waves representation as depicted in Figure 2.7. Also, spatial non-stationarity which becomes more severe has to be considered in mmWave massive MIMO channel models [95, 112, 113]. Also, for practical realization of such channels, the corresponding high computational rate required for CSI estimation and feedback in high-mobility channels have to be factored into the design [68]. Extensive indoor and outdoor channel measurement campaigns and simulations have been carried out by [60, 94, 114], among others, to deduce these outcomes. Many of these issues have been factored into the different 5G channel models along their evolutionary trails as shown in Tables 2.6 and 2.7. It should be noted, however, that the channel models employed in this work do not consider spherical waves and dual mobility support, as earlier shown in Table 2.6. The thesis assumes plane waves propagation and considers static BSs/APs but mobile users.

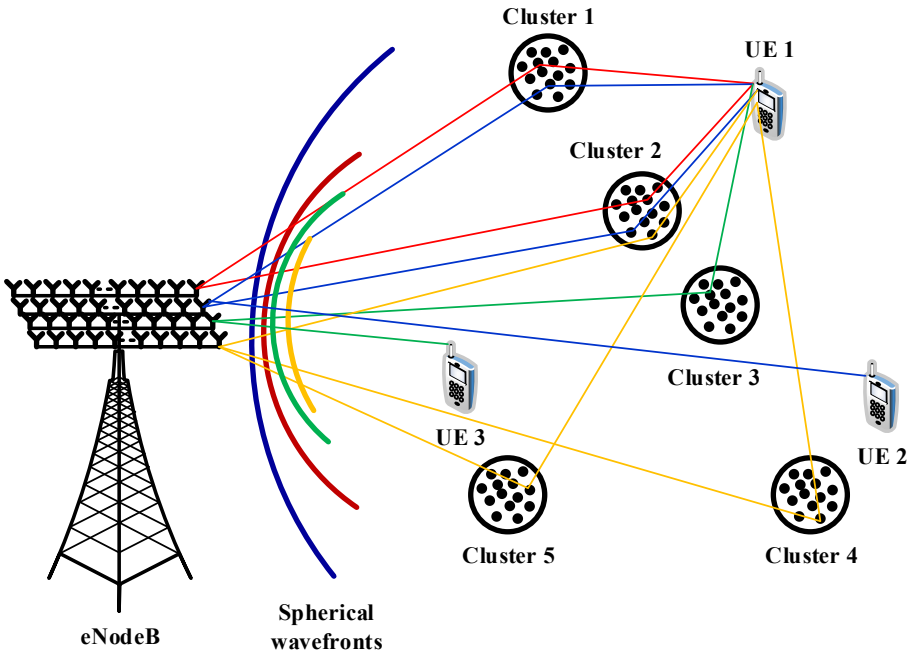

Figure 2.7: Illustration of spherical wavefront phenomena for mmWave massive MIMO (adapted from [112]).

2.3.2 3GPP 3D Channel Models

Over time, several channel models have evolved. These include the COST series (231, 259 and 273), the WINNER family (I and II) and the spatial channel models (SCMs). These channel models were 2D models. However, studies such as [31–33], among others, have shown that 2D channel models underestimate system performance. 3D channel models give a more realistic outlook as they consider the elevation (zenith/vertical) angles alongside the azimuth

(horizontal) angles used by the 2D models. Thus, 3D channel models are essential for the accurate and realistic performance evaluation of mobile networks. In addition, three significant paradigms are shifting interest away from the 2D μWave channel models. The first paradigm is the growing interest in the amazing spectral prospects achievable with mmWave communication. Elevation beamforming, enabled by mmWave massive MIMO and planar antenna arrays, constitutes the second paradigm. Interest in O2I and indoor-to-outdoor (I2O) propagation modeling that account for building, blockage and other limiting effects is the third [84,85,115]. Accordingly, newer (3D) channel models which address these interests have continued to evolve as earlier shown in Tables 2.6 and 2.7.

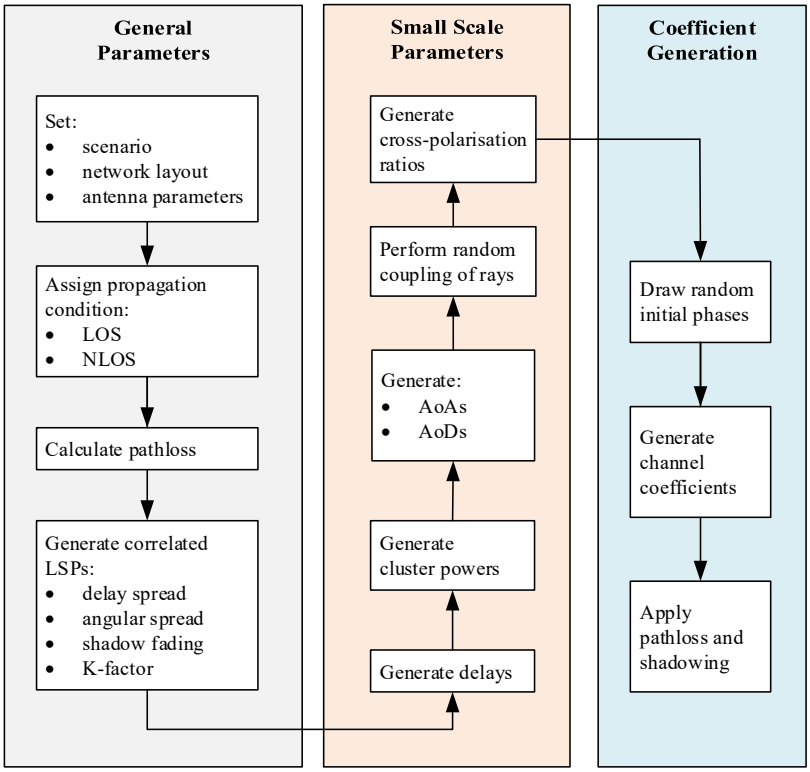

Figure 2.8: Flow chart for the 3GPP 3D geometry-based SCM (adapted from [32,84,85,103]).

Most recent channel model efforts are adopting the 3D geometry-based stochastic model (GBSM) approach. References [76,104,105,116] and [101,117–123] provide a good background on mmWave channel modeling using the GBSM approach. The three 3D 3GPP channel models (i.e., TR 36.873 [84], TR 38.900 [85] and TR 38.901 [103]) are GBSM models and they generally follow the flow chart in Figure 2.8 to estimate channel parameters [32,34]. The 3GPP TR 36.873 [84] is defined for the sub-6 GHz band for LTE while 3GPP TR 38.900 [85] models the mmWave band from above 6 GHz up to 100 GHz. The features of these two models have been shown in Table 2.6. The recent 3GPP TR 38.901 [103] generalizes the channel model from 0.5-100 GHz as shown in Table 2.7. The 3GPP channel models consider the common use cases: urban macrocell (UMa), urban microcell (UMi) or street canyon, rural macrocell (RMa) and indoor office scenarios for LOS, NLOS and O2I propagation environments. The core of the models (i.e., the SSF) is identical to the WINNER+ model. The models consider effects such

as spatial consistency, blockage, atmospheric attenuation and oxygen absorption at mmWave bands. However, the models have limited capabilities for dual mobility, spherical waves and non-stationarity for massive MIMO antenna arrays. Typically, the mmWave models support larger bandwidths (up to 10% of f_c) [4, 100].

The 3GPP 3D channel models parameterize the DS, AS and cluster powers as frequency-dependent and support multiple frequencies in the same scenario. The number of rays within a cluster are generated within a given range based on the intra-cluster DS and AS, as well as the array size. Each MPC may have different delays, powers and angles, with the offset angles within a cluster generated randomly [84,85,100,103]. The models also proposed a map-based hybrid (stochastic-deterministic) model using a combination of the described stochastic model and a deterministic model based on RT and 3D map, considering the influences of the environmental structures and materials [100]. The methodology from these 3GPP channels models have been adopted in our channel implementation and the parameters and values have been extensively used in the baseline SLS [38] used for some of the performance evaluation and results in this investigation.

2.3.3 NYUSIM Channel Model

Following extensive mmWave channel measurements at 28, 38, 60 and 73 GHz bands, a 3GPP-like 5G channel simulator known as NYUSIM [42, 101, 102] was developed by the New York University wireless team. The NYUSIM is a 3D statistical spatial channel model (SSCM) and employs the time cluster-spatial lobe modeling approach [101]. The time cluster (TC) and spatial lobe (SL) concepts describe the temporal and spatial statistics independently, and their description somewhat differs from the cluster structure in the 3GPP/WINNER model. A TC refers to a number of MPCs or rays with close delays and where different clusters are separated by an inter-cluster void interval larger than 25 ns. The different MPCs forming the cluster can however arrive from different directions. The SL, on the other hand, describes a set of MPCs with close angle of arrival (AoA) or angle of departure (AoD) whose powers spread in the azimuth and elevation planes, but whose rays could possibly arrive over hundreds of nanoseconds. The channel impulse response (CIR) is generated for the respective TCs and cluster subpaths (SPs) [100, 101, 121]. The statistical distributions for the TC-SL generation are given in Table 2.8.

Table 2.8: Distribution Parameters for 3D CIR Generation (adapted from [101])

TC / SL	**Symbol**	**Name of Parameter**	**Distribution**
TC	N_{cl}	Number of Time Clusters	Discrete Uniform [1, 6]
	N_{sp}	Number of Sub-paths	Discrete Uniform [1, 30]
	τ_{cl}	Cluster Delays	Exponential
	P_{cl}	Cluster Powers	Lognormal
	ρ_{sp}^{cl}	Sub-path Delays	Exponential
	P_{sp}^{cl}	Sub-path Powers	Lognormal
	$\psi_{cl,sp}$	Sub-path Phases	Uniform $(0, 2\pi)$
SL	N_{lobe}	Number of Spatial Lobes (AoD & AoA)	Poisson
	ϕ_{lobe}	Lobe Azimuth Angles (AoD & AoA)	Uniform $(0, 360)$
	θ_{lobe}	Lobe Elevation Angles (AoD & AoA)	Gaussian
	σ_{ϕ}	RMS Lobe Azimuth Spread (AoD & AoA)	Gaussian
	σ_{θ}	RMS Lobe Elevation Spread (AoD & AoA)	Laplacian

The channel simulator (NYUSIM) has support for large arrays, mmWave communication, gaseous absorption, large bandwidth and 3D propagation [42, 101], and through its updates, has a graphical user interface (GUI), supports wideband communication [102] and proposes support for spatial consistency [115]. It, however, has limited or no support for mobility, blockage and spherical wave modeling. The NYUSIM model has a similar representation to the extended Saleh-Valenzuela model commonly employed for mmWave massive MIMO. The extended model is a narrowband clustered channel representation which allows accurate capturing of the characteristics of mmWave channels. Under this clustered model in (2.15), the discrete-time narrowband channel matrix $\mathbf{H}$ is assumed to be a sum of the contributions of L propagation paths or MPCs [67, 124].

$$\mathbf{H} = \sqrt{\frac{N_{RX}N_{TX}}{L}} \sum_{l=1}^{L} \alpha_l \cdot \wedge_{RX}\left(\phi_l^{RX}, \theta_l^{RX}\right) \cdot \wedge_{TX}^{H}\left(\phi_l^{TX}, \theta_l^{TX}\right) \cdot \mathbf{a}_{RX}\left(\phi_l^{RX}, \theta_l^{RX}\right) \cdot \mathbf{a}_{TX}^{H}\left(\phi_l^{TX}, \theta_l^{TX}\right), \tag{2.15}$$

where α_l is the complex gain of the l^{th} path, $\phi_l^{TX}, \theta_l^{TX}$ are the azimuth and elevation AoDs, respectively, while $\phi_l^{RX}, \theta_l^{RX}$ represent the azimuth and elevation AoAs, respectively. The vectors $\mathbf{a}_{RX}\left(\phi_l^{RX}, \theta_l^{RX}\right)$ and $\mathbf{a}_{TX}\left(\phi_l^{TX}, \theta_l^{TX}\right)$ represent the normalized RX and TX array response vectors at the azimuth (ϕ) and elevation (θ) angles, respectively. $\wedge_{RX}\left(\phi_l^{RX}, \theta_l^{RX}\right)$ and $\wedge_{TX}\left(\phi_l^{TX}, \theta_l^{TX}\right)$ are the RX and TX gains, respectively, which can be set to one within the range of the AoAs and AoDs, for simplicity and without loss of generality [125, 126]. The channel simulator updated with advanced 5G features was used for some of the performance evaluation and results in this investigation.

2.4 Beamforming Techniques

The design of beamforming schemes is highly essential for mmWave massive MIMO systems. Beamforming optimizes the system performance using the concept of interference cancellation in advance by controlling the phases and/or magnitudes of the original signals. It aims at transmitting pencil-shaped beams that point directly at targeted terminals with minimal or no interference projected to non-users of interest. Beamforming schemes can generally be classified into three: analog beamforming (ABF), digital beamforming (DBF) and hybrid beamforming (HBF). While ABF can only be employed for single-stream single-user MIMO systems, both DBF and HBF schemes can be used for single-user as well as multi-user systems [127]. The three beamforming schemes are overviewed in the following subsections. Detailed description and implementation details are provided in the subsequent chapters.

2.4.1 Analog Beamforming

This is used to control the phases of signals (using phase shifters (PSs)) with single data stream (using a single RF chain) in order to realize significant antenna array gain and effective SNR. With perfect knowledge of the CSI available at both the BS and the UE, the analog beamformer employs N_{TX} antennas at the BS with only one RF chain to send a single data stream to a terminal (i.e., UE) with N_{RX} antennas and only one RF chain too [128]. This concept is also called beam steering and aims at the design of the analog precoder (also

known as TX RF beamformer) vector $\mathbf{f}_{\mathrm{RF}}$ and analog combiner (alternatively called RX RF beamformer or postcoder) vector $\mathbf{w}_{\mathrm{RF}}$ that maximize the effective channel/SNR $\left|\mathbf{w}_{\mathrm{RF}}^{H}\mathbf{H}\mathbf{f}_{\mathrm{RF}}\right|$, where $\mathbf{H} \in \mathbb{C}^{N_{RX}\times N_{TX}}$ is the channel. The optimization problem for ABF is thus formulated as in (2.16), where φ_i and φ_l are the AoAs and AoDs, respectively [127]. The analog TX is shown in Figure 2.9 and the analog RX can be similarly illustrated. Here, only one beam is created and is particularly useful in LOS propagation scenarios [53].

$$\begin{aligned}
&\left(\mathbf{w}^{opt}, \mathbf{f}^{opt}\right) = \arg\max \left|\mathbf{w}_{\mathrm{RF}}^{H}\mathbf{H}\mathbf{f}_{\mathrm{RF}}\right| \\
&\text{subject to} \\
&w_i = \sqrt{\frac{1}{N_{RX}}} \cdot e^{j\varphi_i}, \quad \forall i, \\
&f_l = \sqrt{\frac{1}{N_{TX}}} \cdot e^{j\varphi_l}, \quad \forall l.
\end{aligned} \tag{2.16}$$

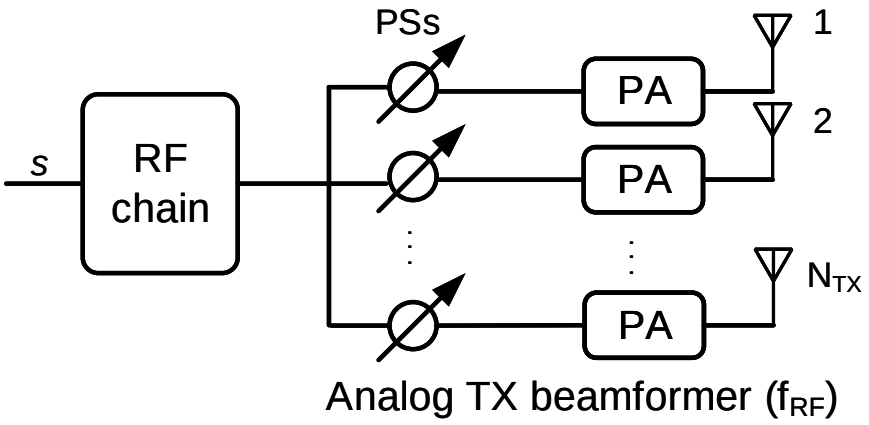

Figure 2.9: Analog beamforming architecture.

Perfect CSI is unrealistic in practical systems, thus necessitating beam training where both the UE and the BS collaborate in selecting the best beamformer (at the BS end) and combiner (at the user end) pair ($|\mathbf{f}| - |\mathbf{w}|$ pair) from pre-defined codebooks in order to optimize system performance [127]. For mmWave massive MIMO systems, the codebook sizes could be very large due to a large number of antennas, together with the accompanying huge overheads. In solving this challenge, a systematic beam training scheme was proposed by Wang *et al.* [129] which reduces the overhead and limits the potentially exhaustive codebooks search using a hierarchical approach. Similarly, Cordeiro *et al.* in [130] proposed a single-sided beam training scheme using a two-step approach which was adopted by the IEEE 802.11ad standard, where the combiner is first fixed to search for the best beamformer exhaustively, and subsequently, the best beamformer is fixed to search for the best combiner exhaustively. Though the ABF scheme has simple hardware requirement (only one RF chain), it suffers severe performance loss as only the phases of transmit signals can be controlled. More so, an extension of the scheme to the multi-user system is not trivial [127]. Therefore, its use in mmWave massive MIMO systems is rather limited as mmWave massive MIMO targets the multi-user case to boost system capacity.

2.4.2 Digital Beamforming

This can control both the phases and amplitudes of transmit signals, and it can be employed in both single-user and multi-user MIMO systems. For the single-user case, the digital beamformer (DBF) $\mathbf{F}_{DBF} \in \mathbb{C}^{N_{TX} \times N_s}$ uses N_{TX} antennas and N_{RF}^{TX} RF chains at the BS to transmit N_s data streams (where $N_s \leq N_{RF}^{TX}$ and $N_{RF}^{TX} = N_{TX}$) to a user with N_{RX} antennas and N_{RF}^{RX} RF chains (where $N_{RF}^{RX} \geq N_s$ and $N_{RF}^{RX} = N_{RX}$). The transmit DBF is shown in Figure 2.10 and RX DBF can be similarly illustrated by replacing the TX components with the corresponding RX components. The DBF can create a number of beams and has flexibility of adapting the beams to multipath and frequency selecting fading [53, 128].

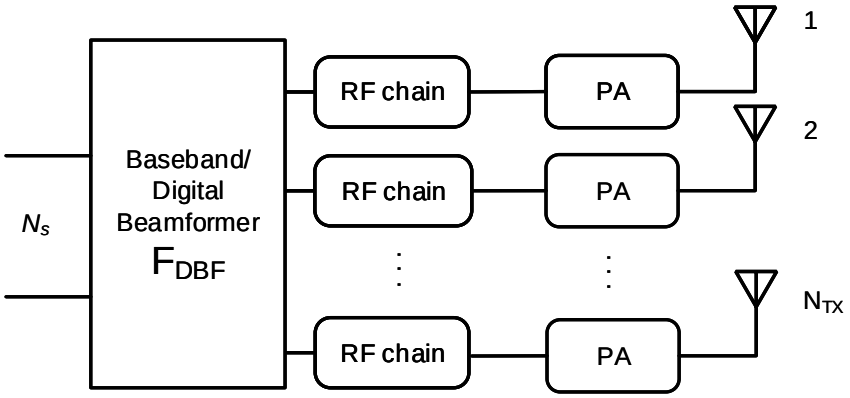

Figure 2.10: Digital beamforming architecture.

Examples of linear digital beamformers include the matched filter (MF), zero forcing (ZF) and the Wiener filter (WF) beamformer, in increasing order of complexity and performance. The digital beamformer models are expressed in (2.17)-(2.19), respectively [127], where $\mathbf{H}$ is the $N_{RX} \times N_{TX}$ channel matrix with normalized power, P_{RX} represents the average received power and σ_n^2 denotes the noise power. The digital combiners/postcoders/beamformers ($\mathbf{W}_{DBF}$) can be similarly formulated.

$$\mathbf{F}_{DBF}^{MF} = \mathbf{H}^H, \tag{2.17}$$

$$\mathbf{F}_{DBF}^{ZF} = \mathbf{H}^H \left(\mathbf{H}\mathbf{H}^H\right)^{-1}, \tag{2.18}$$

$$\mathbf{F}_{DBF}^{WF} = \mathbf{H}^H \left(\mathbf{H}\mathbf{H}^H + \frac{\sigma_n^2 N_s}{P_{RX}} \mathbf{I}_{N_{RX}}\right)^{-1}. \tag{2.19}$$

For digital beamforming, the optimal TX beamformer and RX beamformer can be realized via the singular value decomposition (SVD) of the channel matrix $\mathbf{H}$, since $\mathbf{H}$ can be decomposed as $\mathbf{H} = \mathbf{U}\mathbf{\Sigma}\mathbf{V}^H$. With this decomposition and using (2.20), the optimal TX

beamformer $\mathbf{V}^{opt}$ and RX beamformer $\mathbf{U}^{opt}$ can be set as the first N_s columns of $\mathbf{F}_{DBF}$ and $\mathbf{W}_{DBF}$, respectively [131].

$$[\mathbf{W}_{DBF}, \mathbf{\Sigma}_{DBF}, \mathbf{F}_{DBF}] = \texttt{svd}(\mathbf{H}). \tag{2.20}$$

On the other hand, multi-user systems employing digital beamformers simultaneously transmit to K mobile terminals, where each terminal is equipped with N_{RX} antennas, and the BS is equipped with N_{TX} antennas, N_{RF}^{TX} RF chains and $\mathbf{F}_{DBF} \in \mathbb{C}^{N_{TX} \times N_s K}$ beamformers, such that $(N_s \leq N_{TX})$ and the k^{th} user has $(N_{TX} \times N_s)$ digital beamformer $\mathbf{F}_{DBF}^{k} \in \mathbb{C}^{N_{TX} \times N_s}, \forall k \in \{1, 2, \ldots, K\}$ with total transmit power constraint $\left\|\mathbf{F}_{DBF}^{k}\right\|_F^2 = N_s$. The received signal by the k^{th} terminal is thus expressed as (2.21).

$$\mathbf{y}_k = \mathbf{H}_k \sum_{n=1}^{K} \mathbf{F}_{DBF}^{n} \mathbf{s}_n + \mathbf{n}_k, \tag{2.21}$$

where $\mathbf{s}_n$ of size $(N_s \times 1)$ is the original signal vector with normalized power before beamforming. $\mathbf{H}_k$, which is of size $(N_{RX} \times N_{TX})$, is the channel matrix between the BS and the k^{th} UE, and $\mathbf{n}_k$ is the AWGN vector with entries following i.i.d. distribution $\mathcal{CN}(0, \sigma_n^2)$. From (2.21), the terms $\mathbf{H}_k \mathbf{F}_{DBF}^{n} \mathbf{x}_n$ for $n \neq k$ are interferences to the k^{th} UE. For Block Diagonization (BD) beamformer design [132], $\mathbf{F}_{DBF}^{n}$ is chosen to satisfy the condition $\mathbf{H}_k \mathbf{F}_{DBF}^{n} \mathbf{s}_n = 0$, $\forall n \neq k$.

Generally, digital beamformers have best performance in terms of SE (as compared to ABF and HBF) as they are able to control both the phases and amplitudes of transmit signals. However, their use of one dedicated RF chain per antenna can lead to higher energy consumption and prohibitive hardware cost, making them somewhat impractical for mmWave massive MIMO systems. As technology matures and components consume much less power than what they consume today, DBF may become practically feasible for mmWave massive MIMO systems [53,57,131,133]. There are several non-linear digital beamformers such as the optimal Dirty Paper Coding (DPC) [134] and the near optimal Tomlinson-Harashima (TH) beamformers [135], which have superior performance than the aforementioned linear digital beamformers (e.g., MF, ZF and WF) but they also have higher computational complexity [127].

2.4.3 Hybrid Beamforming

This is a promising scheme for mmWave massive MIMO as it offers a significant reduction in the number of required RF chains and the associated energy consumption and cost (when compared with DBF), yet achieving near-optimal performance. It realizes this hybrid configuration by employing a small-size digital beamformer $\mathbf{F}_{\mathrm{BB}}$ with a small number of RF chains $(1 < N_{RF} < N_{TX})$ to cancel interference in the first stage, and a large-size analog beamformer $\mathbf{F}_{\mathrm{RF}}$ with a large number of phase shifters (PSs) in the second stage to increase the antenna array gain [127]. This two-stage hybrid beamformer [136] employs the BS analog beamformer and the UE analog combiner to jointly maximize the desired signal power of each user in the first stage, and in the second stage employs BS digital beamformer to manage multi-user interference (MUI). The TX HBF is illustrated in Figure 2.11 and the RX HBF structure can be similarly illustrated with $\mathbf{W}_{\mathrm{RF}}$ and $\mathbf{W}_{\mathrm{BB}}$ as the analog RF and digital baseband combiner, respectively, as investigated in [125,131,137,138]. The HYB configuration is

capable of creating multiple beams (limited by N_{RF}) which can be adapted to the multipath and frequency-selective fading environment [53, 128].

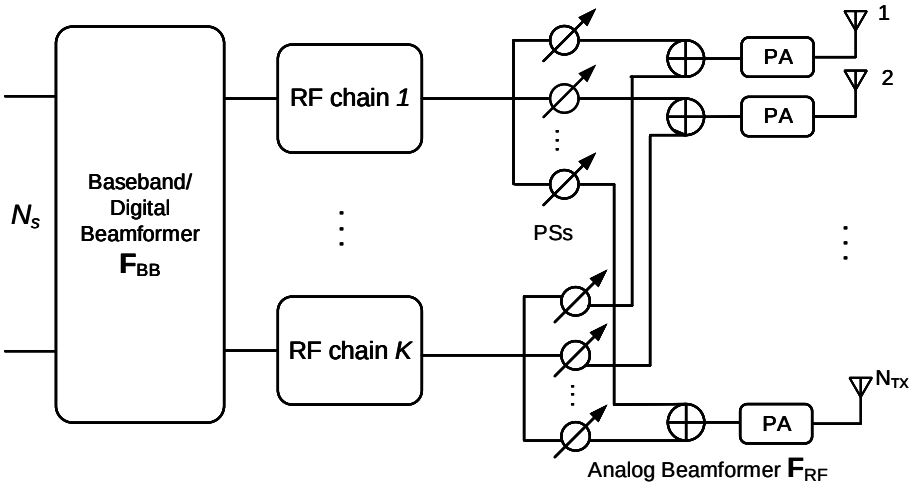

Figure 2.11: Hybrid beamforming architecture.

For a multi-user system with K users served a BS, the RF stage of the HBF architecture essentially involves a coordinated beamforming approach that maximizes the effective channel gain of all users as in (2.22) [125, 131, 137, 138].

$$\max_{\boldsymbol{F}_{\mathrm{RF}},\, \boldsymbol{W}_{\mathrm{RF},k},\forall k} \quad \sum_{k=1}^{K} \left\| \boldsymbol{W}_{\mathrm{RF},k}^{H} \boldsymbol{H}_k \boldsymbol{F}_{\mathrm{RF}} \right\|_F^2 \tag{2.22}$$

subject to

$$\boldsymbol{F}_{\mathrm{RF}}^{H} \boldsymbol{F}_{\mathrm{RF}} = \boldsymbol{I}_{N_{TX}}, \qquad \boldsymbol{W}_{\mathrm{RF},k}^{H} \boldsymbol{W}_{\mathrm{RF},k} = \boldsymbol{I}_{N_{RX,k}}, \qquad \forall k \in \{1, 2, \ldots, K\}.$$

Several approaches in developing $\boldsymbol{F}_{\mathrm{RF}}$ and $\boldsymbol{W}_{\mathrm{RF}}$ have been proposed over time, including the popular orthogonal matching pursuit (OMP) [125] and the generalized low rank approximation of matrices (GLRAM) [137], among others. For the digital baseband stage, popular methods in developing $\boldsymbol{F}_{\mathrm{BB}}$ and $\boldsymbol{W}_{\mathrm{BB}}$ include the maximum ratio transmission/combining (MRT/MRC) and the zero forcing (ZF) and block diagonalization (BD) techniques [138]. For this multi-user case, the baseband beamformers follow from the operations on the concatenated effective channel matrix that is given by (2.23)

$$\tilde{\mathbf{H}}_{\mathrm{eff},k} = [\mathbf{H}_{\mathrm{eff},1}^{T}, \ldots, \mathbf{H}_{\mathrm{eff},k}^{T}, \ldots, \mathbf{H}_{\mathrm{eff},K}^{T}]^{T}, \tag{2.23}$$

where $\mathbf{H}_{\mathrm{eff},k} = \boldsymbol{W}_{\mathrm{k}}^{H} \boldsymbol{H}_k \boldsymbol{F}_{\mathrm{RF}}$; $\mathbf{F}_{\mathrm{BB}}^{\mathrm{MRT}}$ and $\mathbf{F}_{\mathrm{BB}}^{\mathrm{ZF}}$ are respectively given by (2.24) and (2.25), respectively [138]. $\mathbf{W}_{\mathrm{BB}}$ can be similarly determined.

$$\mathbf{F}_{\mathrm{BB}}^{\mathrm{MRT}} = \tilde{\mathbf{H}}_{\mathrm{eff},k}^{H}, \tag{2.24}$$

$$\mathbf{F}_{\mathrm{BB}}^{\mathrm{ZF}} = \tilde{\mathbf{H}}_{\mathrm{eff},k}^{H} (\tilde{\mathbf{H}}_{\mathrm{eff},k} \tilde{\mathbf{H}}_{\mathrm{eff},k}^{H})^{-1}. \tag{2.25}$$

The received signal vector $\mathbf{r}_k$ observed by the k^{th} terminal after beamforming can then be expressed as (2.26) and becomes $\mathbf{y}_k$ after being combined with the RX combiners $\mathbf{W}_{\mathrm{RF,k}}$ and $\mathbf{W}_{\mathrm{BB,k}}$ as in (2.27), where $n = k$ is the desired signal and $n \neq k$ are interference terms for the k^{th} UE.

$$\mathbf{r}_k = \mathbf{H}_k \sum_{n=1}^{K} \mathbf{F}_n^{RF} \mathbf{F}_n^{BB} \mathbf{s}_n + \mathbf{n}_k, \tag{2.26}$$

$$\mathbf{y}_k = \mathbf{W}_{\mathrm{BB,k}}^H \mathbf{W}_{\mathrm{RF,k}}^H \mathbf{H}_k \sum_{n=1}^{K} \mathbf{F}_n^{RF} \mathbf{F}_n^{BB} \mathbf{s}_n + \mathbf{W}_{\mathrm{BB,k}}^H \mathbf{W}_{\mathrm{RF,k}}^H \mathbf{n}_k. \tag{2.27}$$

In [127], the authors established that hybrid beamformers outperform analog beamformers in terms of achievable rate (bps/Hz) and approaches the optimal performance of digital beamformers, particularly as the number of BS antennas increases significantly, which is of benefit for mmWave massive MIMO systems. Thus, hybrid beamforming is currently being extensively explored for mmWave massive MIMO as the digital beamforming counterpart is seen as impractical, due to its prohibitive cost and high energy consumption. However, this assumption is based on current hardware limitations. The development trends show that the cost and power consumption of baseband processing can be reduced in the future when digital beamforming will be the mainstream [57, 133].

Other HBF schemes such as the minimal Euclidean hybrid beamformer [139], mean-squared error (MSE)-based beamforming [140], HBF based on the 1-bit Analog to Digital Converters (ADCs) [141] and beamspace MIMO [142] have recently been proposed, with a view to reducing the energy consumption and hardware cost of beamformers. This is in order to make them realistic and practical for mmWave massive MIMO systems while keeping complexity at a modest level. A comparison of the three beamforming techniques is summarized in Table 2.9.

Table 2.9: Comparison of beamforming techniques.

Features	**Analog**	**Digital**	**Hybrid**
Number of streams	Single-stream	Multi-stream	Multi-stream
Number of users	Single-user	Multi-user	Multi-user
Signal control capability	Phase control only	Phase and amplitude control	Phase and amplitude control
Hardware requirement	Least; one RF chain only	Highest; number of RF chains equal number of transmit antennas	Intermediate; number of RF chains less than number of transmit antennas
Energy consumption	Least	Highest	Intermediate
Cost	Least	Highest	Intermediate
Performance	Least	Optimal	Near-optimal
Suitability for mmWave massive MIMO	Highly-limited; no amplitude control, no multi-user	Impractical; prohibitive cost and high energy consumption	Practical and realistic

2.5 Conclusions

The mmWave massive MIMO UDN technology represents an attempt to harness the promising benefits realizable with the huge available bandwidth in the mmWave bands, the SE improvement that can be obtained with the massive MIMO antenna array systems, and the high capacity gains achievable with UDN. In this chapter, we have presented an overview of the concepts and techniques being proposed for mmWave massive MIMO UDNs, principally with respect to 3D channel modeling and beamforming techniques. In doing so, we highlighted the requirements of the emerging network technology in contrast to legacy systems, and elaborated on key use cases and research challenges for 5G networks and beyond. In particular, this thesis identified the enhanced mobile broadband connectivity use case (5G UDN and C-I2X) as a vehicle for evaluating the key contributions on mmWave massive MIMO UDN. The 2020+ experience is expected to represent a balanced networking ecosystem where technical requirements synchronize well with socio-economic and environmental concerns. Therefore, a higher level of safety, improved health, lower cost and limited energy and CO_2 footprints are among principal drivers for the B5G era, alongside the much-anticipated boost in network capacity, user throughput and SE. Thus, EE is employed as a critical performance metric alongside SE that will be extensively employed throughout this thesis. As we march towards 2020, research on mmWave massive MIMO will continue to mature, and new trends will emerge. No doubt, mmWave massive MIMO UDN demonstates amazing potentials in realizing the 1000-fold capacity objective for 5G networks. The technology will usher in new paradigms for NGMNs and open up new frontiers for cellular services and applications. The background, challenges and open issues on mmWave massive MIMO leading to the compilation of this chapter were the results of the survey that were published in IEEE Communications Surveys and Tutorials[1].

[1]**S. A. Busari**, K. M. S. Huq, S. Mumtaz, L. Dai and J. Rodriguez, "Millimeter-Wave Massive MIMO Communication for Future Wireless Systems: A Survey", *IEEE Communications Surveys and Tutorials*, vol. 20, no. 2, pp. 836-869, May 2018.

Chapter 3

3D Channel Modeling for 5G UDN and C-I2X

This chapter focuses on 3D channel modeling for 5G UDNs and C-I2X networks, which is considered one of the main novelties in this thesis. The 3D channel models are pivotal for realistic characterization and evaluation of mmWave massive MIMO performance. The chapter principally covers three aspects: (i) evaluates the individual performance of 3D μWave and mmWave channels in order to provide insights for coexistence in NGMNs; (ii) assesses the joint performance of the 3D μWave and mmWave channels in the light of 5G UDNs; and (iii) investigates the performance of cellular infrastructure-to-vehicle (C-I2V) channels involving street-level lampost-mount APs and vehicles. This part compares the mmWave massive MIMO channel in this propagation environment with the DSRC and LTE-A channels. The challenges in these 5G scenarios are then highlighted and analyzed.

3.1 Background

The future networks (starting with 5G) are anticipated to be multi-tier HetNets. For the first phase of 5G, the cost-efficient and practical deployment option being exployed is the combination of 5G NR with the legacy LTE-A. In this architecture, the μWave LTE-A tier will provide coverage and signaling while the 5G mmWave tier provides the anticipated capacity boost [35]. There is a consensus in the academia and the telecommunications industry that adding new frequency bands to existing deployments is a future-proof and cost-efficient way to improve performance, meet the growing needs of mobile broadband subscribers and deliver new 5G-based services. More so, 5G at mid and high bands is well suited for deployment at existing site grids, especially when combined with low-band LTE [35]. In order to evaluate the performance of such a network architecture, accurate characterization of the wireless channel is fundamental. Consequently, in this chapter, we first characterize and compare the individual performance of two 3GPP 3D channel models: the LTE channel model for sub-6 GHz [84] and the mmWave channel for frequencies above 6 GHz [85] to provide the basis for coexistence in 5G UDNs. Then, in the light of 5G HetNets, we investigate the joint performance of the two channels using the UMa and UMi scenarios for LOS, NLOS and O2I propagation environments.

Similarly, applying mmWave spectrum at street-level sites is also a good option to provide high rate connectivity to users (cellular and/or vehicular). By placing antennas on lamposts,

outer walls and the likes, it is possible to avoid typical diffraction losses from rooftops and achieve shorter distances to users located in outdoor hotspots or in targeted buildings. This topology also offloads traffic from the regular cellular BSs thereby enhancing the capacity of the network. Along this line, there is a recent partnership of the automotive and telecommunications industries (i.e., the 5G Automotive Association) in the area of intelligent transport systems (ITSs) on the C-V2X paradigm. While the 3GPP has standardized C-V2X in Release 14, its extension to support the 5G NR is anticipated to be finalized in Release 16 for more advanced use cases [143]. While the prospect of 5G NR C-V2X is amazing, the mmWave channel exhibits challenging propagation properties markedly different from the sub-6 GHz channels where both DSRC and LTE-A operate [4, 59]. The differences become even more pronounced for mmWave vehicular channels due to the impact of high mobility [18, 130, 144]. In this chapter, using the enhanced 3D channel model for C-I2X adapted from the implementation in [42, 101, 102], we characterize the mmWave massive MIMO channel between the street-level lampost-mount APs and vehicular users.

3.2 μWave and mmWave Channels: Individual Performance

Many recent studies have attempted system performance assessment of candidate 5G mobile networks. However, most of the studies use simplified channel models (e.g., 2D, LOS-only, outdoor-only, etc.) [145, 146]. These simplified models do not provide accurate and realistic characterization of the radio environment. In this chapter, however, we provide a comprehensive analysis using the 3GPP 3D SCMs. We adopt the 3GPP TR 36.873 channel model for LTE [84] and the 3GPP TR 38.900 channel model for spectrum above 6 GHz [85] for the μWave and mmWave channels, respectively. These models capture diverse channel effects and cater for LOS, NLOS and O2I propagation as well as the building and indoor effects. As 3D channel models account for a high volume of parameters, variables and dependencies, analyses of the system performance require systematic investigation. Thus, in this section, we characterize the large-scale fading (PL and SF) statistics and use it to characterize the signal to interference ratio (SIR), SNR and SINR performance. Following this, we extend the investigation to important calibration metrics such as coupling loss (CL) and geometry factor (GF), and study the impacts of UE height and BS downtilt angle on the channel performance.

In the following subsections, we describe the considered network layout, outline the system parameters for the simulation of the network and present the propagation models employed. Except otherwise stated, we follow strictly the 3GPP-compliant baseline for evaluation in [84] and [85] for the μWave and mmWave bands, respectively. Using CL and GF (SIR, SNR and SINR) as metrics, we present the simulation results for the individual channel performance under four scenarios: UMa-μWave, UMi-μWave, UMa-mmWave and UMi-mmWave.

3.2.1 System Model

We show in Figure 3.1 (on next page) the considered system layout. It is a square grid with 57 BSs composed of 19 tri-sectored sites. The considered are is further divided inton $X \times Y$ smaller squares. Users are deployed in the mapped area with a UE per small square. The four scenarios considered are the UMa and UMi scenarios for both the μWave [84] and the mmWave bands [85]. The simulation parameters for the respective scenario is highlighted in Table 3.1 (shown on next page).

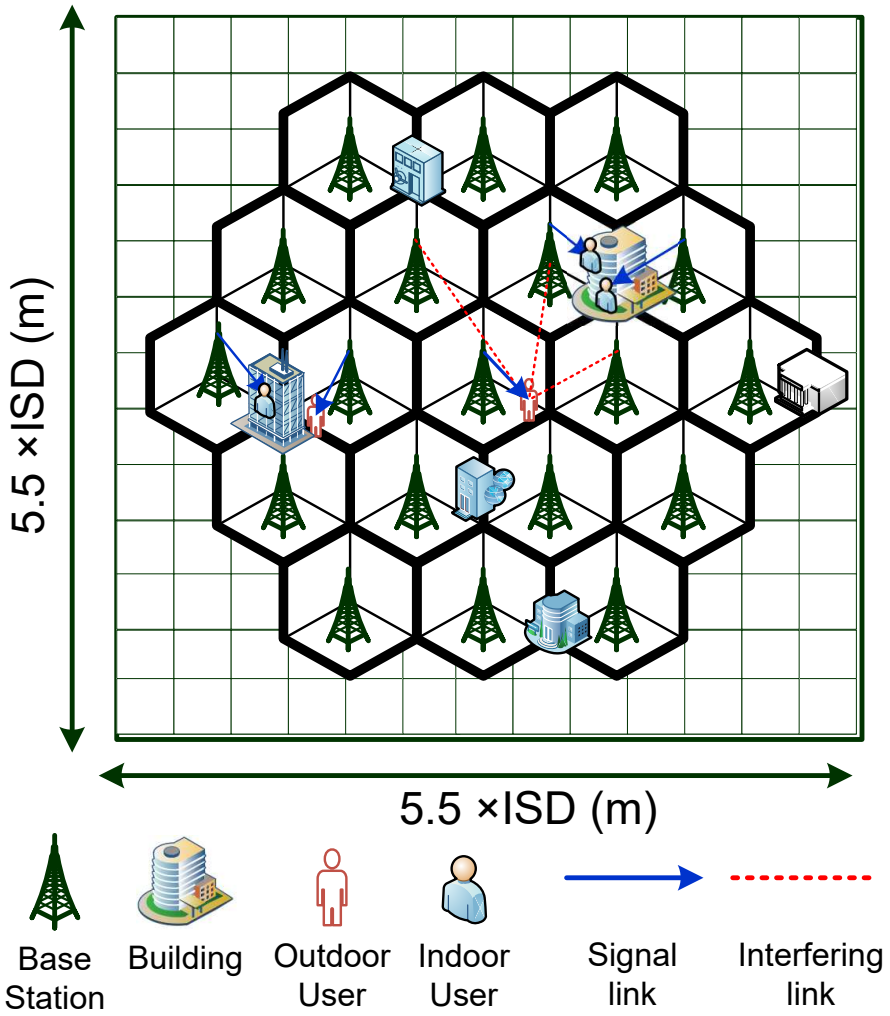

Figure 3.1: Cellular deployment layout for channel performance.

Table 3.1: Simulation parameters for channel performance.

Parameters	**UMa-μWave**	**UMi-μWave**	**UMa-mmWave**	**UMi-mmWave**
f_c (GHz)	2		28	
P_T (dBm)	46		35	
B (MHz)	10		125	
h_{TX} (m)	25	10	25	10
ISD (m)	500	200	500	200

The simulation parameters employed are based on Tables (6.1, 7.1-1, 8.2-1 and 8.2-2) in [84] for the μWave bands and Tables (7.2-1, 7.3-1, 7.8-1 and 7.8-2) in [85] for the mmWave bands. For all scenarios, the BSs have uniform planar arrays (UPAs) with 4×10 AEs while the UEs have uniform linear arrays (ULAs) with 2×1 AEs. All elements are spaced 0.5λ apart along the horizontal and vertical, as the case may be. All antenna ports are co-polarized.

Each element has a gain of 8 dBi with 102^o downtilt at the BS, and a gain of 0 dBi, 9 dB noise figure (NF) and -174 dBm/Hz thermal noise power density (N_o) for the omnidirectional UEs. The scenario-specific parameters are as earlier given in Table 3.1, where B is the bandwidth and h_{TX} is the TX height.

3.2.2 Map-based Simulation Framework

The simulation flow follows the framework described in this subsection. The inputs are the BSs' transmit powers (P_T^j) and the 2D coordinates of the BSs (x_j, y_j) and the UEs (x_k, y_k), $\forall j \in \{1, 2, \ldots, J\}$ and $\forall k \in \{1, 2, \ldots, K\}$. The output is the reference signal received power (RSRP) for all users in the mapped area. Using the parameters in Tables 3.1, the P_{LOS}, PL and SF are computed using Table 3.2 (on bottom of page) and Table 3.3 (on next page), based on Tables 7.2-1 [84] and 7.4.1-1 [85] for the μWave and mmWave bands, respectively. The transmit antenna gains (G_{TX}) are calculated based on Tables 7.1-1 [84] and 7.3-1 [85], for the μWave and mmWave, respectively. The SF is modeled as a distance-dependent log-normal distribution $\mathcal{N}(0, \sigma)$, with zero mean and standard deviation (σ) following the Claussen correlated SF map [147] implementation in [38]. Claussen in [147] proposed an efficient low-complexity method where each new fading value is generated based only on the correlation with a small number of selected neighboring values in the SF map. This leads to a significant reduction in computational complexity and memory requirements, in contrast to other classical methods.

Table 3.2: LOS probability (adapted from [84, 85]).

Scenario	**LOS probability** (distances and heights are in meters)
UMa-μWave	$P_{LOS} = \left(\min\left(\frac{18}{d_{2D}}, 1\right)\left(1 - \exp\left(\frac{-d_{2D}}{63}\right)\right) + \exp\left(\frac{-d_{2D}}{63}\right)\right)\left(1 + C\left(d_{2D,h_{RX}}\right)\right)$
UMi-μWave	$P_{LOS} = \left(\min\left(\frac{18}{d_{2D}}, 1\right)\left(1 - \exp\left(\frac{-d_{2D}}{36}\right)\right) + \exp\left(\frac{-d_{2D}}{36}\right)\right)$
UMa-mmWave	$P_{LOS} = \begin{cases} 1, & d_{2D} \leq 18 \\ \left(\frac{18}{d_{2D}} + \exp\left(\frac{-d_{2D}}{63}\right)\left(1 - \frac{18}{d_{2D}}\right)\right)\left(1 + C\left(d_{2D,h_{RX}}\right)\right), & 18 < d_{2D} \end{cases}$
UMi-mmWave	$P_{LOS} = \begin{cases} 1, & d_{2D} \leq 18 \\ \left(\frac{18}{d_{2D}} + \exp\left(\frac{-d_{2D}}{36}\right)\left(1 - \frac{18}{d_{2D}}\right)\right), & 18 < d_{2D} \end{cases}$
where: $C\left(d_{2D}, h_{RX}\right) = \begin{cases} 1, & d_{2D} \leq 18 \\ 1 + 1.25C'\left(h_{RX}\right)\left(\frac{d_{2D}}{100}\right)^3 \exp\left(\frac{-d_{2D}}{150}\right), & 18 < d_{2D} \end{cases}$ $C'\left(h_{RX}\right) = \begin{cases} 0, & h_{RX} \leq 13 \\ \left(\frac{h_{RX} - 13}{10}\right)^{1.5}, & 13 < h_{RX} \leq 23 \end{cases}$ and d_{2D} (is the outdoor separation distance, hereafter referred to as d_{2D-out}) [84], [85]	

Table 3.3: Path loss models (adapted from [84, 85]).

Scenario	**Path loss (dB)**	σ_{SF} (dB)
UMa-μWave	$PL_{LOS} = \begin{cases} 28 + 22\log_{10}(d_{3D}) + 20\log_{10}(f_c), & 10 < d_{2D} < d_{BP} \\ 28 + 40\log_{10}(d_{3D}) + 20\log_{10}(f_c) - 9\log_{10}((d_{BP})^2 + (25 - h_{RX})^2), & d_{BP} < d_{2D} < 5000 \end{cases}$	4
	$PL_{NLOS} = 69.51 + 39.09\log_{10}(d_{3D}) + 20\log_{10}(f_c) + 7.5\log_{10}(h_{RX}) - 0.6h_{RX} - 0.0825(h_{RX})^2$	6
	$PL_{O2I} = PL_{LOS/NLOS} + 20 + 0.5(d_{2D-in})$	7
UMi-μWave	$PL_{LOS} = \begin{cases} 28 + 22\log_{10}(d_{3D}) + 20\log_{10}(f_c), & 10 < d_{2D} < d_{BP} \\ 28 + 40\log_{10}(d_{3D}) + 20\log_{10}(f_c) - 9\log_{10}((d_{BP})^2 + (10 - h_{RX})^2), & d_{BP} < d_{2D} < 5000 \end{cases}$	3
	$PL_{NLOS} = 23.15 + 36.7\log_{10}(d_{3D}) + 26\log_{10}(f_c) - 0.3h_{UE}$	4
	$PL_{O2I} = PL_{LOS/NLOS} + 20 + 0.5(d_{2D-in})$	7
UMa-mmWave	$PL_{LOS} = \begin{cases} 32.4 + 20\log_{10}(d_{3D}) + 20\log_{10}(f_c), & d10 < d_{2D} < d_{BP} \\ 32.4 + 40\log_{10}(d_{3D}) + 20\log_{10}(f_c) - 10\log_{10}((d_{BP})^2 + (25 - h_{RX})^2), & d_{BP} < d_{2D} < 5000 \end{cases}$	4
	$PL_{NLOS} = 14.44 + 39.08\log_{10}(d_{3D}) + 20\log_{10}(f_c) - 0.6h_{RX}$	6
	$PL_{O2I} = PL_{LOS/NLOS} + PL_{wall} + 0.5(d_{2D-in})$	7
UMi-mmWave	$PL_{LOS} = \begin{cases} 32.4 + 21\log_{10}(d_{3D}) + 20\log_{10}(f_c), & 10 < d_{2D} < d_{BP} \\ 32.4 + 40\log_{10}(d_{3D}) + 20\log_{10}(f_c) - 9.5\log_{10}((d_{BP})^2 + (10 - h_{RX})^2), & d_{BP} < d_{2D} < 5000 \end{cases}$	4
	$PL_{NLOS} = 22.85 + 35.3\log_{10}(d_{3D}) + 21.3\log_{10}(f_c) - 0.3h_{UE}$	7.82
	$PL_{O2I} = PL_{LOS/NLOS} + PL_{wall} + 0.5(d_{2D-in})$	7
NOTES:	f_c is in GHz; d_{2D}, d_{3D} and h_{RX} are in meters; $d_{BP} = 320((h_{RX} - 1)f_c)$ for UMa and $d_{BP} = 120((h_{RX} - 1)f_c)$ for UMi. d_{BP} is the break-point distance [84], [85] and PL_{wall} is the wall/penetration loss based on Tables 7.4.3-(1 & 2) in [85].	

For each scenario, a UE may be in LOS or NLOS, in either O2O or O2I environment to each BS. Consequently, the various UE maps (indoor distance (d_{2D-in})), outdoor distance (d_{2D-out}), UE height (h_{RX}), LOS probability (P_{LOS}), etc.) are calculated as follows. Note that j and k subscripts represent BS and UE, respectively. Also, X and Y represented the length and breadth of the mapped area, respectively (scaled according to a 10:1 map resolution for complexity reduction), where `binornd`, `randi` and `rand` denote the binomial random number, uniformly distributed pseudorandom integer and uniformly distributed random number operators, respectively.

(i) ***Generate UE indoor-outdoor map***
This is generated based on the indoor (r_{in}) - outdoor (r_{out}) ratio. According to the 3GPP baseline in [84] and [85], $r_{in} = 0.8$ and $r_{out} = 0.2$, representing 80% indoor and 20% outdoor users.

$$\chi = \texttt{binornd}(1, r_{in}, X, Y), \tag{3.1}$$

$$\chi_k = \begin{cases} 0, & k \rightarrow \ outdoor \\ 1, & k \rightarrow \ indoor. \end{cases} \tag{3.2}$$

(ii) ***Generate building floor map***
The number of floors the indoor users are distributed into is computed as follows.

$$n_{fl}^{map} = \texttt{randi}([n_{fl}^{min}, n_{fl}^{max}]), \tag{3.3}$$

$$n_{fl} = \texttt{randi}(n_{fl}^{map}, X, Y), \tag{3.4}$$

where $n_{fl}^{min} = 4$ and $n_{fl}^{min} = 8$ [84, 85]. The actual maximum number of floors used for the height distribution of the UEs is n_{fl}^{map}, where the floor number of each user k in the X-Y mapped area falls between 1 and n_{fl}^{k}, $\forall k \in \{1, 2, \ldots, K\}$.

(iii) ***Generate indoor distance map***
The indoor distance of the users are computed as:

$$d_{2D-in} = 25 \times \texttt{rand}(X, Y), \tag{3.5}$$

Using (3.1)-(3.5) and Table 3.1 as inputs, the computation of RSRP for the users follows the framework in Algorithm 1. Users are attached to the respective BSs based on the maximum RSRP criterion. The values of the variable parameters depend on the state of the simulation with respect to the scenario and user location in each run and/or transmission time interval (TTI). For each scenario, 1000 simulation runs are performed and averaged. The empirical cumulative distribution function (ECDF) is used to analyze the results.

Algorithm 1: Map-based simulation framework.

Inputs :

P_T^j, h_j $\quad \forall j \in \{1, 2, \cdots, J\}$ $\quad \leftarrow$ Table 3.1

χ, n_{fl} and d_{2D-in} $\quad \leftarrow$ (3.1)-(3.5)

Output:

$RSRP_k$, $\quad \forall k \in \{1, 2, \cdots, K\}$

for $k \rightarrow 1$ **to** K **do**

I- Compute UE height map

$$h_k = 1.5 + (\chi_k \times [3(n_{fl}^k - 1)]) \tag{3.6}$$

for $j \rightarrow 1$ **to** J **do**

II- Compute 2D & 3D distances to all BSs

$$d_{2D}^{k,j} = \sqrt{(x_j - x_k)^2 + (y_j - y_k)^2} \tag{3.7}$$

$$d_{3D}^{k,j} = \sqrt{(d_{2D}^{k,j})^2 + (h_j - h_k)^2} \tag{3.8}$$

$$d_{2D-out}^{k,j} = d_{2D}^{k,j} - (\chi_k \times d_{2D-in}^k) \tag{3.9}$$

III- Compute P_{LOS} using Table 3.2

$$\xi_{k,j} = \texttt{binornd}(1, P_{LOS}^{k,j}(d_{2D-out}^{k,j})) \tag{3.10}$$

$$\xi_{k,j} = \begin{cases} 0, & k,j \rightarrow \ NLOS \\ 1, & k,j \rightarrow \ LOS \end{cases} \tag{3.11}$$

IV- Compute $PL_{k,j}$ using Table 3.3

$$\{\chi_k, \xi_{k,j}\} = \begin{cases} \{0,0\} & \rightarrow PL_{NLOS} \\ \{0,1\} & \rightarrow PL_{LOS} \\ \{1,0\} & \rightarrow PL_{O2I-NLOS} \\ \{1,1\} & \rightarrow PL_{O2I-LOS} \end{cases} \tag{3.12}$$

V- Compute $SF_{k,j}$ using Table 3.3

VI- Compute $G_{TX}^{k,j}$, $G_{RX}^{k,j}$ using Table 3.4 (shown on next page) [84, 85];

VII- Compute $RSRP_{k,j}$

$$RSRP_{k,j} = P_T^{k,j} + G_{TX}^{k,j} + G_{RX}^{k,j} - PL_{k,j} - SF_{k,j} \tag{3.13}$$

$$RSRP_k = max(RSRP_{k,(1:J)}) \tag{3.14}$$

`Assign` user $k \rightarrow j^{th}$ BS with $maxRSRP_k$

Table 3.4: Antenna radiation pattern (adapted from [84, 85]).

Parameter	**Values**
Antenna element horizontal radiation pattern (dB)	$A_{E,H} = -\min\left\{12\left(\frac{\phi}{65^o}, 30\ dB\right)\right\}$
Antenna element vertical radiation pattern (dB)	$A_{E,V} = -\min\left\{12\left(\frac{\theta - 90^o}{65^o}, 30\ dB\right)\right\}$
Combining method for 3D antenna element pattern (dB)	$G_{(\phi,\theta)} = -\min\left\{-\left[A_{E,H}(\phi) + A_{E,V}(\theta)\right], 30\ dB\right\}$
Maximum directional gain of an antenna element ($G_{AE,max}$)	8 dBi

3.2.3 Simulation Results

In this section, we present the simulation results for the four scenarios considered using the CL and GF (using the SINR, SNR and SIR) as performance metrics.

(a) Coupling Loss

The difference between the received signal and the transmitted signal along the LOS direction is the CL [31]. For each user and its attached BS, the CL (dB) and the RSRP (dB) are defined as (3.15) and (3.16), respectively.

$$CL_k = RSRP_k - P_T^{k,j}, \tag{3.15}$$

$$RSRP_{k,j} = P_T^{k,j} + G_{TX}^{k,j} + G_{RX}^{k,j} - PL_{k,j} - SF_{k,j}. \tag{3.16}$$

CL depends only on the slow fading (i.e., large-scale) parameters. It captures all attenuation sources between a UE and its attached BS. As can be seen from substituting (3.16) into (3.15), CL is independent of P_T [148]. It is used in the Phase 1 calibration by standardization bodies such as 3GPP to bring companies and organizations involved in channel measurements and modeling to a common ground with respect to reported channel results [33]. In Figure 3.2, we show results for CL (i.e., the LOS curves) for the four scenarios.

In Figure 3.2, the minimum CL is ∼45 dB for both μWave-UMa and μWave-UMi, and ∼35 dB and ∼75 dB for mmWave-UMa and mmWave-UMi, respectively. The results in Figures 3.2(a) and 3.2(b) are consistent with [84], and Figure 3.2(d) is consistent with the corresponding case in [148]. Further in Figures 3.2(a)-(d), we provide loss curves for the NLOS UEs and the overall loss curves involving all UEs (both LOS and NLOS UEs combined, denoted on Figures 3.2(a)-(d) as LOS+NLOS). A penalty of around 20-35 dB is observed between the LOS and NLOS cases for the μWave band and around 20-50 dB for the mmWave case.

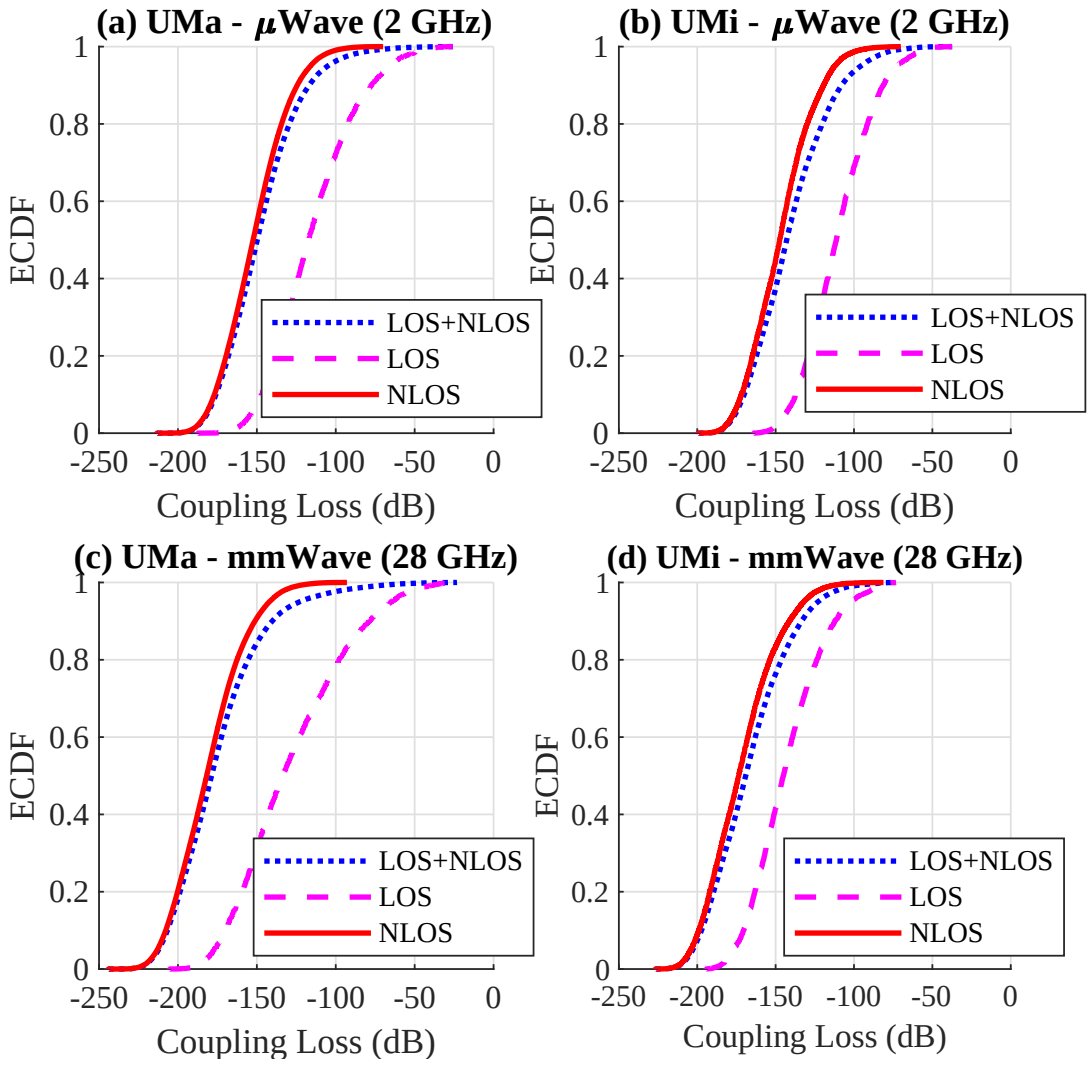

Figure 3.2: ECDF of coupling loss.

(b) Geometry Factor

The GF captures the statistics of the SINR [148] or SIR [31] or either of the two [85]. These are necessary in order to compute the SE, UE throughput and cell capacity. The SINR, SIR and SNR for a given UE are defined as (3.17), (3.18) and (3.19), respectively. GF measures the performance of users with respect to the received signal strength relative to the interference from other BSs (as SINR (with noise) or SIR (without noise)). It is also used in Phase 1 calibration to assess performance as a measure of UEs' SE and throughput [31]. The SNR performance, on the other hand, characterizes the maximum achievable capacity in interference-free scenarios [4].

$$SINR_k = RSRP_{k,j} - (\sum_{j=1,\, k \not\to j}^{J} RSRP_{k,j} + N_k), \tag{3.17}$$

$$SIR_k = RSRP_{k,j} - (\sum_{j=1,\, k \not\to j}^{J} RSRP_{k,j}), \tag{3.18}$$

$$SNR_k = RSRP_{k,j} - N_k, \tag{3.19}$$

$$N_k = N_o + 10 \log_{10} B_k + NF. \tag{3.20}$$

The SNR/SIR/SINR performance for the four scenarios are shown in Figure 3.3. In all cases, the SINR curves expectedly characterize the worst-case performance as they incorporate both the noise and interference terms. The SIR curves in Figures 3.3(a) and 3.3(b) overlap the SINR curves, for the μWave UMa and μWave UMi scenarios, respectively. This outcome shows that μWave network is interference-limited. As for the mmWave scenarios, it is the SNR curves that overlap the SINR curves as shown in Figures 3.3(c) and 3.3(d), for mmWave UMa and mmWave UMi cases, respectively. It reveals that the mmWave network is noise-limited for the considered scenario. However, for ultra-dense mmWave network with much shorter ISDs, the mmWave network could be interference-limited also due to transition from NLOS to LOS interference [149].

For all scenarios, the GF follows a similar trend consistent with the results in [31] and [84] for the μWave scenarios, and [148] for the mmWave bands. In comparing the SNR/SIR/SINR performance for the four scenarios, we use the 0 dB point which translates to an SE of 1 bps/Hz. The point where the ECDF curve first crosses the 0 dB point gives the percentage of users that will achieve a SE of 1 bps/Hz or less. For SNR, {4.5, 1.3, 68.9, 72.5}% of users achieve up to 0 dB (or SE of 1 bps/Hz) for the UMa-μWave, UMi-μWave, UMa-mmWave and UMi-mmWave scenarios, respectively. Therefore, while more than 95% of μWave users achieve SE greater than 1 bps/Hz in the μWave networks, only ∼30% of mmWave users will achieve the same feat. As for SIR, {7.1, 8.8, 6.4, 7.6}% of users achieve up to 0 dB while in terms of SINR, {12.0, 8.9, 68.4, 74.6}% of users achieve up to 0 dB, for the same order in scenario. Again, mmWave systems perform poorly with only ∼30% of users achieving the 1 bps/Hz SINR, compared to ∼90% in the μWave set-ups. This SINR bottleneck is of great concern for mmWave networks expected to provide the much-anticipated multi-Gbps throughputs in 5G/B5G networks. The results shown here are with 125 MHz mmWave bandwidth based on [145], as 100 MHz is projected as the practical size for a component carrier in mmWave systems [3]. SINR degradation will therefore be of more significant consequences if much larger mmWave bandwidths (up to 1-2 GHz) are used, due to the expected increase in noise with increasing bandwidth as can be seen from (3.20).

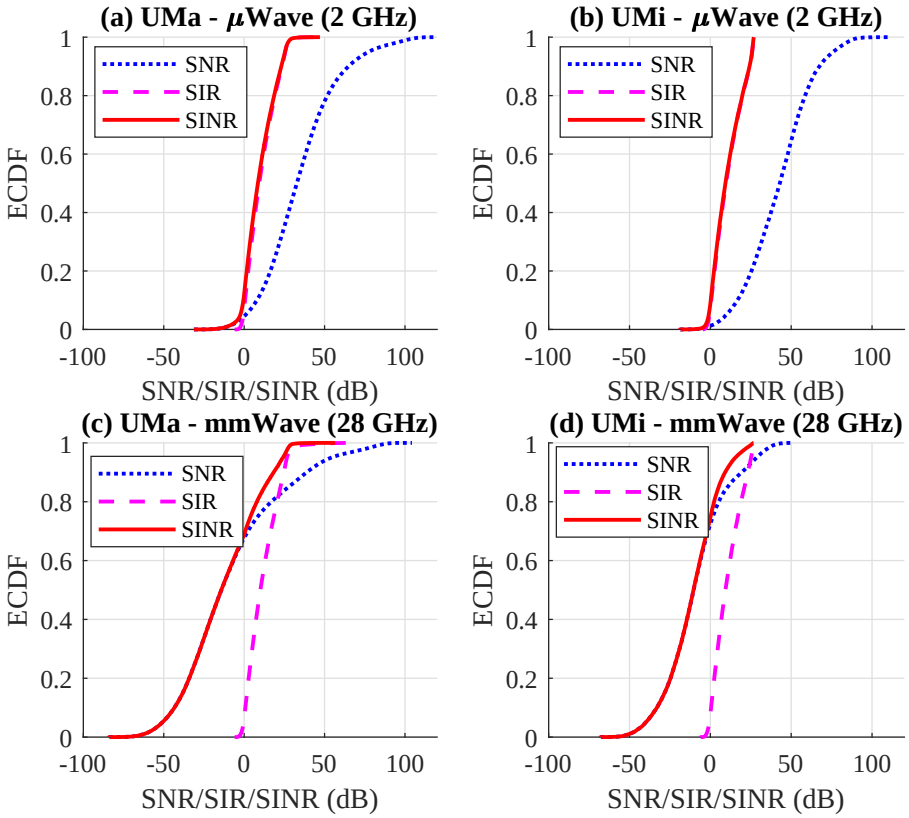

Figure 3.3: ECDF of geometry factor.

The individual performance of the μWave and mmWave channels for UMa and UMi scenarios have been shown in Figures 3.2 and 3.3. However, 5G HetNets is anticipated to feature UMa-μWave (LTE) and UMi-mmWave (5G) channels as the feasible and cost-effective option for increasing cell capacities in early 5G deployments [35]. The UMa-μWave is expected to provide coverage. Low data rates from such cells are acceptable and the research on them is more established. On the other hand, the UMi-mmWave tier is foreseen to provide the much-anticipated capacity to meet the explosive data rate demands projected for the 5G/B5G era. The results from Figure 3.3(d), however, show low performance. In the following subsections, we investigate further the factors responsible for low SINR in 3D UMi mmWave channels.

(c) Impact of UE height and BS downtilt

In Figure 3.4, we show the effect of wall/penetration losses and indoor losses on the SINR performance. The two extremes are the cases when all UEs are indoors and when all UEs are outdoors. For the other cases, 20% of UEs are outdoors while the remaining 80% indoor users are randomly distributed according to the maximum number of floors. For example, the curve named "3 floors" means that the 80% indoor users are randomly distributed in floors 1-3, the curve named "7 floors" means that the 80% indoor users are randomly distributed in floors 1-7, and so on. A significant 20-30 dB gap exists between when all the UEs are outdoors and when they are all indoors. Further, in the 3GPP's case with 20% of UEs outdoors and 80% indoors, the distribution of the indoor UEs across floors (i.e., the effect of UE heights) does

not amount to significant impact on average performance. The differences are paled by the high number of UEs at system-level. Further, we show in Figure 3.5 the results of simulations for the two extreme cases only (i.e., all UEs indoors and all UEs outdoors) with different BS downtilt angles.

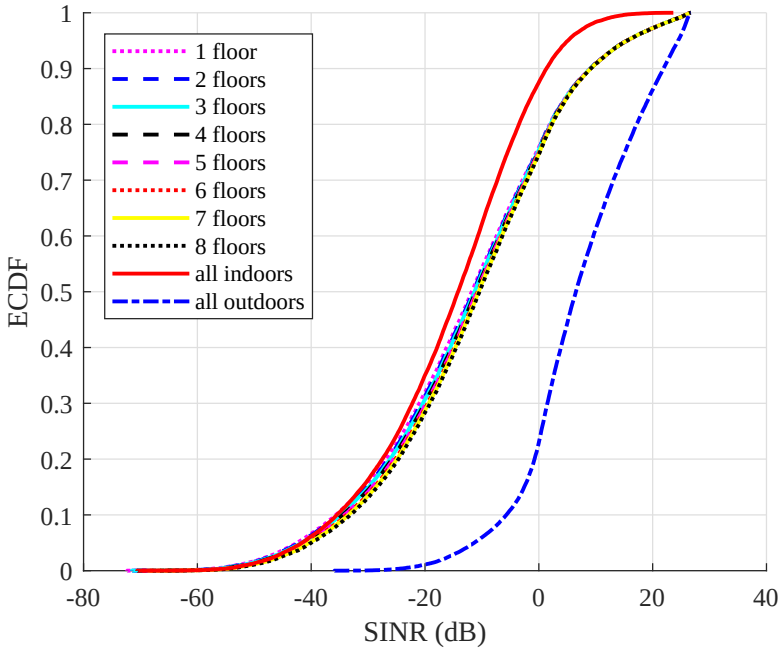

Figure 3.4: Impact of UE height (floor level) on SINR.

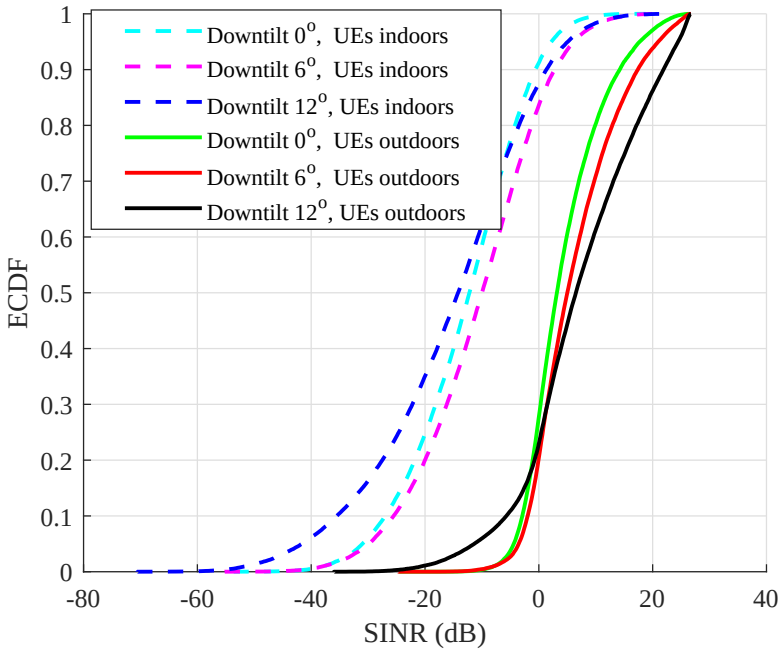

Figure 3.5: Impact of BS downtilt angle on SINR.

The results show that the BS downtilt angle does not significantly impact average performance. The observable gap between when all UEs are outdoors and when all UEs are indoors is attributable, again, to the wall and indoor losses.

3.3 Joint Channel Performance for 5G UDN

In this section, we present results for the system-level performance for the joint μWave-mmWave UDNs featuring both outdoor and indoor users. For the evaluation, we employ the 3GPP 3D channel model [84] and [85] for the μWave and mmWave bands, respectively. First, we describe the considered network layout, outline the system parameters for the simulation of the network and then present the system-level performance of the coexisting μWave-mmWave UDN, in terms of SE, UE throughput and cell capacity. The challenges and solutions for the 5G eMBB setups are also highlighted.

3.3.1 Deployment Layout

As shown in Figure 3.6, the considered two-tier UDN consists of the μWave massive MIMO-based MCs and the mmWave massive MIMO-based SCs densely deployed in each MC. Buildings with four to eight floors are randomly situated within the coverage area. Also, the UEs are randomly and uniformly distributed in the cells with a probability following the indoor-to-outdoor ratio. Outdoor UEs are at a height of 1.5 m. Each indoor UE is at a random height between 1.5 and 22.5 m, evaluated using $h_{UE} = 1.5 + 3(n_{fl} - 1)$ where n_{fl} is the floor number of the user [84, 85].

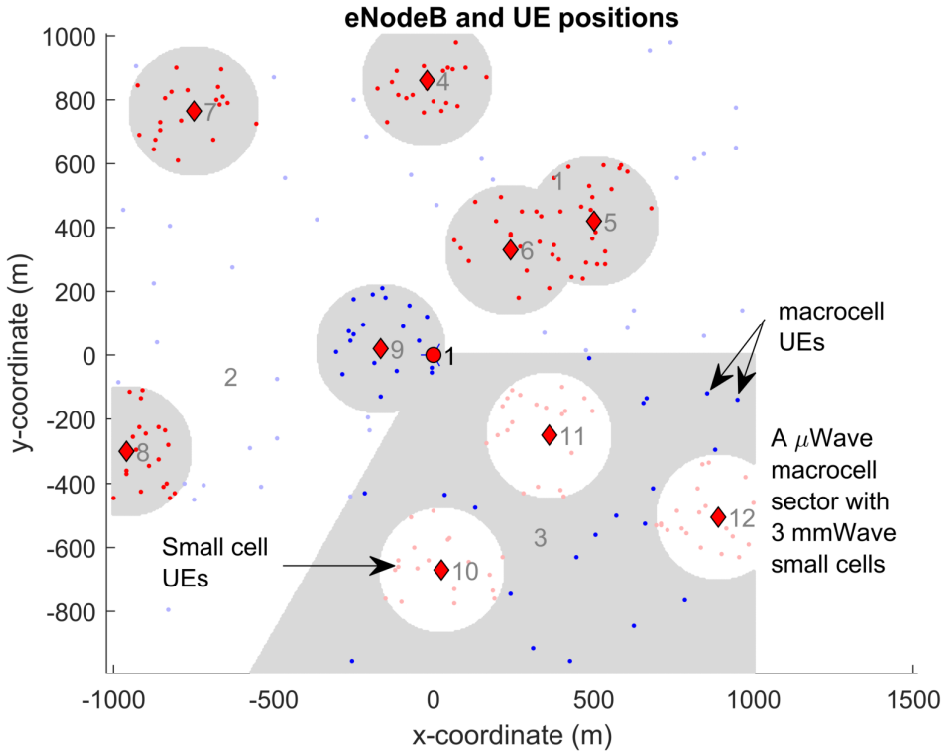

Figure 3.6: 5G UDN deployment layout.

The simulation parameters are presented in Table 3.5. The simulations consider a multi-user DL scenario and employ the MIMO-orthogonal frequency division multiplexing (OFDM) PHY numerology for LTE [38] and mmWave [145] cells. For the channel model, the MC tier follows the 3GPP UMa scenario of TR 36.873 [84] while the SC tier follows the 3GPP UMi scenario of TR 38.900 [85]. For the most part, the simulation parameters are in line with the 3GPP evaluation guidelines in [84] and [85] for the μWave and mmWave frequencies, respectively.

Further to the simulation parameters in Table 3.5, the simulations employ the closed loop spatial multiplexing (CLSM) transmit mode and frequency division duplexing (FDD). Also, homogeneous power allocation (i.e., equal power per resource block (RB)) was employed. For resource allocation, the proportional fair (PF) scheduler is adopted as it strikes a balance between maximizing system throughput and maintaining fairness among users. For a time slot t, the PF algorithm schedules (i.e., allocates RB(s)) to user k^* with the largest $\frac{R_k(t)}{T_k(t)}$ among all active users in the system, where $R_k(t)$ is the user requested rate and $T_k(t)$ is the average user throughput updated at specified time window [38].

Table 3.5: Simulation parameters for system performance.

Network elements	**Parameters**	**Macrocell (MC)**	**Small cell (SC)**
BS	Number of cells	3	9 (3 SCs/MC sector)
	Sector layout	Tri-sector	Radial
	Inter-site Distance [ISD] (m)	500	200
	Height [h_{TX}] (m)	25	10
	Planar array elements (vertical x horizontal)	10×4	10×4
	Carrier frequency [f_c] (GHz)	2	28
	Bandwidth (MHz)	20	{125, 250, 500, 1000}
	Transmit Power [P_T] (dBm)	49	35
	Minimum Coupling Loss [MCL] (dB)	70	45
UE	Number of UEs per MC sector and SC	20	20
	Outdoor height [h_{RX}] (m)	1.5	1.5
	Indoor height [h_{RX}] (m)	{1.5-22.5}	{1.5-22.5}
	Linear array elements (vertical x horizontal)	1×4	1×4
	UEs' speed (kmph)	3	3
	Noise Figure [NF] (dB)	9	9
	Noise power spectral density[N_o] (dBm/Hz)	-174	-174
3D Channel	Pathloss, Shadow fading and fast fading	3GPP TR 36.873 [84]	3GPP TR 38.900 [85]

Cell capacity is employed as the main performance metric for the network. The capacity (C) of each cell is evaluated as $C = B \cdot \log_2(1 + SINR)$ where SINR is evaluated using (3.21).

$$SINR\,(dB) = (P_T + G_{TX} + G_{RX} - PL - SF) - \left[\left(\sum_{n=1}^{N_{int}} I_n\right) + (N_o + 10\log_{10} B + NF)\right], \tag{3.21}$$

where I_n is the interference from non-target links operating on same frequency band. The PL includes the penetration/wall and indoor losses while the TX and RX antenna element gains

are 8 dBi and 0 dBi, respectively. The SE, expressed as C/B (bps/Hz), suggests that the abundant bandwidth results in significant capacity gains only when sufficient SINR is already guaranteed.

Table 3.6 compares and contrasts the propagation characteristics of the MC with the SC tier, following [84] and [85], respectively. The comparison is done using (3.21). The presented values are obtained by plugging the respective ISD values in the 3GPP models [84] and [85], for the MC and SC, respectively. However, the actual values for each user will vary depending on the user location. Overall, as illustrated in Table 3.6, the SINR in the mmWave SC appears smaller than that in the μWave MC tier (when compared at the same ISD) due to the higher losses and noise level at mmWave. If all other parameters are kept constant, the SINR (and by extension the SE) continues to decrease with increasing amount of mmWave bandwidth employed. However, the capacity continues to grow but not at the same rate as the increasing bandwidth.

Table 3.6: Comparison of μWave MC and mmWave SC.

Properties		**Macrocell (ISD = 500 m, fc = 2 GHz) [84]**	**Small cell (ISD = 200 m, fc = 28 GHz) [85]**
Signal	P_T	49 dBm	35 dBm
	PL	$LOS_{max} = 93.4$ dB	$LOS_{max} = 103.3$ dB
		$NLOS_{max} = 136.8$ dB	$NLOS_{max} = 123.8$ dB
		$O2I_{max} = 169.3$ dB (including penetration and indoor loss)	$O2I_{max} = 154.2$ dB (including indoor and penetration losses using low-loss model (i.e., glass and concrete walls)).
	SF	Zero mean log-normal distribution with std of 4, 6 and 7 for LOS, NLOS and O2I, respectively	Zero mean log-normal distribution with std of 3.1, 7.8 and 9 for LOS, NLOS and O2I, respectively
Interference	$\sum_{n=1}^{N_{int}} I_n$	Less number of interferers but higher interference due to directed interference and longer range	More interferers due to higher small cell density but with less interference due to strong attenuation resulting from higher path losses.
Noise	N_o	-174 dBm/Hz	-174 dBm/Hz
	NF	9 dB	9 dB
	$10\log_{10} B$	73 dB at $B = 20$ MHz. Noise here is lower than in mmWave SCs with larger bandwidths.	$B = \{125, 250, 500, 1000\}$ MHz. Noise increases with increasing bandwidth.

3.3.2 Simulation Results and Analyses

We present the simulation results and analyze the performance of the network. The results are from simulations using the parameters in Table 3.5. It is instructive to note that all results are given per MC sector.

(a) Average Cell Capacity

The average MC capacity (AC_{MC}), average SC capacity (AC_{SC}) and average cell capacity (AC_{cell}) when all the UEs are outdoor and when 80% of the UEs are indoor (according to the 3GPP in [84] and [85]) are shown in Figures 3.7 and 3.8, respectively. In both cases,

$AC_{cell} = AC_{MC} + (3 \times AC_{SC})$. This is the direct result of deploying three SCs within each MC sector. In Figure 3.7, the AC_{MC} from the 20 MHz LTE bandwidth is ∼40 Mbps. The AC_{SC}, on the other hand, increased from roughly 120 Mbps to 500 Mbps by moving from 125 MHz to 1 GHz mmWave bandwidth, respectively. Correspondingly, the AC_{cell} increased from 400 Mbps to 1.53 Gbps. It can be observed that the AC_{cell} increased dramatically with UDN (40× for the 1 GHz bandwidth case) compared to the 40 Mbps realizable if it were a MC-only set-up. However, the AC_{SC} does not increase linearly with increasing bandwidth. For example, doubling the SC bandwidth (e.g., from 500 MHz to 1 GHz) only brought about 44.6% increase in AC_{SC} (i.e., 343.3 to 496.4 Mbps).

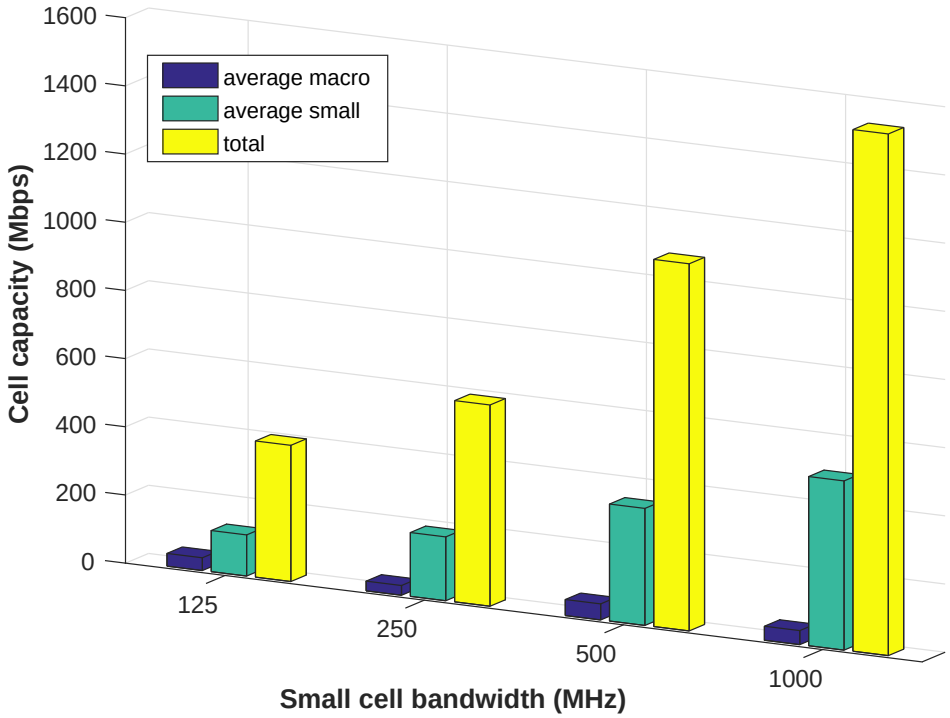

Figure 3.7: Impact of bandwidth on cell capacity with all users outdoors.

The results for the 3GPP case (with 80% of the UEs indoors) are shown in Figure 3.8. Compared to the outdoor scenario, the performance in this case is highly degraded. Using the 1 GHz case for example, the AC_{MC}, AC_{SC} and AC_{cell} are 3.73, 41.59 and 128.51 Mbps, respectively. Despite the 1 GHz bandwidth, the performance is even much lower than the 125 MHz case for the outdoor scenario. As highlighted earlier, the aggregate PL in O2I environment is higher than in outdoor cases. This is due to the additional wall and indoor losses experienced by indoor users. These losses further reduce the received signal strength, thereby degrading the SINR and the cell capacity. Our simulations show that the network performance decreases as the percentage of indoor users increases from outdoor-only (0%) to indoor-only (100%).

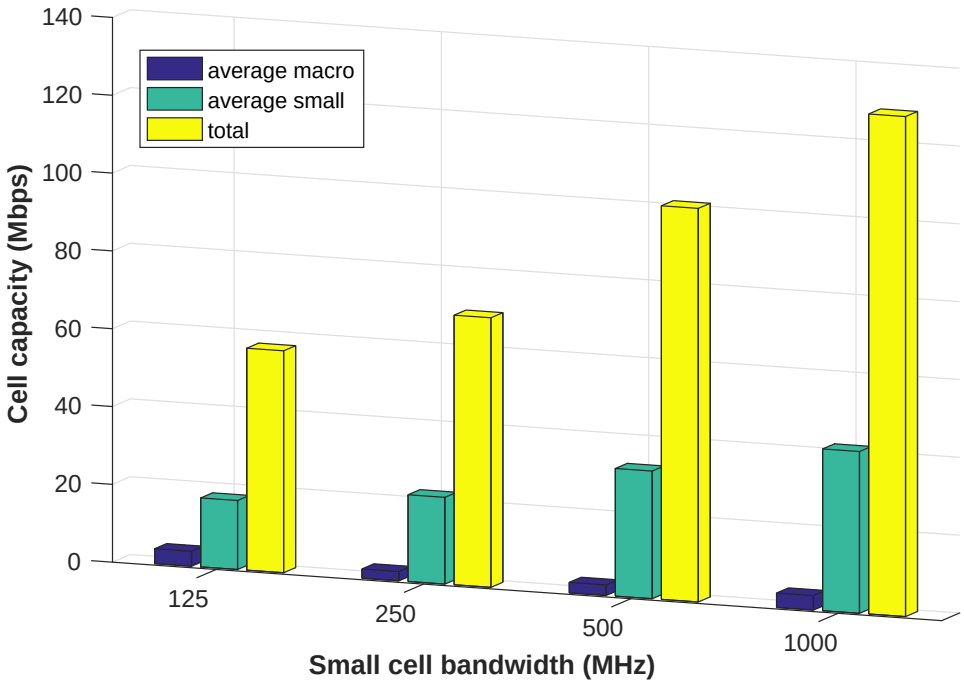

Figure 3.8: Impact of bandwidth on cell capacity with 80% of the UEs indoors.

(b) Average UE Throughput

The average UE throughputs for the SCs in indoor, 3GPP and outdoor environments are presented in Figure 3.9. In each case, the UE throughput increased with increasing mmWave bandwidth. Again, in all cases, the throughput increase is not proportional to the increase in bandwidth. For the same reasons explained earlier, there is significant degradation in performance for the fully indoor and the 3GPP scenarios, as compared to the fully outdoor environment. In Figure 3.9, the three scenarios correspond to the 100, 80 and 0% of indoor UEs, respectively. For the 1 GHz mmWave bandwidth, for example, the average UE throughput for the indoor, 3GPP and outdoor scenarios are 3.96, 10.4 and 124.09 Mbps, respectively.

(c) Spectral Efficiency

For the SC tier, the average SE for the three environments considered are shown in Figure 3.10. In each environment, the SE decreased with increasing bandwidth, moving from {0.25, 0.46, 1.48} bps/Hz at 125 MHz to {0.07, 0.24, 1.03} bps/Hz at 1 GHz for the indoor, 3GPP and outdoor environment, respectively. With all parameters remaining constant in (3.21), increasing the bandwidth expectedly leads to a reduction in SINR and SE. The emphasis is on the SCs due to the investigation of the impact of increasing bandwidth on network performance. For the MCs, the 20 MHz LTE bandwidth was employed for all scenarios, and so not considered in the analysis.

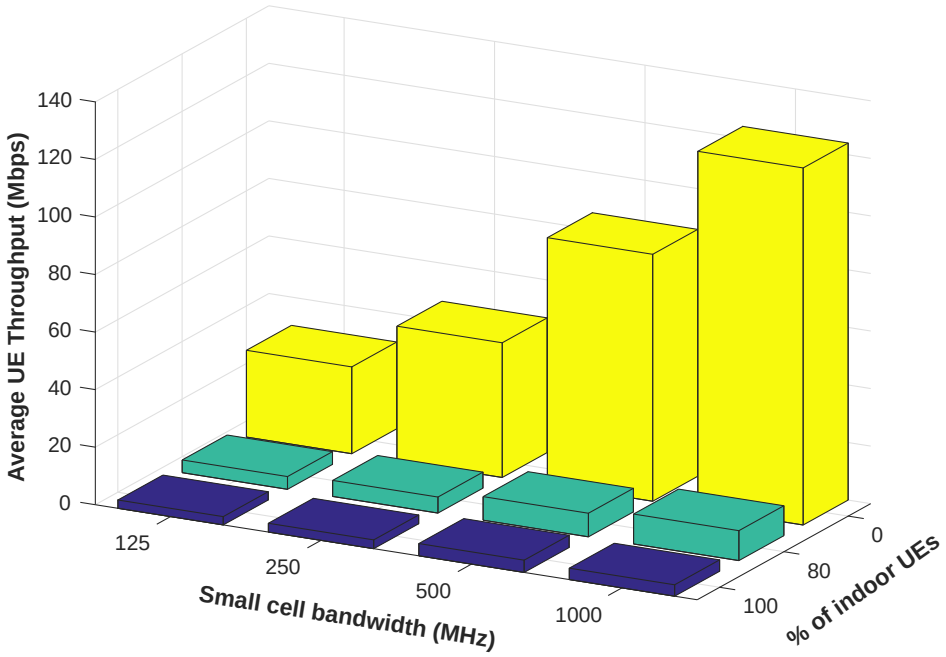

Figure 3.9: Impact of bandwidth on SC user throughput.

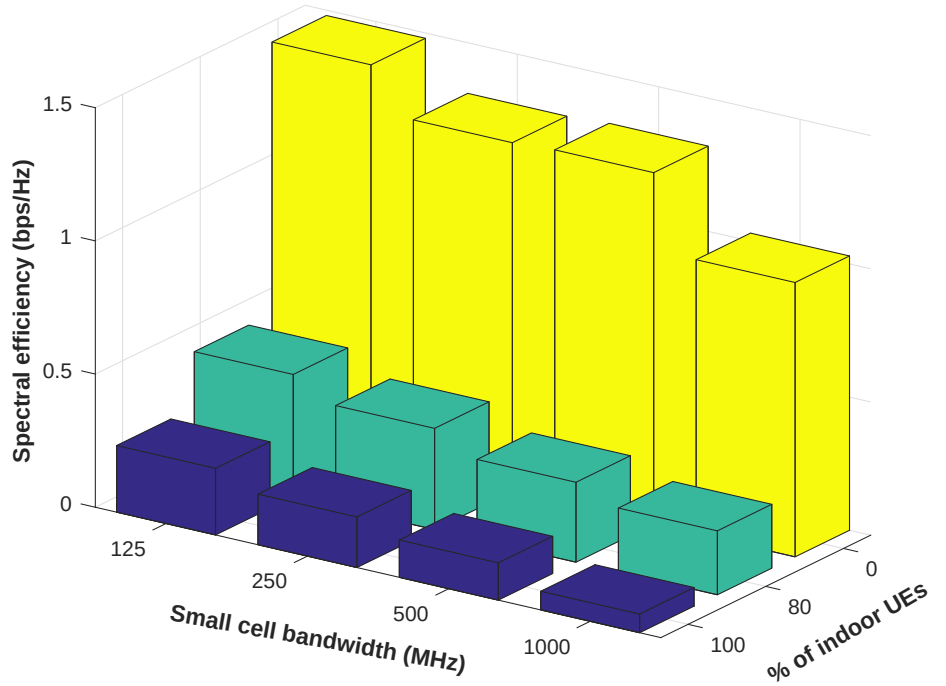

Figure 3.10: Impact of bandwidth on SC spectral efficiency.

3.3.3 Challenges and Proposed Solutions

The SINR is degraded in mmWave systems due to the higher PL, increased noise, and other additional losses, such as wall/penetration and indoor losses (for indoor users) and the absorption losses (for the 57-63 GHz bands) [59, 85, 150]. In scenarios with very low received signals, it is not unusual for the SCs to have poorer performance than the MCs (or even complete outage), despite the much larger bandwidth in the SCs. This situation, in addition to the high susceptibility to blockage, makes higher frequency (i.e., mmWave and THz) links highly opportunistic and potentially unreliable, despite the amazing spectral prospects [4]. Two possible options to overcome the SINR bottleneck in mmWave systems are signal power enhancement and interference mitigation.

(a) Signal Power Enhancement

Increasing the transmit powers of the mmWave SCs can enhance the received signal strength. In Figure 3.11, we show that the capacity of mmWave SCs increases with increasing transmit power (in steps from 30 to 49 dBm). The capacity increase with the increasing transmit power in outdoor scenario is markedly significant. On the contrary, the performance with both the 80% and 100% indoor UEs are poor. For the 49 dBm case, for example, the AC_{SC} is only 200 Mbps, compared to almost 1.4 Gbps in the outdoor scenario.

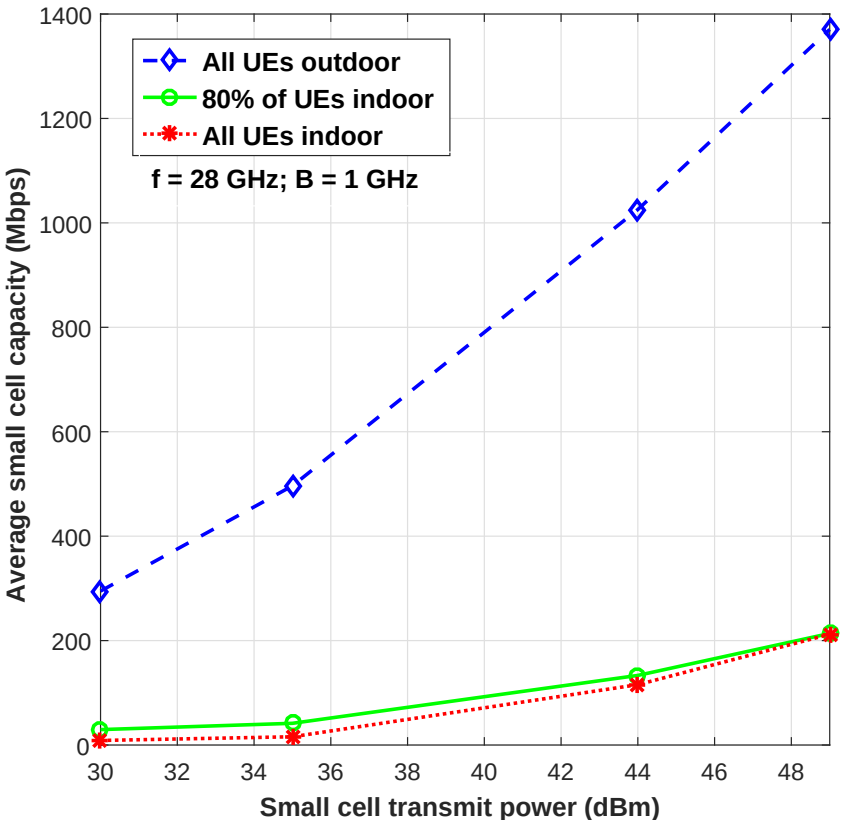

Figure 3.11: Impact of transmit power on cell performance.

However, the SC transmit powers cannot practically be increased indiscriminately due to the following constraints, among others: (i) transmit powers are limited by regulation; (ii) excessive power will increase the interference level as well, in addition to enhancing the signal; and (iii) more transmit power will increase the energy consumption of the network which is undesirable for 5G networks. Therefore, the optimal transmit power is a critical design goal.

(b) Interference Mitigation

Beamforming to target UEs mitigates interference from other BSs. This will also enhance the signal level through its transmit and receive beamforming gains. However, this requires pencil-like beams whose performance heavily depends on beam steering, beam tracking and beam alignment efficiencies, alongside other complexity challenges. In Figure 3.12, we show the performance of the SCs with directional (8 dBi gain, 65^o half power beamwidth (HPBW)) and omnidirectional antenna (0 dBi), for both full buffer and mixed traffic scenarios. The implemented mixed traffic is a multi-class traffic type composed of the hypertext transfer protocol (HTTP), file transfer protocol (FTP), gaming, voice over internet protocol (VoIP) and video. The distribution of each of the traffic type is given in Table 3.7 following the 3GPP traffic model evaluation methodology [48] and represents a more realistic user pattern than the full buffer which assumes that users have infinite buffers and are active all the time.

Table 3.7: Multi-class traffic model (adapted from [48]).

Application	**Traffic Category**	**Percentage of Users** (%)
FTP	Best effort	10
HTTP	Interactive	20
Video	Streaming	20
VoIP	Real-time	30
Gaming	Interactive real-time	20

With respect to directivity, the results are shown in Figure 3.12. The network performance with directional antenna is poorer than that with omnidirectional antenna, despite the higher antenna gain in the directional case. This is due to the fact that we employed static beamforming [32], where only a part of the users (i.e., those within the coverage zone of the beams) is served. In radial SCs with users randomly in all directions, dynamic beamforming where the locations of the users are continuously scanned and tracked is the solution. In such a case, a better performance can be achieved with narrower beams and higher gains. Although, this would result in a much higher complexity due to beam tracking requirements.

As for the traffic type, the performance with the mixed traffic is slightly better than the full buffer scenario in each case, as shown in Figure 3.12. Users in the mixed traffic scenario do not request data all the time as they have finite buffers. In such inactive time instants, the interference level in the network is reduced. This accounts for the increased cell capacity when averaged over the entire transmission period. The results when f_c increases from 28 GHz to 0.1 THz is shown in Figure 3.13.

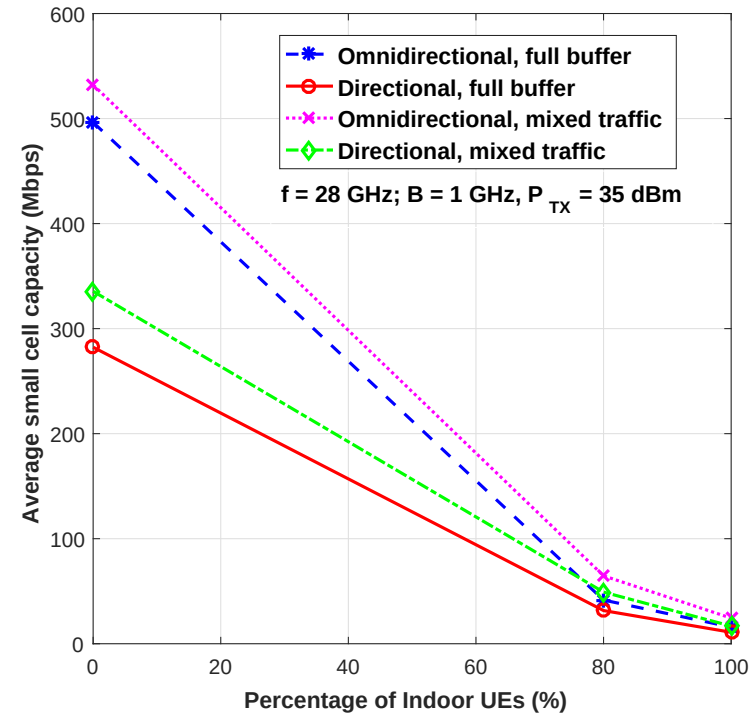

Figure 3.12: Impacts of antenna directivity and traffic type on cell performance.

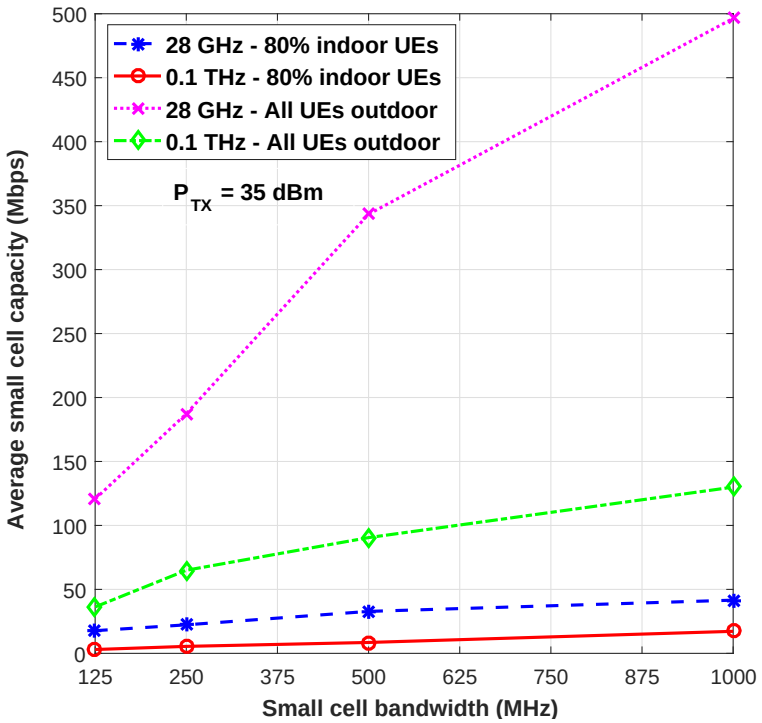

Figure 3.13: Impact of carrier frequency on cell performance.

In Figure 3.13, the performance of the SC network gets poorer as higher frequencies are employed. This trend is due to the increasing PL with increasing f_c. At 0.1 THz (100 GHz), the AC_{SC} for the outdoor scenario is ∼130 Mbps using 1 GHz bandwidth, compared to ∼500 Mbps at 28 GHz. In the 80% indoor UEs case, the performance is much worse. The AC_{SC} is ∼20 Mbps at 0.1 THz compared to ∼45 Mbps at 28 GHz.

It is evident from the results in Figures 3.11-3.13 that appropriate transmit power coupled with adequate beamforming gains will overcome the SINR bottleneck. This will consequently boost the performance of indoor users served from outdoor mmWave SC networks, and further boost the performance of outdoor users. In addition, as the mmWave frequency increases up to the THz bands, the ISD would have to be correspondingly decreased. As of now, only a coverage range (or ISD) up to 10 m can be seen as realistic for THz band application in cellular systems, as compared to the maximum of 200 m for mmWave systems [151].

3.4 C-I2V Channel Performance

Autonomous driving is an innovative and revolutionary paradigm for future intelligent transport systems (ITS). To be fully-functional and efficient, vehicles will use hundreds of sensors and generate terabytes of data that will be used and shared for safety, infotainment and allied services. Vehicle-to-vehicle (V2V) and vehicle-to-infrastructure (V2I) communication thus requires data rate, latency and reliability far beyond what the legacy DSRC and LTE-A systems can support. This has motivated the use of mmWave massive MIMO to facilitate gigabits-per-second (Gbps) communication for C-V2X scenarios. Focusing on C-I2V, this section characterizes the mmWave massive MIMO vehicular channel using metrics such as PL, root-mean-square (RMS) DS, KF, cluster and ray distribution, PDP, channel rank and condition number (CN) as well as data rate. We then compare the mmWave performance with the DSRC and LTE-A capabilities and offer useful insights on vehicular channels.

Currently, DSRC (known as ITS-G5 in Europe) is the legacy system for vehicular communication and safety. It operates on the 5.9 GHz band using transceivers based on the IEEE 802.11p standard [152]. Unfortunately, DSRC can only support data rates up to 27 Mbps, with typical average of 2-6 Mbps. This is grossly inadequate for next-generation applications foreseen to require multi-Gbps rates. Similarly, legacy 4G systems can only support a maximum data rate of 100 Mbps in high mobility (vehicular) scenarios. The same story goes for the bandwidth, reliability and latency requirements. Consequently, the industrial and academic research communities have identified the mmWave bands to come to the rescue [18, 152, 153]. Fortunately, the mmWave bands are being extensively explored for 5G services and applications due to their amazing spectral opportunities. The mmWave band is expected to support the high rate vehicular applications to facilitate future emerging use cases in infrastructure-assisted and autonomous driving, and enable high-rate infotainment and ultra-reliable safety services. This is in addition to the anticipated benefits of enhanced vehicular safety, better traffic management, more efficient toll collection and commute time reduction, among others. The mmWave spectrum is already being used in standardized systems such as IEEE 802.11ad (60 GHz) and radar (76 GHz) [18].

ITS-supported vehicles will be equipped with tens to hundreds of sensors (e.g., LIDAR, ultrasonic, radar, camera, etc.) which together with the on-board communication chipsets will enable diverse services such as live map download, videos streaming, environmental data gathering and broadcast for different vehicular applications like sensor data sharing, cloud pro-

cessing, cooperative perception, platooning, intent/trajectory sharing, real-time local updates, path planning, collision avoidance, blind-spot removal and general warnings [18,152,153]. For V2I links, the infrastructure can gather sensing data (about the vehicles or the surrounding traffic) from the vehicles. The sensed data can be processed in the cloud and used to provide live images or real-time maps of the environment. These maps can be used by the transportation control system for congestion avoidance, general warnings (such as dangerous situations) and overall traffic efficiency improvement. Also, automakers can use the sensed data for fault or potential failure diagnosis of the vehicles. The infrastructure can also be used to provide high rate internet access to the vehicles for automated driving and infotainment services such as media download and video streaming [18, 143]. Similarly, the potential V2V applications include cooperative perception where perceptual data from neighbouring vehicles can be used to create a satellite view of the surrounding traffic. The view can be used to extend the perception range of each vehicle in order to reveal hidden objects, cover blind spots and avoid a collision with other vehicles. Shared data among the vehicles can also be used for other applications such as path planning and trajectory sharing, among others [18, 152].

Many authors have attempted to address different aspects of the challenges. Majority of the works centre on the V2V and V2I scenarios in urban street [154, 155], highway [152, 153] and high speed rail (HSR) [156] environments. The works on I2V consider the infrastructures as BSs or SCs with typical range 200-500 m, which translate to sub-6 GHz and mmWave channels with many clustered blockers and scatterers and where models such as [102, 103] can be readily adopted. However, [102] does not consider mobility while [103] supports only pedestrian mobility and is reported to have excessive number of clusters and SPs that is unsupported by measurement [157]. This section, however, motivates the use of mmWave massive MIMO lampost-mount APs spaced at very short intervals, typically 20 m for dense road side unit (RSU) deployment [18]. We then characterize the mmWave vehicular channel and compare its performance with the DSRC and LTE-A (sub-6 GHz) vehicular channels to provide insights for 5G NR C-I2V.

3.4.1 Network Deployment

In this section, we present the network layout, antenna and channel models as well as the precoding technique employed. We show in Figure 3.14 the deployment layout for the C-I2V scenario. We consider a $d_r = 500$ m-long section of the road in an UMi street environment. Stationary APs are mounted a height $h_{TX} = 5$ m on street lampost with a density of $\Omega_{TX} = 50$ BS/km. This corresponds to 25 evenly-spaced APs for the considered distance. The vehicles traverse the route at a speed of $v_{RX} = 36$ km/h $= 10$ m/s, and have roof-mount antennas with height $h_{RX} = 1.5$ m above the reference ground level. Further, we assume that the APs are connected by high rate backhaul links. The DL connectivity is by LOS with the roof-top positioning of vehicle antenna. Therefore, the relatively high position of the APs (compared to a V2V scenario) ensures good link [158]. Also, the 3D separation distance (d_{3D}) between the vehicle (RX) and its serving AP (TX) at each time instant of the considered scenario gives a LOS probability $P_{LOS} \approx 1$, according to (3.22) [101]. As a result, the I2V communication in this scenario is by LOS. It should, however, be noted that LOS here does not mean pure LOS as there is still sparse blockage and scattering effects from pedestrians, trees and road signs as illustrated in Figure 3.14.

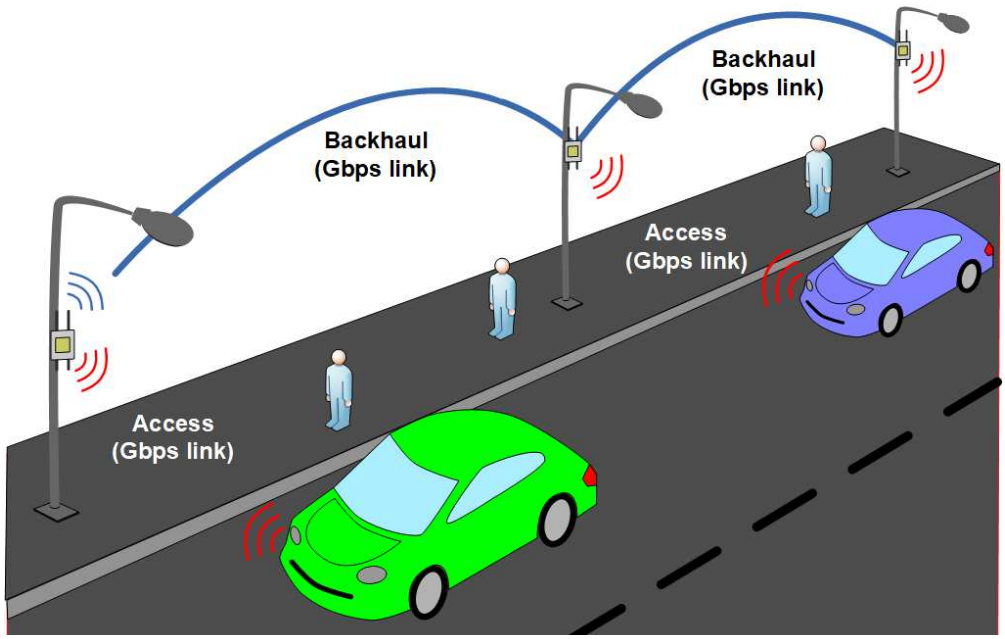

Figure 3.14: C-I2V deployment layout.

$$P_{\mathrm{LOS}}(d_{3D}) = \left[\min\left(\frac{27}{d}, 1\right)\left(1 - e^{-\frac{d}{71}}\right) + e^{-\frac{d}{71}}\right]^2. \tag{3.22}$$

3.4.2 Channel Model

We consider a clustered 3D SSCM based on the implementation in [42, 101, 102], but adapted and enhanced for C-I2V. The fast-fading double-directional CIR (h_{dir}) with N_{cl} clusters and N_{sp} SPs, rays or MPCs per cluster for each transmission link is given by (3.23).

$$h_{dir}(t, \phi, \theta) = \sum_{c=1}^{N_{cl}} \sum_{s=1}^{N_{sp,c}} P_{RX,c,s} \cdot e^{j\varphi_{c,s}} \cdot \delta(t - \tau_{c,s}) \cdot G_{TX}(\phi - \phi_{c,s}, \theta - \theta_{c,s}) \cdot G_{RX}(\phi - \phi_{c,s}, \theta - \theta_{s,t}), \tag{3.23}$$

where, in (3.23), $P_{RX,c,s}$, $\varphi_{c,s}$ and $\tau_{c,s}$ denote the received power magnitude, phase and propagation time delay of the cluster-SP combinations, respectively; t is time, ϕ and θ are the angle offsets from the boresight direction for the azimuth and elevation, respectively. For each ray, $\phi_{c,s}$ and $\theta_{c,s}$ are the azimuth AoD and elevation AoD at the AP (or azimuth AoA and elevation AoA for the vehicle, as the case may be). G_{TX} and G_{RX} are the TX and RX antenna gains modeled as in (3.24) and (3.25) [101].

$$G(\phi, \theta) = \max\left(G_0 e^{\alpha\phi^2 + \beta\theta^2}, \frac{G_o}{100}\right), \tag{3.24}$$

$$G_o = \frac{41253 \cdot \xi}{\phi_{3dB}^2 \theta_{3dB}^2}, \quad \alpha = \frac{4\ln(2)}{\phi_{3dB}^2}, \quad \beta = \frac{4\ln(2)}{\theta_{3dB}^2}, \tag{3.25}$$

where G_o is the maximum directive boresight gain, ξ is the average antenna efficiency, ϕ_{3dB} and θ_{3dB} are the azimuth and elevation HPBW, respectively. The variables α and β are evaluated using (3.25).

It should be noted that due to the high vehicular mobility (relative to static and pedestrian cases), the channel becomes time-variant (i.e., the channel coherence time becomes smaller than the observation window). The resulting phase $\varphi_{c,s}$, given by (3.26)-(3.28), is now composed of the distance-dependent phase change $\Theta_{c,s}$ and the velocity-induced Doppler shift $\vartheta_{D(c,s)}$ (caused by the Doppler frequency due to the relative motion between the TX and RX).

$$\varphi_{c,s} = \Theta_{c,s} + \vartheta_{D(c,s)}, \tag{3.26}$$

$$\varphi_{c,s} = 2\pi \left(f_c \tau_{c,s} + f_{D(c,s)} \triangle t \right), \tag{3.27}$$

$$\varphi_{c,s} = 2\pi \left(f_c \tau_{c,s} + \frac{v_{RX} \cos\left(\phi_{c,s}\right)}{\lambda} \triangle t \right), \tag{3.28}$$

where $f_{D(c,s)}$ is the Doppler frequency which is positive when the vehicle is moving towards the AP and negative when moving away from it [49, 159].

3.4.3 Antenna Model

The APs and vehicles are equipped with massive MIMO arrays with N_{TX} and N_{RX} AEs, respectively. We consider ULAs with inter-element spacing $d_{TX} = d_{RX} = \lambda/2$, where $\lambda = c/f_c$ is the wavelength and $c = 3 \times 10^8$ m/s is the speed of light. For the massive MIMO, the $h_{dir}(t, \phi, \theta)$ in (3.23)-(3.28) is extended to $\mathbf{H}(t, \tau)$ in (3.29), where $\mathbf{a}_{RX}$ and $\mathbf{a}_{TX}$ are RX and TX array response vectors given by (3.30) and (3.31), respectively.

$$\mathbf{H} = \sqrt{\frac{N_{RX} N_{TX}}{\sum_{c=1}^{N_{cl}} N_{sp,c}}} \cdot \sum_{c=1}^{N_{cl}} \sum_{s=1}^{N_{sp,c}} \sqrt{PL_{c,s(d_{c,s})}} \cdot e^{j2\pi \left(f_c \tau_{c,s} + \frac{v_{RX} \cos\left(\phi_{c,s}\right)}{\lambda} \triangle t \right)} \cdot \mathbf{a}_{RX}\left(\phi_{c,s}^{RX}\right) \mathbf{a}_{TX}^{H}\left(\phi_{c,s}^{TX}\right), \tag{3.29}$$

$$\mathbf{a}_{RX}\left(\phi_{c,s}^{RX}\right) = \frac{1}{\sqrt{N_{RX}}} \begin{pmatrix} \\ e^{j\frac{2\pi}{\lambda} d_{RX}(n_r - 1) \sin\left(\phi_{c,s}^{RX}\right)} \\ \\ \end{pmatrix}, \qquad \forall n_r = 1, 2, ..., N_{RX}, \tag{3.30}$$

$$\mathbf{a}_{TX}\left(\phi_{c,s}^{TX}\right) = \frac{1}{\sqrt{N_{TX}}} \begin{pmatrix} \\ e^{j\frac{2\pi}{\lambda} d_{TX}(n_t - 1) \sin\left(\phi_{c,s}^{TX}\right)} \\ \\ \end{pmatrix}, \qquad \forall n_t = 1, 2, ..., N_{TX}. \tag{3.31}$$

DSRC and LTE-A use limited numbers of AEs. Typical MIMO configurations are 2×2, 2×4, 4×4 and 2×8 for $N_{RX} \times N_{TX}$. On the other hand, mmWave massive MIMO arrays

employ large number of AEs. At 70 GHz, for example, the arrays can go up to 64×1024 (with typical configurations being 16×64, 16×128 and 32×256 for $N_{RX} \times N_{TX}$ according to the 3GPP. The maximum number of RF chains or number of streams (N_s) at the RX and TX at such frequency are 8 and 32, respectively [3, 4]. The large arrays offer amazing opportunities to beamform highly-directive beam (through ABF) for enhanced signal strength or to multiplex multiple streams (via DBF and HBF) for higher data rates. Many studies advocate for HBF for mmWave massive MIMO for its balanced trade-off between SE and EE, relative to the power-exhaustive DBF and the low-rate ABF [160]. However, for the evaluation in this subsection, we employ ABF while the HBF analysis is employed and presented in greater detail in Chapter 4. We note that we employ ABF for two reasons. First, the short TX-RX separation distance, LOS propagation and high level of antenna correlation due to SU-MIMO and sparse scattering [125] potentially guarantees near-optimal performance with ABF. Second, single-stream beamforming ensures a fair comparison of the performance of mmWave massive MIMO with the DSRC and LTE-A that use a modest number of antennas. The extension to the MU-MIMO case is presented in Chapter 4.

3.4.4 Simulation Results and Analyses

In this subsection, we present the simulation results for the performance of the three considered technologies. We simulate for 50,000 TTIs and average the results over 100 channel realizations. For a fair comparison, we set $NF = 6$ dB, N_o = -174 dBm/Hz, $P_T = 30$ dBm and the PLE = 2. The technology-dependent key simulation parameters for the three systems considered are given in Table 3.8. Using the cumulative distribution function (CDF), we present results for the entire route traversed by vehicle. We also show the results for a representative distance (i.e., 20 m) covered by each AP in the scenario.

Table 3.8: Key simulation parameters for C-I2V.

Parameter	**DSRC**	**LTE-A**	**mmWave**
f_c (GHz)	5.9	2.6	73
B (MHz)	10	20	396
N_{TX}	2	4	64
N_{RX}	2	4	16
ϕ_{3dB}^{TX}	65°	65°	10°
ϕ_{3dB}^{RX}	65°	65°	10°

To compare the performance of DSRC and LTE-A with the mmWave massive MIMO advocated in this work for the considered scenario, we characterize the vehicular channel using PL, KF, RMS DS (τ_{RMS}), number of clusters, number of resolvable MPCs, PDP, channel rank, channel condition number and data rate as follows.

(a) Path Loss

The effective PL (PL_{eff}), which combines the PL and SF is given by (3.32) and (3.33).

$$PL_{\text{eff}} = PL + SF, \tag{3.32}$$

$$PL_{\text{eff}} = 20\log_{10}\left(\frac{4\pi f_c}{c}\right) + 10\bar{n}\log_{10}\left(d_{3D}\right) + X(0,\sigma), \tag{3.33}$$

where $\bar{n}$ is the PLE and X is the log-normal random SF variable with zero mean and σ standard deviation [101]. We note that blockage is modeled inherently in (3.33) as it matches the blockage-dependent PL model (3.34) in [18] when there is `randi`(0,1) number of blockers at each time instant. This appropriately models the LOS and sparse blockage regime of the considered scenario, where κ and Υ are parameters determined by the number of blockers (see Table 7.2 in [18]).

$$PL = 10\kappa \log_{10}(d_{3D}) + \Upsilon + 15\left(\frac{d_{3D}}{1000}\right). \tag{3.34}$$

Using (3.33), the CDFs of PL_{eff} results per link for the three technologies are shown in Figure 3.15. As can be deduced from (3.33), PL expectedly increases with increasing f_c. Hence, the mmWave system at 73 GHz exhibits a penalty of up to 30 dB in PL, compared to the sub-6 GHz DSRC and LTE-A at 5.9 GHz and 2.6 GHz, respectively. The mmWave system, however, compensates for its high PL with large beamforming gains from highly-directive antennas in order to bring the received powers to levels comparable to that of sub-6 GHz systems or even higher [18, 125].

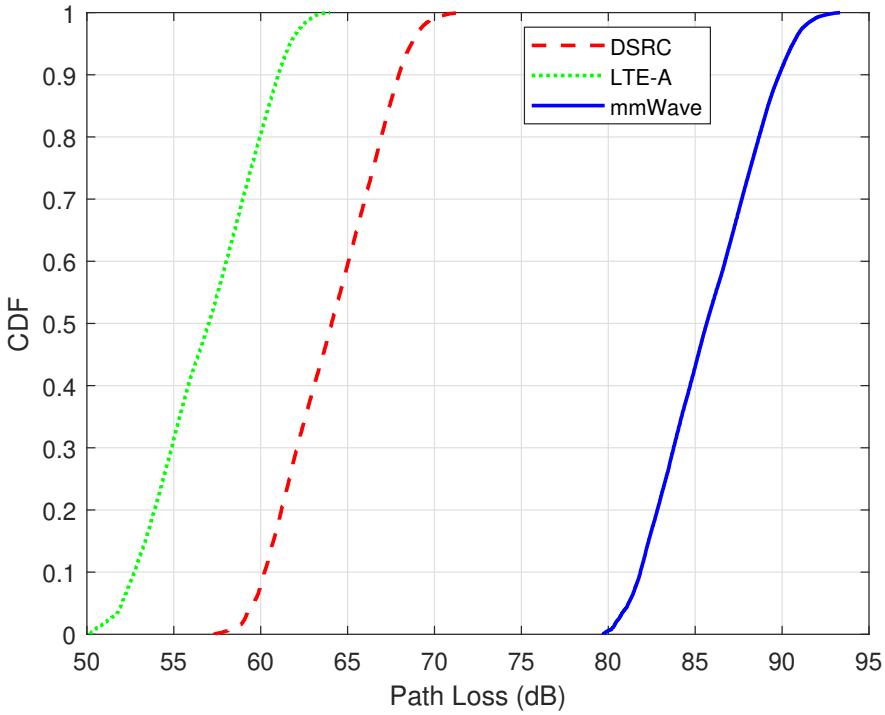

Figure 3.15: CDF of path loss for the three C-I2V technologies.

In Figure 3.16, the PL variation as a function of the distance travelled for an AP-vehicle connection time for the three systems is shown, with and without spatial consistency. Similarly, the PL variations as a function of the distance for the entire 500 m route are shown in Figure 3.17. It should be noted that the plots in Figure 3.17 are periodic in nature due to the inter-AP handovers as the vehicle moves towards and away from the coverage area of each of the densely-deployed APs.

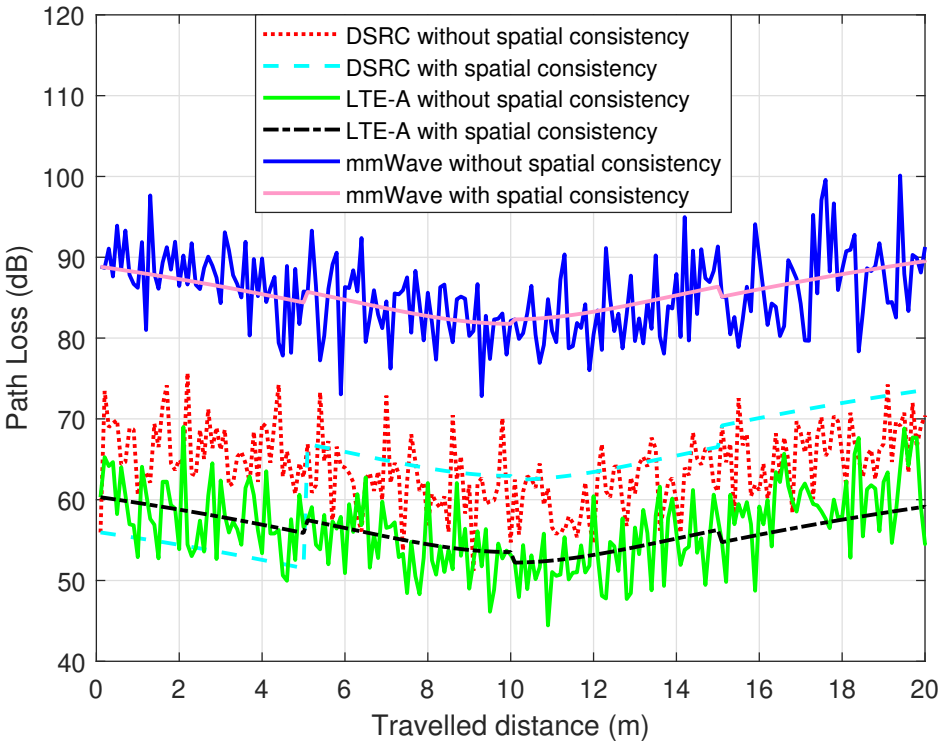

Figure 3.16: Path loss variation for the coverage area of one AP.

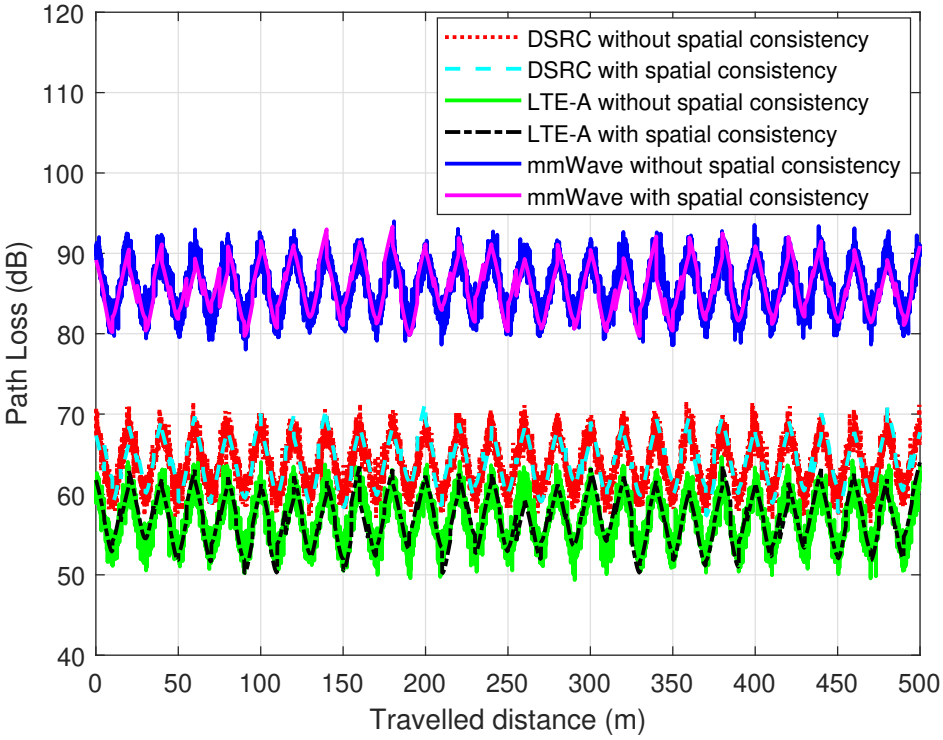

Figure 3.17: Path loss variation for the entire route.

As shown in the Figures 3.16 and 3.17, PL variation is random without spatial consistency, due to the impact of SF. With spatial consistency, the variation is more uniform and systematic. We note that it is important for channel models to incorporate spatial consistency where the channel parameters vary in a realistic and continuous manner as a function of position, and by which closely-placed users have similar channel characteristics as against randomized values [100, 161]. We note that the large-scale parameters (LSPs), such as SF (and as a consequence the PL_{eff} vary more slowly than the fast-fading small-scale parameters (SSPs). The spatial consistency phenomenon leads to three time scales: channel correlation time (T_c) for LSPs, channel update time (T_u) for SSPs, and then the data transmission time (T_t). The time scales are related by (3.35).

$$T_c = \chi \cdot T_u = \chi \cdot \varepsilon \cdot T_t, \tag{3.35}$$

where χ and ε are integer values. We note further that T_t is standardized as 1 ms for 4G and 5G systems. However, it is more realistic for channel-aware schedulers to employ T_u that is used for updating the fast-fading channel parameters as the basis for scheduling. Inspired by [103, 144, 152, 161], we adopt 0.1 m and 1 m as the update and correlation distances, respectively. At $v_{RX} = 10$ m/s employed for the simulation in this subsection, this corresponds to $\chi = 10$, $\varepsilon = 10$. Therefore, $T_u = 10$ TTIs = 10 ms and $T_c = 100$ TTIs = 100 ms. This means that data is transmitted every 1 ms, the SSPs are updated every 10 ms while the LSPs are updated every 100 ms.

(b) Rician K-Factor

The KF statistics is a measure of the ratio of LOS-to-NLOS strength and its value affects the performance of MIMO systems significantly [162]. Higher LOS translates to stronger propagation and higher SNR [157]. The KF is evaluated using (3.36) [162], where the numerator in (3.36) is the LOS component and the denominator is the sum of all NLOS components.

$$KF = \frac{P_{LOS}}{\sum P_{NLOS}} = \frac{P_{RX,c=1,s=1}}{\left(\sum_{c=1}^{N_{cl}} \sum_{s=1}^{N_{sp,c}} P_{RX,c,s}\right) - P_{RX,c=1,s=1}}. \tag{3.36}$$

Figure 3.18 shows the CDFs of the KF for the three systems evaluated using (3.36). It can be readily seen that mmWave has a higher KF than DSRC and LTE-A. This indicates larger LOS strength and higher directivity. Figure 3.18 also shows that the powers of NLOS components dominate only about 20% of time (at 0.2 CDF points) where the KF is less than 0 dB while for the remaining 80%, LOS component dominates. It can also be observed that the curves do not reach the 100% CDF points. The gaps indicate the percentage of pure LOS where only the LOS component is present (i.e., KF= ∞). Figure 3.18 shows that mmWave has higher percentage of pure LOS than the DSRC and LTE-A as can be seen at the saturation points of the CDF curves.

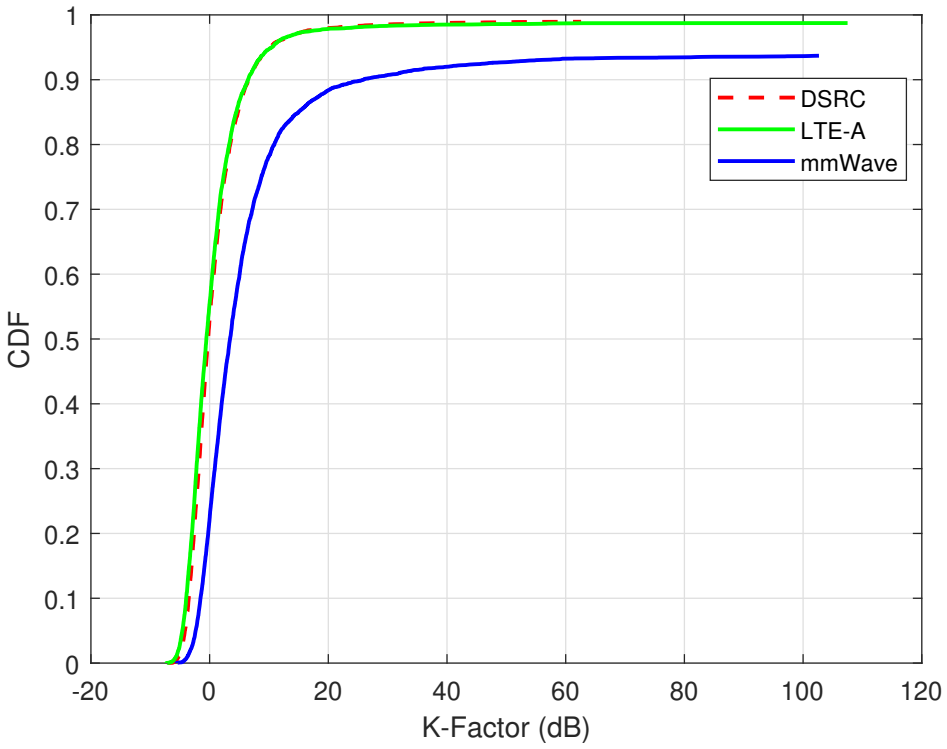

Figure 3.18: CDF of K-Factor for the three C-I2V systems.

(c) RMS Delay Spreads

The RMS DS (τ_{RMS}) is a measure of the delay dispersion of the channel and is evaluated using (3.37) [115]. It is also related to the channel coherence bandwidth (B_c) which characterizes the frequency selectivity of the channel. If $B_c \ll B$ (as is the case in wideband systems like mmWave), the channel will be frequency-selective thereby leading to inter-symbol interference (ISI). To combat this, OFDM is employed in 4G and 5G systems to convert the frequency-selective wideband channels to flat-fading channels. The metrics (τ_{RMS}) and B_c are related by (3.38).

$$\tau_{RMS} = \sqrt{\frac{\sum_{c=1}^{N_{cl}} \sum_{s=1}^{N_{sp,c}} \tau_{c,s}^2 P_{RX,c,s}}{\sum_{c=1}^{N_{cl}} \sum_{s=1}^{N_{sp,c}} P_{RX,c,s}} - \left(\frac{\sum_{c=1}^{N_{cl}} \sum_{s=1}^{N_{sp,c}} \tau_{c,s} P_{RX,c,s}}{\sum_{c=1}^{N_{cl}} \sum_{s=1}^{N_{sp,c}} P_{RX,c,s}} \right)^2}, \tag{3.37}$$

$$B_c \approx \frac{1}{2\pi\tau_{RMS}}. \tag{3.38}$$

The CDFs for the τ_{RMS} for the three systems are shown in Figure 3.19. The mmWave system has lower τ_{RMS} due to its narrower beams. According to [18, 144], highly-directive narrow beams can reduce both the delay and Doppler spreads and increase the coherence time in mmWave channels. This resulting outcome lessens the severity of the impact of Doppler spread. More so, the values from the τ_{RMS} CDFs in Figure 3.19 when plugged into (3.38) gives B_c with the range [7,160] MHz which are far higher than the 156.25 kHz [163], 180

kHz [164] and 1.44 MHz [165] for one OFDM RB for DSRC, LTE-A and mmWave systems, respectively. Similarly, the τ_{RMS} with range [1, 22] ns in Figure 3.19 is far less than the OFDM cyclic prefix duration of 1.6 μs [163], 5.2 μs [164] and 4.4 μs / 0.57 μs [165] for the DSRC, LTE-A and mmWave (5G NR) standards, respectively. Therefore, ISI is not a problem with OFDM as the CP duration is larger than the DS.

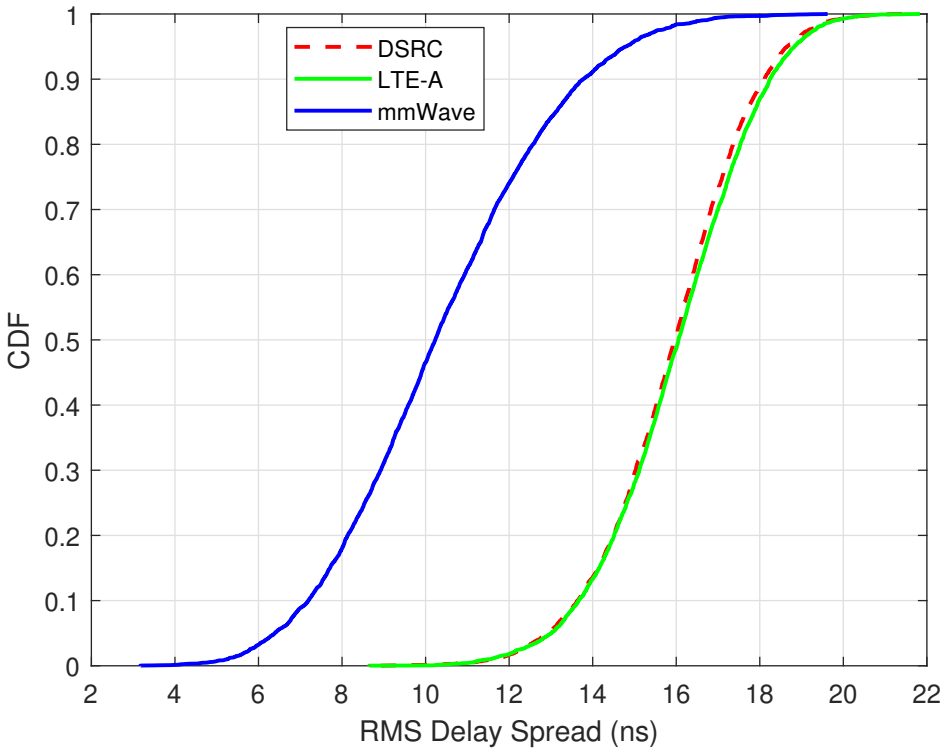

Figure 3.19: CDF of RMS delay spreads for the three C-I2V systems.

(d) Number of Clusters and Sub-paths

The number of clusters (N_{cl}) and SPs (N_{sp}) per cluster are randomly generated as uniform discrete distributions respectively. The cluster (and sub-paths) powers, delays and phases follow lognormal, exponential and uniform (0,2π) distributions respectively [101]. The CDFs for the N_{cl} and N_{sp} are given in Figures 3.20 and 3.21, respectively. Figure 3.20 shows that for the considered scenario, the mmWave system has two clusters on average, while the DSRC and LTE-A have between 3 and 4 clusters. Similarly, as shown in Figure 3.21, the mmWave system has 6 SPs while DSRC and LTE-A both have 24 SPs, for the 50% CDF points. The maximum number of resolvable rays are 9, 40 and 42 for mmWave, LTE-A and DSRC, respectively. Also, Figure 3.21 shows that the mmWave system has limited number of resolvable rays compared to the sub-6 GHz systems. This outcome buttresses the sparse nature of mmWave systems.

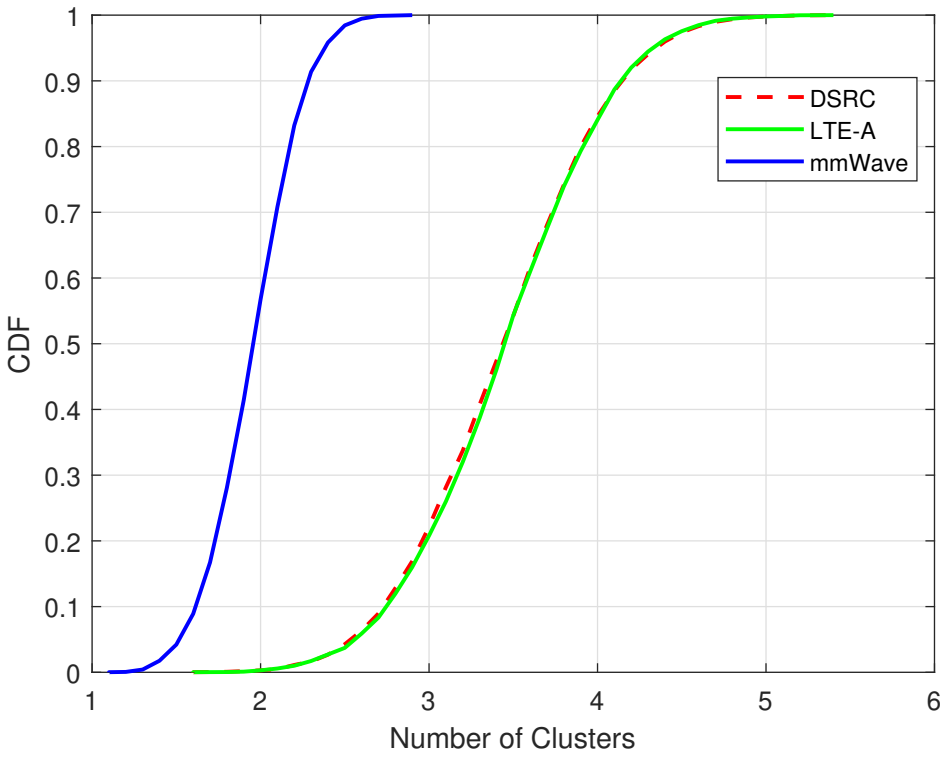

Figure 3.20: CDF for the number of clusters for the three C-I2V systems.

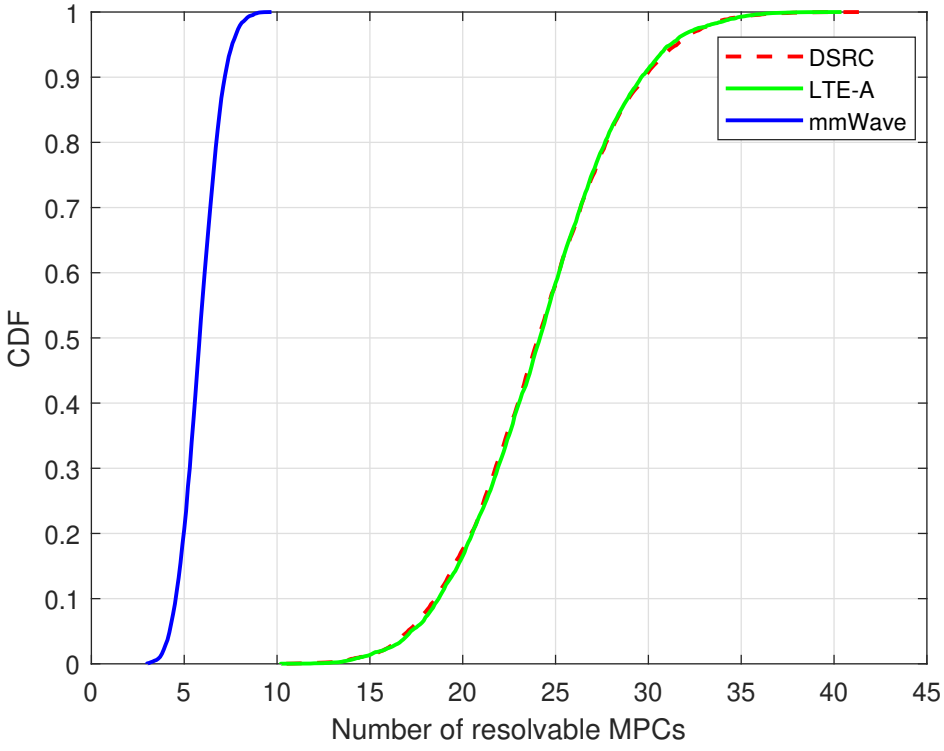

Figure 3.21: CDF for the number of MPCs for the three C-I2V systems.

(e) Power Delay Profile

In Figures 3.22 and 3.23, we show two snapshots of the PDPs for the three systems considered. PDPs show the distribution of the received signal powers of the MPCs with their corresponding time delays, which are used to characterize the channel with respect to the DS and coherence bandwidth [115]. From Figures 3.22 and 3.23, it can be observed that mmWave has lower number of clusters and overall number of rays when compared to the sub-6 GHz DSRC and LTE-A (Figures 3.20 and 3.21), as well as lower number of rays per cluster.

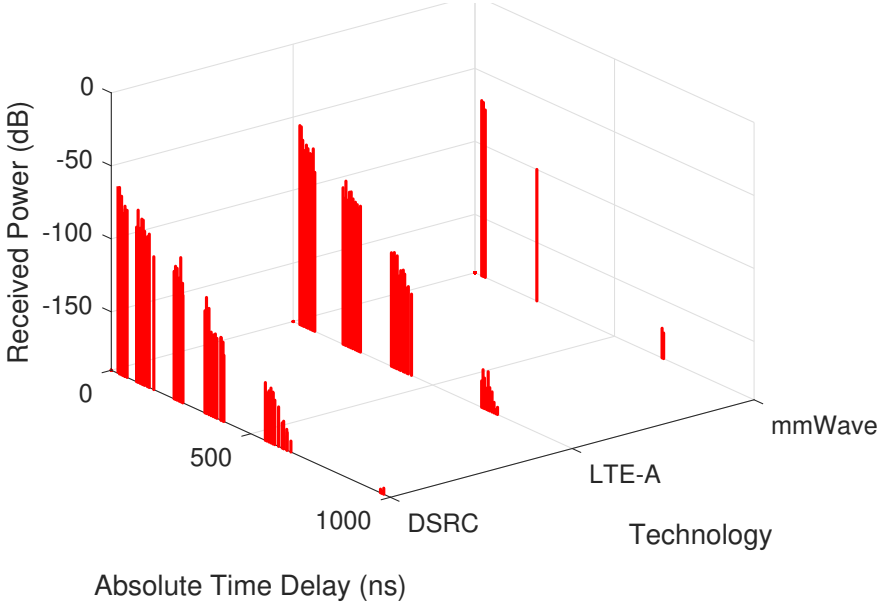

Figure 3.22: Power Delay Profile snapshot from the m^{th} AP.

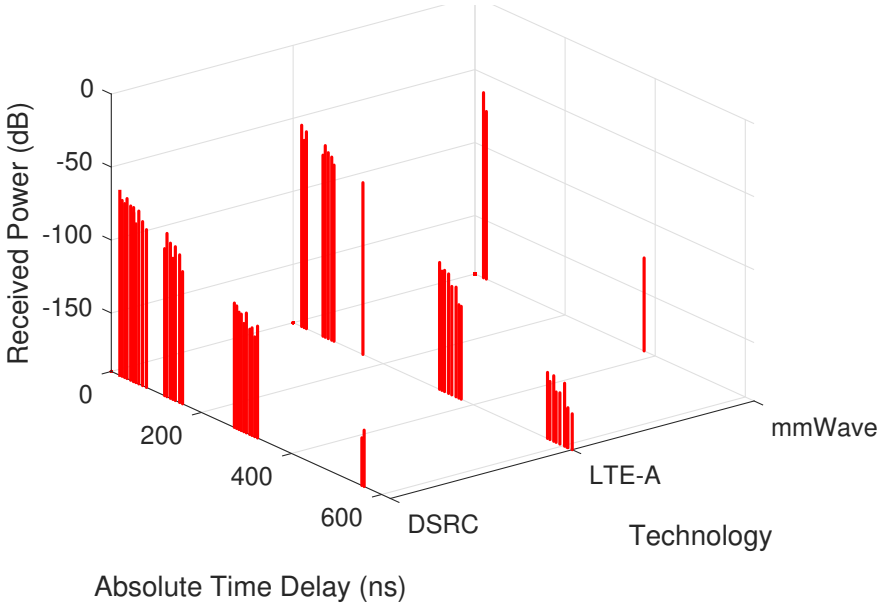

Figure 3.23: Power Delay Profile snapshot from the n^{th} AP.

It should be noted that the first arriving ray is the LOS component. With the sparse nature of the MPCs in mmWave, the LOS-to-NLOS strength will be higher. This is an indication of the higher directivity of the mmWave system as compared to the other two systems with more diffuse scattering and lower directivity. The MPCs with longer delays generally have lower received powers.

While the corresponding MPC (such as the LOS component) in the three systems have comparable received directional powers (since the mmWave antenna gain compensates for the higher PL_{eff}), the sum of received component powers is lower in the mmWave systems due to higher absorption and blockage such that the powers of many rays are below the noise level and so they are filtered out.

(f) Channel Rank and Condition Number

The rank of a channel matrix determines how many data streams can be sent across the channel. A full rank channel, for example, has $\texttt{rank} = \min(N_{RX}, N_{TX})$. While the channel rank is a pointer to the quantitative multiplexing capacity of the channel, it does not indicate the relative strength of the streams. On the other hand, the channel condition number (CN) is the qualitative measure of the MIMO channel.

Using the singular values of the channel matrix, CN indicates the ratio of the maximum to minimum singular values resulting from the singular value decomposition (SVD) of the channel matrix. A channel with $CN = 0$ dB has full rank and thus has equal gains across the channel eigenmodes. With $0 < CN \leq 20$ dB, the channel is rank-deficient with comparable gains across the eigenmodes while $CN > 20$ dB shows that the minimum singular value is close to zero. The rank of the channel gives the measure of how many data streams can be multiplexed while the channel CN is an indicator of the quality of the wireless channel [102]. In Figures 3.24 and 3.25, we show the variations of channel rank and CN, respectively, with the indicated MIMO configurations.

Connecting Figures 3.24 and 3.25, DSRC with rank 2 has $0 < CN \leq 40$ dB. With the relative variation around 20 dB, the channel strengths of the two eigenvalues are comparable. Thus, two streams can be multiplexed over the channel with the water-filling power allocation giving the optimal performance. For LTE-A with 4×4 channel, the rank varies between 3 and 4 while the CN is typically higher than 20 dB, thereby suggesting the multiplexing of streams even lower than the rank for good performance.

Similarly, according to Figures 3.24 and 3.25, the mmWave massive MIMO system with 16×64 antenna configuration has rapid fluctuations in rank between 3 and 7. However, its extremely high CN (i.e., $CN > 160$ dB) suggests relatively few dominant eigenmodes resulting from the high correlation of the tightly-spaced antennas at mmWave. This outcome reveals the rank deficiency of mmWave SU-MIMO where single-stream ABF or HBF with a few streams will give good or optimal performance. For MU-MIMO where the users are more separated in space, many users can be multiplexed. Thus, HBF or DBF becomes more appropriate for higher system capacity.

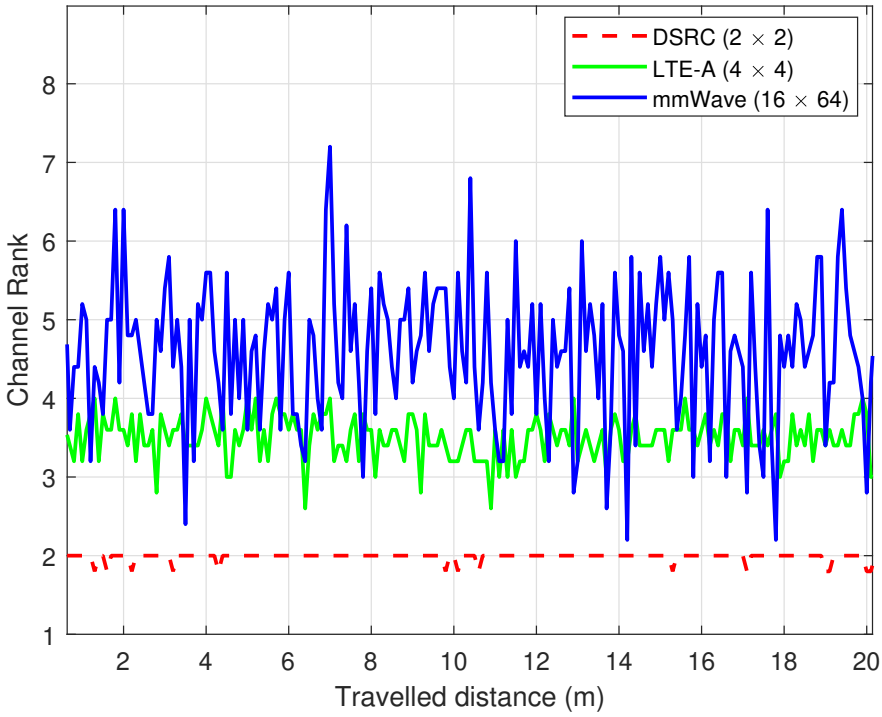

Figure 3.24: Channel rank for the three C-I2V systems.

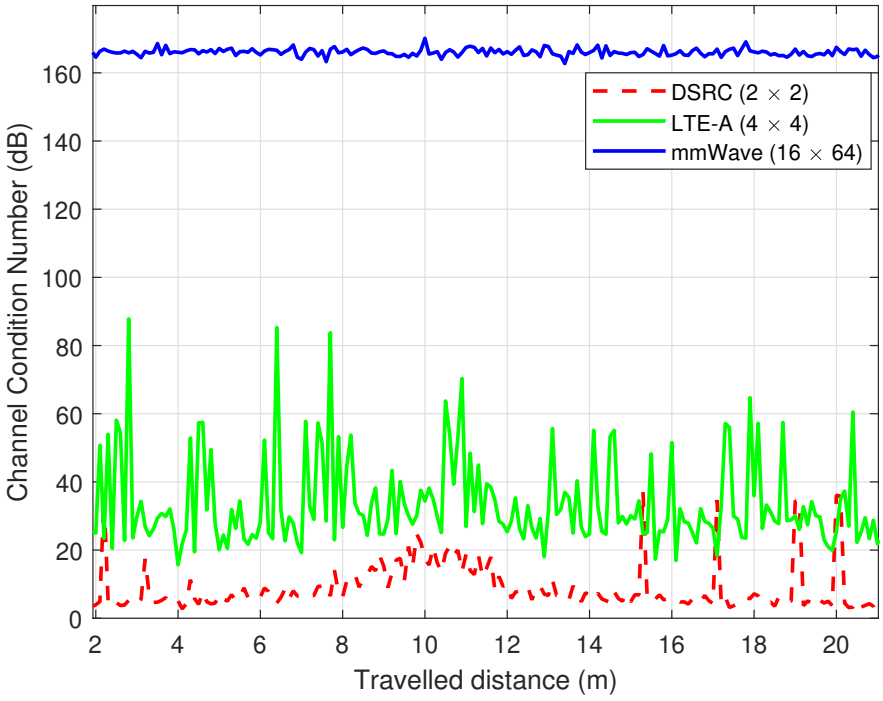

Figure 3.25: Channel condition number for the three C-I2V systems.

(g) Data Rate

Using transceivers with $N_{TX}^{RF} = N_{RX}^{RF} = 1$ RF chain for the ABF processing considered, the beamforming and combining matrices reduce to vectors $\mathbf{f} \in \mathbb{C}^{N_{TX} \times 1}$ and $\mathbf{w} \in \mathbb{C}^{N_{RX} \times 1}$, respectively. The received signal y is then given by (3.39). The achievable data rate is given by (3.40).

$$y = \sqrt{\rho}\mathbf{w}^{\mathbf{H}}\mathbf{H}\mathbf{f}s + \mathbf{w}^{H}\mathbf{n}, \tag{3.39}$$

$$R = B \cdot \log_2\left(1 + \rho R_n^{-1}\mathbf{w}^{H}\mathbf{H}\mathbf{f} \times \mathbf{f}^{H}\mathbf{H}\mathbf{w}\right), \tag{3.40}$$

where $R_n = \sigma_n^2\mathbf{w}^{\mathbf{H}}\mathbf{w}$ is the noise covariance after combining.

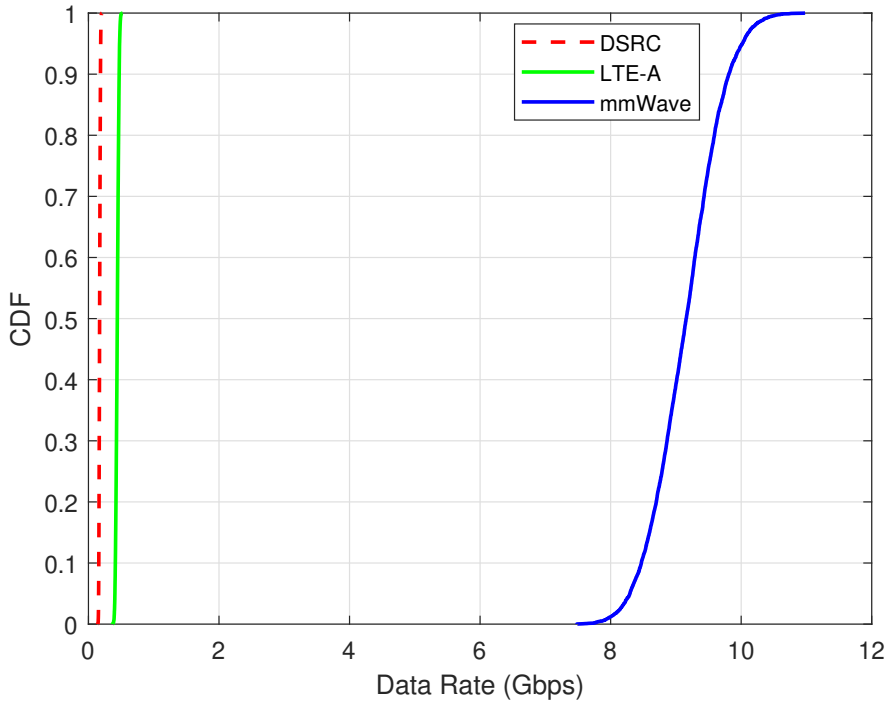

Figure 3.26: Data rates for the three C-I2V systems.

Finally, the data rate performance of the three systems are shown in Figure 3.26. The rate is evaluated using (3.40) and consistently shows the mmWave massive MIMO system realizing Gbps rates, compared to the DSRC and LTE-A. While a direct comparison is unrealistic as we employed different configurations for the three systems based on their respective baseline values according to the operating standards, the results in Figure 3.26 motivates the use mmWave massive MIMO for Gbps vehicular communication, particularly for 5G NR C-I2V investigated in this section. The data rates in Figure 3.26 results from using a bandwidth of 10 MHz for DSRC [163], 20 MHz for LTE-A [164] and 396 MHz for mmWave system [165], as stated in the simulation parameters of Table 3.8.

3.5 Conclusions

This chapter has presented the interplay of massive MIMO, mmWave and UDN as the three big technologies to support the 5G eMBB use case. Using system-level simulations with 3GPP 3D channel models, we showed the performance of 3D μWave and mmWave channel models for UMa and UMi scenarios. The results show that mmWave systems have higher coupling losses than μWave systems. The results also show, for the most part, that μWave systems are interference-limited while mmWave systems are noise-limited for the considered scenarios. Also, indoor users served by outdoor BSs show highly degraded performance. This is due to the additional 20-30 dB wall and indoor losses experienced by indoor users. The degradation will become even more pronounced if much larger mmWave bandwidths are employed due to the expected increase in noise.

For the purpose of coexistence, we also showed the performance of a representative 5G UDN with μWave MCs and mmWave SCs. The impact of large bandwidth, antenna directivity, traffic type and carrier frequency on the SE, UE throughput and cell capacity were also investigated. The results show that, without proper design, the performance of mmWave SCs can be highly degraded despite the abundance of available bandwidth in the mmWave bands. We also showed that while the performance is highly promising for outdoor users, the throughput experienced by indoor users is still generally poor. This results from the SINR bottleneck arising from the noise-limited condition of mmWave systems and the high propagation losses at such frequencies. To overcome this challenge, the design and operation parameters of 5G networks (such as bandwidth, transmit power, beamforming configuration, etc.) have to be carefully considered. This has to be done in a way that optimizes performance and efficiency while maintaining a balance in complexity and cost. By mitigating the SINR challenge, the spectral benefits at mmWave bands can be fully tapped. This will unleash their potential for supporting future cellular networks' services and applications.

We also characterized the vehicular channel for C-I2V communication where the infrastructure are APs mounted on street-level lamposts in a UMi type environment. Using diverse channel metrics, we compared the channel statistics of I2V using mmWave massive MIMO with that of legacy DSRC and LTE-A systems. With modest system configurations, we showed that mmWave massive MIMO system can enable Gbps data rates for C-I2V communication in order to support the anticipated explosive rate demands of future ITS. Finally, we remark that the results in this chapter have been published in the proceedings of IEEE Globecom conference[2], IEEE Communication Magazine[3] and the IET Intelligent Transport Systems journal[4].

[2]**S. A. Busari**, K. M. S. Huq, S. Mumtaz and J. Rodriguez, "Impact of 3D Channel Modeling for ultra-high speed Beyond-5G Networks", *IEEE Global Communications Conference (GLOBECOM) Workshop 2018*, Dubai, United Arab Emirates, pp. 1-6, Dec., 2018.

[3]**S. A. Busari**, S. Mumtaz, S. Al-Rubaye and J. Rodriguez, "5G Millimeter-Wave Mobile Broadband: Performance and Challenges", *IEEE Communications Magazine*, vol. 56, no. 6, pp. 137-143, June 2018.

[4]**S. A. Busari**, M. A. Khan, K. M. S. Huq, S. Mumtaz and J. Rodriguez, "Millimetre-wave massive MIMO for cellular vehicle-to-infrastructure communication", *IET Intelligent Transport Systems*, vol. 13, no. 6, pp. 983-990, June 2019.

Chapter 4

Novel Generalized Framework for Hybrid Beamforming

This chapter focuses on beamforming techniques and the spectral and energy efficiencies analyses for 5G UDNs and C-I2X networks. In the first part of the chapter, we propose a novel generalized framework for HBF in mmWave massive MIMO networks. The proposed framework facilitates the comparative analysis and performance evaluation of the different HBF configurations: the fully-connected, the sub-connected and the overlapped subarray architectures. The performance of the different array structures is evaluated using a C-I2X application scenario involving lampost-mount APs and a combination of pedestrian and vehicular users. The second part considers the C-I2P use case between the street-level APs and pedestrian users and evaluates the performance of the system using three beamforming approaches: analog beamsteering, hybrid precoding with zero forcing and the SVD precoding. The SE and EE performance and trade-off are presented with a view to providing useful insights for enabling high rate and energy-efficient operation for next-generation networks.

4.1 Background

Massive, soft, super-fast and green are the key attributes that will describe NGMNs (5G and beyond). The future networks are envisaged to be massive by concurrently featuring denser cells (UDN), larger bandwidths (mmWave) and a higher number of antennas (massive MIMO) in contrast to legacy cellular networks. This will provide a platform for delivering huge performance gains across all fronts. The soft and super-fast nature of the networks is reflected by their ability to be self-organizing and virtual. However, EE is becoming a critical design factor in addition to SE. This will raise significant design requirements that proliferate throughout the system, that includes efficient beamforming structure that is a key energy consumer in next-generation transceiver designs [36].

Using appropriate antenna array structure and beamforming[5] (or precoding) techniques, massive MIMO can provide the needed array gains to counter the severe effects of the high PL at high frequencies (e.g., mmWave and THz) and thus increase the SNR for user devices. It also provides the opportunity for highly-directional beams to mitigate MUI. The large

[5]Beamforming is used in its widest meaning, throughout this thesis, such that beamforming and precoding refer to exactly the same thing and can be used interchangeably. (cf.: https://ma-mimo.ellintech.se/2017/10/03/what-is-the-difference-between-beamforming-and-precoding/)

arrays can also be leveraged to provide spatial multiplexing gains by transmitting multiple streams so as to boost SE [125, 136]. The combined benefits from the huge bandwidth in mmWave bands as well as the array and multiplexing gains from massive MIMO will lead to significant enhancement in user throughput, QoE and system capacity. Since EE is a critical KPI, the research community has been investigating different system architectures with a view to identifying the optimal model, not only in terms of the SE-EE performance, but also with respect to the hardware requirement, cost and implementation complexity [166–168].

In this chapter, we propose a novel generalized HBF framework for maintaining a balanced SE-EE trade-off in mmWave massive MIMO networks. We focus on the MU-MIMO set-ups employing different HBF architectures at the BSs (or TXs) and comparing their performance with the ABF and DBF schemes. In all cases, the UEs (or RXs) employ the ABF architecture. Performance of the proposed schemes are evaluated in 5G UDN and C-I2X application scenarios. First, we introduce the HBF schemes, followed by the performance metrics, and then the system models, performance evaluation results and discussions.

4.2 Hybrid Beamforming Schemes

For massive MIMO, three beamforming architectures (i.e., ABF, DBF and HBF) have been identified [169]. In the ABF implementation, all the AEs are connected to a single RF chain via a network of PSs. For DBF, each AE is connected to a dedicated RF chain. The HBF architecture uses a reduced number of RF chains. It divides its structure into two stages: the large-sized ABF stage for increasing array gain and the small-sized DBF stage for mitigating MUI [127,136,170]. Comparing the three architectures, HBF maintains a balanced performance between the ABF (with low SE, power consumption, cost and complexity) on the one hand and the DBF (with high SE, power consumption, cost and complexity) on the other. From the perspectives of SE, EE, cost and hardware complexity, HBF thus strikes a balanced performance trade-off when compared to the fully-analog and the fully-digital implementations. As a result, HBF has been copiously demonstrated as a practically-feasible array structure for massive MIMO [167]. It is thus the architecture of interest in this thesis[6].

Using the HBF architecture, it is possible to realize three different array structures, specifically the fully-connected, the sub-connected and the overlapped subarray structures. In this thesis, we present a novel generalized framework for the design and performance analysis of the HBF architectures. The different subarray configurations can be realized by varying the parameter known as the subarray spacing which leads to the corresponding changes in system performance. To proceed, we recall the mmWave massive MIMO channel model and the ULA antenna array responses that will be used throughout this chapter, where L is the number of rays or MPCs and all other parameters are as defined in Chapters 2 and 3.

$$PL_{\text{eff}} = 20\log_{10}\left(\frac{4\pi f_c}{c}\right) + 10\bar{n}\log_{10}\left(d_{3D}\right) + X(0,\sigma), \tag{4.1}$$

[6]It is worth noting that the development trends show that the cost and power consumption of the fully-digital transceiver can be reduced in the future, thereby making it the preferred choice for system implementation due to its superior flexibility and performance [53,133]. For example, the authors in [57] already report interesting results using testbeds based on the fully-digital architecture for mmWave massive MIMO.

$$h_{dir}(t,\phi) = \sum_{l=1}^{L} P_{RX,l} \cdot e^{j\varphi_l} \cdot \delta(t-\tau_l) \cdot G_{TX}(\phi - \phi_l^{TX}) \cdot G_{RX}(\phi - \phi_l^{RX}), \tag{4.2}$$

$$G_{TX/RX}(dB) = G_{AE}(dB) + 10\log_{10}(N_{sub}^{TX/RX}), \tag{4.3}$$

$$\mathbf{H} = \sqrt{\frac{N_{RX}N_{TX}}{L}} \cdot \sum_{l=1}^{L} \sqrt{PL_l(d)} \cdot e^{j2\pi\left(f_c\tau_l + \frac{v_{RX}\cos(\phi_l)}{\lambda}\triangle t\right)} \cdot \mathbf{a}_{RX}\left(\phi_l^{RX}\right)\mathbf{a}_{TX}^{H}\left(\phi_l^{TX}\right), \tag{4.4}$$

$$\mathbf{a}_{RX}\left(\phi_l^{RX}\right) = \frac{1}{\sqrt{N_{RX}}}\begin{pmatrix} e^{j\frac{2\pi}{\lambda}d_{RX}(n_r-1)\sin\left(\phi_l^{RX}\right)} \\ \end{pmatrix}, \qquad \forall n_r = 1,2,...,N_{RX}, \tag{4.5}$$

$$\mathbf{a}_{TX}\left(\phi_l^{TX}\right) = \frac{1}{\sqrt{N_{TX}}}\begin{pmatrix} e^{j\frac{2\pi}{\lambda}d_{TX}(n_t-1)\sin\left(\phi_l^{TX}\right)} \\ \end{pmatrix}, \qquad \forall n_t = 1,2,...,N_{TX}. \tag{4.6}$$

where in (4.3), G_{TX} and G_{RX} are calculated based on the antenna element gain (G_{AE}) and the number of AEs in the respective TX and RX subarrays ($N_{sub}^{TX/RX}$).

4.2.1 Fully-connected HBF architecture

The fully-connected HBF architecture is shown in Figure 4.1. In this structure, each RF chain is connected to all the AEs via a network of PSs [4]. The user signal is first digitally precoded by the baseband precoder ($\mathbf{F}_{BB}$), then processed by every RF chain, then fed to the analog beamformer ($\mathbf{F}_{RF}$) and thereafter transmitted using all AEs in the array [169]. By adjusting the phases of the transmitted signals on all antennas, a highly-directive signal can be achieved. Here, all the elements of $\mathbf{F}_{RF}$ have the same amplitude, thereby achieving the full beamforming gain [4, 168]. This structure is built at the cost of large number of PSs and combiners, where signal processing is carried out over the entire array in RF domain [166]. Thus, it consumes a high amount of energy for the excitation of the phased array network and compensation of the insertion losses of the PSs. It also has a high computational and hardware complexity [167].

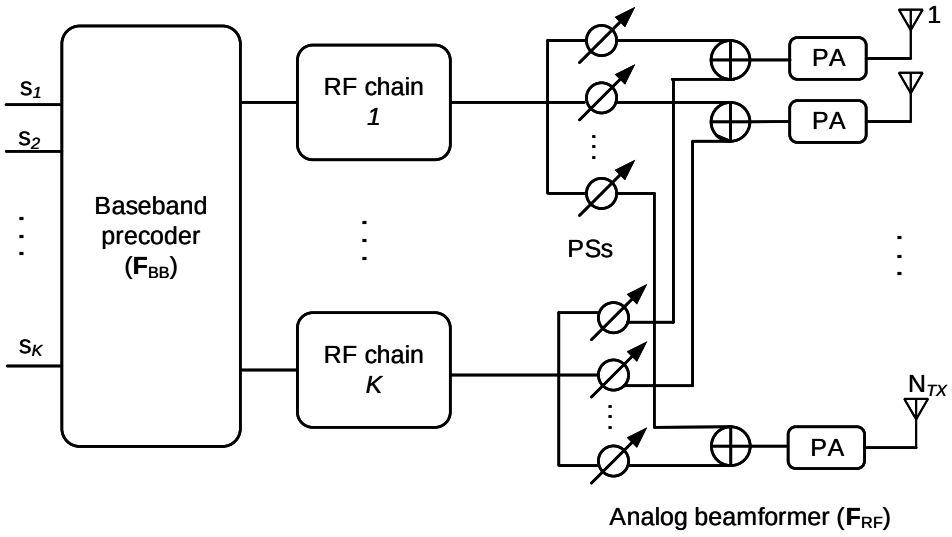

Figure 4.1: Fully-connected HBF architecture.

4.2.2 Sub-connected HBF architecture

The sub-connected HBF architecture is shown in Figure 4.2. In this configuration, each RF chain is only connected to a subarray via a network of PSs [4]. Each user's signal is first digitally precoded by $\mathbf{F}_{BB}$, then processed by a single dedicated RF chain, then fed to the $\mathbf{F}_{RF}$ and thereafter transmitted using only a set of AEs constituting a subarray [169]. For each RF chain, only the transmitted signals on a subarray can be adjusted. Thus, the beamforming gain and directivity is reduced by a factor equal to the number of subarrays. Additionally, $\mathbf{F}_{RF}$ is a block diagonal (BD) matrix in this case where all non-zero elements have the same fixed amplitude [4, 168]. This structure employs less number of PSs (as compared to the fully-connected structure) and does not use combiners as there is no need to add the analog signals [4]. Thus, it consumes less amount of energy for the excitation of the phased array network and compensation in terms of reduced insertion losses of the PSs. It also has a lower computational and hardware complexity when compared to the fully-connected structure [167].

4.2.3 Overlapped subarray HBF architecture

The overlapped subarray HBF architecture is shown in Figure 4.3. In this structure, each RF chain is connected to a subarray via a network of PSs, but the subarrays are allowed to overlap [168, 171]. Here, each RF chain is connected to antennas in more than one subarray. This configuration is different from the sub-connected structure where each RF chain is mapped to only antennas in a single subarray. It is also different from the fully-connected structure with each RF connected to all the antennas. Therefore, each user's signal is first digitally precoded by $\mathbf{F}_{BB}$, then processed by more than one RF chain, then fed to the $\mathbf{F}_{RF}$ and thereafter transmitted using only a set of AEs constituting the mapped subarrays. With this configuration, the hardware complexity and the required number of components are reduced compared to the fully-connected structure whilst maintaining system performance typically

in between the fully-connected and the sub-connected architectures [168]. It is noteworthy to mention that the overlapped structure offers a broad range of opportunities that can be explored as many configurations are realizable in the overlapped structure (i.e., all possibilities between the two extremes of the fully-connected and the sub-connected structures). The opportunities even become wider as the system's N_{TX} and N_{RF} increase.

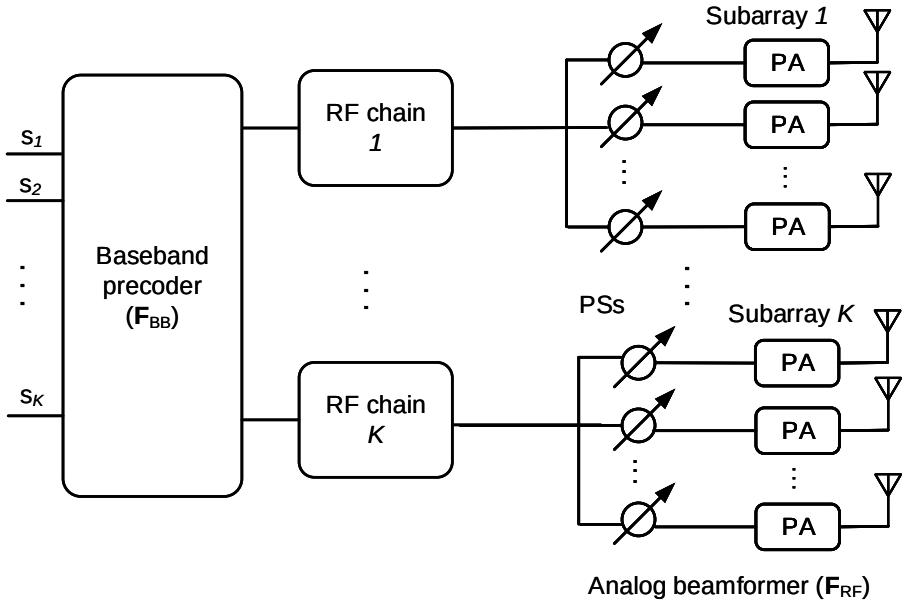

Figure 4.2: Sub-connected HBF architecture.

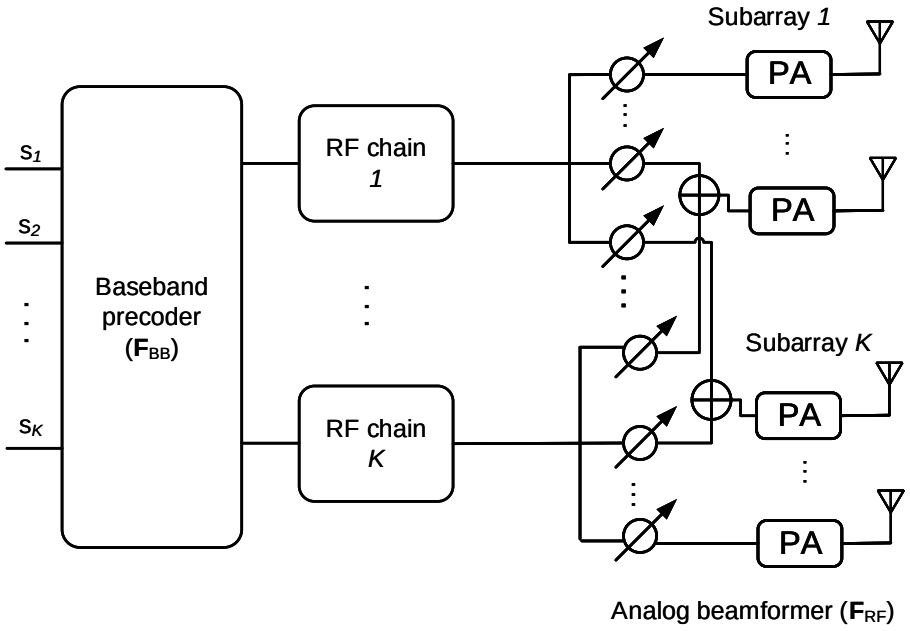

Figure 4.3: Overlapped subarray HBF architecture.

4.2.4 Proposed Generalized Framework for HBF architectures

With respect to the HBF architecture, three classes of structures can be realized depending on the interconnection among the RF chains, PSs and AEs (i.e., the RF-PS-AE mapping). The three structures that have been proposed are the: (i) fully-connected structure [167, 170], (ii) sub-connected structure [167, 169, 170], (also known as the partially-connected or array-of-subarrays [166]) and (iii) overlapped subarray structure [168, 171]. In addition, the fully-connected and the sub-connected array structures have received considerable attention in the literature [136, 166, 167]. However, the investigation of the overlapped subarray structure is rather limited [168, 171]. A parameter known as the subarray spacing ($\triangle M_s$) in [171] and ($\triangle N$) in [168] was introduced for the overlapped subarray structure such that varying its value leads to the different subarray configurations and the consequent changes in system performance. However, no generalized framework is available in the literature for a comprehensive comparative analysis of the different structures in a unified and systematic manner.

In this section, a novel generalized framework for the design and analysis of HBF antenna array structures is proposed. Beyond the state of the art, the proposed generalized model facilitates not only the SE analysis of the different HBF array structures but also the EE analysis. Using the generalized framework, it is possible to realize the three different HBF structures and quantify the required number of the different components for the architectures as well as the beam power allocation. The generalized HBF architecture is shown in the TX side[7] of Figure 4.4 (on next page) and the step-wise procedures for the design and analysis of the generalized framework are outlined as follows.

(i) Set the transmit power (P_T) for the BS, noting the appropriate regulation on the effective isotropic radiated power (EIRP) limits.

(ii) Set the number of AEs (N_{TX}) for the BS of the massive MIMO system under consideration.

(iii) Determine the number of RF chains (N_{RF}) based on the expected maximum multiplexing capability of the BS and such that $\frac{N_{TX}}{N_{RF}}$ is an integer. Note that for any HBF structure, $1 < N_{RF} < N_{TX}$.

(iv) Set the inter-subarray spacing ($\triangle N$) where $\triangle N \in \left\{0, 1, 2, \ldots, \frac{N_{TX}}{N_{RF}}\right\}$. For the generalized framework proposed in this work, note that $\triangle N$ is the critical parameter that determines the specific array structure, as given by (4.7).

$$\triangle N = \begin{cases} 0 & \rightarrow \text{fully-connected} \\ \left[1, 2, \ldots, \left(\frac{N_{TX}}{N_{RF}} - 1\right)\right] & \rightarrow \text{overlapped} \\ \frac{N_{TX}}{N_{RF}} & \rightarrow \text{sub-connected.} \end{cases} \tag{4.7}$$

[7]The receivers/UEs of the considered systems in this chapter employ ABF, leading to the (multi-beam) TX hybrid and RX analog (single stream per user) configuration. For the short-range C-I2X scenarios investigated, the RXs/UEs are assumed to exhibit LOS communication and spatial correlation and are power-constrained such that ABF becomes optimal for each UE.

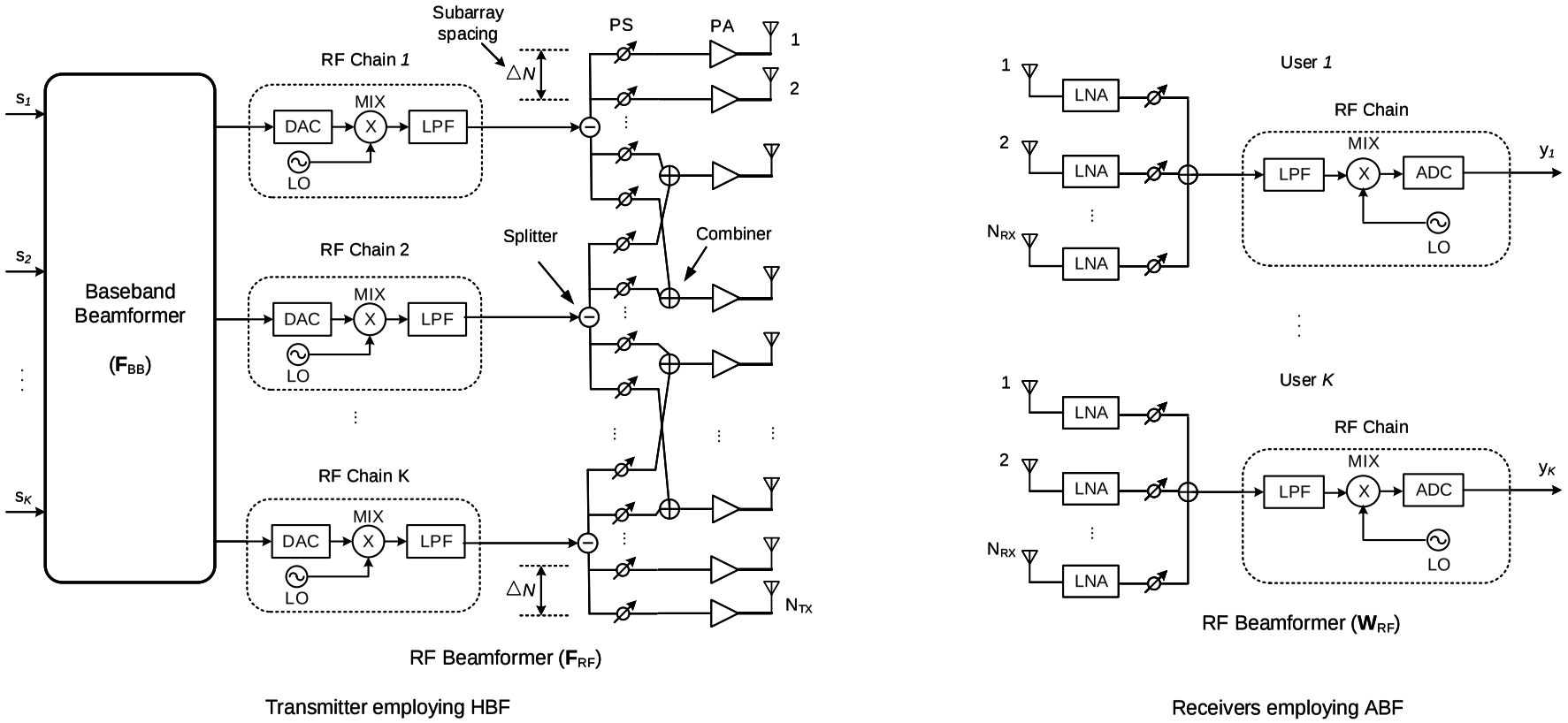

Figure 4.4: Generalized HBF architecture.

(v) Determine the required number of PSs for each RF chain $\left(N_{PS}^{k}, \quad \forall k \in \{1, 2, \ldots, N_{RF}\}\right)$ using (4.8). The total number of required PSs (N_{PS}) for a BS is then determined using (4.9).

$$N_{PS}^{k} = N_{TX} - \triangle N \left(N_{RF} - 1\right), \tag{4.8}$$

$$N_{PS} = \sum_{k=1}^{N_{RF}} N_{PS}^{k} = N_{RF} \times N_{PS}^{k}. \tag{4.9}$$

(vi) For each RF chain, develop the mapping index vector $\mathbf{m}_k$ using (4.10) where $\forall k \in \{1, 2, \ldots, N_{RF}\}$. The entries in $\mathbf{m}_k$ give the indices of the AEs connected to the k^{th} RF chain.

$$\mathbf{m}_k = [(k-1) \triangle N + 1, \ldots, N_{TX} - \triangle N \left(N_{RF} - k\right).] \tag{4.10}$$

Note that the number of AEs in a subarray $\left(N_{sub}^{TX}\right)$ equals the number of PSs connected to each RF chain, where $N_{sub}^{TX} = N_{PS}^{k} = |\mathbf{m}_k|$.

(vii) Develop the $N_{TX} \times N_{RF}$ mapping index matrix ($\mathbf{M}$) by stacking the $\mathbf{m}_k$'s. Elements of $\mathbf{M}$ are given by (4.11) and each element shows the connection index of the k^{th} RF chain to the j^{th} AE, $\forall k \in \{1, 2, \cdots, K\}$, $\forall j \in \{1, 2, \ldots, J\}$ by letting $K = N_{RF}$ and $J = N_{TX}$. We note that $\mathbf{M}$ becomes a block diagonal matrix (`blkdiag`) for the sub-connected array structure.

$$\mathbf{M} = \begin{bmatrix} m_{1,1} & \mathbf{0} & \cdots & \mathbf{0} \\ \vdots & m_{\triangle N+1,2} & \cdots & \mathbf{0} \\ m_{N_{sub},1} & \vdots & \cdots & m_{J-N_{sub}+1,K} \\ \mathbf{0} & m_{\triangle N+N_{sub},2} & \ddots & \vdots \\ \mathbf{0} & \mathbf{0} & \mathbf{0} & m_{J,K} \end{bmatrix}. \tag{4.11}$$

(viii) Develop the $N_{TX} \times N_{RF}$ (or $J \times K$) boolean/binary matrix $\mathbf{B}$ by replacing all nonzero elements of $\mathbf{M}$ in (4.11) with ones ($\mathbf{1's}$) as shown in (4.12).

$$\mathbf{B} = \begin{bmatrix} 1 & \mathbf{0} & \cdots & \mathbf{0} \\ \vdots & 1 & \cdots & \mathbf{0} \\ 1 & \vdots & \cdots & 1 \\ \mathbf{0} & 1 & \ddots & \vdots \\ \mathbf{0} & \mathbf{0} & \mathbf{0} & 1 \end{bmatrix}. \tag{4.12}$$

(ix) Develop the $N_{TX} \times 1$ combiner vector ($\mathbf{g}$), given by (4.13) indicating the number of RF chains connected to the j^{th} AE.

$$\mathbf{g} = \begin{bmatrix} g_1 \\ g_2 \\ \vdots \\ g_{N_{TX}} \end{bmatrix}, \qquad g_j = \sum_{k=1}^{N_{RF}} \mathbf{B}_{j,k}, \qquad \forall j \in \{1, 2, \ldots, N_{TX}\}. \tag{4.13}$$

(x) Determine the number of combiners (N_{comb}) needed for the specific array structure using (4.14). Note that AEs connected to just a single RF chain do not need combiners. As a result, the sub-connected structure has zero combiners as each AE is connected to a single RF chain while the fully-connected has the maximum number of combiners as every AE is connected to all RF chains.

$$N_{comb} = \left| [g_j > 1]_{j=1}^{N_{TX}} \right| = \begin{cases} N_{TX} & \rightarrow \text{fully-connected} \\ N_{TX} - 2 \triangle N & \rightarrow \text{overlapped} \\ 0 & \rightarrow \text{sub-connected.} \end{cases} \tag{4.14}$$

(xi) Determine the transmit beam power $\left(P_b^k\right)$ for each of the K beams using (4.15) where $(\cdot)$ is the weighting factor and g_j is evaluated using (4.13). The total transmit power constraint set in step (i) is enforced by (4.16).

$$P_b^k = \frac{P_T}{N_{TX}} \left(\sum_{j \in \mathbf{m}_k} (g_j)^{-1} \right), \tag{4.15}$$

$$P_T = \sum_{k=1}^{N_{RF}} P_b^k. \tag{4.16}$$

Based on the enumerated design procedures, the required number of components for the different subarray configurations can be determined depending on the choice of $\triangle N$. We remark that while the design procedures outlined above focus on the BS or AP, the generalized framework is equally applicable for the RXs or UEs by replacing the appropriate TX components with the corresponding RX components.

4.3 Precoding and Postcoding

Since HBF is considered at the TX, the AP uses a baseband precoder or beamformer $\mathbf{F}_{BB} \in \mathbb{C}^{K \times K}$ followed by an RF precoder $\mathbf{F}_{RF} \in \mathbb{C}^{N_{TX} \times N_{RF}^{TX}}$. The transmit symbol vector $\mathbf{s} \in \mathbb{C}^{K \times 1}$ and the sampled transmit signal vector $\mathbf{x} \in \mathbb{C}^{N_{TX} \times 1}$ in (4.17) are related by (4.18).

$$\mathbf{s} = [s_1, s_2, \cdots, s_K]^T, \qquad \mathbf{x} = [x_1, x_2, \cdots, x_{N_{TX}}]^T. \tag{4.17}$$

$$\mathbf{x} = \mathbf{F}_{RF}\mathbf{F}_{BB}\mathbf{s}. \tag{4.18}$$

Since ABF is considered at each of the users, each UE employs an RF postcoder[8] or equalizer $\mathbf{w}_{RF}^{k} \in \mathbb{C}^{N_{RX}\times 1}$. The received signal vector (after the precoding and postcoding operations) is $\mathbf{y} = [y_1, y_2, \cdots, y_K]^T$ where y_k for each user $\forall k \in \{1, 2, \cdots, K\}$ is given by (4.19) and $n = k$ is the desired signal while $n \neq k$ are interference terms for the k^{th} UE..

$$y_k = \mathbf{w}_k^H \mathbf{H}_k \sum_{n=1}^{K} \mathbf{F}_{RF}\mathbf{f}_n^{BB} s_n + \mathbf{w}_k^H n_k. \tag{4.19}$$

In (4.19), $\mathbf{H}_k \in \mathbb{C}^{N_{RX}^k \times N_{TX}}$ is the channel matrix between the AP and the k^{th} UE and n_k is the AWGN following a complex normal distribution $\mathcal{CN}(0, \sigma)$ with zero mean and σ standard deviation. The precoding and postcoding schemes considered in this thesis are described as follows.

4.3.1 Analog-only Beamsteering

In the analog-only beamsteering (AN-BST) scheme, the RF beamformer $\mathbf{f}_{RF}^{k} \in \mathbb{C}^{N_{TX}\times 1}$ at the BS/AP and the RF postcoder at the UE $\mathbf{w}_{RF}^{k} \in \mathbb{C}^{N_{RX}\times 1}, \forall k \in \{1, 2, \cdots, K\}$ are all implemented with analog PSs using (4.20) and (4.21), respectively.

$$\left[\mathbf{f}_k^{RF}\right] = \frac{1}{\sqrt{N_{TX}}} e^{j\phi_k} = \mathbf{a}_{TX}\left(\phi_l^{TX}\right), \tag{4.20}$$

$$\left[\mathbf{w}_k^{RF}\right] = \frac{1}{\sqrt{N_{RX}}} e^{j\phi_k} = \mathbf{a}_{RX}\left(\phi_l^{RX}\right), \tag{4.21}$$

where $\mathbf{F}_{RF} \in \mathbb{C}^{N_{TX}\times K}$ and $\mathbf{W}_{RF} \in \mathbb{C}^{N_{RX}\times K}$ are given by (4.22) and (4.23), respectively. The elements of both matrices ($\mathbf{F}_{RF}$ and $\mathbf{W}_{RF}$) are constrained to have constant magnitude, though with variable phases. As given by (4.20) and (4.21), the beamsteering codebooks $\mathbf{F}_{RF}$ and $\mathbf{W}_{RF}$ are parameterized by the TX and RX array response vectors $\mathbf{a}_{TX}\left(\phi_l^{TX}\right)$ and $\mathbf{a}_{RX}\left(\phi_l^{RX}\right)$, respectively. The beamsteering codebooks are particularly suitable for sparse and single-path channels (i.e., mmWave and THz channels) [125, 166], as opposed to the Grassmanian codebooks which are usually designed for the rich channels of traditional MIMO systems [136, 172].

$$\mathbf{F}_{RF} = \left[\mathbf{f}_1^{RF}, \mathbf{f}_2^{RF}, \ldots, \mathbf{f}_K^{RF}\right], \tag{4.22}$$

$$\mathbf{W}_{RF} = \left[\mathbf{w}_1^{RF}, \mathbf{w}_2^{RF}, \ldots, \mathbf{w}_K^{RF}\right]. \tag{4.23}$$

[8]Recall that we use beamforming and precoding interchangeably. Also, we use postcoding to mean combining or equalization at the UEs. However, the use of term "combiner" was avoided in order to avoid confusion with the combiner used for adding the phase-shifted signals at the TX.

4.3.2 Hybrid Precoding with Baseband Zero Forcing

The analog stage of the hybrid precoding with baseband zero forcing (HYB-ZF) scheme employs $\mathbf{F}_{RF}$ and $\mathbf{W}_{RF}$ as in (4.22) and (4.23), respectively. The digital stage then employs the popular zero forcing (ZF) precoder $\mathbf{F}_{BB} \in \mathbb{C}^{K \times K}$ given by (4.24) and (4.25) to mitigate MUI.

$$\mathbf{F}_{BB} = \left[\mathbf{f}_1^{BB}, \mathbf{f}_2^{BB}, \cdots, \mathbf{f}_K^{BB}\right], \tag{4.24}$$

$$\mathbf{F}_{BB} = \mathbf{H}_{\text{eff}}^H \left(\mathbf{H}_{\text{eff}} \mathbf{H}_{\text{eff}}^H\right)^{-1}, \tag{4.25}$$

where $\mathbf{H}_{\text{eff}} = \mathbf{w}_k^H \mathbf{H}_k \mathbf{F}_{RF}$ is the effective channel after applying the RF beamformer and combiner to the channel. The total transmit power (P_T) constraint is enforced by normalizing $\mathbf{F}_{BB}$ according to (4.26) and (4.27). The two-stage hybrid precoding algorithm is given in Algorithm 2.

$$\mathbf{f}_k^{BB} = \frac{\mathbf{f}_k^{BB}}{||\mathbf{F}_{RF}\mathbf{F}_{BB}||_F}, \quad \forall k = \{1, 2, \ldots, K\}, \tag{4.26}$$

$$||\mathbf{F}_{RF}\mathbf{F}_{BB}||_F^2 = K. \tag{4.27}$$

4.3.3 Singular Value Decomposition Precoding

For the singular value decomposition precoding as upper bound (SVD-UB), precoding and combining employ the unitary matrices ($\mathbf{F}_k$ and $\mathbf{W}_k^H$, respectively) resulting from the SVD of $\mathbf{H}_k \in \mathbb{C}^{N_{RX}^k \times N_{TX}}$, $\forall k \in \{1, 2, \ldots, K\}$ - the channel matrix between the AP and the k^{th} UE, according to (4.28).

$$[\mathbf{W}_k, \mathbf{\Sigma}_k, \mathbf{F}_k] = \texttt{svd}(\mathbf{H}_k), \tag{4.28}$$

where $\mathbf{H}_k = \mathbf{W}_k \mathbf{\Sigma}_k \mathbf{F}_k^H$ and $\mathbf{\Sigma}_k$ represents the diagonal matrix for the channel's singular values. SVD-UB uses Σ_k^{max} value for calculating the single-user rate which denotes the upper bound. It also represents the case with no MUI.

Algorithm 2: Two-Stage Multi-User Hybrid Beamforming with Baseband Zero Forcing

Inputs :

$\mathbf{H}_k,\ \mathbf{a}_{RX}^k,\ \mathbf{a}_{TX}^k \qquad \forall k \in \{1, 2, \ldots, K\} \qquad \leftarrow$ (4.4)-(4.6)

Outputs:

$\mathbf{F}_{BB},\ \mathbf{F}_{RF},\ \mathbf{W}_{RF}$

First Stage: Analog Beamforming

for $k \rightarrow 1$ **to** K **do**

- Set the RF beamformers $\mathbf{f}_{RF}^k$ and $\mathbf{w}_{RF}^k$ to the beamsteering codebooks or array steering vectors $\mathbf{a}_{TX}^k$ and $\mathbf{a}_{RX}^k$, respectively.

$$\mathbf{f}_k^{RF} = \mathbf{a}_{TX}^k,$$

$$\mathbf{w}_k^{RF} = \mathbf{a}_{RX}^k.$$

- Set $\mathbf{F}_{RF} = \left[\mathbf{f}_1^{RF}, \mathbf{f}_2^{RF}, \ldots, \mathbf{f}_K^{RF}\right]$ and $\mathbf{W}_{RF} = \left[\mathbf{w}_1^{RF}, \mathbf{w}_2^{RF}, \ldots, \mathbf{w}_K^{RF}\right]$, according to (4.22) and (4.23), respectively.

Second Stage: Digital Beamforming

for $k \rightarrow 1$ **to** K **do**

- Estimate the effective channel

$$\mathbf{H}_{\text{eff}}^k = \mathbf{w}_k^H \mathbf{H}_k \mathbf{F}_{RF}.$$

- The linear baseband zero forcing precoder $\mathbf{F}_{BB} = \left[\mathbf{f}_1^{BB}, \mathbf{f}_2^{BB}, \cdots, \mathbf{f}_K^{BB}\right]$ is designed using (4.25)
- The total power constraint is enforced using the $\mathbf{f}_k^{BB}$ normalizations in (4.26), $\forall k \in \{1, 2, \ldots, K\}$

4.4 Power Consumption Model

The power consumption model of the generalized HBF array structure in Figure 4.1 is given in this subsection. We model a realistic power consumption framework considering not only the power consumption at the RAN (P_{RAN}), but also the backhaul power consumption (P_{BH}). The total consumed power (P_{total}) is thus given by (4.29). The components of P_{RAN} and P_{BH} are further described as follows.

$$P_{total} = P_{RAN} + P_{BH}. \tag{4.29}$$

(i) RAN Power (P_{RAN}): For the coverage of a single BS, the P_{RAN}, given by (4.30), consists of the transmit power of the BS (P_T), the circuit power of the BS (P_{cct}^{TX}) and the combined RX circuit powers (P_{cct}^{RX}) of all the N_{UE} users served by the BS. Different from most existing studies such as [37, 166, 167], we include the power consumed by the RXs in the model.

$$P_{RAN} = P_T + P_{cct}^{TX} + N_{UE}\left(P_{cct}^{RX}\right). \tag{4.30}$$

(ii) Backhaul Power (P_{BH}): This involves the power consumed for the communication between the BS and the core network. It is given by (4.31) and it is dependent on the data rate (R) or the amount of data transferred per unit time ($bits/s$).

$$P_{BH} = L_{BH} \cdot R. \tag{4.31}$$

In (4.31), $L_{BH} = 250$ mW/(Gbits/s) [173] is the power per unit data rate while the P_{RFC}^{TX} and P_{RFC}^{RX} are given by (4.32) and (4.33), respectively [166]. The P_{cct}^{TX}, P_{cct}^{RX} and P_{total} are correspondingly given by (4.34)-(4.36). The breakdown of the values of the different components are given in Table 4.1. We assume a fixed miscellaneous power $P_{FIX} = 1$ W (noting that SC BSs or APs do not have any active cooling system [174]).

Table 4.1: Power consumption of components

TX Component	**Notation**	**Unit power [mW]**	**RX Component**	**Notation**	**Unit Power [mW]**
Digital to Analog Converter	P_{DAC} [175]	110	Analog to Digital Converter	P_{ADC} [175]	200
Mixer	P_{MIX} [166]	23	Mixer	P_{MIX} [166]	23
Local Oscillator	P_{LO} [166]	5	Local Oscillator	P_{LO} [166]	5
Low Pass Filter	P_{LPF} [166]	15	Low Pass Filter	P_{LPF} [166]	15
Phase Shifter	P_{PS} [175]	30	Phase Shifter	P_{PS} [175]	30
Power Amplifier	P_{PA} [175]	16	Low Noise Amplifier	P_{LNA} [175]	30
Baseband precoder	P_{BB} [175]	243	-	-	-
Combiner	P_{comb} [173]	19.5	-	-	-

$$P_{RFC}^{TX} = P_{DAC} + P_{MIX} + P_{LO} + P_{LPF}, \tag{4.32}$$

$$P_{RFC}^{RX} = P_{ADC} + P_{MIX} + P_{LO} + P_{LPF}, \tag{4.33}$$

$$P_{cct}^{TX} = N_{RF}^{TX} P_{RFC}^{TX} + N_{RF}^{TX} N_{sub}^{TX} P_{PS}^{TX} + N_{TX} P_{PA} + N_{comb}^{TX} P_{comb}^{TX} + P_{BB}^{TX} + P_{FIX}, \tag{4.34}$$

$$P_{cct}^{RX} = N_{RF}^{RX} P_{RFC}^{RX} + N_{RF}^{RX} N_{sub}^{RX} P_{PS}^{RX} + N_{RX} P_{LNA}, \tag{4.35}$$

$$\begin{aligned} P_{total} =& P_T + \left[N_{RF}^{TX} P_{RFC}^{TX} + N_{RF}^{TX} N_{sub}^{TX} P_{PS}^{TX} + N_{TX} P_{PA} + N_{comb}^{TX} P_{comb}^{TX} + P_{BB}^{TX} + P_{FIX}\right] \\ & N_{UE} \left[N_{RF}^{RX} P_{RFC}^{RX} + N_{RF}^{RX} N_{sub}^{RX} P_{PS}^{RX} + N_{RX} P_{LNA}\right] + L_{BH} \cdot R. \end{aligned} \tag{4.36}$$

4.5 Spectral and Energy Efficiency

Following the given generalized HBF antenna structure and the channel, beamforming and power consumption models, we give the expressions for the performance of the system in this section, in terms of the achievable sum data rate (R), spectral efficiency (η_{SE}) and energy efficiency (η_{EE}). The main objective is to efficiently design $\mathbf{F}_{RF}$, $\mathbf{F}_{BB}$ and $\mathbf{W}_{RF}$ to maximize the system performance.

4.5.1 Spectral Efficiency and Achievable Rate

Given the received signal y_k in (4.19), the η_{SE}^k [(bits/s)/Hz], R_k (bits/s) of the k^{th} user and R for sum data rate of all users are given by (4.37)-(4.39), where B_k is the bandwidth allocated to the k^{th} user and the SINR for the respective precoding techniques are given in (4.40)-(4.42), $\forall k = \{1, 2, \ldots, K\}$.

$$\eta_{SE}^k = \log_2 \left(1 + SINR_k\right), \tag{4.37}$$

$$R_k = B_k \times \eta_{SE}^k, \tag{4.38}$$

$$R = \sum_{k=1}^{K} R_k, \tag{4.39}$$

$$SINR_k^{AN-BST} = \frac{P_T^k \cdot \left|\mathbf{w}_k^H \mathbf{H}_k \mathbf{f}_k^{RF}\right|^2}{\sum_{n \neq k} P_T^n \cdot \left|\mathbf{w}_k^H \mathbf{H}_k \mathbf{f}_n^{RF}\right|^2 + \sigma_k^2}, \tag{4.40}$$

$$SINR_k^{HYB-ZF} = \frac{P_T^k \cdot \left|\mathbf{w}_k^H \mathbf{H}_k \mathbf{F}_{RF} \mathbf{f}_k^{BB}\right|^2}{\sum_{n \neq k} P_T^n \cdot \left|\mathbf{w}_k^H \mathbf{H}_k \mathbf{F}_{RF} \mathbf{f}_n^{BB}\right|^2 + \sigma_k^2}, \tag{4.41}$$

$$SINR_k^{SVD-UB} = P_T^k \cdot |\Sigma_k^{max}|^2. \tag{4.42}$$

4.5.2 Energy Efficiency

The EE (bits/J) of the system is the ratio of the system throughput or sum data rate R (given by (4.39)) to the total power consumption P_{total} (expressed as (4.36).

$$\eta_{EE} = \frac{sum\ rate}{total\ power\ consumed} = \frac{R}{P_{total}}. \tag{4.43}$$

The optimal EE as a function of the SE, $\eta^*_{EE}(\eta_{SE})$ is given according to the fundamental EE-SE relation [176] by (4.44).

$$\left|\frac{d\eta^*_{EE}(\eta_{SE})}{d\eta_{SE}}\right|_{\eta_{SE}=\frac{R}{BW}} = 0, \tag{4.44}$$

where $\eta^*_{EE}(\eta_{SE}) = \max\left(\eta_{EE}(\eta_{SE})\right)$ is strictly quasiconcave in η_{SE} when P_{total} includes both the transmit power P_T and the circuit power P_{cct} [176, 177].

4.6 Hybrid Beamforming for C-I2X

The performance analyses of the HBF structures have been investigated for diverse scenarios. The authors in [125, 167, 178] considered single-cell, single-user, multi-stream communication while the authors in [136, 171] analyzed for the single-cell, multi-user, multi-stream system. In [138], the HBF evaluation was extended to the multi-cell, multi-user, multi-stream scenario. However, these evaluations consider the typical cellular deployments with ISD $\geq$ 500 m for the μWave setups and 50-200 m for the mmWave scenarios. Extension to the short-range domain using street-level lampost-mount APs with ISDs $\leq$ 10 m, particularly for outdoor applications, is still missing. Using the generalized HBF framework, we evaluate the performance of different HBF configurations using a C-I2X application scenario involving both cellular and vehicular users. We employ a realistic power consumption model to assess the performance of the respective systems not only in terms of the SE and EE, but also the power and hardware cost for the network. Different from most existing works, our comprehensive power consumption model includes the TX power, the TX circuit power, RX circuit power as well as the backhaul power as given in Section 4.4.

4.6.1 System Model and Parameters

We consider the network deployment layout for C-I2X already introduced in Figure 1.6. We focus on the single-cell, multi-user DL scenario where a massive MIMO AP communicates N_{UE} user devices (i. e., the sum of cellular and vehicular users being scheduled in each TTI). We consider an urban street deployment where the APs are mounted on street lamposts along a road 500 m long. The APs are evenly spaced at 10 m interval and are mounted at a height $h_{TX} = 5$ m on the walkway lamposts. All UEs are at a height of $h_{RX} = 1.5$ m. Each cellular user (cUE) traverses the route at a pedestrian speed of $v^c_{RX} = 3.6$ km/h while each vehicular user (vUE) moves at $v^v_{RX} = 36$ km/h, respectively. The width (w) of the walkway for cUEs is 2 m while the vUEs are at a further 3 m from the walkway. At each time instant, the I2X DL connectivity is by LOS as the 3D separation distance between each user and its serving AP gives a LOS probability $P_{LOS} \approx 1$, according to (3.21) [101]. We consider the channel model earlier given by (4.1)-(4.6). Given that G_{AE} is the gain of an AE and N^{TX}_{sub} and N^{RX}_{sub} are the number of TX and RX AEs in a subarray, respectively, G_{TX} and G_{RX} are given by (4.45) and (4.46), respectively [179].

$$G_{TX}(dB) = G_{AE}(dB) + 10\log_{10}(N^{TX}_{sub}), \tag{4.45}$$

$$G_{RX}(dB) = G_{AE}(dB) + 10\log_{10}(N^{RX}_{sub}). \tag{4.46}$$

Using the generalized structure introduced in Section 4.2.4, a table such as Table 4.2 can be populated with the appropriate entries based on the values set and determined using (4.7)-(4.16). In Table 4.2, we give the values of the required number of components for the sample scenario considered in this work where the AP is equipped with $N_{TX} = 64$, $N_{RF}^{TX} = 8$ and $\triangle N = \{0, 2, 4, 6, 8\}$. The AP employs the generalized HBF structure as shown in Figure 4.4. This leads to the fully-connected structure when $\triangle N = 0$ and leads to the sub-connected structure when $\triangle N = N_{TX}/N_{RF} = 8$ while $\triangle N = \{2, 4, 6\}$ represent the overlapped subarray structure.

For the UEs, we consider $N_{RX} = 8$, $N_{RF}^{RX} = 1$ and $\triangle N = 0$ for all the $K = 8$ users. This corresponds to a fully-connected structure for the single stream per user ABF configuration at the UEs. The numbers of the respective required components for each UE are also given in Table 4.2. Thus, we focus on the multi-user beamforming case with a single stream per user. Therefore, the total number of streams is $N_s = N_{UE} = N_{RF}^{TX} = 8$.

Table 4.2: HBF array structure components

TX	$\triangle N = 0$	$\triangle N = 2$	$\triangle N = 4$	$\triangle N = 6$	$\triangle N = 8$	**RX**	$\triangle N = 0$
N_{TX}	64	64	64	64	64	N_{RX}	8
N_{PA}	64	64	64	64	64	N_{LNA}	8
N_{RF}	8	8	8	8	8	N_{RF}	1
N_{sub}	64	50	36	22	8	N_{sub}	8
N_{PS}	512	400	288	176	64	N_{PS}	8
N_{comb}	64	60	56	52	0	N_{comb}	0

Different from most works in the literature where $P_T^k = P_T/K$, we note that this is simply not the case for P_T^k for the generalized framework explored in this work, particularly for the overlapped subarray structure as already given in (4.15). In the literature where the fully-connected or sub-connected subarray structures are typically employed, it is easy to assume the uniform power allocation. In such settings, each AE is connected to either all the RF chains (as in the fully-connected case) or to one RF chain only (for the sub-connected subarray configuration). However, for the overlapped subarray structure, each of the AEs is connected to different amount of RF chains depending on the configuration (based on $\triangle N$). Hence, the beam power is dependent on the RF chain-AE mapping.

Table 4.3: Power allocation for the array structures.

Beam	$\triangle N = 0$	$\triangle N = 2$	$\triangle N = 4$	$\triangle N = 6$	$\triangle N = 8$
1	1	1.2107	1.4214	1.5000	1
2	1	0.9964	0.9928	0.9583	1
3	1	0.9130	0.8261	0.7917	1
4	1	0.8797	0.7595	0.7500	1
5	1	0.8797	0.7595	0.7500	1
6	1	0.9130	0.8261	0.7916	1
7	1	0.9964	0.9928	0.9583	1
8	1	1.2107	1.4214	1.5000	1
P_T (W)	8	8	8	8	8

To illustrate (4.15), for the configurations considered in this work where the AP/BS is equipped with $N_{TX} = 64$, $N_{RF}^{TX} = 8$, $\triangle N = \{0, 2, 4, 6, 8\}$, $K = 8$ and $P_T = 8$ W, the beam

power to each of the 8 users for the different values of $\triangle N$ are given in Table 4.3. In each case, the total power constraint is enforced. As evident from the Table 4.3, the fully-connected ($\triangle N = 0$) and the sub-connected ($\triangle N = 8$) structures have equal power allocation while the overlapped structures have unequal power allocation.

4.6.2 Simulation Results

In this section, simulation results are provided to illustrate the system performance in terms of η_{SE}, η_{EE} and hardware cost, and to compare the performance of the different sub-array configurations. Further to the given deployment parameters, the other key simulation parameters are further given in Table 4.4. In each run or channel realization, users are randomly deployed for the first TTI. Thereafter, each UE follows its mobility course (with respect to speed and direction) throughout subsequent TTIs. The results are averaged over the simulations runs and TTIs.

Table 4.4: Simulation parameters for C-I2X scenario.

Parameter	**Description**	**Value**
f_c	Carrier frequency	100 GHz
B	Bandwidth	2 GHz
$X(\mu, \sigma)$	Shadow fading	(0, 7) dB
N_o	Noise power spectral density	-174 dBm/Hz
NF	Noise figure	6 dB
P_T	Transmit power	$[0.1, \cdots, 8]$ W
G_{AE}	Antenna element gain	8 dBi
$G_{TX,max}$	Maximum transmit gain	26 dBi
$G_{RX,max}$	Maximum receive gain	17 dBi
$nRuns$	Number of channel realizations	1000

(a) Power and Hardware Costs

First, we provide a comparative performance analysis of the structures with respect to the hardware requirement and power consumption. In Table 4.2, we provided a breakdown of the hardware components needed to realize each of the structures for the case where $N_{TX} = 64, N_{RF}^{TX} = 8$ for the AP and $N_{RX} = 8, N_{RF}^{RX} = 1$ for each of the $K = 8$ UEs. For the phased array network, the number of required PSs (N_{PS}) changes significantly with the specific structure. In Figure 4.5, we show how N_{PS} varies with the N_{RF} for a fixed N_{TX}.

With a $P_{PS} = 30$ mW per unit PS, the overlapped subarray structures offer a window of opportunity between the fully-connected and the sub-connected structures at the two extreme ends, in terms of power consumption. The case is similar with respect to the number of combiners N_{comb} required for each of the structures. However, the contribution of the PSs to the P_{total} is far greater than that of the combiners, both in terms of the number required as well as the unit component power cost as can be seen in Tables 4.1 and 4.2, respectively.

With respect to the overall power consumption of the network, Figure 4.6 shows the P_{total} for the different structures as well as the proportions of the contributing components (i.e., the consumed power at the TX (P_{TX}), the consumed power at all RX (P_{RXs}) and the power consumed for backhauling (P_{BH}) when $P_T = 1$ W. Note that $P_{total} = P_{TX} + P_{RXs} + P_{BH}$, where P_T is included in P_{TX}.

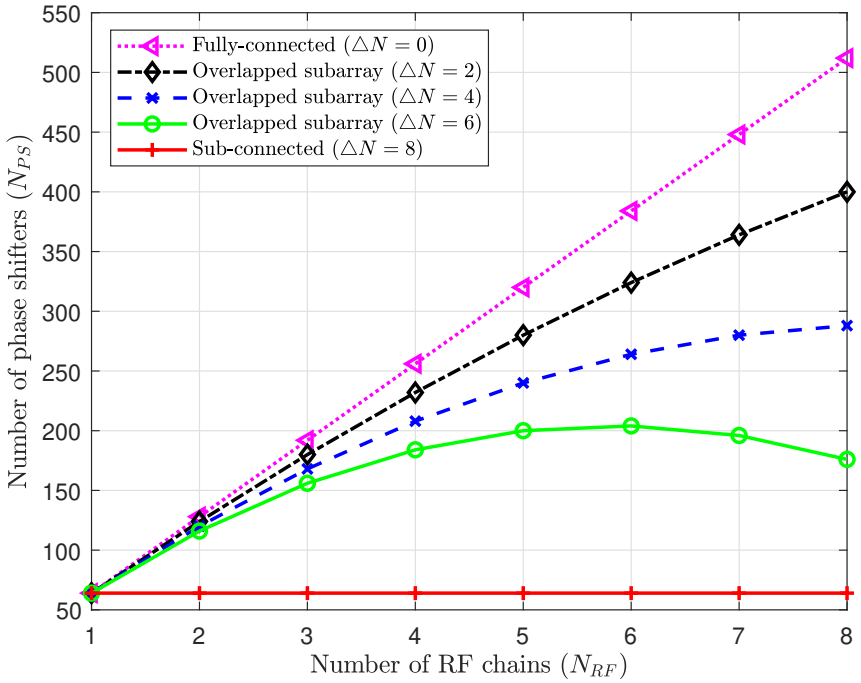

Figure 4.5: Number of PSs required for different structures ($N_{TX} = 64$).

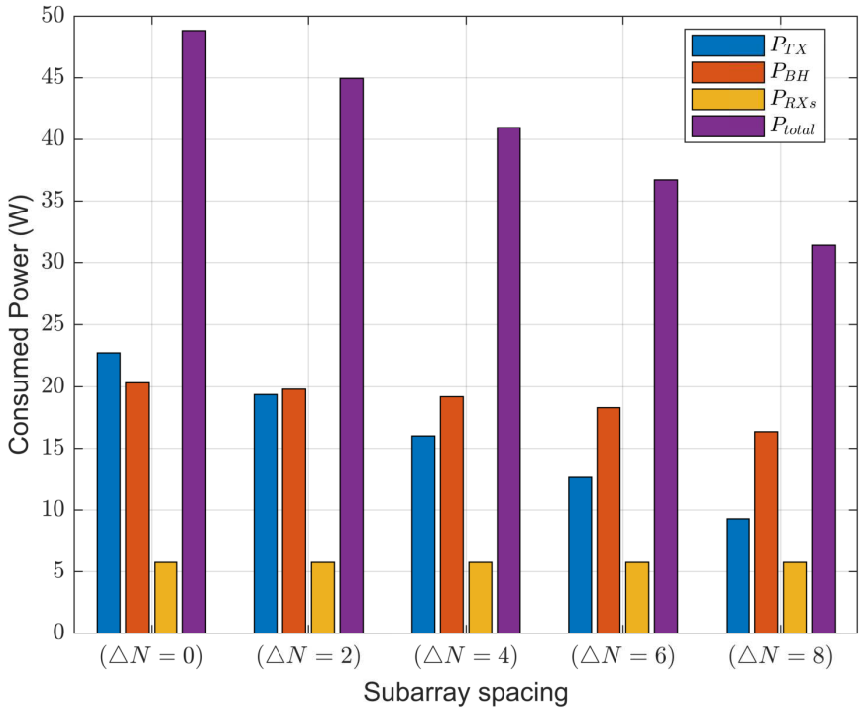

Figure 4.6: Power consumption of components for different $\triangle N$ ($P_T = 1$ W).

From Figure 4.6, it can be seen that P_{total} decreases as we move from the fully-connected ($\triangle N = 0$), through the overlapped subarray, to the sub-connected structure ($\triangle N = 8$).

Similarly, as we move from $\triangle N = 0$ to $\triangle N = 8$, the contribution of P_{TX} and P_{BH} reduces, with P_{TX} reducing at a faster rate than P_{BH}. Except for the fully-connected structure, $P_{BH} > P_{TX}$ for all structures. As noted in [174], the computation and backhaul power consumption will constitute the largest of the total power consumption of future networks. For all cases, the P_{RXs} maintain steady values, constituting roughly 10% and 15% of P_{total} for the fully-connected and sub-connected structures, respectively.

(b) Spectral and Energy Efficiency

The sum SE and the EE performance for different transmit powers (P_T) for all the considered structures are shown in Figures 4.7 and 4.8, respectively. For all the subarray structures in Figure 4.7, the SE increases logarithmically as P_T increases. The trend for the EE is however different. As shown in Figure 4.8, the EE first increases, peaks (at the optimal value) and then decreases as P_T increases. The optimal EE point is critical for the design of energy-efficient networks, as the increase in P_T beyond the optimal value leads to performance degradation of the system with respect to the EE, though the SE continues to increase.

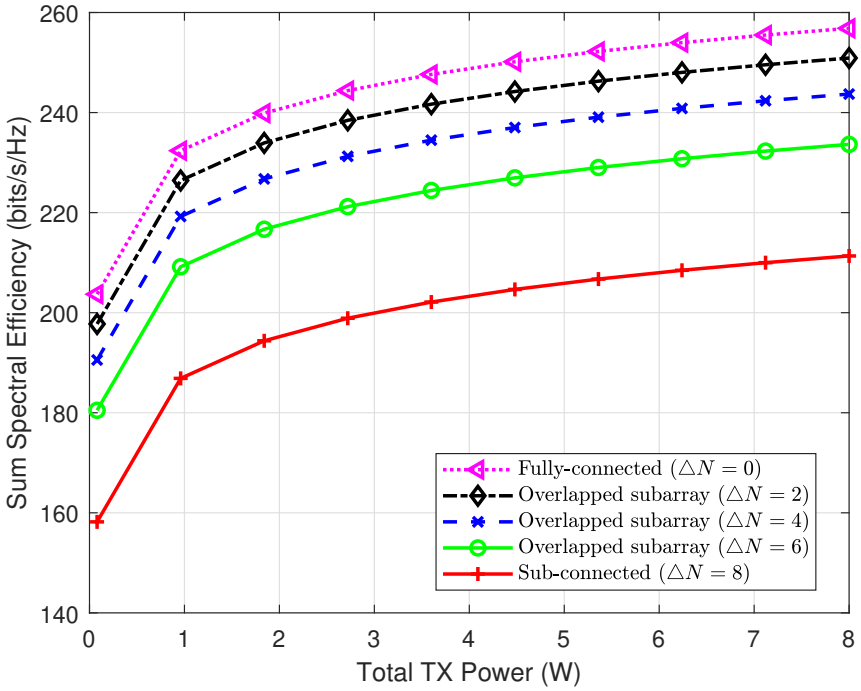

Figure 4.7: Sum Spectral efficiency versus total transmit power.

Figure 4.9 shows the EE-SE performance trade-off curves for the different subarray structures. For each structure, the EE starts to increase as the SE increases. It then reaches the optimal point (given by (4.46)) and thereafter continues to decrease as SE increases. Each curve follows a quasi-concave (bell-shaped) trend, which is consistent with the results in [166, 176, 177]. Further, it can be observed that each of the structures has different performance. The fully-connected structure has the highest SE and lowest EE on one end, while the sub-connected structure has the lowest SE and highest EE on the other end. In between these two ends, the different overlapped subarray structures show varying performance depending

on $\triangle N$. For example, the overlapped structure with $\triangle N = 4$ strikes a good balance in EE-SE performance for the considered scenario.

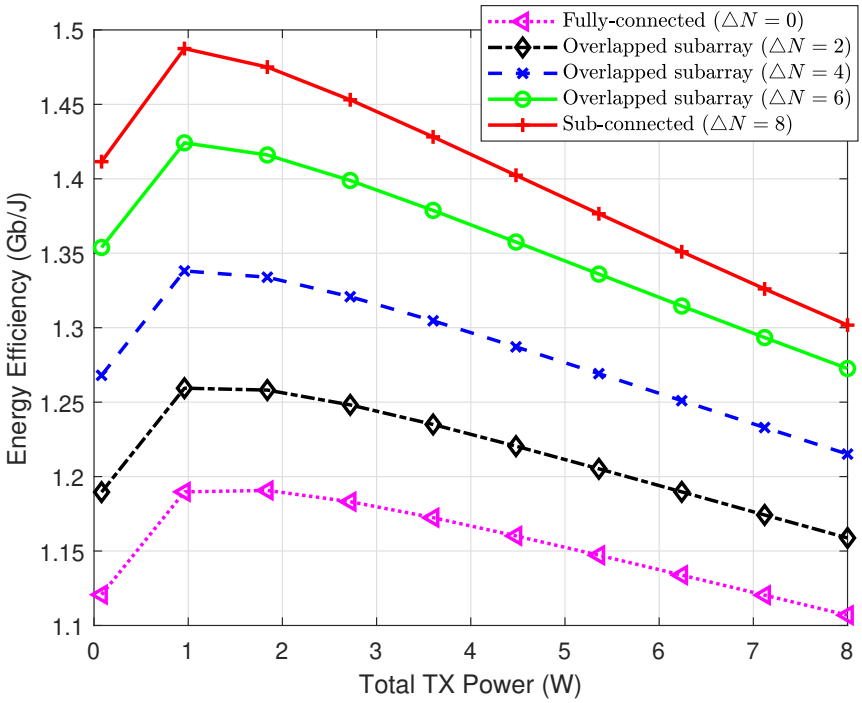

Figure 4.8: Energy efficiency versus total transmit power.

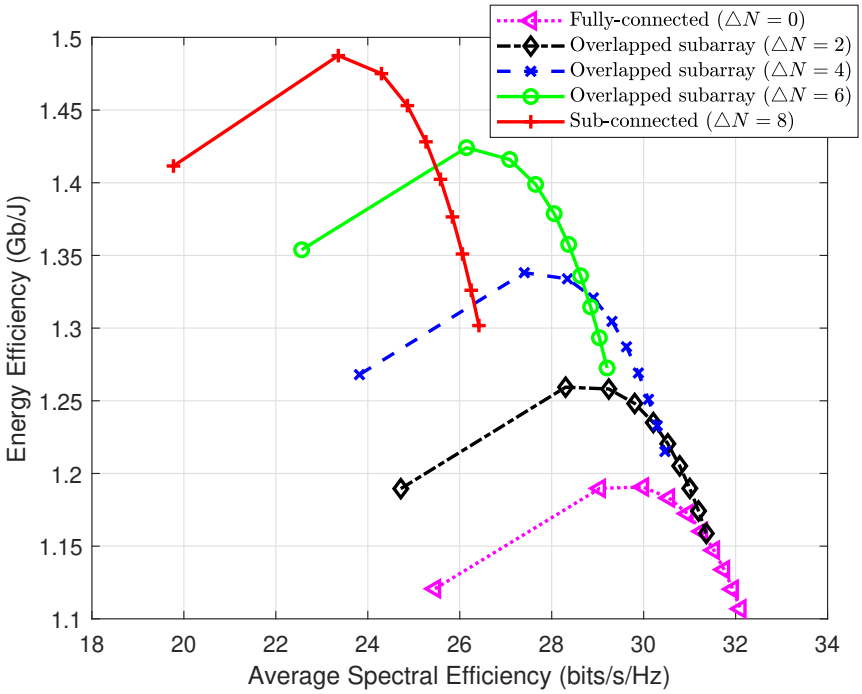

Figure 4.9: Energy efficiency versus spectral efficiency.

(c) User Performance

In Figure 4.10, we show the SE performance for all the users as the P_T increases. Similarly, the EE performance for all users with increasing P_T is shown in Figure 4.11. We show the results for only the overlapped subarray case with $\triangle N = 4$, which was previously shown as the structure having a balanced performance trade-off with respect to SE and EE.

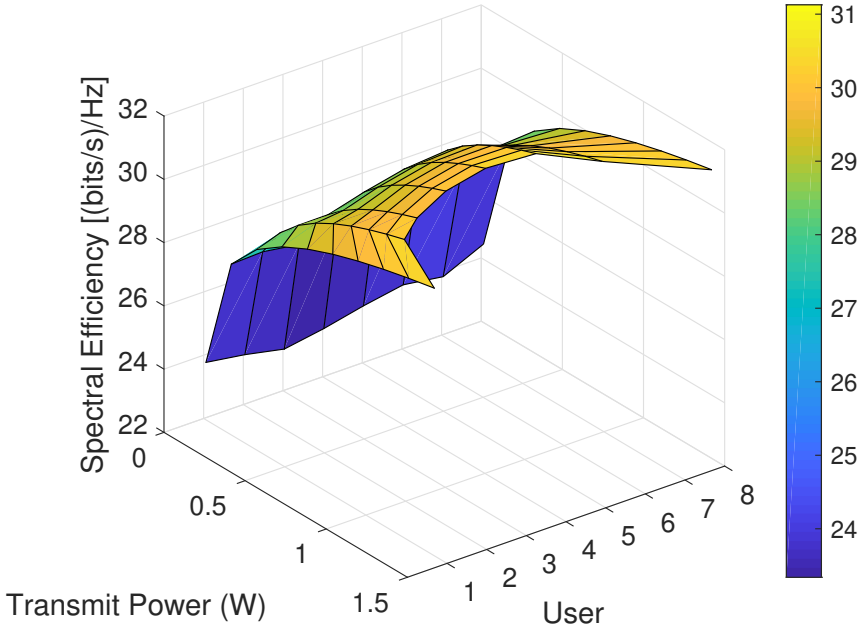

Figure 4.10: Spectral efficiency vs transmit power for each user ($\triangle N = 4$).

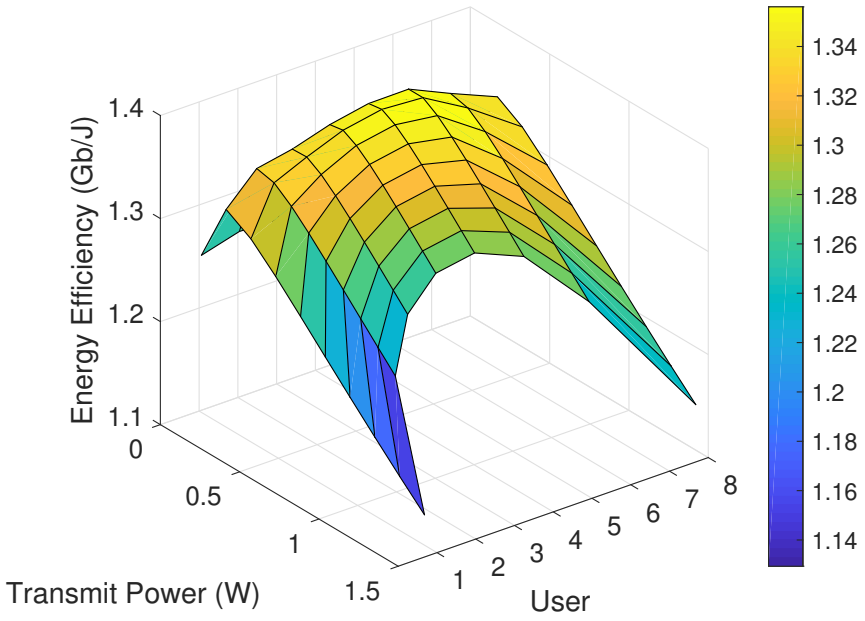

Figure 4.11: Energy efficiency vs transmit power for each user ($\triangle N = 4$).

In Figures 4.10 and 4.11, it can be seen that the performance of each of the users are very close in values at each P_T point, thus guaranteeing a level of fairness among users. As typical, Figure 4.10 follows the logarithmically-increasing trend in SE as P_T increases for each of the users. Similarly, the curves in Figure 4.11 follows the quasi-concave trend in EE as the P_T increases for each of the users. In addition, with equal bandwidth allocation per user, $R_k = \eta_{SE}^k \times (B/K)$. Therefore, each user is able to reach a data rate of more than 5 Gbps with a minimum SE of 20 bits/s/Hz in a 2 GHz bandwidth for 8 users.

4.7 Hybrid Beamforming for C-I2P

While the analysis in Section 4.6 involves both cellular and vehicular users (C-I2X), this section provides discussion on the C-I2P scenario. Among several use cases, the authors in [151] proposed that mmWave/THz APs mounted on street lamposts can be used to provide ultra-broadband connectivity to low-mobility (pedestrian) users along street walkways and similar hotspots. The proximity of users to these APs and the abundant bandwidth at mmWave and THz frequencies make the setup a viable candidate to offload traffic from the BSs in B5G networks. Unlike in the C-I2X scenario where the focal point was on the performance of the different HBF configurations, in C-I2P we direct the attention towards the performance of the different precoder designs (i.e., AN-BST, HYB-ZF and SVD-UB) as highlighted in Section 4.3.

4.7.1 System Model and Parameters

The deployment layout for the massive MIMO network is shown in Figure 4.12. For the walkway scenario, we focus on the DL where the evenly-spaced APs provide connectivity to the pedestrian users. We assume the APs are connected by high-rate wireless backhaul links and that each user is connected to a single AP at each time instant. For the walkway scenario, the AP is mounted at a height $h_{TX} = 5$ m on a street lampost, thus stationary. Each user is at a height of $h_{RX} = 1.5$ m and traverses the route at a pedestrian speed of $v_{RX} = 3.6$ km/h. The width (w) of the walkway is 2 m. With the short TX-RX separation distance d, we consider a single-path channel $L = 1$ and assume LOS connectivity between the AP and the UEs, as $P_{LOS} \approx 1$, according to [101].

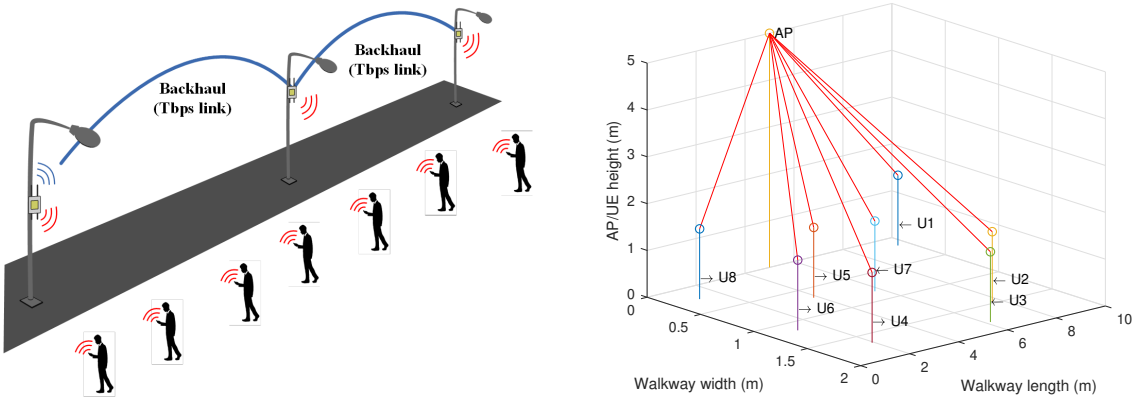

Figure 4.12: Deployment layout for C-I2P scenario.

Using the two-stage multi-user HBF scheme, consider the system with N_{TX} AP antennas and N_{RF}^{TX} RF chains such that $N_{RF}^{TX} < N_{TX}$ (TX HBF), and K terminals each with N_{RX} antennas and only one RF chain (RX ABF). For a fully connected hybrid beamformer system, the AP employs a baseband (BB) digital beamformer $\mathbf{F}_{BB} \in \mathbb{C}^{N_{RF}^{TX} \times N_s}$ followed by the analog RF beamformer $\mathbf{F}_{RF} \in \mathbb{C}^{N_{TX} \times N_{RF}^{TX}}$ such that the transmitted signal becomes $\mathbf{x} = \mathbf{F}_{RF}\mathbf{F}_{BB}\mathbf{s}$. The received signal vector $\mathbf{r}_k$ observed by the k^{th} terminal after beamforming can then be expressed as (4.47). After being combined with the analog combiner $\mathbf{w}_k$, where $\mathbf{w}_k$ has similar constraints as the analog beamformer $\mathbf{F}_{RF}$, the signal y_k becomes (4.48). The multibeam TX hybrid-analog RX configuration thus described is shown in Figure 4.13, where the HBF TX employs the fully-connected array structure.

$$\mathbf{r}_k = \mathbf{H}_k \sum_{n=1}^{K} \mathbf{F}_{RF}\mathbf{f}_n^{BB} s_n + \mathbf{n}_k, \tag{4.47}$$

$$y_k = \mathbf{w}_k^H \mathbf{H}_k \sum_{n=1}^{K} \mathbf{F}_{RF}\mathbf{f}_n^{BB} s_n + \mathbf{w}_k^H \mathbf{n}_k. \tag{4.48}$$

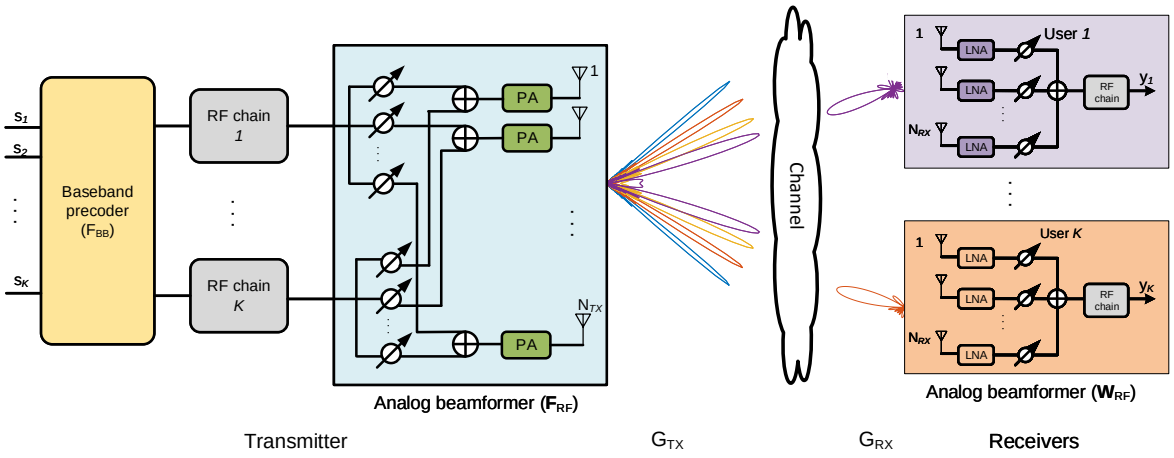

Figure 4.13: Hybrid (multi-beam) beamforming and analog combining (single beam per user) system architecture.

In each run, the users are randomly deployed for the first TTI. Thereafter, each UE follows its mobility course (with respect to speed and direction) throughout subsequent TTIs. At 1 m/s speed and TTI length of 1 ms, it takes 10,000 TTIs to traverse the coverage area of the AP (10 m end-to-end). The results are averaged over 200 simulations runs (where each run is 10,000 TTIs). First, we evaluate the system performance using the baseline simulation parameters given in Table 4.5 and thereafter, we investigate the impacts of other key parameters such as carrier frequency, bandwidth, antenna gain, etc.

Table 4.5: Baseline simulation parameters for C-I2P scenario

Parameter	Value	Parameter	Value
f_c	100 GHz	B	1 GHz
$X(\mu, \sigma)$	(0, 4) dB	$\bar{n}$	2
N_o	-174 dBm/Hz	NF	6 dB
N_{TX}	64	N_{RX}	8
h_{TX}	5 m	h_{RX}	1.5 m
G_{TX}	25 dBi	G_{RX}	9 dBi
K	8	v_{RX}	3.6 km/h
P_T	[0:50] dBm	P_{RF}	153 mW
P_{PS}	30 mW	P_{PA}	16 mW
P_{BB}	243 mW	L_{BH}	250 mW/(Gb/s)
$nTTIs$	10,000	$nRuns$	200

4.7.2 Simulation Results

In this section, we present the simulation results using the SE and EE performance for the three sets of precoding techniques described in Section 4.3.

(a) Baseline Performance

The baseline results realized with the key simulation parameters and values in Table 4.5 are shown in Figure 4.14. As P_T increases, the average (i.e., per user) SE for the HYB-ZF and SVD-UB schemes increase almost linearly. A gap of about 4 bits/s/Hz exists between the HYB-ZF and the SVD-UB that serves as the upper bound on the achievable rate. While the SVD-UB considers no interference at all, the HYB-ZF only mitigates the interference. As for AN-BST, the SE performance is almost flat. This results from the inability of the technique to mitigate MUI, thereby leading to a somewhat low SINR, relative to the other two schemes. In this kind of scenario where the users are very close to the TX and thus have high SNRs, interference mitigation is critical in order to lower the interference levels and guarantee good SINR levels.

The EE curves in Figure 4.14 show the typical quasi-concave trend where the EE first increases as P_T increases, then reach the peak points and thereafter continue to reduce [177]. From the performance curves in Figure 4.14, the optimal P_T for the joint EE-SE optimization are the points where the EE and SE curves intersect for the respective precoding technique. The optimal P_T is in the range 40-41 dBm for both HYB-ZF and SVD-UB. Increasing the P_T beyond the optimal points leads to increase in SE, but at the expense of reduction in the EE of the system. More so, the average SE of $\sim$27 bits/s/Hz translates to up to 3.37 Gbps throughput per user and $\sim$2.7 Gbits/J in terms of EE for HYB-ZF at the joint EE-SE optimal P_T of 40 dBm, for example. However, at the peak EE point of 2.9 Gbits/J for HYB-ZF (where $P_T = 30$ dBm), the SE reduces to 24 bits/s/Hz (i.e., 3 Gbps per-user throughput).

It is instructive to note, however, that EE would be a more critical design goal than SE in order to facilitate the green operation of future networks. The performance of AN-BST follows a markedly different trend. With the relatively-low flat average SE of 4 bits/s/Hz, lower P_T appears more energy-efficient as increase in P_T does not bring about any corresponding increase in SE. This is due to the limiting impact of interference on the achievable rate. This, again, provides the impetus for interference mitigation in MU-MIMO systems.

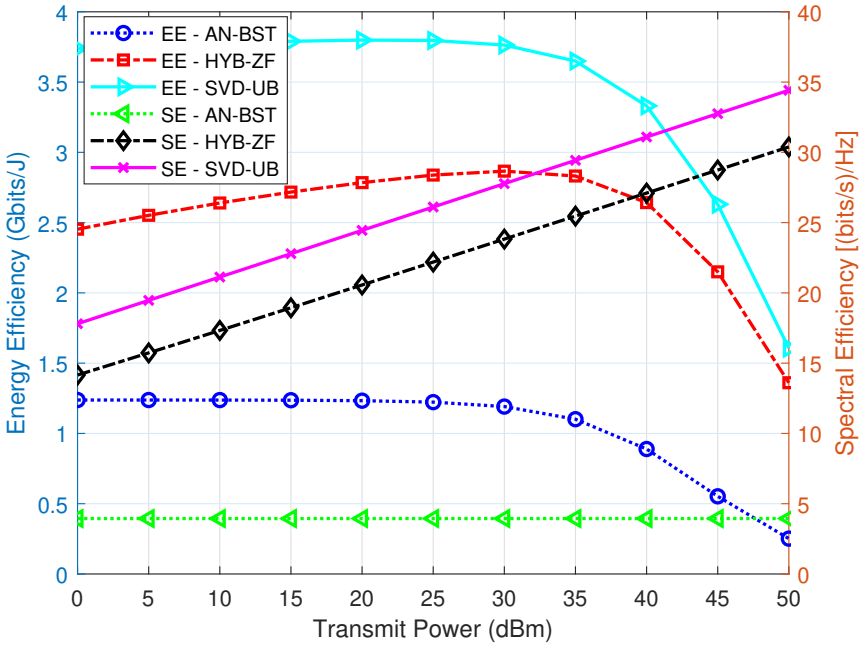

Figure 4.14: EE-SE performance as a function of P_T (baseline).

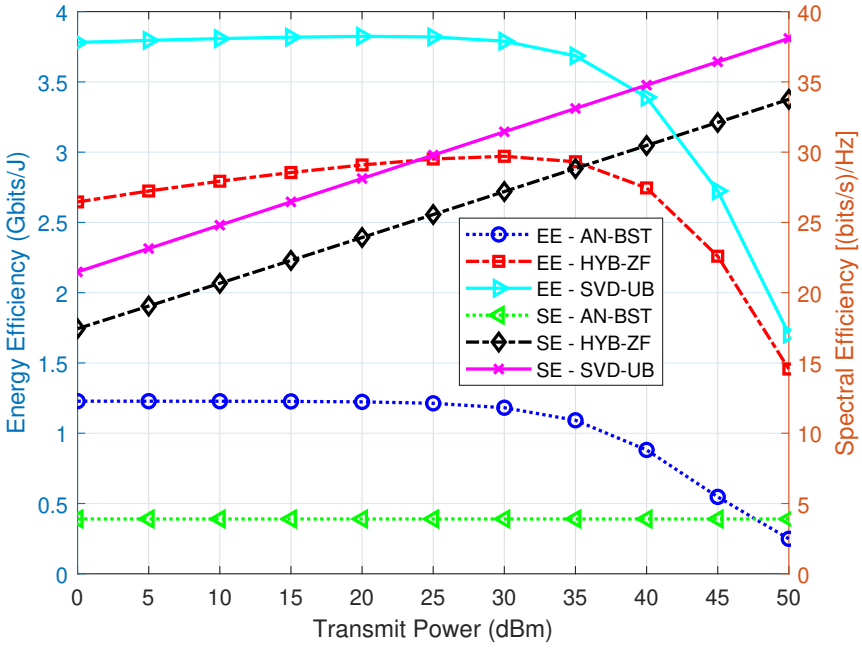

Figure 4.15: EE-SE performance as a function of P_T [$f_c = 28$ GHz].

(b) Impact of carrier frequency

To show the impact of f_c on the baseline results, we changed f_c from 100 GHz to 28 GHz while keeping all other baseline system parameters constant. The system performance at 28 GHz is shown in Figure 4.15. It can be observed that the trends of the EE and SE

curves are the same as those of the baseline results in Figure 4.14. However, the SE plots for SVD-UB and HYB-ZF are around 3 bits/s/Hz higher at 28 GHz in Figure 4.15 in contrast to the 100 GHz baseline plots of Figure 4.14. This outcome results from the expected effect of reduction in PL as f_c decreases. However, the larger available bandwidth and the higher antenna gain realizable at higher mmWave bands offer gains that will translate to higher overall throughputs in the higher mmWave bands (100 GHz) than at the lower mmWave frequencies (28 GHz).

(c) Impact of bandwidth

With respect to the effect of bandwidth on system performance, Figure 4.16 shows the performance when the bandwidth of the 100 GHz setup is increased from 1 GHz (Figure 4.14) to 5 GHz (Figure 4.16) while all other baseline parameters remain constant. The performance trend remains the same for both figures and for all techniques, and evidently for both the EE and SE metrics. However, a decrease of 2-3 bits/s/Hz can be observed on the SE performance for SVD-UB and HYB-ZF as the bandwidth increased from 1 GHz to 5 GHz. This reduction in SE is attributable to the increase in noise as the bandwidth increased. Nevertheless, the larger bandwidth leads to increased user throughput and capacity for the 100 GHz mmWave system.

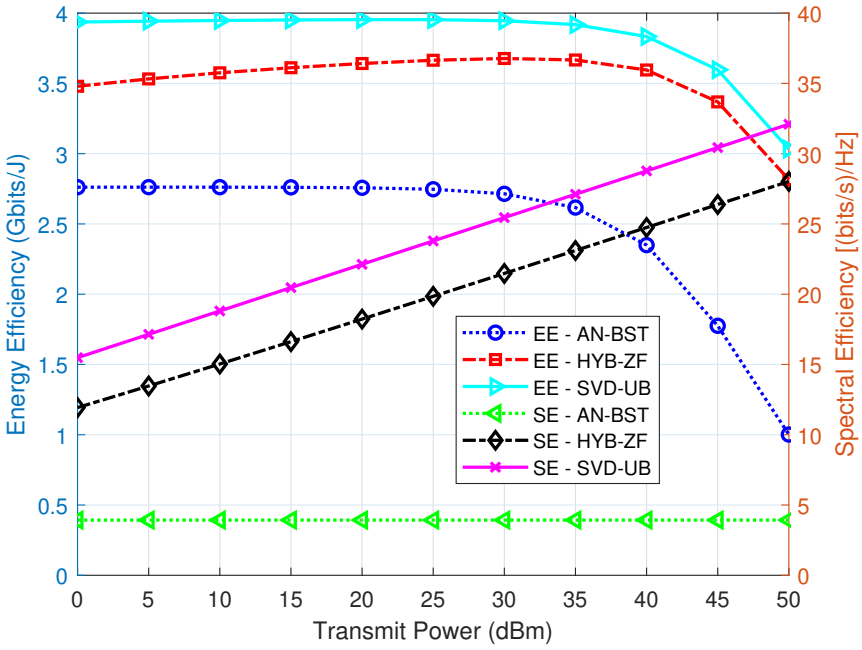

Figure 4.16: EE-SE performance as a function of P_T [B = 5 GHz].

(d) Impact of antenna gain

In Figure 4.17, we show the SE-EE performance of the system when the TX antenna gain is reduced from 25 dBi (Figure 4.14) to 18 dBi (Figure 4.17), while keeping the UE gain at 9 dBi as before. The results follow a similar pattern as the baseline, though with a reduction in the SE. The lower G_{TX} at the AP translates to wider beams, that potentially causes higher interference, leading to reduced performance in Figure 4.17 relative to the baseline in Figure

4.14. Therefore, sharper and narrower beams are more advantageous in scenarios like the one considered in this work.

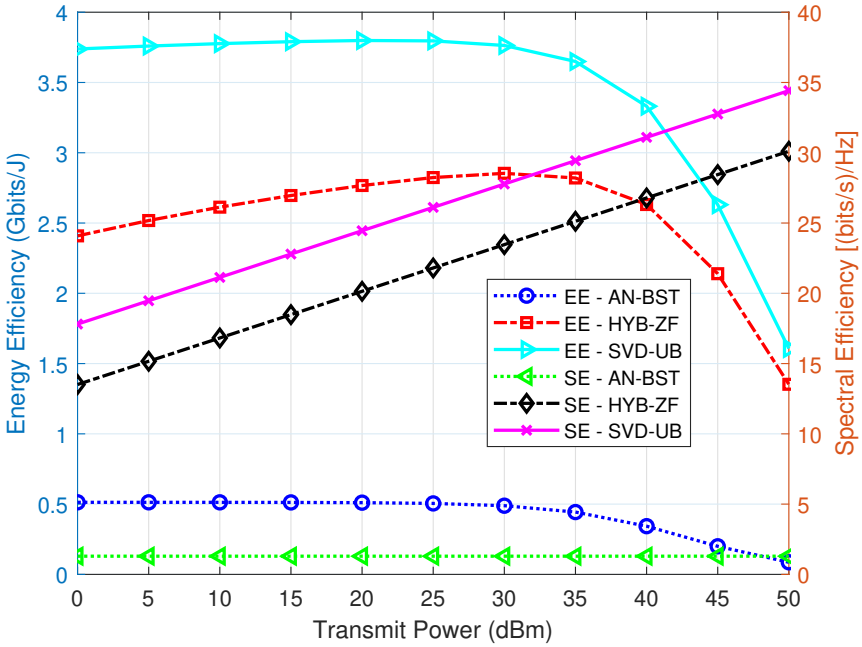

Figure 4.17: EE-SE performance as a function of P_T [$G_{TX} = 18$ dBi].

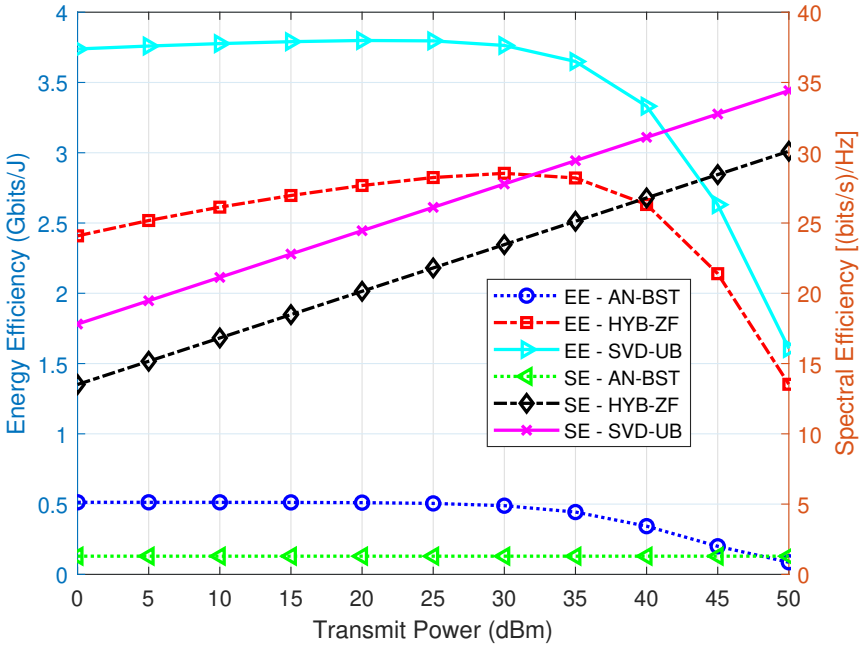

Figure 4.18: EE-SE performance as a function of P_T [TX = UPA].

(e) Impact of antenna geometry

Keeping the carrier frequency at 100 GHz, bandwidth at 1 GHz and other parameters employed for Figure 4.14 constant, we changed the AP antenna geometry from ULA to UPA. The resulting plots in Figure 4.18 show similar trends (i.e., linear in SE and quasi-concave in EE) as those in the baseline results (Figure 4.14). While the HYB-ZF and SVD-UB results in both Figures 4.14 and 4.18 are relatively the same, the EE and SE values for the AN-BST are lower in Figure 4.18 than in Figure 4.14. With the antenna elements arranged in planar form, inter-beam interference is higher with UPA than in ULA for the scenario under consideration. This interference effect is not mitigated in the AN-BST (unlike the HYB-ZF and SVD-UB) schemes, hence lower the lower SE and EE performance. It is instructive to note that the impact of antenna geometry would be obvious with scenarios having users at different heights where 3D beamforming would provide the opportunity to discriminate users at same azimuth but different elevation angles [13].

4.8 Conclusions

In this chapter, we proposed a novel generalized HBF array structure for the DL multi-user mmWave massive MIMO network. The generalized framework enables the design and comparative performance analysis of different possible subarray configurations (i.e., the fully-connected, the sub-connected and the overlapped subarray structures). The performance of the proposed model was analyzed within a C-I2X application scenario, where "X" is combination of pedestrian users and high-mobility vehicular users. The results show that the overlapped subarray structure can provide a balanced performance trade-off in terms of SE, EE and hardware costs in contrast to the popular fully-connected structure (with high SE and limited EE) and the sub-connected structure (with reduced SE and high EE).

In particular, the overlapped subarray structures (depending on $\triangle N$) can provide SE gains in the range of 11-25% over the sub-connected array structure, while approaching the 27.5% gain in SE of the fully-connected architecture. In a similar vein, the overlapped subarray structure suffers between 3.4 to 14.9% reduction in EE relative to the sub-connected structure in contrast to the 19.6% loss in EE of the fully-connected architecture. With a balanced SE-EE trade-off, the overlapped subarray structure, therefore, shows potential for NGMNs that targets both high-rate and energy-efficient operation of the network.

Similarly, using a C-I2P application scenario, we have shown the impacts of carrier frequency, bandwidth, antenna gain and antenna geometry on the EE and SE performance using a candidate 5G scenario (with street-level lampost-mount APs providing connectivity to pedestrian users). Using a single-cell multi-user setup where a massive MIMO AP communicates to multiple users with single stream per user, we compared the performance of the three precoding schemes: AN-BST, HYB-ZF and SVD-UB. The results show that the AN-BST scheme (with no baseband precoder for MUI mitigation) shows poor performance when compared to the other two schemes.

On the other hand, the HYB-ZF scheme which employs a baseband ZF precoder for MUI mitigation approaches the performance of the upper bound SVD-UB with a gap of $\sim$5 bits/s/Hz in SE, and a gap of $\sim$1 Gbits/J in EE at the optimal operating points for the energy and spectrally-efficient network operation. Finally, we note that the results in this chapter

have been published in the IEEE Transactions on Vehicular Technology[9] and the proceedings of IEEE International Conference on Communications (ICC)[10].

[9] **S. A. Busari**, K. M. S. Huq, S. Mumtaz, J. Rodriguez, Y. Fang, D. C. Sicker, S. Al-Rubaye and A. Tsourdos, "Generalized Hybrid Beamforming for Vehicular Connectivity using THz Massive MIMO", *IEEE Transactions on Vehicular Technology*, pp. 1-12, June 2019.

[10] **S. A. Busari**, K. M. S. Huq, S. Mumtaz and J. Rodriguez, "Terahertz Massive MIMO for Beyond-5G Wireless Communication", *IEEE International Conference on Communications (ICC) 2019*, Shanghai, P.R. China, pp. 1-6, May, 2019.

Chapter 5

Conclusions and Future Work

This chapter provides the summary of the principal findings, and design recommendations on the concepts investigated in this thesis: channel modeling, beamforming and system-level simulations of mmWave massive MIMO for 5G UDNs and C-I2X. The future research directions are then presented as related open issues for NGMNs, in the areas of THz channel modeling, ultra-massive MIMO, quantum machine learning and EE optimization for the forthcoming 6G era.

5.1 Thesis Summary

The data traffic forecasts for the 5G era (2020 onwards) imply that the available bandwidths in the sub-6 GHz μWave bands will be insufficient to meet the data rate demands of users. Next-generation cellular and vehicular applications, for example, are envisaged to require DL data rates in the order of multi-Gbps. For these two domains of mobile wireless connectivity, the mmWave spectrum can provide the multi-GHz contiguous bandwidths required to meet the projected throughput demands [180,181]. As a result, mmWave communication has received considerable attention in the research community in the present decade. This trend is expected to continue as the progress being made in various areas of mmWave communication (such as electronic components, channel modeling, spectrum allocation, standardization, use cases, etc.) continue to spur further research activities [151, 166].

To enable mmWave communications, the TXs (and RXs) must use massive MIMO antenna arrays [151]. This is because the free space path loss (FSPL) increases as the f_c increases, according to the fundamental Friis equation [18]. Fortunately, a 10$\times$ increase in f_c (e.g., from 2.8 GHz to 28 GHz) correspondingly leads to a 10-fold reduction in λ. As a result, the dimensions of the AEs as well as their inter-element spacing become incredibly small (due to their dependence on λ). It thus becomes possible to pack a large number of AEs in a physically-limited space thus enabling the mmWave massive MIMO paradigm. The high PL at mmWave frequencies constrains the systems employing mmWave massive MIMO to distances much shorter than the ISDs of legacy cellular networks. This enables the application of scenarios such as 5G UDN and short-range C-I2X use cases. The use of mmWave massive MIMO in this ultra-dense domain has been the central focus of the investigation in this thesis.

With the huge available bandwidth in the mmWave spectrum, the aggressive spatial multiplexing realizable with massive MIMO arrays and the expected high capacity gains from the densely-deployed BSs or APs, the amalgam of the three technologies can meet the projected

explosive user data demand and thereby support the 5G eMBB use case. However, despite the potential of this architecture, a number of challenges surface regarding system implementation. Some of these challenges are investigated in this thesis, as highlighted hereunder. Some others that are subject to future investigations are presented in the next section.

5.1.1 Channel Modeling

The accurate characterization of the wireless channel is fundamental to the realistic evaluation of system performance. Different from legacy systems, 5G networks bring to the forefront many different new perspectives for the wireless channel modeling. Moving to the mmWave spectrum introduces new dynamics to channel modeling. Among the newly-introduced challenges are the need to model and support: massive MIMO, 3D beamforming, wide frequency range, broad bandwidth, smooth time evolution, spatial and frequency consistency, mobility, coexistence and diverse use cases or scenarios. Consequently, in Chapter 3 of this thesis:

- We adopted the 3GPP 3D channel models for LTE (TR 36.873 [84]) and mmWave (TR 38.900 [85]) frequencies as legacy 2D channel models have been shown to underestimate performance [31–34], and do not cater for future emerging 5G scenarios such as sky-rise buildings and vehicular scenarios that require a 3D perspective. These were implemented and form part of an integrated 5G SLS with enhanced functionalities based on LTE-A SLS [38]. Some of the added features include: 3GPP 3D mmWave channel model (TR 38.900 [85]), 5G NR frame structure [165], multi-tier and multi-frequency HetNet, inter-tier handover (leading to uneven cell loading), among others.

- We calibrated the channels using the appropriate metrics, standards and references. With the evolved 5G simulator, we characterized the individual performance of the 3D μWave and mmWave channels using the UMa and UMi scenarios in LOS, NLOS and O2I propagation environments. Focusing on the mmWave SC tier that is particularly required to provide the anticipated capacity boost for 5G, we investigated parameters such as BS downtilt and UE height, that could impact system performance. Our results show that the mmWave channel was underwhelming in terms of expected multi-Gbps data rate due to SINR bottleneck, particularly for indoor users served by outdoor BSs. The SINR statistics reveal that indoor users experience up to 30 dB additional losses from wall and in-building objects. It also reveals the degrading impact of the higher noise levels resulting from the larger bandwidths employed in mmWave systems.

- The performance of the joint use of the two channel models in a 5G UDN deployment framework with μWave MCs and densely-deployed mmWave SCs was also evaluated. This multi-tier scenario investigates the impact and interplay of the so-called "big three" technologies for 5G: UDN, massive MIMO and mmWave communications. The results show that much higher capacity can be realized with UDNs than in MC-only set-ups. The results also reveal that performance does not scale proportionally with increase in the employed mmWave bandwidth. The corresponding increase in noise (due to larger bandwidths) reduces the SINR. Outdoor users experience promising data rates notwithstanding, but the throughputs of indoor users are highly degraded. This is due to the additional wall and indoor losses (on top of the inherently high PL at mmWave frequencies) which further reduce the SINR of indoor users.

- In the last part of Chapter 3, we adopted the measurement-based 3D mmWave massive MIMO channel-only simulator [42] and enhanced its capabilities for the investigation of the C-I2V scenario involving street-level lampost-based APs (or infrastructure or BS) and vehicles with roof-mount antennas as receivers. We upgraded the channel simulator by implementing blockage model, spatial consistency, mobility and advanced 5G features with respect to the 5G NR frame structure, beamforming and scheduling. Using the upgraded simulator, we then fully characterized the mmWave massive MIMO vehicular channel using metrics such as PL, RMS-DS, Rician KF, cluster and ray distribution, PDP, channel rank, channel condition number and data rate. We also compared the mmWave performance with the DSRC and LTE-A capabilities and offered useful insights on vehicular channels in such scenarios.

Given the 3D channel implementation and characterization for 5G UDN and C-I2V scenarios, the aggregate results indicate that outdoor users show promising performance in mmWave 3D channels for 5G eMBB use cases. On the other hand, the additional wall and indoor losses (on top of the inherently high PL at mmWave frequencies) significantly degrade the performance of indoor users served by outdoor BSs. Therefore, overcoming the collective impact of the increasing noise, higher PL and indoor losses remains a challenge for indoor users in the mmWave tier of 5G HetNets where high rates are anticipated. Thus, the practical option advocated in this thesis, and supported by recent findings and deployment [35, 53] is to employ the UMa-μWave for coverage, whilst using the UMi-mmWave for high-rate outdoor UDN users, and serving indoor users using the indoor femtocells, or WiFi APs. Similarly, mmWave massive MIMO can deliver Gbps rates for supporting vehicular safety, infotainment and allied services for applications such as autonomous driving. The mmWave access can be made available by using the 5G cellular infrastructure, dedicated mmWave V2X/I2X/I2V or modified IEEE 802.11ad unlicensed band, as advocated for example by 3GPP Release 15 for 5G-V2X [182].

5.1.2 Hybrid Beamforming

Beamforming is required in mmWave massive MIMO systems to provide large array gains to overcome the high PL, enable highly-directional beams to mitigate ICI, provide spatial multiplexing gains to boost system capacity as well as facilitate the mitigation of MUI [136]. With possibilities for ABF, HBF and DBF architectures, the HBF array structure has been extensively demonstrated as a practically-feasible architecture for massive MIMO. Considering the SE, EE, cost and hardware complexity, the HBF approach strikes a balanced performance trade-off when compared to the fully-analog and the fully-digital implementations. Using the HBF architecture, it is possible to realize three different subarray structures, specifically the fully-connected, sub-connected and the overlapped subarray structures. However, no generalized framework exists for the comparative performance of these structures. More so, the performance of HBF schemes in 5G UDN and short-range C-I2P and C-I2X scenarios have not received adequate attention.

Therefore, in Chapter 4 of this thesis:

- We developed a generalized model for the design and analysis of any HBF array structure or configuration using mmWave massive MIMO. We outlined, in a step-wise manner, the procedures for the design, and then analyzed the performance of quintessential configurations comparatively, using the C-I2X application scenario involving both cellular

and vehicular users. A parameter known as the subarray spacing is introduced, such that varying its value leads to the different subarray configurations and the consequent changes in system performance.

- Using a realistic power consumption model, we assessed the performance of the system not only in terms of the SE and EE, but also the power and hardware cost for the network. Different from most existing works, our comprehensive power consumption model includes the TX power, TX circuit power, RX circuit power as well as the backhaul power. Our results reveal that the backhaul power constitute the largest percentage of the total power consumption in the 5G scenario as ultra-high data rates are exchanged between the TX and the core network. This result is contrary to the situation with relatively low-rate legacy networks where the TX power takes the largest chunk of the total power consumption.

- Moreover, using the HBF structure, we investigated the performance of the hybrid precoding with baseband zero forcing for MUI mitigation in C-I2P scenario, and assessed its superiority over the analog-only beamsteering approach and how its performance approaches the SVD precoding as the upper bound. The impacts of system parameters such as carrier frequency, bandwidth, antenna gain and antenna geometry on the SE-EE performance of the network were also assessed.

Thus, Chapter 4 presented a novel generalized framework for the design and performance analysis of the different HBF architectures. The objective of this work is two-fold: generalized framework and performance trade-off with respect to the existing solutions. Firstly, while the fully-connected and the sub-connected structures are popular and widely investigated, the overlapped subarray structure has not received significant attention. Thus, this work provides a generalized framework to realize any of the configurations for performance comparison. Secondly, as the results show, the overlapped subarray implementation maintains a balanced trade-off in terms of SE, EE, complexity and hardware cost when compared to the popular fully-connected and the sub-connected structures. The overlapped structure, therefore, offers promising potential for 5G networks employing mmWave massive MIMO to deliver ultra-high data rates whilst maintaining a balance in the EE of the network.

5.2 Future Research Directions

As we march towards 2020, activities on 5G networks are moving from research, field trials and standardization to real deployments. The 5G Phase 1 has been finalized, 5G Phase 2 has recently been defined by the 3GPP and the research on 6G networks is picking up pace. Since 6G networks are expected to address the limitations and challenges of 5G and surpass its performance, the future research directions presented in this thesis are in the following 6G research areas.

5.2.1 THz Channel Modeling

Spectrum use will undoubtedly move to the 0.3-10 THz bands in the 6G mobile system era. With enormous bandwidths far greater than the amount available in the sub-6 GHz and mmWave bands combined, THz band communications (THzBC) will open up new frontiers for exciting services and applications requiring ultra-broadband (Tbps) connectivity. To combat

high PL at THz frequencies, directional and dynamic ultra-massive MIMO antennas are expected to be used. High directionality and dynamic ultra-massive MIMO antennas lead to narrow beamwidth and very limited interference. Thus, very high data rate per area or per link can be expected. However, there are also critical fundamental challenges for applying THz communications in mobile networks. For example, the channel modeling is still largely unknown in the THz band [183] except those below 300 GHz for stationary indoor scenarios [184]. Moreover, ultra-high rates lead to ultra-high energy consumption. Thus, energy-efficient communications are needed on both the digital signal processing and radio interface levels.

Since the future ultra-fast 6G THz network will be modeled in ultra-dense setups consisting of numerous hotspots, stochastic modeling approaches have to be extended towards the 3D channel modeling to account for effects such as 3D beamforming in THz networks. Moreover, analytical validation would have to be complemented with real experimentation in order to assess the feasibility of the design within the 6G networking scenario that includes practical models for characterizing the channel, data traffic, and mobility within a multi-user environment. Modeling the impact of mobility and dual mobility for THz cellular and vehicular networks is still a fundamental challenge for the forthcoming 6G system. In addition, extension of the mmWave channel models to cover new and extreme application scenarios such as tunnel, underground, underwater, human body, molecular and unmanned aerial vehicle (UAV) communication is still largely missing or sparingly explored. Moreover, 6G will integrate terrestrial, airborne and satellite networks leading to future emerging use cases and extreme scenarios that will benefit from THzBC [12, 100]. How to exploit THzBC and performance analysis will be a topic for future research. Also, design and development of integrated multi-band transceivers that will facilitate the coexistence of μWave, mmWave and THz communication will be a fundamental component of 6G and is thus a research outlook.

5.2.2 Ultra-massive MIMO

The extremely small size of THz antennas will enable ultra-massive MIMO (UM-MIMO) or extra-large scale massive MIMO (XL-MIMO) arrays with elements far greater than the number expected in 5G systems. UM-MIMO is being explored as the practical technology to combat the distance or range challenge in THz systems, while offering amazing opportunities for beamforming and spatial multiplexing in delivering ultra-high capacities for 6G systems. The ultra-large arrays, however, bring about new set of challenges with respect to THz UM-MIMO fabrication, channel modeling, modulation, waveform design and beamforming, multi-carrier antenna configurations, spatial modulation, and other challenges across all layers of the protocol stack [151, 185–187].

In UM-MIMO or XL-MIMO, the array dimension is pushed to the extreme. For example, XL-MIMO arrays can be integrated into large structures such as the walls of buildings in a megacity, in airports, large shopping malls or along the structure of a stadium and thereby serve a large number of user devices. This use case is considered a distinct operating regime of massive MIMO and comes with its own challenges and opportunities [188]. The prospective use cases that would be the subject of 6G research activities include the use of THz UM-MIMO for communication and sensing, on-chip/chip-to-chip communication and data centers and other cellular, vehicular, biological and molecular applications [185, 189].

5.2.3 6G for Energy Efficiency

Hardware cost, complexity and power consumption have largely limited 5G antenna and beamforming designs to the hybrid architectures which have reduced flexibility and rate when compared to the fully-digital implementation. However, the development trends show that the cost and power consumption of fully-digital transceivers can be reduced in the future, thereby making digital precoding a good choice for spectral- and energy-efficient 6G system implementation [53, 57]. Another technology being considered for EE optimization in 6G systems is wireless communication with reconfigurable intelligent surfaces (RISs) or large intelligent surfaces (LISs) for centralized, distributed or cell-free UM-MIMO systems [12,188, 190,191].

LISs generically denote active large electromagnetic surfaces that possesses communication capabilities. The walls of buildings, room and factory celings, laptop cases and human clothing, among others, can be used as intelligent surfaces for smart environment in 6G. They will be equipped with metamaterial-based antennas, programmable metasurfaces, fluid antennas or software-defined material for wireless communication [11]. RIS refers to a meta-surface equipped with integrated electronic circuits that can be programmed to alter an incoming electromagnetic field in a customizable way. It can be readily fabricated using lithography and nano-printing methods and is attractive from an energy consumption standpoint as it amplifies and forwards the incoming signals without employing any power amplifier thereby consuming less energy than legacy transceiver designs [190, 191]. In harnessing the benefits of LIS/RIS technology, new transceiver designs are being considered for energy-efficient 6G networks and are thus continuing topics for future research.

5.2.4 Quantum Machine Learning

An ultra-massive and complex networking scenario is foreseen for 6G systems, from extra-large scale MIMO and ultra-wideband spectrum to ultra-dense small and tiny cells, LIS and massive IoT/internet of everything (IoE) deployment. The anticipated huge scale of data, no doubt, necessitates the use of artificial intelligence (AI) tools for intelligent adaptive learning, accurate prediction and reliable decision making for efficient network management. Some of the areas where AI would be applied include: channel estimation/detection, radio resource management, energy modeling, cell/channel selection association, location prediction, beam tracking and management, cell/user clustering, switch and handover among HetNets, spectrum sensing/access, signal dimension reduction, user behavior analysis, mobility management, intrusion/fault/anomaly detection, complexity reduction and system optimization [9, 192, 193].

Due to the advances in AI techniques, especially deep learning and the availability of massive training data, the interest in using AI for the design and optimization of wireless networks has significantly increased and it is widely accepted that AI will be at the heart of 6G [11]. Machine learning (ML), as a subbranch of AI, enables machines to learn, perform, and improve their operations by exploiting the operational knowledge and experience gained in the form of data. ML (via supervised, unsupervised or reinforcement learning) can potentially assist big data analytics to realize self-sustaining, proactive and efficient wireless networks. Also, the tremendous potential of parallelism offered by quantum computing (QC) and related quantum technologies over classical computing paradigms is further enabling ML. Quantum machine learning (QML) has, therefore, emerged as a technology paradigm to ad-

dress the evolving challenges of the increasing human and machine interconnectivity, big data, autonomous management and self-organization demands in 6G networks [9].

In summary, the above-named subjects constitute the principal future research directions as a natural evolution from the 5G technology enablers investigated in this thesis, whose solution can be considered the first building block of 6G. Like the 5G enablers, these 6G concepts are inter-connected. THz spectrum enables UM-MIMO and their joint use demands QML in the foreseen complex communication scenarios (cellular, vehicular, etc) where EE would be a critical performance metric. Therefore, the interplay of these technologies together with the associated issues of use cases, standardization, health and safety, business model and performance optimization remain interesting open issues that are subjects for future works. 6G would be a stimulating research area with both evolutionary and revolutionary paradigms that would deliver innovative solutions for NGMNs. Finally, we remark that the open issues and future research directions presented in this chapter were the results of the surveys that were published in IEEE Network[11] and IEEE Communications Surveys and Tutorials[12].

[11]K. M. S. Huq, **S. A. Busari**, J. Rodriguez, V. Frascolla, W. Buzzi and D. C. Sicker, "Terahertz-enabled Wireless System for Beyond-5G Ultra-Fast Network: A Brief Survey", *IEEE Network*, vol. 33, no. 4, pp. 89-95, July/August, 2019.

[12]**S. A. Busari**, K. M. S. Huq, S. Mumtaz, L. Dai and J. Rodriguez, "Millimeter-Wave Massive MIMO Communication for Future Wireless Systems: A Survey", *IEEE Communications Surveys and Tutorials*, vol. 20, no. 2, pp. 836-869, May 2018.

Bibliography

[1] ITU-R, "IMT vision - Framework and overall objectives of the future development of IMT for 2020 and beyond - Recommendation ITU-R M.2083-0," ITU-R, Geneva, Switzerland, Tech. Rep., Sep. 2015, last accessed: 26-02-2020. [Online]. Available: https://www.itu.int/dms_pubrec/itu-r/rec/m/R-REC-M.2083-0-201509-I!!PDF-E.pdf

[2] S. Mumtaz, J. Rodriguez, and L. Dai, "Introduction to mmWave massive MIMO," in *mmWave Massive MIMO: A Paradigm for 5G*, S. Mumtaz, J. Rodriguez, and L. Dai, Eds. Academic Press, 2017, pp. 1–18.

[3] M. Shafi, A. F. Molisch, P. J. Smith, T. Haustein, P. Zhu, P. D. Silva, F. Tufvesson, A. Benjebbour, and G. Wunder, "5G: A Tutorial Overview of Standards, Trials, Challenges, Deployment, and Practice," *IEEE Journal on Selected Areas in Communications*, vol. 35, no. 6, pp. 1201–1221, June 2017.

[4] M. Xiao, S. Mumtaz, Y. Huang, L. Dai, Y. Li, M. Matthaiou, G. K. Karagiannidis, E. Björnson, K. Yang, I. Chih-Lin, and A. Ghosh, "Millimeter Wave Communications for Future Mobile Networks," *IEEE Journal on Selected Areas in Communications*, vol. 35, no. 9, pp. 1909–1935, Sep. 2017.

[5] ITU, "Minimum Requirements Related to Technical Performance for IMT-2020 Radio Interface(s), document ITU-R M. [IMT-2020.TECH PERF REQ.]," ITU, Tech. Rep., Oct. 2016, last accessed: 26-02-2020. [Online]. Available: https://www.itu.int/dms_pub/itu-r/opb/rep/R-REP-M.2410-2017-PDF-E.pdf

[6] F. B. Saghezchi *et al.*, *Drivers for 5G: The 'Pervasive Connected World'.* John Wiley & Sons Ltd., UK, 2015, chapter 1, pp. 1–27, in Rodriguez J. (Ed.), Fundamentals of 5G Mobile Networks.

[7] T. Chen, M. Matinmikko, X. Chen, X. Zhou, and P. Ahokangas, "Software defined mobile networks: concept, survey, and research directions," *IEEE Communications Magazine*, vol. 53, no. 11, pp. 126–133, Nov. 2015.

[8] A. Gupta and R. K. Jha, "A Survey of 5G Network: Architecture and Emerging Technologies," *IEEE Access*, vol. 3, pp. 1206–1232, 2015.

[9] S. J. Nawaz, S. K. Sharma, S. Wyne, M. N. Patwary, and M. Asaduzzaman, "Quantum Machine Learning for 6G Communication Networks: State-of-the-Art and Vision for the Future," *IEEE Access*, vol. 7, pp. 46 317–46 350, 2019.

[10] "5G vision requirements and enabling technologies," 5G South Korea, South Korea, Tech. Rep., Mar. 2016.

[11] F. Tariq, M. R. A. Khandaker, K. Wong, M. A. Imran, M. Bennis, and M. Debbah, "A Speculative Study on 6G," *CoRR*, vol. abs/1902.06700, 2019. [Online]. Available: http://arxiv.org/abs/1902.06700

[12] W. Saad, M. Bennis, and M. Chen, "A Vision of 6G Wireless Systems: Applications, Trends, Technologies, and Open Research Problems," *IEEE Network*, pp. 1–9, 2019.

[13] E. Calvanese Strinati, S. Barbarossa, J. L. Gonzalez-Jimenez, D. Ktenas, N. Cassiau, L. Maret, and C. Dehos, "6G: The Next Frontier: From Holographic Messaging to Artificial Intelligence Using Subterahertz and Visible Light Communication," *IEEE Vehicular Technology Magazine*, vol. 14, no. 3, pp. 42–50, Sep. 2019.

[14] I. F. Akyildiz, S. Nie, S.-C. Lin, and M. Chandrasekaran, "5G roadmap: 10 key enabling technologies," *Computer Networks*, vol. 106, pp. 17–48, 2016.

[15] S. Vahid, R. Tafazolli, and M. Filo, *Small Cells for 5G Mobile Networks*. John Wiley & Sons Ltd., UK, 2015, chapter 3, pp. 63–104, in Rodriguez J. (Ed.), Fundamentals of 5G Mobile Networks.

[16] J. G. Andrews, S. Buzzi, W. Choi, S. V. Hanly, A. Lozano, A. C. K. Soong, and J. C. Zhang, "What Will 5G Be?" *IEEE Journal on Selected Areas in Communications*, vol. 32, no. 6, pp. 1065–1082, June 2014.

[17] F. Khan and Z. Pi, "mmWave mobile broadband (MMB): Unleashing the 3300GHz spectrum," in *34th IEEE Sarnoff Symposium*, May 2011, pp. 1–6.

[18] V. Va, T. Shimizu, G. Bansal, and R. W. H. Jr., "Millimeter Wave Vehicular Communications: A Survey," *Foundations and Trends in Networking*, vol. 10, no. 1, pp. 1–113, 2016.

[19] W. H. Chin, Z. Fan, and R. Haines, "Emerging technologies and research challenges for 5G wireless networks," *IEEE Wireless Communications*, vol. 21, no. 2, pp. 106–112, April 2014.

[20] E. G. Larsson, O. Edfors, F. Tufvesson, and T. L. Marzetta, "Massive MIMO for next generation wireless systems," *IEEE Communications Magazine*, vol. 52, no. 2, pp. 186–195, February 2014.

[21] T. L. Marzetta, "Noncooperative Cellular Wireless with Unlimited Numbers of Base Station Antennas," *IEEE Transactions on Wireless Communications*, vol. 9, no. 11, pp. 3590–3600, November 2010.

[22] F. Rusek, D. Persson, B. K. Lau, E. G. Larsson, T. L. Marzetta, O. Edfors, and F. Tufvesson, "Scaling Up MIMO: Opportunities and Challenges with Very Large Arrays," *IEEE Signal Processing Magazine*, vol. 30, no. 1, pp. 40–60, Jan 2013.

[23] Q. C. Li, H. Niu, A. T. Papathanassiou, and G. Wu, "5G Network Capacity: Key Elements and Technologies," *IEEE Vehicular Technology Magazine*, vol. 9, no. 1, pp. 71–78, March 2014.

[24] Z. S. Bojkovic, M. R. Bakmaz, and B. M. Bakmaz, "Research challenges for 5G cellular architecture," in *2015 12th International Conference on Telecommunication in Modern Satellite, Cable and Broadcasting Services (TELSIKS)*, Oct 2015, pp. 215–222.

[25] D. Feng, C. Jiang, G. Lim, L. J. Cimini, G. Feng, and G. Y. Li, "A survey of energy-efficient wireless communications," *IEEE Communications Surveys & Tutorials*, vol. 15, no. 1, pp. 167–178, 2013.

[26] E. Hossain, M. Rasti, H. Tabassum, and A. Abdelnasser, "Evolution toward 5G multi-tier cellular wireless networks: An interference management perspective," *IEEE Wireless Communications*, vol. 21, no. 3, pp. 118–127, June 2014.

[27] "Ericsson Mobility Report November 2018," Ericsson, Tech. Rep., Nov. 2018, last accessed: 26-02-2020. [Online]. Available: https://www.ericsson.com/assets/local/mobility-report/documents/2018/ericsson-mobility-report-november-2018.pdf

[28] Ericsson. Traffic Exploration Tool. Online. Ericsson. Accessed: 27-02-2020. [Online]. Available: http://www.ericsson.com/TET/trafficView/loadBasicEditor.ericsson

[29] E. Björnson, J. Hoydis, and L. Sanguinetti, "Massive MIMO Networks: Spectral, Energy, and Hardware Efficiency," *Foundations and Trends® in Signal Processing*, vol. 11, no. 3-4, pp. 154–655, 2017.

[30] W. Liu and Z. Wang, "Non-Uniform Full-Dimension MIMO: New Topologies and Opportunities," *IEEE Wireless Communications*, vol. 26, no. 2, pp. 124–132, April 2019.

[31] A. Kammoun, H. Khanfir, Z. Altman, M. Debbah, and M. Kamoun, "Preliminary Results on 3D Channel Modeling: From Theory to Standardization," *IEEE Journal on Selected Areas in Communications*, vol. 32, no. 6, pp. 1219–1229, June 2014.

[32] F. Ademaj, M. Taranetz, and M. Rupp, "3GPP 3D MIMO channel model: a holistic implementation guideline for open source simulation tools," *EURASIP Journal on Wireless Communications and Networking*, vol. 2016, no. 1, p. 55, Feb 2016.

[33] R. N. Almesaeed, A. S. Ameen, E. Mellios, A. Doufexi, and A. Nix, "3D Channel Models: Principles, Characteristics, and System Implications," *IEEE Communications Magazine*, vol. 55, no. 4, pp. 152–159, April 2017.

[34] F. Ademaj, M. Taranetz, and M. Rupp, "Implementation, validation and application of the 3GPP 3D MIMO channel model in open source simulation tools," in *2015 International Symposium on Wireless Communication Systems (ISWCS)*, Aug 2015, pp. 721–725.

[35] F. Kronestedt, H. Asplund, A. Furuskar, D. H. Kang, M. Lundevall, and K. Wallstedt, "The advantages of combining 5G NR with LTE," Ericsson, Tech. Rep., Nov. 2018, last accessed: 26-02-2020. [Online]. Available: https://www.ericsson.com/en/ericsson-technology-review/archive/2018/the-advantages-of-combining-5g-nr-with-lte

[36] C.-L. I, "Seven fundamental rethinking for next-generation wireless communications," *APSIPA Transactions on Signal and Information Processing*, vol. 6, p. e10, 2017.

[37] K. M. S. Huq, S. Mumtaz, J. Bachmatiuk, J. Rodriguez, X. Wang, and R. L. Aguiar, "Green HetNet CoMP: Energy Efficiency Analysis and Optimization," *IEEE Transactions on Vehicular Technology*, vol. 64, no. 10, pp. 4670–4683, Oct 2015.

[38] M. Rupp, S. Schwarz, and M. Taranetz, *The Vienna LTE-Advanced Simulators: Up and Downlink, Link and System Level Simulation*, 1st ed., ser. Signals and Communication Technology. Springer Singapore, 2016.

[39] M. K. Müller, F. Ademaj, T. Dittrich, A. Fastenbauer, B. Ramos Elbal, A. Nabavi, L. Nagel, S. Schwarz, and M. Rupp, "Flexible multi-node simulation of cellular mobile communications: the Vienna 5G System Level Simulator," *EURASIP Journal on Wireless Communications and Networking*, vol. 2018, no. 1, p. 227, Sep 2018.

[40] S. Pratschner, B. Tahir, L. Marijanovic, M. Mussbah, K. Kirev, R. Nissel, S. Schwarz, and M. Rupp, "Versatile mobile communications simulation: the Vienna 5G Link Level Simulator," *EURASIP Journal on Wireless Communications and Networking*, vol. 2018, no. 1, p. 226, Sep 2018.

[41] P. Alvarez, C. Galiotto, J. van de Belt, D. Finn, H. Ahmadi, and L. DaSilva, "Simulating dense small cell networks," in *2016 IEEE Wireless Communications and Networking Conference*, April 2016, pp. 1–6.

[42] New York University, "NYUSIM v1.6," 2017, last accessed: 26-02-2020. [Online]. Available: http://wireless.engineering.nyu.edu/5g-millimeter-wave-channel-modeling-software/

[43] S. Chen, X. Ji, C. Xing, Z. Fei, and H. Wang, "System-level performance evaluation of ultra-dense networks for 5G," in *TENCON 2015 IEEE Region 10 Conference*, 2015, pp. 1–4.

[44] X. Ge, S. Tu, G. Mao, C. X. Wang, and T. Han, "5G Ultra-Dense Cellular Networks," *IEEE Wireless Communications*, vol. 23, no. 1, pp. 72–79, 2016.

[45] L. Lu, G. Y. Li, A. L. Swindlehurst, A. Ashikhmin, and R. Zhang, "An Overview of Massive MIMO: Benefits and Challenges," *IEEE Journal of Selected Topics in Signal Processing*, vol. 8, no. 5, pp. 742–758, Oct 2014.

[46] L. G. Ordez, D. P. Palomar, and J. R. Fonollosa, "Fundamental diversity, multiplexing, and array gain tradeoff under different MIMO channel models," in *2011 IEEE International Conference on Acoustics, Speech and Signal Processing (ICASSP)*, May 2011, pp. 3252–3255.

[47] S. Mattigiri and C. Warty, "A study of fundamental limitations of small antennas: MIMO approach," in *2013 IEEE Aerospace Conference*, March 2013, pp. 1–8.

[48] F. Khan, *LTE for 4G Mobile Broadband: Air interface technologies and performance*. Cambridge University Press, New York, USA, 2009.

[49] A. Goldsmith, *Wireless Communications*. Cambridge University Press, Cambridge, United Kingdom, 2005.

[50] Q. Li, G. Li, W. Lee, M. Lee, D. Mazzarese, B. Clerckx, and Z. Li, "MIMO techniques in WiMAX and LTE: a feature overview," *IEEE Communications Magazine*, vol. 48, no. 5, pp. 86–92, May 2010.

[51] H. Inanolu, "Multiple-Input Multiple-Output System Capacity: Antenna and Propagation Aspects," *IEEE Antennas and Propagation Magazine*, vol. 55, no. 1, pp. 253–273, Feb 2013.

[52] S. Wang, Y. Xin, S. Chen, W. Zhang, and C. Wang, "Enhancing spectral efficiency for lte-advanced and beyond cellular networks [Guest Editorial]," *IEEE Wireless Communications*, vol. 21, no. 2, pp. 8–9, April 2014.

[53] E. Björnson, L. Van der Perre, S. Buzzi, and E. G. Larsson, "Massive MIMO in Sub-6 GHz and mmWave: Physical, Practical, and Use-Case Differences," *IEEE Wireless Communications*, vol. 26, no. 2, pp. 100–108, April 2019.

[54] J. Lota, S. Sun, T. S. Rappaport, and A. Demosthenous, "5G Uniform Linear Arrays With Beamforming and Spatial Multiplexing at 28, 37, 64, and 71 GHz for Outdoor Urban Communication: A Two-Level Approach," *IEEE Transactions on Vehicular Technology*, vol. 66, no. 11, pp. 9972–9985, Nov 2017.

[55] S. Sun, T. S. Rappaport, R. W. Heath, A. Nix, and S. Rangan, "Mimo for millimeter-wave wireless communications: beamforming, spatial multiplexing, or both?" *IEEE Communications Magazine*, vol. 52, no. 12, pp. 110–121, December 2014.

[56] G. Liu, X. Hou, J. Jin, F. Wang, Q. Wang, Y. Hao, Y. Huang, X. Wang, X. Xiao, and A. Deng, "3-D-MIMO With Massive Antennas Paves the Way to 5G Enhanced Mobile Broadband: From System Design to Field Trials," *IEEE Journal on Selected Areas in Communications*, vol. 35, no. 6, pp. 1222–1233, June 2017.

[57] B. Yang, Z. Yu, J. Lan, R. Zhang, J. Zhou, and W. Hong, "Digital Beamforming-Based Massive MIMO Transceiver for 5G Millimeter-Wave Communications," *IEEE Transactions on Microwave Theory and Techniques*, vol. 66, no. 7, pp. 3403–3418, July 2018.

[58] C. Chen, V. Volski, L. Van der Perre, G. A. E. Vandenbosch, and S. Pollin, "Finite Large Antenna Arrays for Massive MIMO: Characterization and System Impact," *IEEE Transactions on Antennas and Propagation*, vol. 65, no. 12, pp. 6712–6720, Dec 2017.

[59] S. Mumtaz, J. Rodriguez, and L. Dai, Eds., *mmWave massive MIMO: A Paradigm for 5G*. Academic Press, UK, 2017.

[60] T. S. Rappaport, S. Sun, R. Mayzus, H. Zhao, Y. Azar, K. Wang, G. N. Wong, J. K. Schulz, M. Samimi, and F. Gutierrez, "Millimeter Wave Mobile Communications for 5G Cellular: It Will Work!" *IEEE Access*, vol. 1, pp. 335–349, 2013.

[61] ITU-R. (2015, Jun.) Technology trends of active services in the frequency range 275-3000 GHz. Online. Last accessed: 05-03-2020. [Online]. Available: https://www.itu.int/pub/R-REP-SM.2352

[62] L. Zakrajsek, D. Pados, and J. M. Jornet, "Design and performance analysis of ultra-massive multi-carrier multiple input multiple output communication in the terahertz band," in *Proc. SPIE*, vol. 10209, Apr. 2017, pp. 1–12.

[63] L. Wei, R. Q. Hu, Y. Qian, and G. Wu, "Key elements to enable millimeter wave communications for 5G wireless systems," *IEEE Wireless Communications*, vol. 21, no. 6, pp. 136–143, December 2014.

[64] S. Hur, T. Kim, D. J. Love, J. V. Krogmeier, T. A. Thomas, and A. Ghosh, "Millimeter Wave Beamforming for Wireless Backhaul and Access in Small Cell Networks," *IEEE Transactions on Communications*, vol. 61, no. 10, pp. 4391–4403, October 2013.

[65] H. Shokri-Ghadikolaei, C. Fischione, P. Popovski, and M. Zorzi, "Design aspects of short-range millimeter-wave networks: A MAC layer perspective," *IEEE Network*, vol. 30, no. 3, pp. 88–96, May 2016.

[66] T. S. Rappaport, G. R. MacCartney, M. K. Samimi, and S. Sun, "Wideband Millimeter-Wave Propagation Measurements and Channel Models for Future Wireless Communication System Design," *IEEE Transactions on Communications*, vol. 63, no. 9, pp. 3029–3056, Sep. 2015.

[67] Z. Pi and F. Khan, "An introduction to millimeter-wave mobile broadband systems," *IEEE Communications Magazine*, vol. 49, no. 6, pp. 101–107, June 2011.

[68] A. L. Swindlehurst, E. Ayanoglu, P. Heydari, and F. Capolino, "Millimeter-wave massive MIMO: the next wireless revolution?" *IEEE Communications Magazine*, vol. 52, no. 9, pp. 56–62, Sep. 2014.

[69] M. Ding, D. Lopez-Perez, H. Claussen, and M. A. Kaafar, "On the Fundamental Characteristics of Ultra-Dense Small Cell Networks," *IEEE Network*, vol. 32, no. 3, pp. 92–100, May 2018.

[70] D. Lopez-Perez, M. Ding, H. Claussen, and A. H. Jafari, "Towards 1 Gbps/UE in Cellular Systems: Understanding Ultra-Dense Small Cell Deployments," *IEEE Communications Surveys Tutorials*, vol. 17, no. 4, pp. 2078–2101, Fourthquarter 2015.

[71] S. Buzzi and C. D'Andrea, "Doubly Massive mmWave MIMO Systems: Using Very Large Antenna Arrays at Both Transmitter and Receiver," in *2016 IEEE Global Communications Conference (GLOBECOM)*, Dec 2016, pp. 1–6.

[72] S. Buzzi and C. DAndrea, "The doubly massive MIMO regime in mmWave communications," Sep. 2016, proc. Tyrrhenian Int. Workshop Digit. Commun. pp. 1-28. [Online]. Available: Available:http://tyrr2016.cnit.it/tyrr-content/uploads/The-doubly-massive-MIMOregime-in-mmWave_DAndrea_TIW16.pdf.

[73] V. Ezzati, M. Fakharzadeh, F. Farzaneh, and M. R. Naeini, "Effect of Antenna Coupling on the SNR Improvement of Mm-Wave Massive MIMO for 5G," in *2019 IEEE International Symposium on Antennas and Propagation and USNC-URSI Radio Science Meeting*, July 2019, pp. 417–418.

[74] J. A. Zhang, X. Huang, V. Dyadyuk, and Y. J. Guo, "Hybrid antenna array for mmWave massive MIMO," in *mmWave Massive MIMO: A Paradigm for 5G*, S. Mumtaz, J. Rodriguez, and L. Dai, Eds. Academic Press, 2017, pp. 39 – 61.

[75] V. Petrov, D. Solomitckii, A. Samuylov, M. A. Lema, M. Gapeyenko, D. Moltchanov, S. Andreev, V. Naumov, K. Samouylov, M. Dohler, and Y. Koucheryavy, "Dynamic Multi-Connectivity Performance in Ultra-Dense Urban mmWave Deployments," *IEEE Journal on Selected Areas in Communications*, vol. 35, no. 9, pp. 2038–2055, Sep. 2017.

[76] M. R. Akdeniz, Y. Liu, M. K. Samimi, S. Sun, S. Rangan, T. S. Rappaport, and E. Erkip, "Millimeter Wave Channel Modeling and Cellular Capacity Evaluation," *IEEE Journal on Selected Areas in Communications*, vol. 32, no. 6, pp. 1164–1179, June 2014.

[77] Z. Shi, R. Lu, J. Chen, and X. S. Shen, "Three-dimensional spatial multiplexing for directional millimeter-wave communications in multi-cubicle office environments," in *2013 IEEE Global Communications Conference (GLOBECOM)*, Dec 2013, pp. 4384–4389.

[78] C. Kourogiorgas, S. Sagkriotis, and A. D. Panagopoulos, "Coverage and outage capacity evaluation in 5G millimeter wave cellular systems: impact of rain attenuation," in *2015 9th European Conference on Antennas and Propagation (EuCAP)*, April 2015, pp. 1–5.

[79] T. S. Rappaport, J. N. Murdock, and F. Gutierrez, "State of the Art in 60-GHz Integrated Circuits and Systems for Wireless Communications," *Proceedings of the IEEE*, vol. 99, no. 8, pp. 1390–1436, Aug 2011.

[80] Z. Qingling and J. Li, "Rain Attenuation in Millimeter Wave Ranges," in *2006 7th International Symposium on Antennas, Propagation EM Theory*, Oct 2006, pp. 1–4.

[81] S. Joshi and S. Sancheti, "Foliage loss measurements of tropical trees at 35 GHz," in *2008 International Conference on Recent Advances in Microwave Theory and Applications*, Nov 2008, pp. 531–532.

[82] S. A. Hosseini, E. Zarepour, M. Hassan, and C. T. Chou, "Analyzing diurnal variations of millimeter wave channels," in *2016 IEEE Conference on Computer Communications Workshops (INFOCOM WKSHPS)*, April 2016, pp. 377–382.

[83] T. E. Bogale, X. Wang, and L. B. Le, "mmWave communication enabling techniques for 5G wireless systems: A link level perspective," in *mmWave Massive MIMO: A Paradigm for 5G*, S. Mumtaz, J. Rodriguez, and L. Dai, Eds. Academic Press, 2017, pp. 195 – 225.

[84] "Study on 3D channel model for LTE, v12.2.0 , 3GPP TR 36.873," 3GPP, Tech. Rep., 2014, last accessed: 26-02-2020. [Online]. Available: http://www.3gpp.org/ftp//Specs/archive/36_series/36.873

[85] "Study on channel model for frequency spectrum above 6 GHz, v14.2.0, 3GPP TR 38.900," 3GPP, Tech. Rep., 2016, last accessed: 26-02-2020. [Online]. Available: http://www.3gpp.org/ftp//Specs/archive/38_series/38.900

[86] T. Wu, T. S. Rappaport, and C. M. Collins, "Safe for Generations to Come: Considerations of Safety for Millimeter Waves in Wireless Communications," *IEEE Microwave Magazine*, vol. 16, no. 2, pp. 65–84, March 2015.

[87] ——, "The human body and millimeter-wave wireless communication systems: Interactions and implications," in *2015 IEEE International Conference on Communications (ICC)*, June 2015, pp. 2423–2429.

[88] "European 7th Framework Programme Project MiWEBA," MiWEBA, Tech. Rep., Jan. 2018. [Online]. Available: Available:http://www.miweba.eu.

[89] K. Sakaguchi, G. K. Tran, H. Shimodaira, S. Nanba, T. Sakurai, K. Takinami, I. Siaud, E. C. Strinati, A. Capone, I. Karls, R. Arefi, and T. Haustein, "Millimeter-Wave Evolution for 5G Cellular Networks," *IEICE Transactions on Communications*, vol. E98.B, no. 3, pp. 388–402, 2015.

[90] "European 7 th Framework Programme Project MiWaveS," MiWaveS, Tech. Rep., Jan. 2018. [Online]. Available: Available:http://www.miwaves.eu.

[91] V. Frascolla, M. Faerber, E. C. Strinati, L. Dussopt, V. Kotzsch, E. Ohlmer, M. Shariat, J. Putkonen, and G. Romano, "MmWave use cases and prototyping: A way towards 5G standardization," in *2015 European Conference on Networks and Communications (EuCNC)*, June 2015, pp. 128–132.

[92] H. Shokri-Ghadikolaei, C. Fischione, G. Fodor, P. Popovski, and M. Zorzi, "Millimeter Wave Cellular Networks: A MAC Layer Perspective," *IEEE Transactions on Communications*, vol. 63, no. 10, pp. 3437–3458, Oct 2015.

[93] "Understanding 3GPP Release 12: Standards for HSPA+ and LTE Enhancements," Bellevue WA USA, Tech. Rep., Feb. 2015, last accessed: 26-02-2020. [Online]. Available: Available:http://www.5gamericas.org/files/6614/2359/0457/4G_Americas_-_3GPP_Release_12_Executive_Summary_-_February_2015.pdf.

[94] S. L. H. Nguyen, K. Haneda, J. Jarvelainen, A. Karttunen, and J. Putkonen, "On the Mutual Orthogonality of Millimeter-Wave Massive MIMO Channels," in *2015 IEEE 81st Vehicular Technology Conference (VTC Spring)*, May 2015, pp. 1–5.

[95] K. Zheng, S. Ou, and X. Yin, "Massive MIMO Channel Models: A Survey," *International Journal of Antennas and Propagation*, vol. 2014, no. 848071, p. 10 pages, 2014.

[96] J. M. Jornet and I. F. Akyildiz, "Channel Modeling and Capacity Analysis for Electromagnetic Wireless Nanonetworks in the Terahertz Band," *IEEE Transactions on Wireless Communications*, vol. 10, no. 10, pp. 3211–3221, October 2011.

[97] T. Kürner and S. Priebe, "Towards THz Communications - Status in Research, Standardization and Regulation," *Journal of Infrared, Millimeter, and Terahertz Waves*, vol. 35, no. 1, pp. 53–62, Jan 2014.

[98] R. Piesiewicz, C. Jansen, D. Mittleman, T. Kleine-Ostmann, M. Koch, and T. Kurner, "Scattering Analysis for the Modeling of THz Communication Systems," *IEEE Transactions on Antennas and Propagation*, vol. 55, no. 11, pp. 3002–3009, Nov 2007.

[99] M. Jacob, S. Priebe, R. Dickhoff, T. Kleine-Ostmann, T. Schrader, and T. Kurner, "Diffraction in mm and Sub-mm Wave Indoor Propagation Channels," *IEEE Transactions on Microwave Theory and Techniques*, vol. 60, no. 3, pp. 833–844, March 2012.

[100] C. Wang, J. Bian, J. Sun, W. Zhang, and M. Zhang, "A Survey of 5G Channel Measurements and Models," *IEEE Communications Surveys Tutorials*, vol. 20, no. 4, pp. 3142–3168, Fourthquarter 2018.

[101] M. K. Samimi and T. S. Rappaport, "3-D Millimeter-Wave Statistical Channel Model for 5G Wireless System Design," *IEEE Transactions on Microwave Theory and Techniques*, vol. 64, no. 7, pp. 2207–2225, July 2016.

[102] S. Sun, G. R. MacCartney, and T. S. Rappaport, "A novel millimeter-wave channel simulator and applications for 5G wireless communications," in *2017 IEEE International Conference on Communications (ICC)*, May 2017, pp. 1–7.

[103] "Study on channel model for frequencies from 0.5 to 100 GHz, v14.3.0, 3GPP TR 38.901," 3GPP, Tech. Rep., Dec. 2017, last accessed: 26-02-2020. [Online]. Available: http://www.3gpp.org/ftp//Specs/archive/38_series/38.901[{lastaccessed14Jan.,2019}]

[104] S. Jaeckel, L. Raschkowski, K. Brner, and L. Thiele, "QuaDRiGa: A 3-D Multi-Cell Channel Model With Time Evolution for Enabling Virtual Field Trials," *IEEE Transactions on Antennas and Propagation*, vol. 62, no. 6, pp. 3242–3256, 2014.

[105] S. Jaeckel, M. Peter, K. Sakaguchi, W. Keusgen, and J. Medbo, "5G Channel Models in mm-Wave Frequency Bands," in *European Wireless 2016;* 22^{nd} *European Wireless Conference*, 2016, pp. 1–6.

[106] "H2020-ICT-671650-mmMAGIC/D2.2, v1, Measurement results and final mmMAGIC channel models," Tech. Rep., Dec. 2017.

[107] A. Ghosh, "5G Channel Model for Bands up to 100 GHz," San Diego CA USA, Tech. Rep., Dec. 2015. [Online]. Available: Available:http://www.5gworkshops.com/5GCM.html.

[108] S. Wu, C. Wang, e. M. Aggoune, M. M. Alwakeel, and X. You, "A General 3-D Non-Stationary 5G Wireless Channel Model," *IEEE Transactions on Communications*, vol. 66, no. 7, pp. 3065–3078, July 2018.

[109] METIS, "METIS channel models deliverable 1.4 version 3," Sweden, Tech. Rep., Jul. 2015.

[110] L. Liu, C. Oestges, J. Poutanen, K. Haneda, P. Vainikainen, F. Quitin, F. Tufvesson, and P. D. Doncker, "The COST 2100 MIMO channel model," *IEEE Wireless Communications*, vol. 19, no. 6, pp. 92–99, December 2012.

[111] ITU-R, "Preliminary draft new report ITU-R M. [IMT-2020.EVAL], R15-WP5D-170613-TD-0332," Tech. Rep., Jun. 2017.

[112] B. Ai, K. Guan, G. Li, and S. Mumtaz, "mmWave massive MIMO channel modeling," in *mmWave Massive MIMO: A Paradigm for 5G*, S. Mumtaz, J. Rodriguez, and L. Dai, Eds. Academic Press, 2017, pp. 169 – 194.

[113] I. F. Akyildiz, J. M. Jornet, and C. Han, "TeraNets: ultra-broadband communication networks in the terahertz band," *IEEE Wireless Communications*, vol. 21, no. 4, pp. 130–135, August 2014.

[114] S. Priebe, M. Jacob, and T. Krner, "Calibrated broadband ray tracing for the simulation of wave propagation in mm and sub-mm wave indoor communication channels," in *European Wireless 2012; 18th European Wireless Conference 2012*, April 2012, pp. 1–10.

[115] B. Ai, K. Guan, R. He, J. Li, G. Li, D. He, Z. Zhong, and K. M. S. Huq, "On Indoor Millimeter Wave Massive MIMO Channels: Measurement and Simulation," *IEEE Journal on Selected Areas in Communications*, vol. 35, no. 7, pp. 1678–1690, July 2017.

[116] X. Zhao, S. Li, Q. Wang, M. Wang, S. Sun, and W. Hong, "Channel Measurements, Modeling, Simulation and Validation at 32 GHz in Outdoor Microcells for 5G Radio Systems," *IEEE Access*, vol. 5, pp. 1062–1072, 2017.

[117] N. A. Muhammad, P. Wang, Y. Li, and B. Vucetic, "Analytical Model for Outdoor Millimeter Wave Channels Using Geometry-Based Stochastic Approach," *IEEE Transactions on Vehicular Technology*, vol. 66, no. 2, pp. 912–926, Feb 2017.

[118] M. K. Samimi, G. R. MacCartney, S. Sun, and T. S. Rappaport, "28 GHz Millimeter-Wave Ultrawideband Small-Scale Fading Models in Wireless Channels," in *2016 IEEE 83rd Vehicular Technology Conference (VTC Spring)*, May 2016, pp. 1–6.

[119] M. K. Samimi and T. S. Rappaport, "Local multipath model parameters for generating 5G millimeter-wave 3GPP-like channel impulse response," in *2016 10th European Conference on Antennas and Propagation (EuCAP)*, April 2016, pp. 1–5.

[120] M. K. Samimi, S. Sun, and T. S. Rappaport, "MIMO channel modeling and capacity analysis for 5G millimeter-wave wireless systems," in *2016 10th European Conference on Antennas and Propagation (EuCAP)*, April 2016, pp. 1–5.

[121] M. K. Samimi and T. S. Rappaport, "Statistical Channel Model with Multi-Frequency and Arbitrary Antenna Beamwidth for Millimeter-Wave Outdoor Communications," in *2015 IEEE Globecom Workshops (GC Wkshps)*, Dec 2015, pp. 1–7.

[122] A. Torabi, S. A. Zekavat, and A. Al-Rasheed, "Millimeter wave directional channel modeling," in *2015 IEEE International Conference on Wireless for Space and Extreme Environments (WiSEE)*, Dec 2015, pp. 1–6.

[123] S. Hur, S. Baek, B. Kim, Y. Chang, A. F. Molisch, T. S. Rappaport, K. Haneda, and J. Park, "Proposal on Millimeter-Wave Channel Modeling for 5G Cellular System," *IEEE Journal of Selected Topics in Signal Processing*, vol. 10, no. 3, pp. 454–469, April 2016.

[124] T. Bai, A. Alkhateeb, and R. W. Heath, "Coverage and capacity of millimeter-wave cellular networks," *IEEE Communications Magazine*, vol. 52, no. 9, pp. 70–77, Sep. 2014.

[125] O. E. Ayach, S. Rajagopal, S. Abu-Surra, Z. Pi, and R. W. Heath, "Spatially Sparse Precoding in Millimeter Wave MIMO Systems," *IEEE Transactions on Wireless Communications*, vol. 13, no. 3, pp. 1499–1513, March 2014.

[126] A. Alkhateeb, O. E. Ayach, G. Leus, and R. W. Heath, "Channel Estimation and Hybrid Precoding for Millimeter Wave Cellular Systems," *IEEE Journal of Selected Topics in Signal Processing*, vol. 8, no. 5, pp. 831–846, Oct 2014.

[127] X. Gao, L. Dai, Z. Gao, T. Xie, and Z. Wang, "Precoding for mmWave massive MIMO," in *mmWave Massive MIMO: A Paradigm for 5G*, S. Mumtaz, J. Rodriguez, and L. Dai, Eds. Academic Press, 2017, pp. 79 – 111.

[128] I. Ahmed, H. Khammari, A. Shahid, A. Musa, K. S. Kim, E. De Poorter, and I. Moerman, "A Survey on Hybrid Beamforming Techniques in 5G: Architecture and System Model Perspectives," *IEEE Communications Surveys Tutorials*, vol. 20, no. 4, pp. 3060–3097, Fourthquarter 2018.

[129] J. Wang, Z. Lan, C. woo Pyo, T. Baykas, C. sean Sum, M. A. Rahman, J. Gao, R. Funada, F. Kojima, H. Harada, and S. Kato, "Beam codebook based beamforming protocol for multi-Gbps millimeter-wave WPAN systems," *IEEE Journal on Selected Areas in Communications*, vol. 27, no. 8, pp. 1390–1399, October 2009.

[130] C. Cordeiro, D. Akhmetov, and M. Park, "IEEE 802.11ad: Introduction and Performance Evaluation of the First Multi-gbps Wifi Technology," in *Proceedings of the 2010 ACM International Workshop on mmWave Communications: From Circuits to Networks*, ser. mmCom '10. New York, NY, USA: ACM, 2010, pp. 3–8.

[131] S. Sun and T. S. Rappaport, "Channel Modeling and Multi-Cell Hybrid Beamforming for Fifth-Generation MillimeterWave Wireless Communications," NYU Wireless, Brooklyn, New York, Technical Report TR 2018-001, May 2018. [Online]. Available: https://wireless.engineering.nyu.edu/static-homepage/tech-reports/TR2018-001_ShuSun.pdf

[132] Z. Shen, R. Chen, J. G. Andrews, R. W. Heath, and B. L. Evans, "Low complexity user selection algorithms for multiuser MIMO systems with block diagonalization," *IEEE Transactions on Signal Processing*, vol. 54, no. 9, pp. 3658–3663, Sep. 2006.

[133] E. Bjrnson, L. Sanguinetti, H. Wymeersch, J. Hoydis, and T. L. Marzetta, "Massive MIMO is a realityWhat is next?: Five promising research directions for antenna arrays," *Digital Signal Processing*, vol. 94, pp. 3–20, 2019.

[134] M. Costa, "Writing on dirty paper (Corresp.)," *IEEE Transactions on Information Theory*, vol. 29, no. 3, pp. 439–441, May 1983.

[135] R. D. Wesel and J. M. Cioffi, "Achievable rates for Tomlinson-Harashima precoding," *IEEE Transactions on Information Theory*, vol. 44, no. 2, pp. 824–831, March 1998.

[136] A. Alkhateeb, G. Leus, and R. W. Heath, "Limited Feedback Hybrid Precoding for Multi-User Millimeter Wave Systems," *IEEE Transactions on Wireless Communications*, vol. 14, no. 11, pp. 6481–6494, Nov 2015.

[137] N. Song, H. Sun, and T. Yang, "Coordinated Hybrid Beamforming for Millimeter Wave Multi-User Massive MIMO Systems," in *2016 IEEE Global Communications Conference (GLOBECOM)*, Dec 2016, pp. 1–6.

[138] S. Sun, T. S. Rappaport, and M. Shafi, "Hybrid beamforming for 5G millimeter-wave multi-cell networks," in *IEEE INFOCOM 2018 - IEEE Conference on Computer Communications Workshops (INFOCOM WKSHPS)*, April 2018, pp. 589–596.

[139] T. E. Bogale and L. B. Le, "Beamforming for multiuser massive MIMO systems: Digital versus hybrid analog-digital," in *2014 IEEE Global Communications Conference*, Dec 2014, pp. 4066–4071.

[140] M. Kim and Y. H. Lee, "MSE-Based Hybrid RF/Baseband Processing for Millimeter-Wave Communication Systems in MIMO Interference Channels," *IEEE Transactions on Vehicular Technology*, vol. 64, no. 6, pp. 2714–2720, June 2015.

[141] A. Alkhateeb, J. Mo, N. Gonzalez-Prelcic, and R. W. Heath, "MIMO Precoding and Combining Solutions for Millimeter-Wave Systems," *IEEE Communications Magazine*, vol. 52, no. 12, pp. 122–131, December 2014.

[142] J. Brady, N. Behdad, and A. M. Sayeed, "Beamspace MIMO for Millimeter-Wave Communications: System Architecture, Modeling, Analysis, and Measurements," *IEEE Transactions on Antennas and Propagation*, vol. 61, no. 7, pp. 3814–3827, July 2013.

[143] Qualcomm, "5G NR based C-V2X," last accessed: 26-02-2020. [Online]. Available: https://www.qualcomm.com/media/documents/files/5g-nr-based-c-v2x-presentation.pdf[lastaccessed:14-01-2019]

[144] V. Va, J. Choi, and R. W. Heath, "The Impact of Beamwidth on Temporal Channel Variation in Vehicular Channels and Its Implications," *IEEE Transactions on Vehicular Technology*, vol. 66, no. 6, pp. 5014–5029, June 2017.

[145] F. Khan, Z. Pi, and S. Rajagopal, "Millimeter-wave mobile broadband with large scale spatial processing for 5G mobile communication," in *2012 50th Annual Allerton Conference on Communication, Control, and Computing (Allerton)*, Oct 2012, pp. 1517–1523.

[146] N. F. Abdullah, D. Berraki, A. Ameen, S. Armour, A. Doufexi, A. Nix, and M. Beach, "Channel Parameters and Throughput Predictions for mmWave and LTE-A Networks in Urban Environments," in *2015 IEEE 81st Vehicular Technology Conference (VTC Spring)*, May 2015, pp. 1–5.

[147] H. Claussen, "Efficient modelling of channel maps with correlated shadow fading in mobile radio systems," in *2005 IEEE 16th International Symposium on Personal, Indoor and Mobile Radio Communications*, vol. 1, Sept 2005, pp. 512–516.

[148] N. Rupasinghe, Y. Kakishima, and . Gven, "System-level performance of mmWave cellular networks for urban micro environments," in *2017 XXXIInd General Assembly and Scientific Symposium of the International Union of Radio Science (URSI GASS)*, Aug 2017, pp. 1–4.

[149] A. H. Jafari, J. Park, and R. W. Heath, "Analysis of interference mitigation in mmWave communications," in *2017 IEEE International Conference on Communications (ICC)*, May 2017, pp. 1–6.

[150] G. Yang, J. Du, and M. Xiao, "Maximum Throughput Path Selection With Random Blockage for Indoor 60 GHz Relay Networks," *IEEE Transactions on Communications*, vol. 63, no. 10, pp. 3511–3524, Oct 2015.

[151] I. F. Akyildiz, J. M. Jornet, and C. Han, "Terahertz band: Next frontier for wireless communications," *Physical Communication*, vol. 12, pp. 16–32, 2014.

[152] C. Perfecto, J. D. Ser, and M. Bennis, "Millimeter-Wave V2V Communications: Distributed Association and Beam Alignment," *IEEE Journal on Selected Areas in Communications*, vol. 35, no. 9, pp. 2148–2162, Sept 2017.

[153] A. Tassi, M. Egan, R. J. Piechocki, and A. Nix, "Modeling and Design of Millimeter-Wave Networks for Highway Vehicular Communication," *IEEE Transactions on Vehicular Technology*, vol. 66, no. 12, pp. 10 676–10 691, Dec 2017.

[154] Y. Wang, K. Venugopal, A. F. Molisch, and R. W. Heath, "Analysis of Urban Millimeter Wave Microcellular Networks," in *2016 IEEE 84th Vehicular Technology Conference (VTC-Fall)*, Sept 2016, pp. 1–5.

[155] ——, "MmWave Vehicle-to-Infrastructure Communication: Analysis of Urban Microcellular Networks," *IEEE Transactions on Vehicular Technology*, vol. 67, no. 8, pp. 7086–7100, Aug 2018.

[156] M. Gao, B. Ai, Y. Niu, Z. Zhong, Y. Liu, G. Ma, Z. Zhang, and D. Li, "Dynamic mmWave beam tracking for high speed railway communications," in *2018 IEEE Wireless Communications and Networking Conference Workshops (WCNCW)*, April 2018, pp. 278–283.

[157] T. S. Rappaport, S. Sun, and M. Shafi, "Investigation and Comparison of 3GPP and NYUSIM Channel Models for 5G Wireless Communications," in *2017 IEEE 86th Vehicular Technology Conference (VTC-Fall)*, Sept 2017, pp. 1–5.

[158] J. Choi, V. Va, N. Gonzalez-Prelcic, R. Daniels, C. R. Bhat, and R. W. Heath, "Millimeter-Wave Vehicular Communication to Support Massive Automotive Sensing," *IEEE Communications Magazine*, vol. 54, no. 12, pp. 160–167, December 2016.

[159] S. Buzzi and C. D'Andrea, "On clustered statistical MIMO millimeter wave channel simulation," May 2016, last accessed: 26-02-2020. [Online]. Available: https://arxiv.org/abs/1604.00648.

[160] J. Zhang, Y. Huang, T. Yu, J. Wang, and M. Xiao, "Hybrid Precoding for Multi-Subarray Millimeter-Wave Communication Systems," *IEEE Wireless Communications Letters*, vol. 7, no. 3, pp. 440–443, June 2018.

[161] S. Ju and T. S. Rappaport, "Millimeter-wave Extended NYUSIM Channel Model for Spatial Consistency," in *2018 IEEE Global Communications Conference (GLOBECOM)*. IEEE, Aug. 2018, pp. 1–6.

[162] S. Mukherjee, S. S. Das, A. Chatterjee, and S. Chatterjee, "Analytical Calculation of Rician K-Factor for Indoor Wireless Channel Models," *IEEE Access*, vol. 5, pp. 19 194–19 212, 2017.

[163] M. S. A. Abdulgader and L. Wu, "The Physical layer of the IEEE 802.11p WAVE Communication Standard: The Specifications and Challenges," in *Proceedings of the World Congress on Engineering and Computer Science (WCECS)*, vol. II, San Fransisco, USA, Oct. 2014, pp. 1–8.

[164] 3GPP. LTE physical layer framework for performance verification. TSG RAN1 48, R1070674. Last accessed: 26-02-2020. [Online]. Available: http://www.3gpp.org/DynaReport/TDocExMtg--R1-48--26033.htm

[165] ——, " TS 38.211 Technical Specification Group Radio Access Network; NR, Physical channels and modulation v15.1.0," 2018, last accessed: 26-02-2020. [Online]. Available: http://www.3gpp.org/ftp//Specs/archive/38_series/38.211/

[166] C. Lin and G. Y. Li, "Energy-Efficient Design of Indoor mmWave and Sub-THz Systems With Antenna Arrays," *IEEE Transactions on Wireless Communications*, vol. 15, no. 7, pp. 4660–4672, July 2016.

[167] X. Gao, L. Dai, S. Han, C. L. I, and R. W. Heath, "Energy-Efficient Hybrid Analog and Digital Precoding for MmWave MIMO Systems With Large Antenna Arrays," *IEEE Journal on Selected Areas in Communications*, vol. 34, no. 4, pp. 998–1009, April 2016.

[168] Z. Wang, J. Zhu, J. Wang, and G. Yue, "An Overlapped Subarray Structure in Hybrid Millimeter-Wave Multi-User MIMO System," in *2018 IEEE Global Communications Conference (GLOBECOM 2018)*, Abu Dhabi, United Arab Emirates, Dec. 2018, pp. 1–6.

[169] S. Kutty and D. Sen, "Beamforming for Millimeter Wave Communications: An Inclusive Survey," *IEEE Communications Surveys Tutorials*, vol. 18, no. 2, pp. 949–973, Secondquarter 2016.

[170] S. Han, C. L. I, Z. Xu, and C. Rowell, "Large-scale antenna systems with hybrid analog and digital beamforming for millimeter wave 5G," *IEEE Communications Magazine*, vol. 53, no. 1, pp. 186–194, Jan. 2015.

[171] N. Song, T. Yang, and H. Sun, "Overlapped Subarray Based Hybrid Beamforming for Millimeter Wave Multiuser Massive MIMO," *IEEE Signal Processing Letters*, vol. 24, no. 5, pp. 550–554, May 2017.

[172] N. Zorba and H. S. Hassanein, "Grassmannian beamforming for Coordinated Multipoint transmission in multicell systems," in *38th Annual IEEE Conference on Local Computer Networks - Workshops*, Oct 2013, pp. 65–69.

[173] A. Pizzo and L. Sanguinetti, "Optimal design of energy-efficient millimeter wave hybrid transceivers for wireless backhaul," in *2017 15th International Symposium on Modeling and Optimization in Mobile, Ad Hoc, and Wireless Networks (WiOpt)*, May 2017, pp. 1–8.

[174] X. Ge, J. Yang, H. Gharavi, and Y. Sun, "Energy Efficiency Challenges of 5G Small Cell Networks," *IEEE Communications Magazine*, vol. 55, no. 5, pp. 184–191, May 2017.

[175] S. Buzzi and C. D'Andrea, "Are mmWave Low-Complexity Beamforming Structures Energy-Efficient? Analysis of the Downlink MU-MIMO," in *2016 IEEE Globecom Workshops (GC Wkshps)*, Dec 2016, pp. 1–6.

[176] C. Xiong, G. Y. Li, S. Zhang, Y. Chen, and S. Xu, "Energy- and Spectral-Efficiency Tradeoff in Downlink OFDMA Networks," *IEEE Transactions on Wireless Communications*, vol. 10, no. 11, pp. 3874–3886, November 2011.

[177] K. M. S. Huq, S. Mumtaz, J. Rodriguez, and R. Aguiar, "Overview of Spectral- and Energy-Efficiency Trade-off in OFDMA Wireless System," in *Green Communication for 4G Wireless Systems*, S. Mumtaz and J. Rodriguez, Eds. River Publishers, Aalborg, 2013.

[178] O. E. Ayach, R. W. Heath, S. Rajagopal, and Z. Pi, "Multimode precoding in millimeter wave MIMO transmitters with multiple antenna sub-arrays," in *2013 IEEE Global Communications Conference (GLOBECOM)*, Dec 2013, pp. 3476–3480.

[179] S. Sun, T. S. Rappaport, M. Shafi, P. Tang, J. Zhang, and P. J. Smith, "Propagation Models and Performance Evaluation for 5G Millimeter-Wave Bands," *IEEE Transactions on Vehicular Technology*, vol. 67, no. 9, pp. 8422–8439, Sep. 2018.

[180] S. Mumtaz, J. M. Jornet, J. Aulin, W. H. Gerstacker, X. Dong, and B. Ai, "Terahertz Communication for Vehicular Networks," *IEEE Transactions on Vehicular Technology*, vol. 66, no. 7, pp. 5617–5625, July 2017.

[181] K. M. S. Huq, J. M. Jornet, W. H. Gerstacker, A. Al-Dulaimi, Z. Zhou, and J. Aulin, "THz Communications for Mobile Heterogeneous Networks," *IEEE Communications Magazine*, vol. 56, no. 6, pp. 94–95, June 2018.

[182] L. Zhao, X. Li, B. Gu, Z. Zhou, S. Mumtaz, V. Frascolla, H. Gacanin, M. I. Ashraf, J. Rodriguez, M. Yang, and S. Al-Rubaye, "Vehicular Communications: Standardization and Open Issues," *IEEE Communications Standards Magazine*, vol. 2, no. 4, pp. 74–80, December 2018.

[183] C. Han and Y. Chen, "Propagation Modeling for Wireless Communications in the Terahertz Band," *IEEE Communications Magazine*, vol. 56, no. 6, pp. 96–101, June 2018.

[184] S. Priebe and T. Kurner, "Stochastic Modeling of THz Indoor Radio Channels," *IEEE Transactions on Wireless Communications*, vol. 12, no. 9, pp. 4445–4455, Sep. 2013.

[185] I. F. Akyildiz and J. M. Jornet, "Realizing Ultra-Massive MIMO (1024 x 1024) communication in the (0.06-10) Terahertz band," *Nano Communication Networks*, vol. 8, pp. 46–54, 2016, electromagnetic Communication in Nano-scale.

[186] K. Tekbiyik, A. R. Ekti, G. K. Kurt, and A. Grin, "Terahertz band communication systems: Challenges, novelties and standardization efforts," *Physical Communication*, vol. 35, p. 100700, 2019.

[187] C. Han, J. M. Jornet, and I. Akyildiz, "Ultra-Massive MIMO Channel Modeling for Graphene-Enabled Terahertz-Band Communications," in *2018 IEEE 87th Vehicular Technology Conference (VTC Spring)*, June 2018, pp. 1–5.

[188] E. de Carvalho, A. Ali, A. Amiri, M. Angjelichinoski, and R. W. Heath Jr., "Non-Stationarities in Extra-Large Scale Massive MIMO," *CoRR*, vol. abs/1903.03085, 2019. [Online]. Available: http://arxiv.org/abs/1903.03085

[189] A. Faisal, H. Sarieddeen, H. Dahrouj, T. Y. Al-Naffouri, and M.-S. Alouini, "Ultra-Massive MIMO Systems at Terahertz Bands: Prospects and Challenges," *arXiv e-prints*, p. arXiv:1902.11090, Feb 2019.

[190] C. Huang, A. Zappone, G. C. Alexandropoulos, M. Debbah, and C. Yuen, "Reconfigurable Intelligent Surfaces for Energy Efficiency in Wireless Communication," *arXiv e-prints*, p. arXiv:1810.06934, Oct 2018.

[191] A. Taha, M. Alrabeiah, and A. Alkhateeb, "Enabling Large Intelligent Surfaces with Compressive Sensing and Deep Learning," *CoRR*, vol. abs/1904.10136, 2019. [Online]. Available: http://arxiv.org/abs/1904.10136

[192] M. G. Kibria, K. Nguyen, G. P. Villardi, O. Zhao, K. Ishizu, and F. Kojima, "Big Data Analytics, Machine Learning, and Artificial Intelligence in Next-Generation Wireless Networks," *IEEE Access*, vol. 6, pp. 32 328–32 338, 2018.

[193] C. Jiang, H. Zhang, Y. Ren, Z. Han, K. Chen, and L. Hanzo, "Machine Learning Paradigms for Next-Generation Wireless Networks," *IEEE Wireless Communications*, vol. 24, no. 2, pp. 98–105, April 2017.